Imaging of intracellular trafficking of the HIV-1 nucleocapsid protein

Iryna Lysova

▶ **To cite this version:**

Iryna Lysova. Imaging of intracellular trafficking of the HIV-1 nucleocapsid protein. Virology. Université de Strasbourg, 2017. English. NNT : 2017STRAJ092 . tel-02917956

HAL Id: tel-02917956
https://theses.hal.science/tel-02917956

Submitted on 20 Aug 2020

HAL is a multi-disciplinary open access archive for the deposit and dissemination of scientific research documents, whether they are published or not. The documents may come from teaching and research institutions in France or abroad, or from public or private research centers.

L'archive ouverte pluridisciplinaire **HAL**, est destinée au dépôt et à la diffusion de documents scientifiques de niveau recherche, publiés ou non, émanant des établissements d'enseignement et de recherche français ou étrangers, des laboratoires publics ou privés.

UNIVERSITÉ DE STRASBOURG

ÉCOLE DOCTORALE DES SCIENCES DE LA VIE ET DE LA SANTÉ

UMR CNRS 7312 Laboratory of Biophotonics and Pharmacology

THÈSE présentée par :

Iryna LYSOVA

soutenue le : **07 Juliet 2017**

pour obtenir le grade de : **Docteur de l'université de Strasbourg**
Discipline/ Spécialité : Sciences de la vie/Biophysique

Imagerie quantitative du traffic intracellulaire de VIH-1

THÈSE dirigée par :
M. MELY Yves Professeur, université de Strasbourg
M. DMITRUK Igor Professeur, université nationale Taras Chevtchenko de Kyiv

RAPPORTEURS :
Mme BONNEAU Stéphanie Maitre de Conférences, université Pierre et Marie Curie
M. SEKSEK Olivier Chargé de Recherche CNRS, université Paris Sud

---

AUTRES MEMBRES DU JURY :
M. RUFF Marc Directeur de recherches CNRS, IGBMC
Mme ANTON Halina Chargé de Recherche CNRS, université de Strasbourg

Table of contents

List of abbreviations

a.a.	amino acids
AFM	atomic force microscopy
AIDs	acquired immunodeficiency
ATP	adenosine triphosphate
AZT	azidothymidine
CA	capsid
CCD	camera coupled charged devices
CLEM	correlative light electron microscopy
CTD	carboxy-terminal domain
DAB	3,3'-diaminobenzidine
EDT	ethandithiol
EM	electron microscopy
EMCCD	electron multiplier CCD
Env	envelope
ER	endoplasmic reticulum
ESCRT	endosomal sorting complex required for transport
ET	electron tomography
FG	phenylalanine-glycine
FIB-SEM	focused ion beam-sEM
FPs	fluorescent proteins
Gag	group specific antigen
GFP	green fluorescent protein
Gp	glycoprotein
gRNA/vRNA	genomic/viral RNA
GSD	ground-state-depletion microscopy
GTP	guanosine triphosphate
HIV	human immunodeficiency
HR	high resolution
HTLV	human T-lymphotropic virus
IN	integrase
KPN	karyopherin
LTR	long terminal repeat
MA	matrix
MEA	cysteamine
NA	nucleic acids
NA	numerical aperture
NCp7	nucleocapsid protein 7super-resolution
NES	nuclear export signal
NLS	nuclear localization signal
NPC	nuclear pore complex
NTD	amino-terminal domain
Nup	nucleoporins
PAFPs	photoactivatable fluorescent protein
PAINT	point accumulation for imaging in nanoscale topography
PALM	photoactivation localization microscopy
PALMIRA	PALM with independently running acquisition
PBS	primary binding site
PBS	phosphate buffer saline

PIC	preintegration complex
Pol	polymerase
PPT	poly purine tract
PPTc	poly purine tract central
PR	protease
PSF	point spread function
QDs	quantum dots
R	repeat
Ran	Ras-related nuclear protein
RESOLFT	reversible saturable optical linear fluorescence transitions
RNP	ribonucleoprotein complex
RRE	rev response element
RT	reverse transcriptase
RT	reverse transcription
RTC	reverse transcription complex
SEM	scanning electron microscopy
SIM	structured illumination microscopy
SL	stem-loops
SP	spacer to peptide
SR	super-resolution
ssDNA/dsDNA	single/double stranded DNA
SSIM	saturated structured illumination microscopy
ssTEM	serial-section TEM
STED	state stimulated emission depletion
STORM	stochastic optical reconstruction microscopy
SVT	single virus tracing
TAR	transactivation response element
TC	tetracystein
TEM	transmission electron microscopy
TIRF	total internal fluorescence illumination
U	unique
UTR	untranslated region
vDNA	viral DNA
VLP	virus like particle
Vpr	viral protein R
VSV	vesicular stomatitis virus
ZF	zinc finger
βME	β-mercaptoethanol

Chapter 1: Introduction

1.1. AIDS and HIV

Acquired immune-deficiency syndrome (AIDS), is a disease caused by the Human Immunodeficiency Virus (HIV) types 1 and 2. These viruses attack specifically the cells of the immune system. The infection causes severe immunodeficiency and the infected individual becomes vulnerable to HIV related opportunistic infections. The first period of infection is characterized by acute infection symptoms including fever, inflammation of the throat and of the lymph nodes. Then, follows a latency period that can last from several weeks to several years. At the final stage of infection, the number of immune cells strongly decreases, which leads to secondary infections that lead to death.

HIV belongs to the retroviral family and lentiviral subgroup. Retroviruses are enveloped viruses. A single-stranded positive sense RNA molecule codes their genome. They express a specific viral enzyme called reverse transcriptase, which catalyzes the conversion of viral RNA into DNA.

First cases of AIDS were reported in 1981 with the cases of *Pneumocystis carinii* and Kaposi sarcoma in the USA (1981). Shortly after, a new virus called lymphadenopathy-associated virus (LAV) was discovered in 1983 in Institute Pasteur, Paris by Barre-Sinoussi (Barre-Sinoussi, Chermann et al. 1983). One year later, Popovic and Gallo studied the development of infected cells and described the Human T-lymphotropic virus type III (HTLV-III) (Gallo, Salahuddin et al. 1984; Popovic, Read-Connole et al. 1984). The International Committee on the Taxonomy of viruses (ICTV) referred these viruses and other viruses from patients with AIDS as HIV in 1986. Almost in the same year, another retrovirus (later assigned as HIV-2) was discovered in patients from West Africa. HIV-1 is found worldwide whereas HIV-2 is restricted to the West African region. Soon after isolation of the HIV viral particles, its genetic information and its specific interactions with CD4 cells were actively studied. The first antiviral treatment based on the azidothymidine (AZT), a specific inhibitor of the reverse transcriptase, was developed in 1987 (Furman, Fyfe et al. 1986; Yarchoan, Klecker et al. 1986; Brook 1987). Figure 1.1.1. represents the crucial points of HIV-1 history from the first detection in 1981 until the development of a combined treatment leading to the decrease of death rates in 2000s. In 2008, the French scientists, F.Barre-Sinoussi and L. Montagnier received the Nobel Prize for HIV-1 discovery.

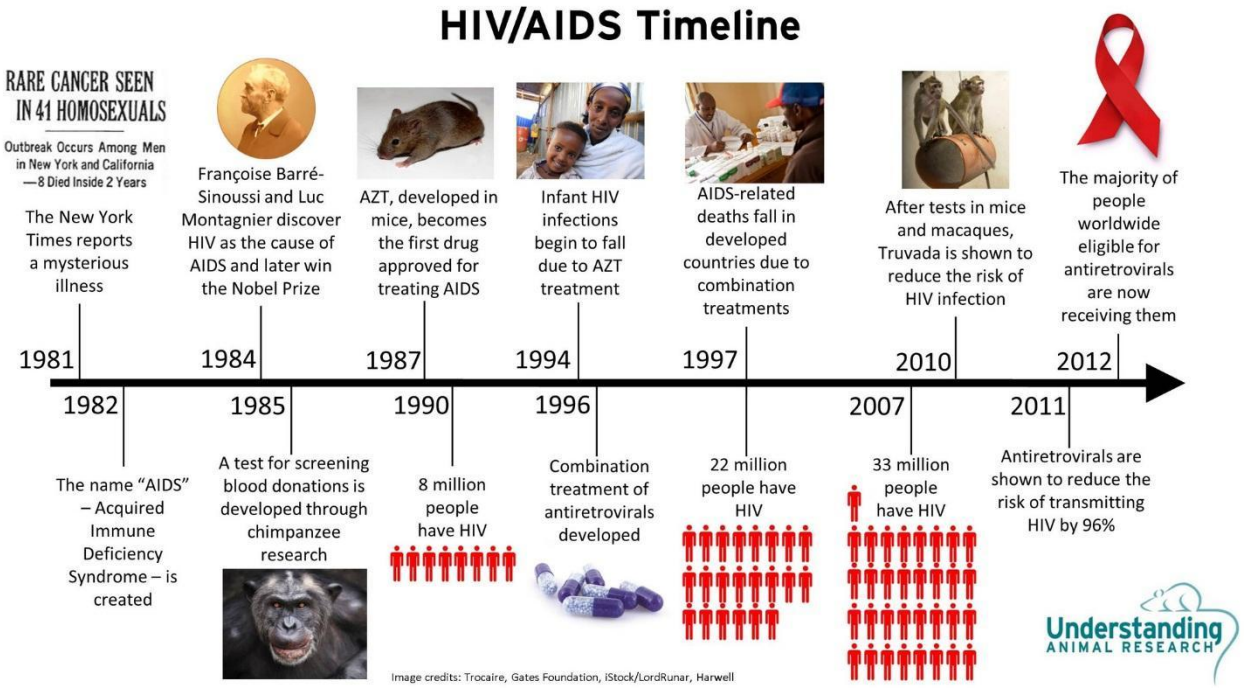

Figure 1.1.1. History of HIV. From the detection of the illness (1981) until first treatment (AZT, 1987) passed just 6 years. Despite extensive research efforts on AIDS/HIV during the past 30 years, more than 30 million people are still infected and no drug is able to eradicate the virus from infected patients.

Progress of HIV infection into AIDS is related to the fact that the virus infects immune cells that do not divide (Fig. 1.1.2.). HIV infected CD4+T cells lose their function and are not replaced by new ones. During the early stages of HIV infection (within 3-12 weeks), the level of CD4+T cells decreases but the hyperactivated immune system maintains the lymphocytic homeostasis by increasing the production of CD8+T cells (Margolick, Munoz et al. 1995). During this period, the anti-HIV-1 antibodies are not yet present in the blood, so that the diagnosis can only be made by detection of viral RNA or p24 (capsid protein of HIV) in the plasma of infected persons. This first acute phase is followed by a latent period that can last up to several years (Pantaleo, Graziosi et al. 1993). Finally, the immune system collapses and the virus mutations activate the latent HIVs. A characteristic of this phase is lymphadenopathy, which coincides with a low viral replication in lymph nodes and accumulation of virions at the surface of follicular dendritic cells (Burton, Keele et al. 2002). The symptomatic phase or AIDS is declared when the number of CD4 + T cells is below 200 cells / μL (normal value 600-1200 cells / μL). At this stage, the infected person develops opportunistic infections and malignant diseases (lymphoma or non-Hodgkin KS) which cause the patient death (Pantaleo, Graziosi et al. 1993).

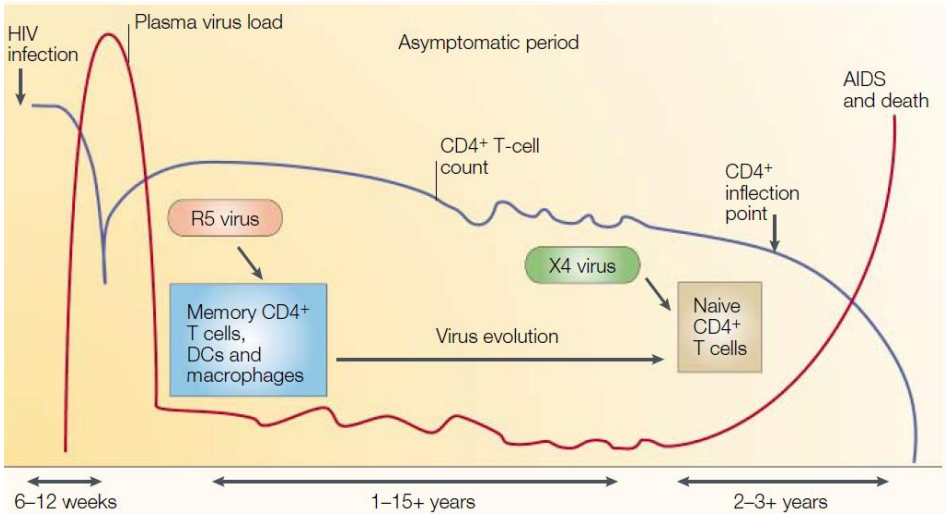

Figure 1.1.2. Course of HIV infection. A clear dependence between the load of viruses (red line) and number of CD4+ cells (blue line) is observed in non-treated cases (Adapted from (Rowland-Jones and Whittle 2007)).

Since its discovery almost 30 years ago, nearly 25.3 million people died of AIDS-related illnesses (UNAIDS, 2015: fact sheet: 2014 statistics). In 2014, 0.8% of the global population was living with HIV (UNAIDS, 2015: How AIDS changed everything). This illness caused two millions of deaths per year all around the world. The peak of the epidemic was detected in 1999 (UNAIDS report on the global AIDS epidemic 2010, 2012). Advances in antiretroviral treatment, based on combinations of drugs, cause the decline of the disease rate.

1.2. Subtypes of HIV

The genome of HIV was sequenced in 1985. The genetic information was used for the characterization of the origin and evolution of the virus (Sanchez-Pescador, Power et al. 1985). The sequence revealed that HIV-1 and HIV-2 might result from a cross-species transmission of the simian immunodeficiency virus (SIV) (Hirsch, Olmsted et al. 1989; Peeters, Honore et al. 1989).

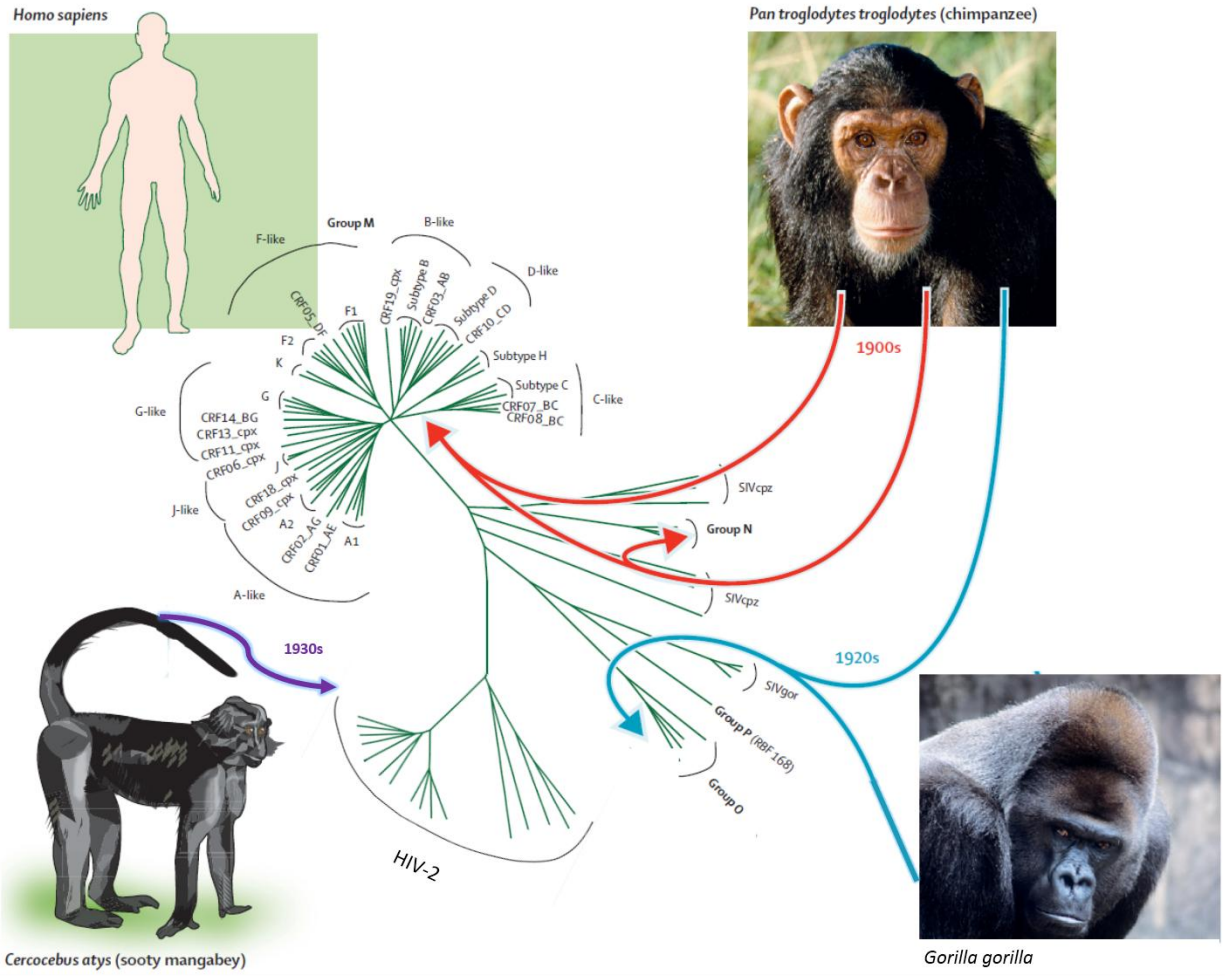

Figure 1.2.1. Origins of HIV. Genetic diversity in HIV-1 M, N, O, and P and HIV-2 with patterns of cross-species transmissions. Indicated years are the estimated times of recent common ancestors of HIV-1 and HIV-2 (Adapted from (Tebit and Arts 2011)).

The diversity of genetically HIV-related groups is the result of the viral phylogeny (evolution) in distinct geographic regions (Fig. 1.2.1.). Nowadays four viral groups (called M, N, O and P) are assigned for HIV-1. The group M (further divided into 9 subtypes) is responsible for 98% of worldwide infection. The origin of the HIV-1 virus is still debated. Several studies revealed that HIV-1 is close to the simian immunodeficiency virus (SIV) found in the captive chimpanzees (Huet, Cheynier et al. 1990). However, only M and N groups were shown to be of the chimpanzees region, whereas no ape virus closely similar to O group was found. Moreover, a similar virus was detected in gorillas (Van Heuverswyn, Li et al. 2006). A smaller viral load (Popper, Sarr et al. 2000) and a frequent arrest of the infection in the latent phase without progress to AIDS (Rowland-Jones and Whittle, 2007) characterize the HIV-2 subtype. Similarly, the SIV strains found in the sooty mangabeys is non-pathogenic in its natural host (Silvestry, 2005)(Silvestri, Fedanov et al. 2005) (Fig. 1.2.1). HIV-2 virus is classified into 8 (A – H) lineages with independent host transfer. Groups A and B are identified to be the most spread among humans, other 6 subtypes are rare and are thought to be ‘dead-end’ transmissions.

1.3. HIV-1: structure and functions of viral components

Mature HIV-1 virion is a spherical particle of 90-120 nm. It contains two strands of viral RNA, viral proteins and few host cell proteins. All these components are surrounded by a lipid bilayer (derived from the host cell membrane) covered with two types of glycoproteins (gp120 and gp41). Under the lipid bilayer, the matrix shell is composed of ~2000 matrix (MA) proteins. The mature viral particle contains the conical viral capsid, composed of capsid proteins (CA) organized in a fullerene-like structure. The capsid contains the genomic RNA dimer (9.2 kb), stabilized by the nucleocapsid proteins (NCp7), viral enzymes (reverse transcriptase, integrase and Protease) (Frankel and Young 1998; Turner and Summers 1999) and accessory proteins (Vpr, Vif and Nef) (Figure 1.3.1.). Viral particles contain also cellular components such as tRNA ^{Lys3} (Kleiman and Cen 2004), actin (Ott, Coren et al. 2003; Chertova, Chertov et al. 2006), ribosomal proteins (Mekdad, Boutant et al. 2016), and cyclophilin A (Braaten, Franke et al. 1996).

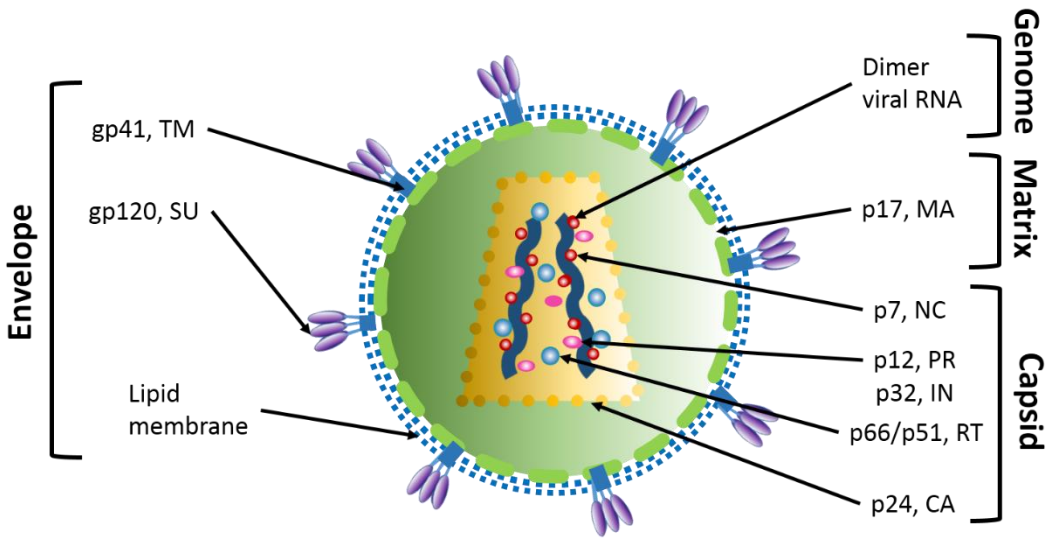

Figure 1.3.1. Structure of the mature HIV virion. Main structural departments of the virion are: envelope, matrix and capsid containing viral genome.

1.3.1. Viral genome

Viral RNA

The genome of HIV-1 consists of two copies of positive-sense single stranded RNA molecules (9193 nucleotides) (Wain-Hobson 1998) that form a stable dimer form, involving the 5' dimer linkage structure (DLS). It is produced after integration of the viral DNA into the host

cell genome and after transcription by cellular polymerases. The architecture and secondary structure of the genome were resolved (Watts, Dang et al. 2009).

The viral genome contains both coding and non-coding elements. The three major coding regions correspond to polyproteins *gag*, *pol* and *env (*representing the structural and enzymatic proteins*)*. It codes also for the regulatory proteins (Tat, Rev) and auxiliary proteins (Nef, Vif, Vpr and Vpu). Coding regions are flanked at both ends by noncoding regions and untranslated regions (UTR): 5'-UTR and 3'-UTR (Coffin, Hughes et al. 1997)(Fig. 1.3.2.). During reverse transcription, the vRNA is used as a template for the synthesis of proviral DNA and UTR regions became LTR (Long Terminal Repeat), which are important during the integration and transcription processes.

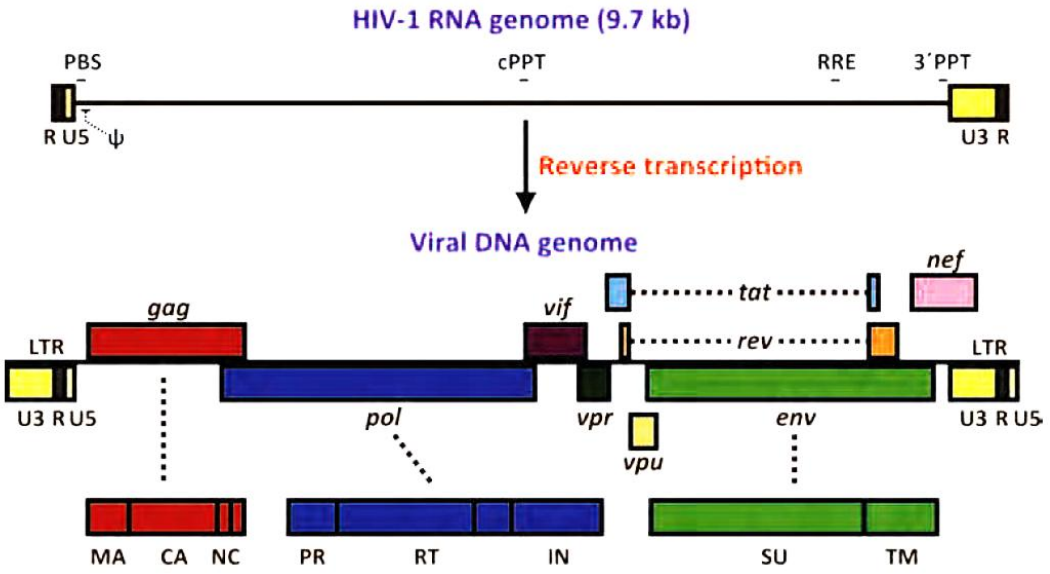

Figure 1.3.2. HIV-1 genome. The viral genomic RNA contains coding regions, which are flanked by the non-translated regions UTR (UnTranslated Region). During reverse transcription, the viral RNA is reverse transcribed into the viral DNA. The three main central regions code for *gag*, *pol* and *env*, which encode the structural (MA, CA, NC), enzymatic (PR, RT, IN) and envelope (SU, TM) proteins (Suzuki and Suzuki 2011).

The **5'-UTR region** is the most conserved part of the HIV-1 genome. It plays an important role during reverse transcription, splicing, packaging and dimerization of the vRNA (Russell, Liang et al. 2004). It is composed of the R (Repeat), U5 (unique 5), PBS (Primary Binding Site), and the encapsidation sequence (called Ψ) (Fig. 1.3.3.).

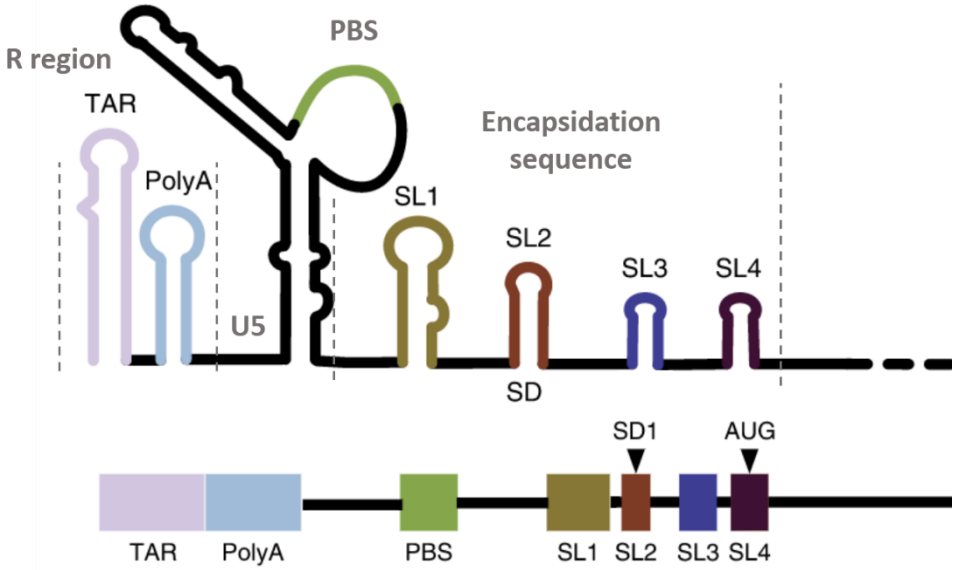

Figure 1.3.3. 5'UTR region of the HIV-1 genome. R region is composed of TAR and PolyA loops, latter is followed by the U5 and PBS regions. Encapsidation sequence comprises 4 stem-loops and psi region (Adapted from Smyth, 2015).

The R sequence, found in two identical copies at the 5' and 3'termini of the HIV-1 genome, is composed of two stem-loops, the Transactivation Response element (TAR) and the poly (A) hairpin. The TAR sequence, composed of 57 nucleotides is the Tat interaction site and is crucial for the initiation of reverse transcription (Peterlin, Luciw et al. 1986; Harrich, Ulich et al. 1996). The PolyA stem-loop contains the AAUAAA polyadenylation signal (Berkhout 1996) that induces the addition of the poly-A tail at the 3' terminus of the messenger RNA (Klasens, Thiesen et al. 1999).

The **U5 region** is a sequence of 85 nucleotides located at the 5□-end of the gRNA and is the first transcribed sequence during reverse transcription.

The **PBS (Primer Binding Site)** is composed of 18 nucleotides and is complementary to the 18 3'-terminal of $tRNA^{Lys3}$ which is the primer of the reverse transcription (Mak and Kleiman 1997; Kleiman 2002).

The **encapsidation sequence** is composed of 4 stem-loops (SL1-SL4) and is located next to the PBS and includes the starting codon for *gag* translation (AUG).

- SL1 contains the Dimer Initiation Site (DIS), a sequence of six nucleotides (GUGCAC) implicated in the dimerization of the viral RNA (Skripkin, Paillart et al. 1994)
- SL2 has a major splice donor site called "SD" where all transcripts of HIV-1 are cleaved generating various viral mRNA.

- SL3 contains the packaging signal (Ψ) responsible for vRNA encapsidation during the assembly of the newly formed virions (Lever, Gottlinger et al. 1989)
- SL4 contains the initiation codon of *gag* translation.

Other non-coding regions of the viral genome are **PPT** (Poly Purine Tract), **PPTc** (Poly Purine Tract central) and **RRE** (Rev Response Element). PPT and PPTc are regions with high purine content. They are resistant to the RNase H activity of the reverse transcriptase and serve as primers for the synthesis of plus-strand DNA (Charneau, Alizon et al. 1992). PPT_C is also responsible for the formation of the DNA flap in the pre-integration complex (PIC), a structure that may play an important role during the nuclear import of the PIC (Arhel, Souquere-Besse et al. 2007; Riviere, Darlix et al. 2010). The RRE segment is a ~ 350-nucleotide sequence located in the *env* gene. It interacts with the Rev protein, which allows the nuclear export of non-spliced or single-spliced RNAs (Farjot, Sergeant et al. 1999).

Proviral DNA

The HIV-1 proviral DNA in its integrated form is approximately 9.8 kb in length. The sequence is flanked on both ends by the Long Terminal Repeats (LTRs) that are crucial for the integration and the transcription of the vDNA. The coding genes of HIV are located in the central region of the proviral DNA and encode three major polyproteins- Gag (Group specific antigen), Pol (polymerase), and Env (envelope), as well as the regulatory proteins (Tat, Rev) and the accessory proteins (Vpu, Vpr, Vif, Nef) (Frankel and Young 1998; Freed 2001). The structural proteins are further cleaved. The matrix, capsid, nucleocapsid protein, p6, SP1 and SP2 peptide result from the cleavage of the Gag polyprotein. Pol (polymerase) provides the protease (PR), reverse transcriptase (RT) and integrase (IN). Env (envelope), cleaved by a cellular protease, generates the envelope glycoproteins gp120 and gp41.

1.3.2. Structural protein Gag

The HIV-1 *gag* gene encodes a 55 kDa Gag polyprotein that is the principal structural unit able to form the viral particles at the cell plasma membrane. This protein is composed of several domains that are cleaved by the viral protease during the maturation of the virus. This cleavage is a complex and highly regulated process (Pettit, Lindquist et al. 2005) . The products of the proteolytic cleavage of Gag are MA, CA, NC and the low molecular products SP1, SP2 and p6 (Fig. 1.3.4.).

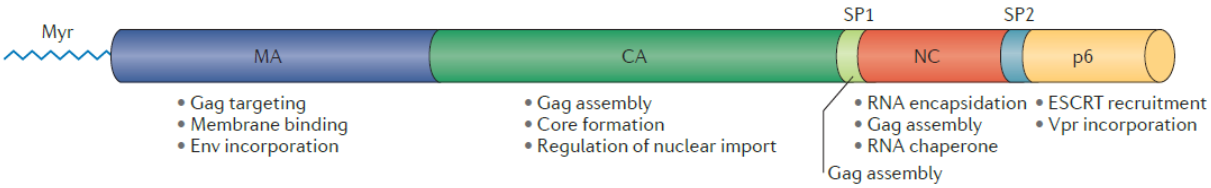

Figure 1.3.4. Map of the Gag precursor polyprotein and major functions of its domains. Due to its myristilated region and basic domain, MA allows stable anchoring of Gag at the plasma membrane. The CA domain is responsible for Gag-Gag interactions and the formation of the viral core. The NC region binds specifically the viral RNA, acts as a chaperone of nucleic acids and protects the viral RNA. P6 is implicated in the release of newly formed viral particles (Adapted from (Freed 2015)).

Matrix

The matrix protein (132 amino acids) presents five α-helices, two short 3_{10} helical stretches and a three-strand mixed β-sheet (Massiah, Starich et al. 1994; Matthews, Mikhailov et al. 1996). In the mature viral particle, the MA protein lines the inner surface of the viral envelope (Frankel and Young 1998). This multifunctional protein is implicated in early and late stages of the viral life cycle. In the early stages, p17 participates in the preintegration of viral complex in the host cell nucleus (Bukrinskaya, Vorkunova et al. 1992; Bukrinsky, Haggerty et al. 1993) . During the assembly step, the basic residues of the MA domain of Gag interact electrostatically with the inner leaflet of the plasma membrane (Saad, Miller et al. 2006; Saad, Loeliger et al. 2007). Additional contribution to Gag binding att the plasma membrane is ensured by the myristic acid moiety (Myr) that anchors the Gag polyprotein to the phosphatidylinositol rich regions of the inner leaflet of the plasma membrane (Ono, Ablan et al. 2004; Saad, Miller et al. 2006). Furthermore, the Highly Basic Region (HBR) platform allows MA to bind the gRNA in a non-specific manner, suggesting the participation of MA in the recruitment of viral and cellular RNA during assembly (Ott, Coren et al. 2005; Rulli, Hibbert et al. 2007).

Capsid

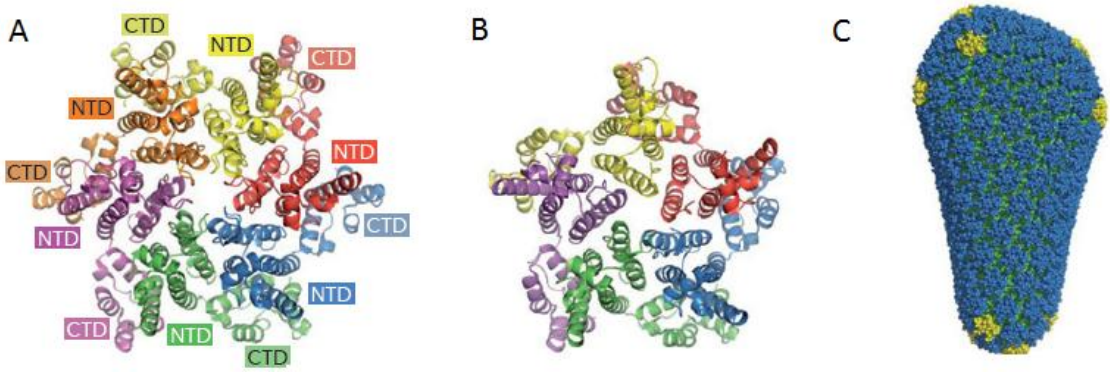

Figure 1.3.5. HIV-1 CA spatial organization. Crystal structures of hexameric (A) and pentameric (B) CA assemblies. Individual proteins are colored. Each protein contains NTD and CTD regions. (C) 3D representation of the HIV-1 capsid model, NTDs of hexameric and pentameric regions are shown in blue and yellow, respectively and CTD are green (Pornillos, Ganser-Pornillos et al. 2011).

CA is a 231 amino acids protein, composed of an amino-terminal domain (NTD) that is connected by a linker with a 3_{10}-helix to the carboxy-terminal domain (CTD) (Gitti, Lee et al. 1996; Gamble, Yoo et al. 1997)(Fig. 1.3.5.). CTD is implicated in Gag-Gag multimerization (Briggs and Krausslich 2011), and plays a role in the stabilization of Gag oligomers during the assembly (Tanaka, Robinson et al. 2015). In the mature HIV-1, ~1200 CA molecules are organized in a cone like shell (Pornillos, Ganser-Pornillos et al. 2011; Sundquist and Krausslich 2012; Zhao, Perilla et al. 2013). In the cone, the NTD and CTD regions are positioned outside and inside the capsid, respectively (Meng, Zhao et al. 2011). The broad end contains the high-density region formed by the ribonucleoprotein complex (RNP). The narrow end is in contact with the MA protein (Li, Hill et al. 2000; Mayo, Huseby et al. 2003; Briggs and Krausslich 2011; Zhao, Perilla et al. 2013). By interacting with the Nups, the CA protein is probably involved in the nuclear import of the viral genome (Dismuke and Aiken 2006).

Nucleocapsid

The HIV-1 nucleocapsid proteins (NC) are characterized by two zinc fingers similar to the zinc-finger motifs typical of DNA binding proteins. The NC is a small, 55 amino acid, (7 kDa) protein that exists as a functional domain of Gag and as a free protein in its mature form. NC shows a nucleic acid chaperone activity. Detailed structure and functions of NCp7 will be discussed below.

Protein p6, peptides SP1 and SP2

The p6 protein consists of 52 amino acids and is located at the C-terminus of the Gag polyprotein. P6 interacts with several cellular proteins of the ESCRT (Endosomal Sorting Complex Required for Transport) family and is required for the viral release (Huang, Orenstein et al. 1995).

SP1 and SP2 spacer peptides that separate the CA from NC and the NC from the P6, respectively. SP1 is involved in Gag multimerization (Datta, Temeselew et al. 2011). The function of SP2 is less defined.

1.3.3. Enzymatic proteins

HIV-1 enzymatic proteins are the products of the gag-pol gene translation. This gene encodes for the precursor Pr160Gag-Pol polyprotein, produced as a result of the programmed ribosomal frameshift (5 % frequency) during the translation of Gag/Gag-Pol mRNA. As a result, the Gag to Gag-Pol ratio in the cell is 20 to 1.

The first enzymatic HIV-1 protein structurally characterized was the viral **protease** (PR) (Miller, Schneider et al. 1989). PR is released from the $Pr160^{Gag\text{-}Pol}$ by an autocatalytic reaction (Farmerie, Loeb et al. 1987; Jacks, Power et al. 1988). The enzyme is a homodimer, stabilized by an antiparallel β-sheet. The active site of PR is localized at the interface between the two subunits (Navia, Fitzgerald et al. 1989) and bears the catalytic triad, which is responsible for PR cleavage activity. During the maturation of viral particles, PR participates in the proteolytic processing and cleavage of Gag/GagPol (Prabu-Jeyabalan, Nalivaika et al. 2002; Alvizo, Mittal et al. 2012), that results in the formation of mature and ready for infection viruses.

Reverse transcriptase (RT) is a flexible DNA polymerase. The mature form of the protein is a heterodimer, composed of two polypeptide chains p66 and p51. Reverse transcriptase drives the synthesis of the double-stranded DNA (dsDNA) genome from the plus-stranded RNA (Hu and Hughes 2012). In addition to its DNA- and RNA-dependent DNA polymerase activity, the reverse transcriptase exhibits also an endonuclease activity (RNase H) that degrades the RNA template in the RNA/DNA duplex. Reverse transcription takes place in the cytosol of infected cells after viral entry.

HIV-1 **integrase (IN)** is composed of three structural domains, the N-terminal, central catalytic and N-terminal domain. Inside HIV-1, IN can be found in a tetramer form (Jenkins, Engelman et al. 1996). IN is crucial for the incorporation of the viral DNA into the genome of the host cell trough the IN strand transfer reaction (Wu, Liu et al. 1999; Zhu, Dobard et al. 2004; Tekeste, Wilkinson et al. 2015) by stimulating both the initiation and elongation steps of the (Dobard, Briones et al. 2007). Finally, IN may also play a role in the nuclear import of the PIC by interacting with the nucleoporins (Ao, Jayappa et al. 2012).

1.3.4. Envelope proteins

Env proteins are derived from the polyprotein precursor $Pr160^{Env}$. Env is organized in three subunits of non-covalently associated heterodimers of gp120 surface protein (SU) and gp41 transmembrane protein (TM). The Env trimer recognizes CD4 receptors at the surface of T cells and mediates viral entry. gp41 is composed of an N-terminal ectodomain, a transmembrane domain and a C-terminal intraviral segment. During the fusion step, the binding to CD4 and to chemokine co-receptor allows TM to reorient parallel to the membranes, which facilitates the insertion of the gp41 fusogenic peptide into the cellular membrane (Fig. 1.3.6.) (Caffrey, Cai et al. 1998). SU is glycosylated and forms surface-exposed loops (Leonard, Spellman et al. 1990).

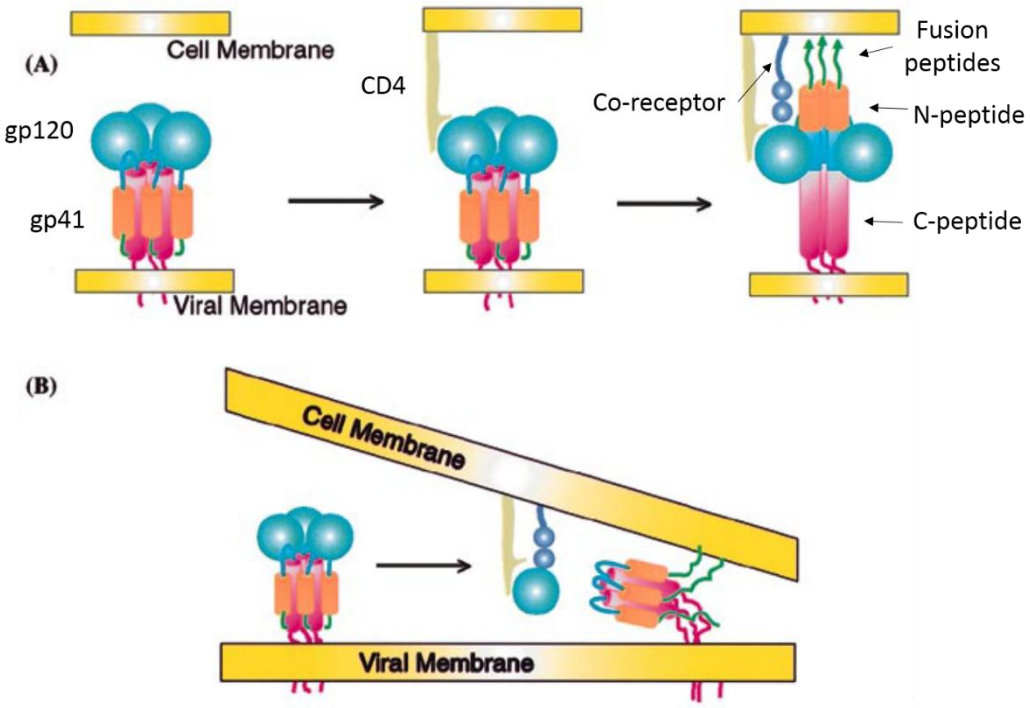

Figure 1.3.6. CD4 and chemokine receptor induced fusion of the viral and cellular membranes followed by reorientation of the TM protein. (a) Binding of the gp120 to the CD4 receptor is followed by the displacement of the gp41 N-terminal fusogenic peptides toward the cellular membrane triggered by the connection to the chemokine co-receptor; (b) CD4 and chemokine binding causes the loss of the SU proteins enables TM reorientation and membrane fusion (Adapted from (Turner and Summers 1999)).

1.3.5. Regulatory and accessory proteins

The viral DNA codes also for the accessory (Nef, Vif, Vpr, Vpu) and regulatory (Tat, Rev) (Frankel and Young 1998) proteins. The accessory proteins Vpr, Nef, and Vif are encapsidated during assembly, whereas Rev, Tat and Vpu do not appear to be encapsidated.

Nef, the HIV-1 negative factor is a 206 amino acid residues myristilated regulatory factor that localizes in the inner leaflet of the host cell membrane. Nef stimulates the decrease of the number of CD4 receptors at the surface of infected cells (Goldsmith, Warmerdam et al. 1995). Nef also downregulates the co-receptors CXCR4, CCR5 and participates in the prevention of the super-infection of the cells (Michel, Allespach et al. 2005).

Virion Infectivity Factor or **Vif** is composed of 192 amino acids (its complete 3D structure has not been yet resolved) (Barraud, Paillart et al. 2008). It is integrated in the virion by binding to the 5' region of RNA or/and to the C-terminal domain of Gag (Huvent, Hong et al. 1998; Henriet, Richer et al. 2005). Vif plays a regulatory function as a nucleic acid chaperone all

over the viral life cycle (Batisse, Guerrero et al. 2012). Moreover, it acts as inhibitor of the APOBEC-3G antiviral activity (Mariani, Chen et al. 2003).

Vpr (Viral Protein R) is highly conserved and consists of 96 amino acids. Vpr is bound to the RNA in the viral capsid (Welker, Hohenberg et al. 2000). It participates in numerous stages during the viral life cycle (Guenzel, Herate et al. 2014), especially in the early phase. Vpr is implicated in reverse transcription and during the nuclear import via its interactions with nucleoporins (Le Rouzic, Mousnier et al. 2002). As well, Vpr is responsible for the G2 cell cycle arrest with following apoptosis by the interaction with mitochondrial pores proteins (Basanez and Zimmerberg 2001).

Vpu (Viral protein U) is composed of 81 amino acids (Maldarelli, Chen et al. 1993). It is organized in a transmembrane domain and two regions of alpha helices. Vpu is thought to: 1) decrease the level of CD4 receptors by stimulating their degradation in the endoplasmic reticulum (this degradation stimulates the release of Env (Willey, Maldarelli et al. 1992); 2) favor the budding of viral particles by decreasing the effects of tetherine, known for its antiviral activity (Neil, Zang et al. 2008).

The Transactivator of Transcription (**Tat**) protein consists of five different regions: N-terminal, cysteine-rich, hydrophobic, arginine rich and glutamine-rich domains. Its size may vary between 86 and 101 amino acids (Jeang and Rauscher 1996). Tat basic domain is crucial for the recognition and binding to the TAR RNA sequence (Calnan, Biancalana et al. 1991). This binding stimulates the expression of the viral genome. Tat is also needed for efficient elongation during the initiation of transcription (Tahirov, Babayeva et al. 2010). Once released in the extracellular medium, Tat enters into surrounding non-infected cells and causes their apoptosis. Finally, Tat has been shown to activate viral transcription in latent cells (Debaisieux, Rayne et al. 2012).

The Regulatory of Viral Expression (**Rev)** protein consists of 116 amino acids and contains nuclear export and nuclear localization signals (NES and NLS respectively) (Fischer, Meyer et al. 1994; Meyer and Malim 1994). This protein participates in sequence-specific transport of viral mRNA from the nucleus to the cytoplasm.

1.4. Viral life cycle

The HIV-1 viral cycle can be divided in two main phases (Fig. 1.4.1.):

- **early phase** : starts from binding of the virus to the CD4 receptors on the cell surface, followed by fusion with host cell membrane and entry of the virus into the cytosol, uncoating of the conical capsid, reverse-transcription of the vRNA to the gDNA, nuclear entry and integration of the vDNA into the host cell genome
- **late phase** comprises synthesis of the new viral RNA and expression of viral proteins, assembly of immature virions, budding at the plasma membrane and maturation of the viral particle.

These two phases are separated by a latent period that may last from several days up to several years (Siliciano and Greene 2011).

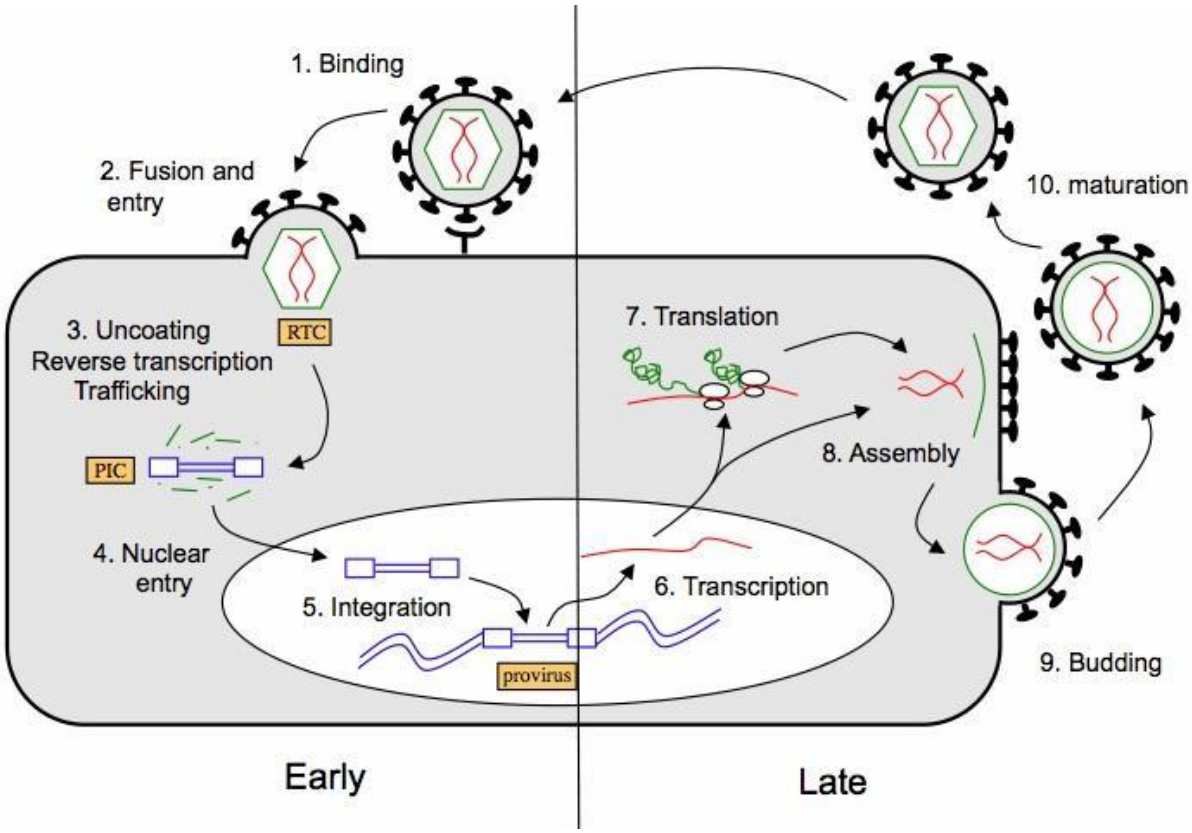

Figure 1.4.1. Schematic diagram of the HIV-1 life cycle. The viral life cycle can be divided in early and late phases. Early phase comprises binding, fusion and entry, uncoating and reverse transcription, followed by nuclear entry and integration. The late phase begins with the expression of viral genes and continues with the release and maturation of the new viral progeny (adapted from Kate Bishop Lab, Francis Crick institute website).

1.4.1. Early stages of infection

Virus entry

HIV-1 infection starts with the attachment of the viral Env glycoprotein to the CD4 and chemokine receptors (CCR5 or CXCR4) at the surface of the host cell. HIV-1 envelope spike

trimers consist of non-covalently linked heterodimers of gp120 and gp41. The interaction of the Env glycoprotein with the cell receptors trigger a sequence of conformational changes leading to the insertion of the fusion peptide at the amino-terminus of gp41, into the host cell membrane. This is then, followed by the formation of a fusion pore permitting the viral entry (Pancera, Zhou et al. 2014). In case of direct cell-to-cell transmission, the virus is transmitted via endocytosis in a cytoskeleton-dependent adhesive junction or so called virological synapse (McDonald, Wu et al. 2003; Jolly, Kashefi et al. 2004; Miyauchi, Kim et al. 2009).

Uncoating and reverse transcription

Cell entry is followed by the uncoating and reverse transcription of the viral genome. These processes seem to be linked however, their order, timing and location are still debated. Three different hypothesis were proposed for the spatial-temporal occurrence of uncoating:

- direct uncoating in close proximity to the cell membrane: this hypothesis is based on the detection of small amounts of CA proteins directly after infection (Bukrinsky, Haggerty et al. 1993; Fassati and Goff 2001; Iordanskiy, Berro et al. 2006) and the inability to detect the capsid inside the infected cells by transmission electron microscopy (Grewe, Beck et al. 1990)
- progressive uncoating during reverse transcription (Arfi, Lienard et al. 2009; Hulme, Perez et al. 2011): this hypothesis is based on the detection of a broad range of HIV-1 complex morphologies inside the cytoplasm (Nermut, Hockley et al. 1998; Nermut and Fassati 2003; Warrilow, Tachedjian et al. 2009)
- loss of capsid near the nucleus, just before nuclear entry (Arhel, Souquere-Besse et al. 2007): this hypothesis is linked to the fact that the intact capsid preserves a high concentration of enzymatic proteins, such as reverse transcriptase needed for completion of reverse transcription

The transport of viral complexes to the perinuclear region is most probably realized by the cellular transport machinery. It was reported that PIC associates with actin cytoskeleton and microtubules (Bukrinskaya, Brichacek et al. 1998; McDonald, Vodicka et al. 2002; Arhel, Munier et al. 2006).

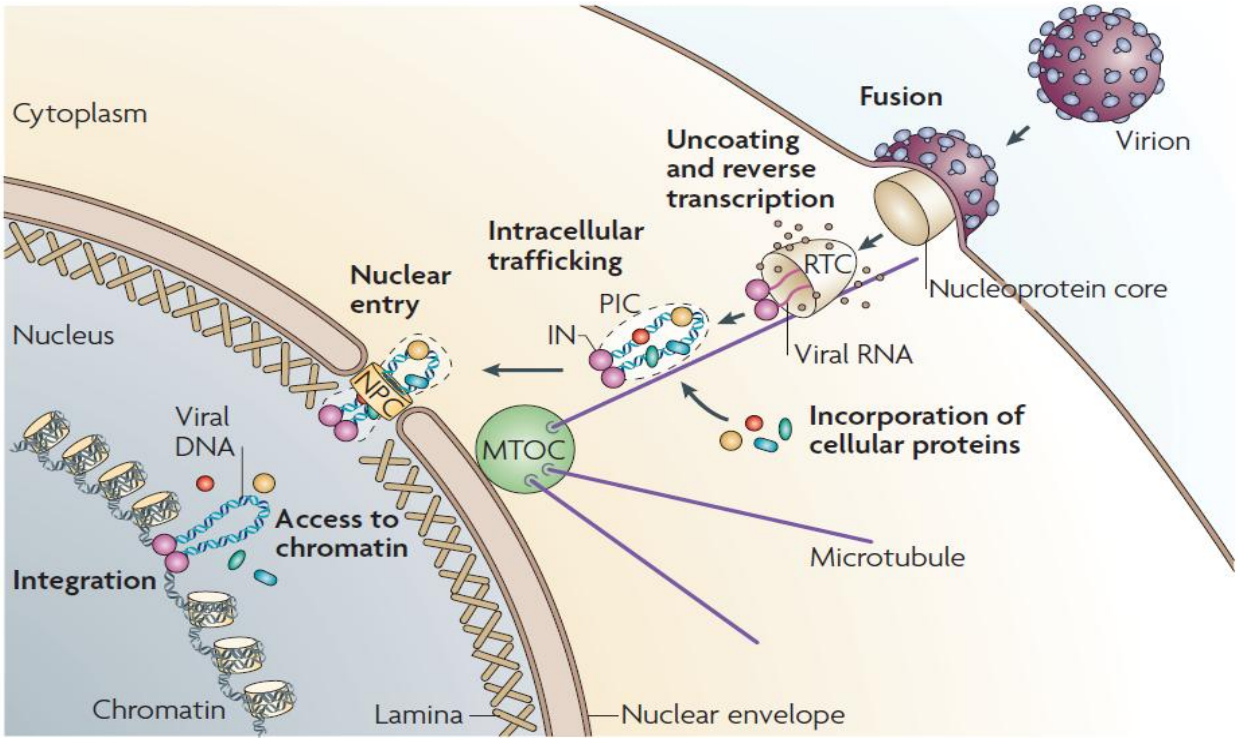

Figure 1.4.2. Early stages of infection. Fusion of the virus with cell membrane is followed by uncoating and reverse transcription during the trafficking to the nucleus. Then, the PIC formed after reverse transcription is translocated through the nuclear envelope by an active import mediated by the NPC. Inside the nucleus, the viral DNA is integrated into the genome of the host cell (Suzuki and Craigie 2007).

Reverse transcription

In the cytosol of infected cells, the ribonucleoprotein (RNP) complex (25-125 copies of RT, 12-60 IN, hundreds of Vpr and RNA dimer covered by ~2000 molecules of NCp7 (Thomas and Gorelick 2008), undergoes the reverse transcription process and is transformed to preintegration complex (PIC) (Fig. 1.4.2.).

In the course of RT, genomic single strand genomic RNA (gRNA) is converted into the double stranded viral DNA (Fig. 1.4.3.). This process is orchestrated by the reverse transcription and facilitated by the NCp7. Notably during the beginning of the RT process NCp7 chaperoning properties are valuable for the initiation of the RT and strand transfer, this will be described below. RT requires primer and template, where the primer is the host tRNA and genomic RNA is a template. In the first step, RT is initiated after the annealing of the PBS region of vRNA by tRNA primer. Then, first strand transfer is made possible by the R sequence on the both ends of the template. Further, synthesis of plus-strand DNA is initiated from the purine-rich regions of gRNA. Second-strand transfer is facilitated by the plus- and minus strand DNA copies of PBS. Finally, termination of the upstream plus-strand DNA requires the central termination sequence.

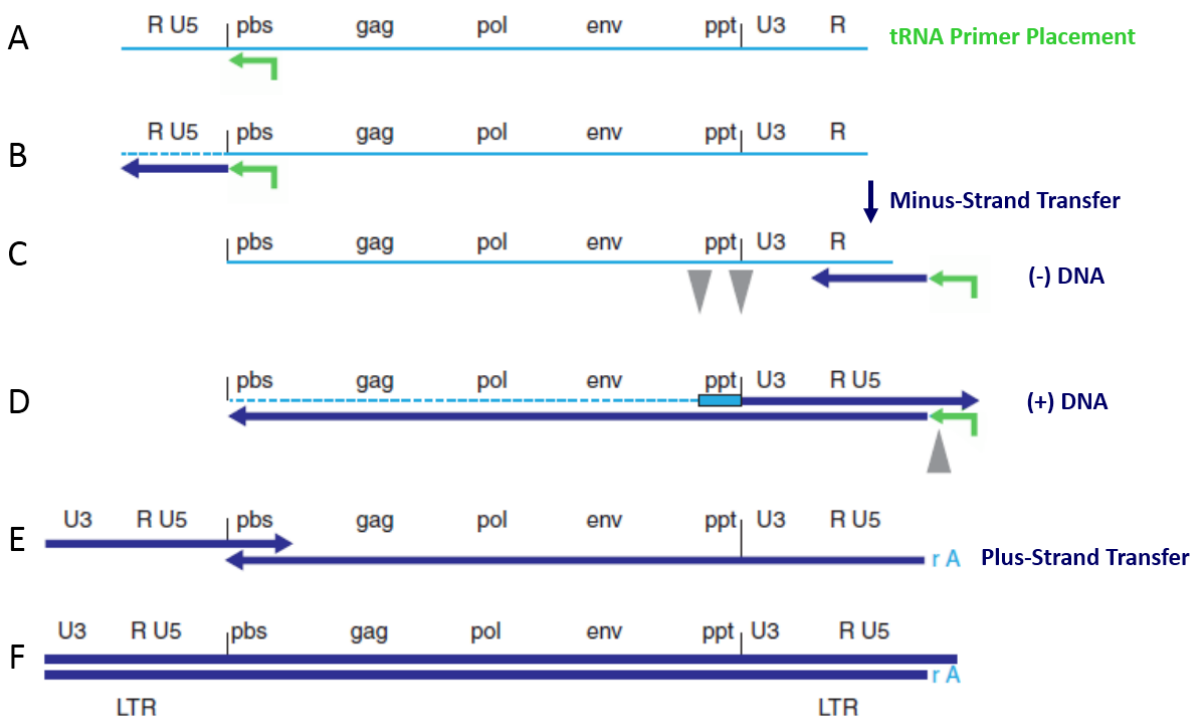

Figure 1.4.3. Mechanism of reverse transcription. (A-B) Initiation of reverse transcription by host tRNA and start of (-) ssDNA synthesis; (C-D) start of (+) ssDNA synthesis after minus-strand transfer; (E-F) second (plus-stranded) transfer (Hu and Hughes 2012).

Nuclear import

Biochemical analyses have revealed that the PIC contains viral DNA, IN, Vpr, MA, CA and cellular proteins (Barrier-to-autointegration factor (BAF), LEDGF-75) (Raghavendra (Raghavendra, Shkriabai et al. 2010) (Ciuffi and Bushman 2006) (Llano, Delgado et al. 2004). However, its precise composition and notably, the presence of NCp7 are still debated (Dismuke and Aiken 2006; Iordanskiy, Berro et al. 2006; Thomas and Gorelick 2008).

Because of its size (~tens of nanometers) (Miller, Farnet et al. 1997), the PIC is actively internalized into the nucleus (Mattaj and Englmeier 1998), through the nuclear pore complexes (NPCs) (Fig. 1.4.2) (Konig, Zhou et al. 2008; Di Nunzio, Danckaert et al. 2012). This internalization pathway requires the presence of specific amino acid sequences called Nuclear Localization Signals (NLS). Canonical NLSs were found in MA (Bukrinsky, Haggerty et al. 1993) and IN (Bouyac-Bertoia, Dvorin et al. 2001). Moreover, non-canonical karyophilic signals were identified in Vpr (Fouchier, Meyer et al. 1998). More than ten NUPs were observed to be involved in the nuclear transport of HIV-1 (Fig. 1.4.4.). Among them are Nup98, Nup153, Nup214, Nup358 and Nup62 (Konig, Zhou et al. 2008; Lee, Ambrose et al. 2010; Monette, Pante et al. 2011; Di Nunzio, Danckaert et al. 2012) 2010). HIV-1 infection is clearly decreased by the depletion of Nup358 (Konig, Zhou et al. 2008) or Nup 153 (Lelek, Casartelli et al. 2015). It seems that the Nups influence also the integration process. Nup62, Nup153 and Nup98 can bind

to transcriptionally active genes (Di Nunzio, Fricke et al. 2013; Kohl, Ng et al. 2014) in the chromatin and serve as intermediate factors that drive the PIC to its integration site (Jayappa, Ao et al. 2012).

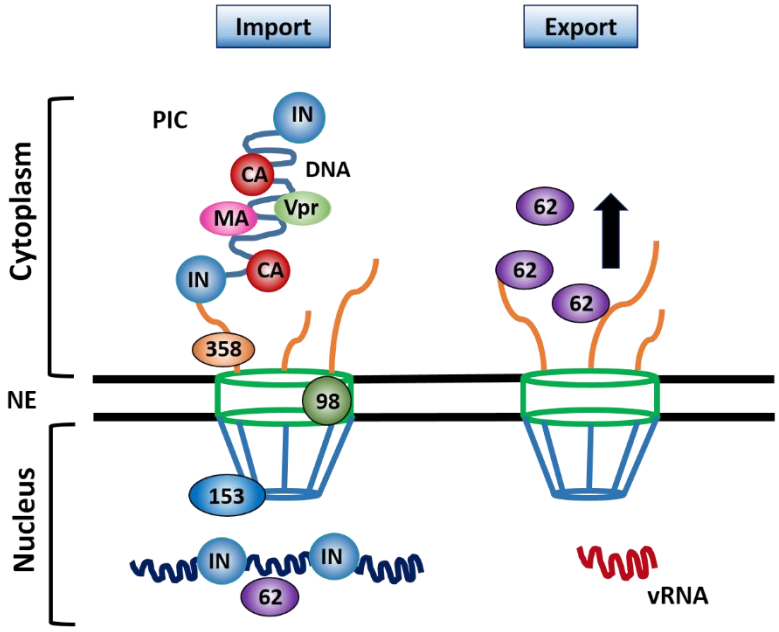

Figure 1.4.4. Interaction of HIV-1 PIC with host cell proteins during translocation through the nuclear envelope (NE). The active import of PIC occurs via Nup358, Nup98, Nup153 and Nup62 proteins (Le Sage and Mouland 2013).

Genome integration

After nuclear import, the proviral DNA is integrated into the genome of the host cell. Initially, the IN specifically binds to the two LTR ends of the viral DNA (Kukolj and Skalka 1995)) and cleaves the last two 3 'nucleotides of each DNA strands releasing a CA dinucleotide and a 3'OH (3 'processing). Subsequently, the tetrameric form of IN cleaves the genomic DNA of the target cell and catalyzes the insertion of the viral genome into the cellular genome (strand transfer). Finally, cellular DNA repair enzymes correct the discontinuities between cellular and viral DNA (Engelman, Mizuuchi et al. 1991; Vink, van Gent et al. 1991; Vink, Yeheskiely et al. 1991). The integrated proviral DNA is replicated in the nucleus of the host cell as any other cellular gene.

1.4.2. Late phase of infection

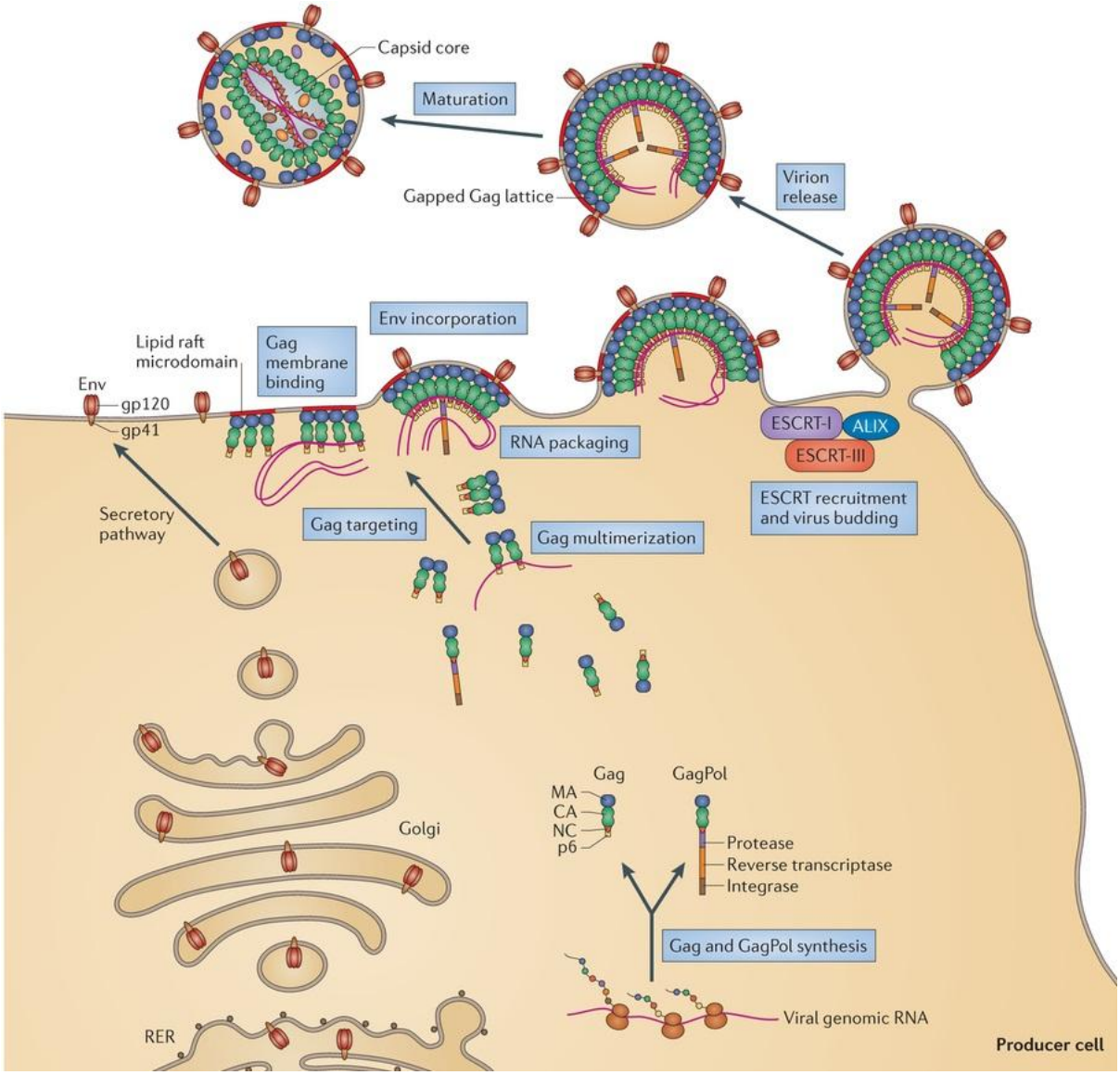

Figure 1.4.5. Late phase of HIV-1 replication. The viral Env is synthesized in the rough endoplasmic reticulum (RER) and transported to the plasma membrane via the secretory pathway. Gag and GagPol precursor polyproteins are synthesized in the cytosol from the full-length vRNA. Gag recruits the viral gRNA, starts to multimerize and reaches the plasma membrane, where it anchors to the membrane lipid rafts. After budding, maturation occurs leading to the formation of the main structural elements and stabilization of genome (Freed 2015).

Late stages of HIV-1 infection start from the transcription of the viral genome, followed by the splicing and the nuclear export of viral RNAs (spliced and unspliced) into the cytoplasm of the host cell (Fig. 1.4.5.). The accessory protein Rev (Freed 2001) that contains a nuclear export signal (NES) and recognizes the RRE sequence on the mRNA mediates the nuclear export. Interestingly, during the Rev-mediated export, the Nup62 is displaced into the cytoplasm (Fig. 1.4.4.) and incorporated into virions (Monette, Pante et al. 2011).

In the cell cytoplasm, the mRNAs are translated into viral proteins. Gag is expressed in ribosomes from the unspliced mRNA as a 55kDa precursor polyprotein. Gag-Pol polyprotein precursor is generated by a translational frameshift. The unspliced mRNA can be also encapsidated as genomic RNA into the new viral particles. The mechanisms regulating the equilibrium between translation and encapsidation are not fully understood. Env, Vif, Vpr and Vpu are expressed from single spliced RNA and Tat, Rev and Nef from multi-spliced RNAs.

In the cytosol, Gag molecules bind to the RNA and form (via CA- CA interactions) small oligomers that diffuse to the cell periphery where the myristilated MA domain binds to the inner leaflet of the plasma membrane. Gag binds preferentially to PIP2-enriched domains connected to raft domains, which serve as platforms for viral assembly and may facilitate the incorporation of Env glycoproteins (Ono and Freed 2001). In the majority of cell types, Gag multimerization and virion assembly takes place at the plasma membrane (Raposo, Moore et al. 2002).

Viral RNAs through their encapsidation sequence are specifically recognized by the NC domain of Gag. The RNA molecule serves as a scaffold for further Gag multimerization at the plasma membrane resulting in the formation of round-shaped virions. The NC domain serves as a chaperone of nucleic acids that drives RNA packaging (Levin, Guo et al. 2005). In immature particles, ~2,400 +/-700 Gag molecules (Carlson, Briggs et al. 2008) are packed radially with the C-terminus of Gag directed towards the center and the MA domain directed to the membrane. The Gag lattice presents a hexameric arrangement (Bharat, Davey et al. 2012; Schur, Hagen et al. 2015). The incorporation of Env may possibly occur through a passive process (co-targeting Gag and Env to the plasma membrane) or a direct recruitment of Env by Gag (Checkley, Luttge et al. 2011).

The cellular ESCRT (Endosomal Sorting Complexes Required For Transport) machinery mediates the membrane fission of the nascent viral particles. Interactions between the cellular membrane, ESCRT and the virus are mediated by the p6 domain of Gag (Morita, Sandrin et al. 2007; Carlton and Martin-Serrano 2009; Morita, Sandrin et al. 2011). It was shown that ESCRT elements accumulate at the head or at the neck of the viral bud (Bleck, Itano et al. 2014; Van Engelenburg, Shtengel et al. 2014). Other cellular proteins such as TsG101 and Alix favor the scission of the viruses by recruitment of ESCRT-III complexes (Jouvenet, Zhadina et al. 2011).

New virions are released in immature and non-infectious forms. Viral maturation is triggered by the proteolytic activity of protease that cleaves the Gag and Gag-Pol, generating the mature structural (MA, CA, NC, p6) and viral enzymes (PR, IN, RT). During the process, the

viral particle is reorganized; the RNA is condensed and forms, together with the NC and RT the RTC complex. CA molecules form a typical cone shaped capsid.

1.5. NCp7: structure and function

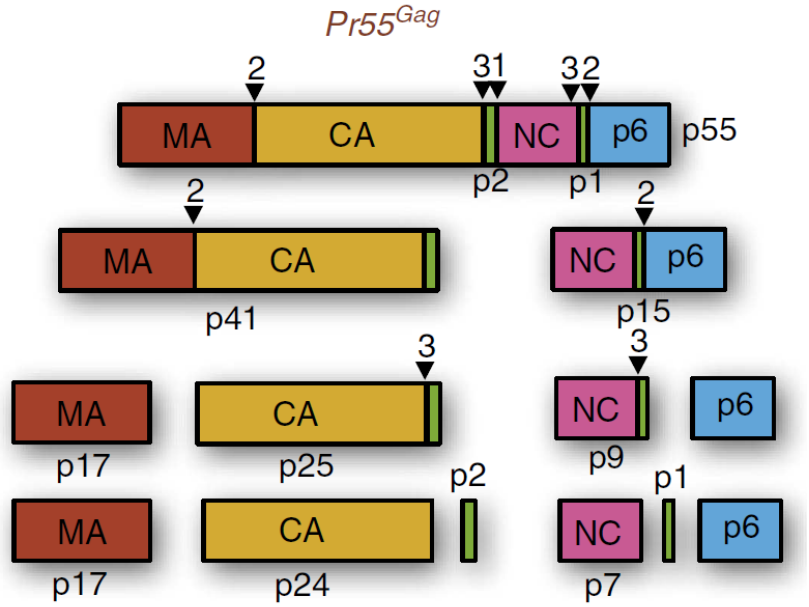

Figure 1.5.1. Diagram of Gag polyprotein maturation. Maturation occurs in three steps and produces subsequently p15, p9 and finally the p7 nucleocapsid protein by liberation of the p1 domain (Adapted from (Abd El-Wahab, Smyth et al. 2014)).

The HIV-1 nucleocapsid protein exists in two forms: as a functional NC domain of Gag during the late phase of infection and in mature form (NCp7), after the proteolytic cleavage of the polyprotein.

The mature form of NC (NCp7) is generated within the virion by a series of cleavages catalyzed by the viral protease (Fig. 1.5.1.) (Erickson-Viitanen, Manfredi et al. 1989; Pettit, Moody et al. 1994). The first cleavage occurs between SP1 and the NC region and leads to the liberation of NCp15 composed of NCp7-SP2-p6 (Shehu-Xhilaga, Kraeusslich et al. 2001). This proteolytic intermediate of NCp contains 123 a.a and is subsequently cleaved (during the second step of maturation, which requires binding to gRNA) to the NCp9 (71 a.a.) (Sheng, Pettit et al. 1997). Finally, the third proteolytic cleavage promotes the release of NCp7 and SP2.

The mature viral capsid contains between 1500 to 2000 NCp7 molecules, which cover the RNA dimer. The NCp7 concentration is of the order of millimolar and the nucleotide/NCp7 ratio is about 8-9 (Darlix, Godet et al. 2011)

1.5.1. Structure

NCp7 is a small basic protein (pI=9.9) containing 55 aa. It comprises two CCHC zinc fingers composed of Cys-X2-Cys-X4-Cys-His-X4 sequence (X represent variable amino acids) (Fig. 1.5.2.A) connected by a short flexible basic peptide linker and flanked by N- and C-domains (Fig. 1.5.2. B). Zinc fingers and the RAPRKKG linker can fold in a globular conformation (Mely, Jullian et al. 1994; Morellet, de Rocquigny et al. 1994; Lee, De Guzman et al. 1998). The affinity of Zn^{2+} to the zinc fingers is very high (K_a ~10^{14} M^{-1}) (Mely, De Rocquigny et al. 1996). Despite the similar amino acid composition of the two fingers, their activity and biochemical properties are not equivalent (Fisher, Rein et al. 1998; Fisher, Fivash et al. 2006; Zargarian, Tisne et al. 2014). ZF1 plays an important role in the destabilization of nucleic acid secondary structures while ZF2 increases the rate of annealing of the RNA and/or DNA during the strand transfer, genome dimerization and maturation (Gorelick, Chabot et al. 1993; Heath, Derebail et al. 2003) (Aduri, Briggs et al. 2013; Wu, Mitra et al. 2014). The disruption of zinc fingers folding by mutations leads to a loss of infectivity (Aldovini and Young 1990; Dorfman, Luban et al. 1993; Gorelick, Chabot et al. 1993).

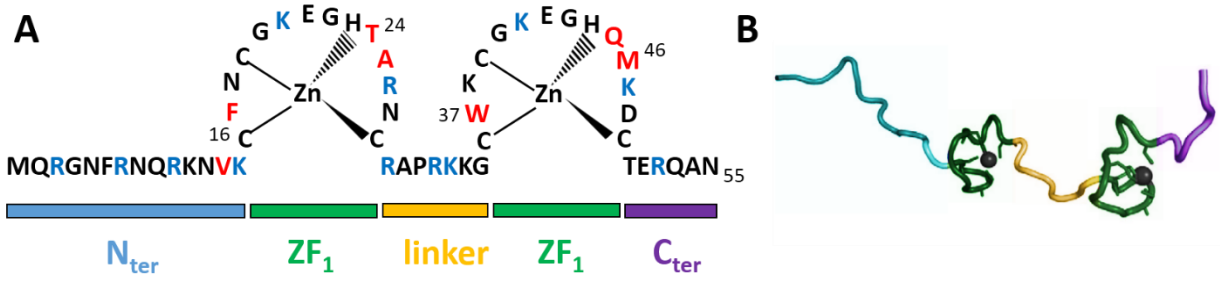

Figure 1.5.2. Structure of NCp7. (A) Amino acid sequence. Zinc fingers are shown in green, the basic linker in yellow, and the two terminals N and C domains are presented in blue and violet respectively. (B) 3D representation of protein structure determined in solution by NMR (Adapted from (Godet, Boudier et al. 2012; Sleiman, Goldschmidt et al. 2012).

1.5.2. Interaction of NCp7 with nucleic acids

NCp7 can bind to almost any nucleic acid sequence of 5-8 nucleotides. Due to its cationic nature, the NC/NA interactions are salt dependent (Urbaneja, Kane et al. 1999; Vuilleumier, Bombarda et al. 1999). The basic residues of NCp7 (notably those of the N-terminal domain and the linker) interact electrostatically with the phosphodiester backbone of any NA (Mely, de Rocquigny et al. 1995).

A number of specific interactions of NCp7 with NA has also been reported (Berglund (Berglund, Charpentier et al. 1997; Wu, Ozarowski et al. 1997; De Guzman, Wu et al. 1998;

Bourbigot, Ramalanjaona et al. 2008). NCp7 binds preferentially to guanosine rich regions of single-stranded DNA or RNA. The interaction is strongly dependent on the hydrophobic plateau formed at the top of zinc fingers by the V13, F16, T24, A25 (N-terminal finger) and W37, Q45, M46 (C-terminal finger) residues (Amarasinghe, De Guzman et al. 2000).

1.5.3. Chaperone properties

By NA binding, condensing and annealing as well as by promoting strand transfer reaction, NCp7 remodels the NA structure to its most thermodynamically stable conformation, and thus, performs chaperone activity.

Remodeling of NA structure by NCp7 is based on binding to the NAs, followed by partial destabilization of NA, rapid on/off kinetics of NC-NA interactions and NA aggregation (Darlix, Godet et al. 2011). During this remodeling, the RNA adopts different conformations, in order to lead to the most stable one (Tompa and Csermely 2004). NCp7 chaperone activity depends on the NA occupancy (Fig. 1.5.N). At low occupancy, NCp7 performs limited chaperone activity, while at high occupancy level; NCp7 promotes aggregation and macromolecular crowding effect, followed by annealing (Lapadat-Tapolsky, Gabus et al. 1997). The occupancy level is changing during the viral lifecycle. It is low during the assembly step (1:100 nt) when NCp7 is part of Gag, (Paillart, Shehu-Xhilaga et al. 2004) but increases with Gag multimerization and during the maturation step (1:2-5nt) (Chertova, Chertov et al. 2006). In mature virions, NCp7 coats and protects the viral genome in the nucleoprotein complex and then, promotes reverse transcription in the infected cell. During the integration step, when almost all NC proteins are released, its chaperone activity is questionable (Darlix, Cristofari et al. 2000).

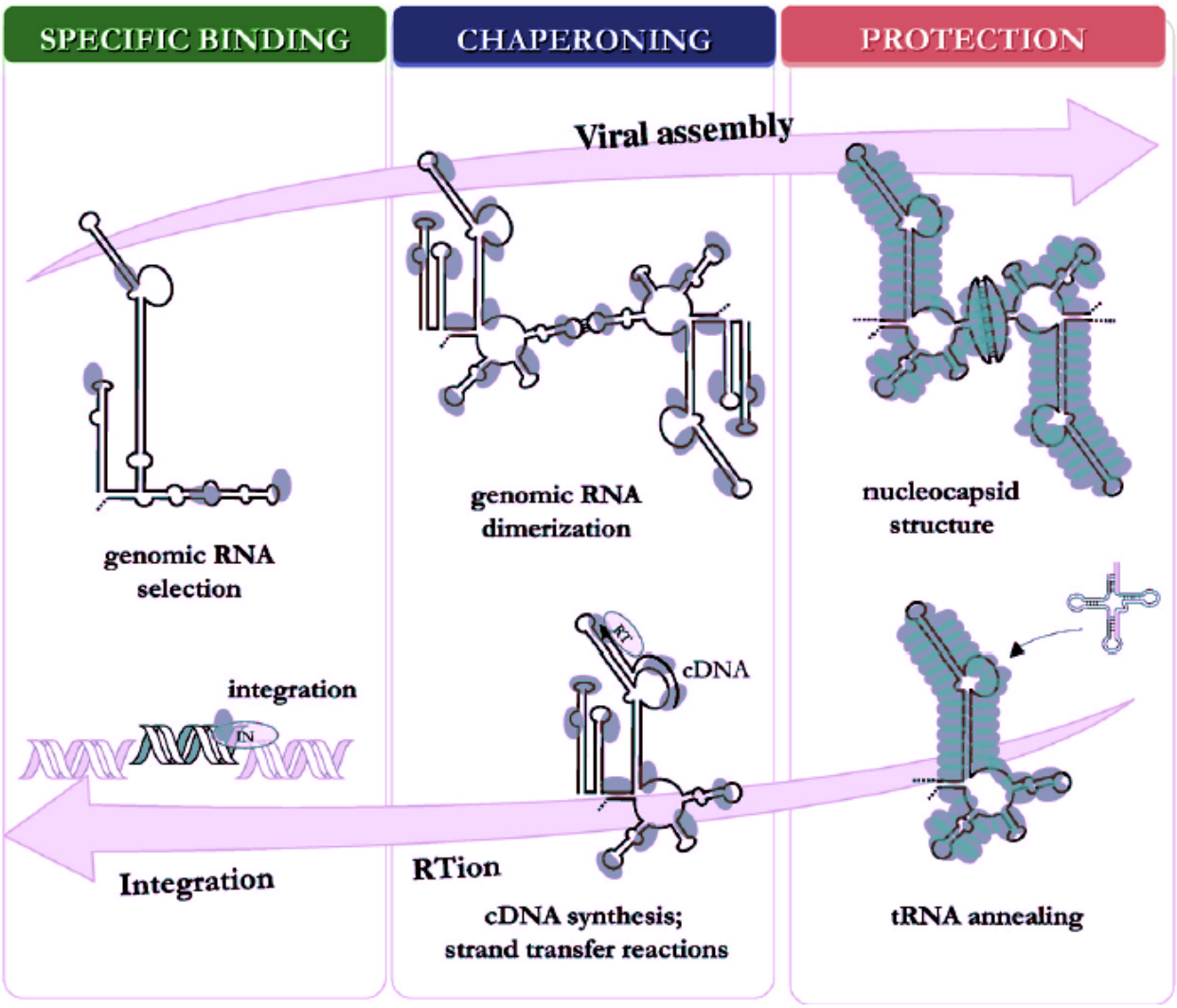

Figure 1.5.3. Activity of NCp7 through the viral life cycle. At high occupancy level, the NCp7 protein protects the RNA, whereas at low occupancy, NCp7 is performing nucleic acid chaperoning and specific binding (Adapted from (Darlix, Godet et al. 2011))

1.5.4. Interactions with cellular proteins

Several host proteins have been identified as specific interactions of NCp7 (Mouland (Mouland, Mercier et al. 2000; Zimmerman, Klein et al. 2002; Ueno, Tokunaga et al. 2004; Popov, Popova et al. 2009).

In the course of HIV-1 assembly, the Tsg101 domain of ESCRT is recruited by the NC and p6 domains of Gag and targeted to the viral assembly sites (Chamontin, Rassam et al. 2015). This targeting favors RNA packaging and the budding process. Another ESCRT factor ALIX is involved in virus budding and release. ALIX interacts via its YPXL pattern with the p6 domain of Gag and via its BRO1 domain with the NC-Gag (Popov, Popova et al. 2008; Dussupt, Javid et al. 2009). However, the role of ALIX is still unclear due to the absence of effect of its depletion on viral egress (Fujii 2009).

Actin interacts with the N-terminal of NC, both in its mature form or as a Gag domain (Liu, Dai et al. 1999; Wilk, Gowen et al. 1999). This interaction seems to play a role during viral budding where it favors the incorporation of actin into the virus (Ott 2008). However, recent studies have revealed that the NC domain of Gag is dispensable for association of cortical actin to the HIV-1 budding sites (Stauffer, Rahman et al. 2014).

Staufen1 is a host factor that is encapsidated into HIV-1 (Mouland, Mercier et al. 2000; Chatel-Chaix, Clement et al. 2004) and plays a role in the trafficking and metabolism of the mRNA. Staufen1 is recruited by the NC domain of Gag (Chatel-Chaix, Boulay et al. 2008) and participates in the packaging of RNA. Moreover, Staufen1 modulates Gag multimerization during HIV-1 assembly (Chatel-Chaix, Abrahamyan et al. 2007).

ABCE1 (HP68 or RNase L inhibitor) is a 68 kDa cellular protein that is a member of the ATP-binding cassette protein family E. It binds to Gag, directly after its translation via the basic residues of the NC domain (Lingappa, Dooher et al. 2006) and promotes ATP-dependent conformational changes of the capsid assembly intermediates crucial for assembly.

Nucleolin is a typical nucleolar protein. In cells infected with HIV-1, nucleolin is translocated to the plasma membrane (Ueno, Tokunaga et al. 2004). It is thought to play a role in the transport of the intron containing nucleocytoplasmic gRNA (Cochrane, McNally et al. 2006). By interacting with NC-Gag and the Ψ region of the genomic RNA, it could favor the assembly of viral particles (Bacharach, Gonsky et al. 2000).

1.5.5. Inhibition

NCp7 and notably CCHC zinc fingers are highly conserved. Point mutations in these sequences lead to a complete loss of infectivity (Dorfman, Luban et al. 1993; Morellet, de Rocquigny et al. 1994; Berg and Shi 1996; Ramboarina, Morellet et al. 1999; Buckman, Bosche et al. 2003; Thomas and Gorelick 2008). As a result, NCp7 appears as a good candidate for antiviral treatment. Several types of NCp7 inhibitors have been developed.

Zinc ejectors act by an electrophilic attack of the cysteine thiol groups, generating disulfide bridges that lead to ejection of zinc atom. This causes the loss of NCp7 activity and results in a loss of HIV-1 infectivity. 3-nitrobenzamide (NOBA) (Rice, Schaeffer et al. 1993), the first zinc ejector developed initiated the synthesis of many other molecules (de Rocquigny, Shvadchak et al. 2008; Turpin, Schito et al. 2008; Goldschmidt, Jenkins et al. 2010; Garg and Torbett 2014; Mori, Kovalenko et al. 2015). Among them are disulfide benzamide (SBIR) (Rice, Supko et al. 1995), azodicarbonamide (ADA) (Rice, Turpin et al. 1997), pyridinioalkanoyl

thioesters (PATEs) (Turpin, Song et al. 1999), s-acyl-2-mercaptobenzamide thioesters (SAMT) (Srivastava, Schito et al. 2004; Jenkins, Byrd et al. 2005), methyl-3-phenyl-2H-[1,2,4]thiazol-5-yideneamine (WDO-217) (Vercruysse, Basta et al. 2012) and N,N′-bis(4-ethoxycarbonyl-1,2,3-thiadiazol-5-yl)benzene-1,2-diamine (NV038) (Pannecouque, Szafarowicz et al. 2010). These inhibitors show an efficient antiviral activity on all HIV-1 strains, leading to the release of noninfectious virus (Turpin, Terpening et al. 1996). The main drawback of these molecules is their cellular toxicity resulting from their non-specific action on cellular proteins containing zinc fingers. More prominent in terms of specificity might be **non-zinc ejecting inhibitors** or non-covalent NC inhibitors (NCIs), targeting the hydrophobic platform of the zinc fingers or nucleic acid partners in the non-covalent mode. "Gallein" compound showed activity at nanomolar concentrations on free NCp7 (Stephen, Worthy et al. 2002). In 2009, Shvadchak and colleagues reported the search strategy for NCIs, based on the high-throughput screening (HTC) assay to identify small molecules for inhibition of NCp7 chaperon activity. This assay was used to screen 4800 chemical substances and five compounds were successfully identified as inhibitors. Later, non-toxic 2-amino-4-phenylthiazole (AN3) compound (Mori, Nucci et al. 2014) have been developed on the base of A10 fragment from HTC assay screening (Shvadchak, Sanglier et al. 2009). Further, HTC assay was used to identify an anti-NCp7 of small methylated oligonucleotides (mODNs), rich in GU, mimicking short sequences of LTR. These mODNs affect the chaperone activity of NCp7 and/or the synthesis of viral DNA resulting in an efficient inhibition of viral infection and replication (Grigorov, Bocquin et al. 2011; Avilov, Boudier et al. 2012).

Some aminoglycosides and intercalating peptides can bind to NCp7 preferential sites on viral RNA, such as SL1 stem loop (Chung, Mujeeb et al. 2008; Chung, Ulyanov et al. 2010), SL3 stem loop (Warui and Baranger 2009) or the TAR and PBS sequences (Sosic, Frecentese et al. 2013) which allows a specific inhibition of the interaction of the NCp7 with these sequences.

1.6. Role of NCp7 during infection

Functions of NCp7 during the viral infection are mainly related to its nucleic acid chaperone properties. NCp7 plays a crucial role during several steps of the early and late infection stages.

Role of NC in reverse transcription

During reverse transcription, NCp7 is required for the proper annealing of the tRNA (Lys3), a crucial step of the initiation of reverse transcription (Saadatmand and Kleiman 2012; Sleiman, Goldschmidt et al. 2012). Next, NCp7 promotes the minus-strand transfer by favoring the annealing of the newly synthesized TAR DNA domain (cTAR) to the TAR RNA at the 3'-end of the genomic RNA (Piekna-Przybylska, DiChiacchio et al. 2010). Moreover, NCp7 participates in the removal of the non-PPT vRNA regions during RT translocation along the (-) DNA template (Jacob and DeStefano 2008; Post, Kankia et al. 2009). It was also shown that NCp7 might protect the newly synthesized vDNA ends from nucleases (Buckman, Bosche et al. 2003).

In the cytoplasm of infected cells, the virus undergoes several transformations. Initially, extremely high concentrations of NCp7 (~ 100 mM) in the ribonucleoprotein complex strongly condense the genomic RNA. During reverse transcription, the RTC is remodeled and progressively transformed into the preintegration complex (PIC). Since the affinity of NCp7 for dsDNA is significantly lower as for ssRNA, it is thought to be progressively released from the viral complex (Fig. 1.6.2.). Nevertheless, it is likely that a pool of NCp7 molecules may bind non-specifically to dsDNA in PIC and promote stable binding of IN to LTR ends (Carteau, Batson et al. 1997).

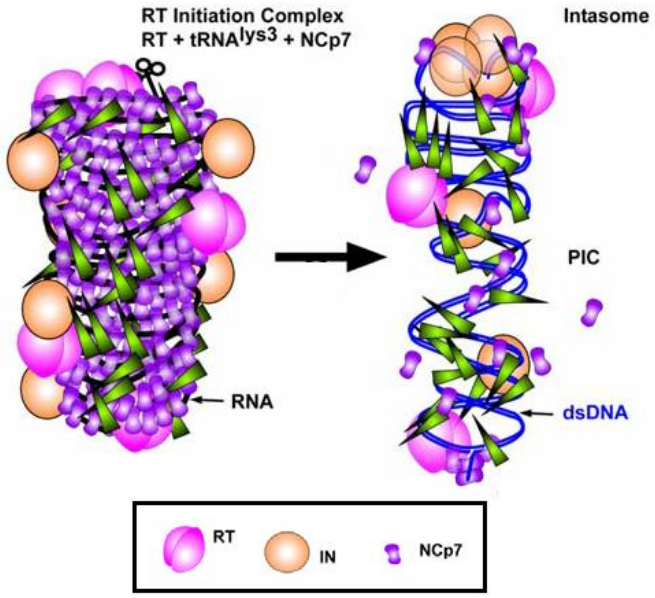

Figure 1.6.2. Model of viral core dismantling controlled by RT. (Adapted from (Mirambeau, Lyonnais et al. 2007).

Role of NCp7 in viral integration

NCp7 was shown to effectively enhance viral DNA integration reactions both in vitro and in in vivo (Carteau, Batson et al. 1997; Buckman, Bosche et al. 2003; Poljak, Batson et al. 2003;

Thomas, Gagliardi et al. 2006) et al., 2006). However, the mechanism by which NCp7 promotes integration is not fully understood. It could, as it was demonstrated "in vitro", directly favor the enzymatic integration steps and assist the formation of a functional integration complex. NCp7 molecules bound to DNA in PIC may mask the non-specific sites for IN binding (Poljak, Batson et al. 2003).

Role of NCp7 in HIV-1 assembly

RNA selection and packaging is a crucial step of the late phase of infection. Two copies of unspliced viral RNA are packed in nascent infectious virions. These molecules are chosen specifically in the pool of spliced viral mRNAs and highly abundant cellular mRNAs. The selection is promoted by the NC domain of Gag (Berkowitz, Fisher et al. 1996) due to the specific recognition and binding of NC to the RNA packaging signals (Ψ-sites). NMR analysis revealed the crucial role of the ZFs in the specific interaction with Ψ-sites (South and Summers 1993). Mutation of NCp7 zinc fingers could significantly reduce the genome packaging (Gorelick, Henderson et al. 1988; Aldovini and Young 1990). The absence of NC domain prevents specific HIV-1 gRNA packaging (Ott, Coren et al. 2005) and results in a severe decrease in the production of virions (Ott, Coren et al. 2003). During the assembly process, the viral genome plays a role of a scaffold for the multimerization of Gag proteins. Deletion of the NC domain or the two ZFs results in impaired Gag oligomerization and delays the production of particles, as compared with the wild Gag (de Rocquigny, El Meshri et al. 2014; El Meshri, Dujardin et al. 2015). The role of NC-Gag in the assembly is likely linked to its ability to bind the RNAs that serves as a scaffold for Gag oligomerization (Cimarelli and Darlix 2002; Alfadhli, Dhenub et al. 2005; Jouvenet, Simon et al. 2009).

NCp7 plays also a crucial role in the dimerization of genomic RNA (Bieth, Gabus et al. 1990; Fu and Rein 1993). This process starts from base pairing between the two RNA molecules, through a "kissing loop structure". NC then facilitates dimer maturation via its chaperone activity, which promotes the more stable extended duplex.

Finally, in the mature virions NCp7 protects and stabilizes the RNA dimer (Feng, Copeland et al. 1996; Rein, Henderson et al. 1998; Jalalirad and Laughrea 2010).

1.7. Microscopy approaches to image the HIV-1

Microscopy techniques represent an important tool for virology research. Visualization of isolated viruses or virions inside host cells can provide a large number information crucial for the

understanding of the infectious process and the viral lifecycle. The first attempt to visualize HIV virions was realized in the 80s by transmission electron microscopy (EM). This technique successfully unraveled the morphology and the structure of the viral particles. Since, technical progresses in the microscopes and the development of cryo-tomography enabled to access the detailed structure of mature and immature HIV-1 viral cores (Briggs and Krausslich 2011). Imaging of HIV-1 in infected cells is more challenging due to the difficulty to identify the virus in a dense intracellular environment. However, using immunolabeling techniques, HIV-1 could be imaged during the early stages of infection (Apostolski, McAlarney et al. 1993; Dundr, Leno et al. 1995). Moreover, viral assembly and budding at the plasma membrane were also investigated by EM studies, which enlightened the mechanisms of the generation of the viral particles, their scission and maturation (Larson, Johnson et al. 2005; Arhel, Souquere-Besse et al. 2007; Finzi, Orthwein et al. 2007; Carlson, Briggs et al. 2008; Strauss, Hammonds et al. 2015). Interestingly, during the last years several atomic force microscopy (AFM) imaging studies emerged in the field of virology and brought interesting information about the size distributions and physical properties of the HIV-1virions (Kuznetsov, Victoria et al. 2003; Kol, Shi et al. 2007).

The use of optical microscopy in HIV-1 studies was for a long time limited because of the lack of a proper labeling strategy that preserves the viral infectivity. For instance, insertion of fluorescent proteins in Gag led to generation of non-infectious viruses (Muller, Daecke et al. 2004; Larson, Johnson et al. 2005). A key step was obtained when pseudoviruses containing GFP fused to Vpr were successfully produced and used for tracking viral particles in infected cells in the pioneering work of McDonald (McDonald, Vodicka et al. 2002). Soon after, the fusion of IN to a tetracystein tag permitted to follow the viral core and to quantify its diffusion in the intracellular environment (Arhel, Munier et al. 2006). Several examples of visualization of viral reorganization in the early steps of infection by application of multi-labeled virions have also been shown (Campbell, Perez et al. 2007; Ma, He et al. 2016), 2016). Recently emerged high-resolution (HR) fluorescent microscopy methods found rapidly their place for imaging HIV. HR microscopy has been used for visualizing the recruitment of host cell proteins in the early (Chojnacki, Staudt et al. 2012) and late steps of infection (Malkusch, Muranyi et al. 2013; Van Engelenburg, Shtengel et al. 2014; Prescher, Baumgartel et al. 2015). Moreover, HR microscopy allowed to visualize morphology changes related to RTC to PIC transition of viral particles (Lelek, Di Nunzio et al. 2012) and dynamics of Gag diffusion at the plasma membrane (Manley, Gillette et al. 2008). In the following chapter, we will describe the general principles of microscopy methods and their applications to HIV-1 imaging.

1.7.1. Electron microscopy

In electron microscopy, the contrast arises from different types of electron-sample interactions. When electrons hit the sample, elastic and inelastic interactions occur inside the teardrop-shaped volume of the specimen (Fig. 1.7.1). Depending on the energy of the electrons, the size of the volume varies from 100 nm to 5 µm. In case of elastic collisions (which are used after in transmission (TEM) and diffraction electron microscopy methods), no energy is transferred from the electron to the sample, similarly to the case where electrons pass through the sample without any interaction. In this case, the electrons are deflected by Coulomb interaction with the positive potential inside the electron cloud. If energy transfer takes place, the interaction is called inelastic and produces X-ray as well as Auger secondary or backscattered electrons. Among these interactions, transmitted and secondary electrons are used for imaging techniques (secondary electrons are used in scanning electron microscopy (SEM) (Krumeich, Zurich) and the transmitted ones are detected in transmission electron microscopy (TEM), while the other ones provide more specific analytical information about the composition, thickness or the structure of the sample.

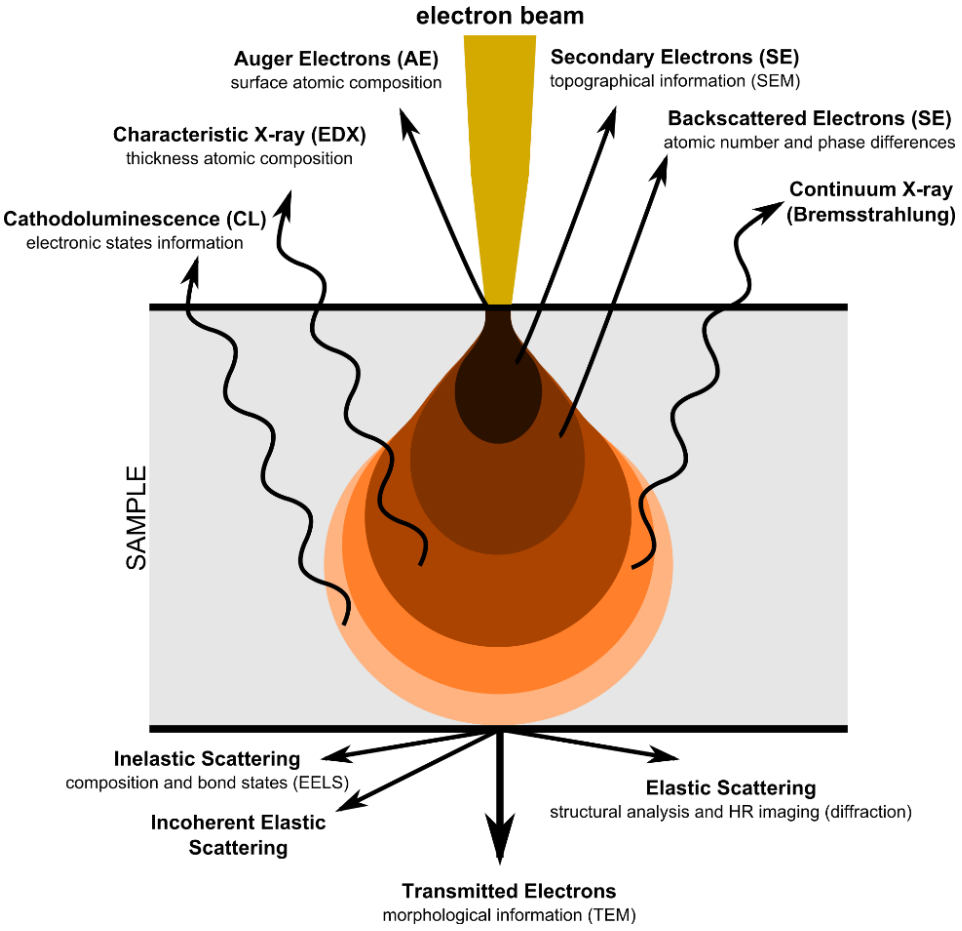

Figure 1.7.1. Interaction of the electrons with the sample. Incident electrons interact with the atoms of the sample and produce detectable output with specific information.

A typical electron microscope is composed of a source of electrons, electromagnetic lenses and a detector. The sources of electrons are electron guns, made from tungsten and lanthanum hexaboride. They produce electrons by Schottky, thermionic or field emission. Produced electrons are accelerated by a voltage of typically 100-200 kV, (however, setups with up to 500 kV voltage provide better resolution) and focused by a set of condenser electromagnetic lenses, on the sample plane. SEM approach requires much lower acceleration and normally operates with ~15-20 kV. In TEM, the electron beam passes through the specimen plane and is then, focused by the objective lenses and expanded onto a fluorescent screen by the projector lenses. Then, a CCD camera (Fig. 1.7.2) records the electron distribution. During the scattering events, electrons are deviated from their direct path and their level of deflection depends on the Coulomb force. The latter is increasing with increasing atomic number. Thus, contrast in areas with heavy atoms will appear darker. In SEM, the electron beam is raster scanning the sample and the secondary electrons generated by the interaction with the sample are detected for the image formation point by point. All systems are operating under vacuum (Fig. 1.7.2).

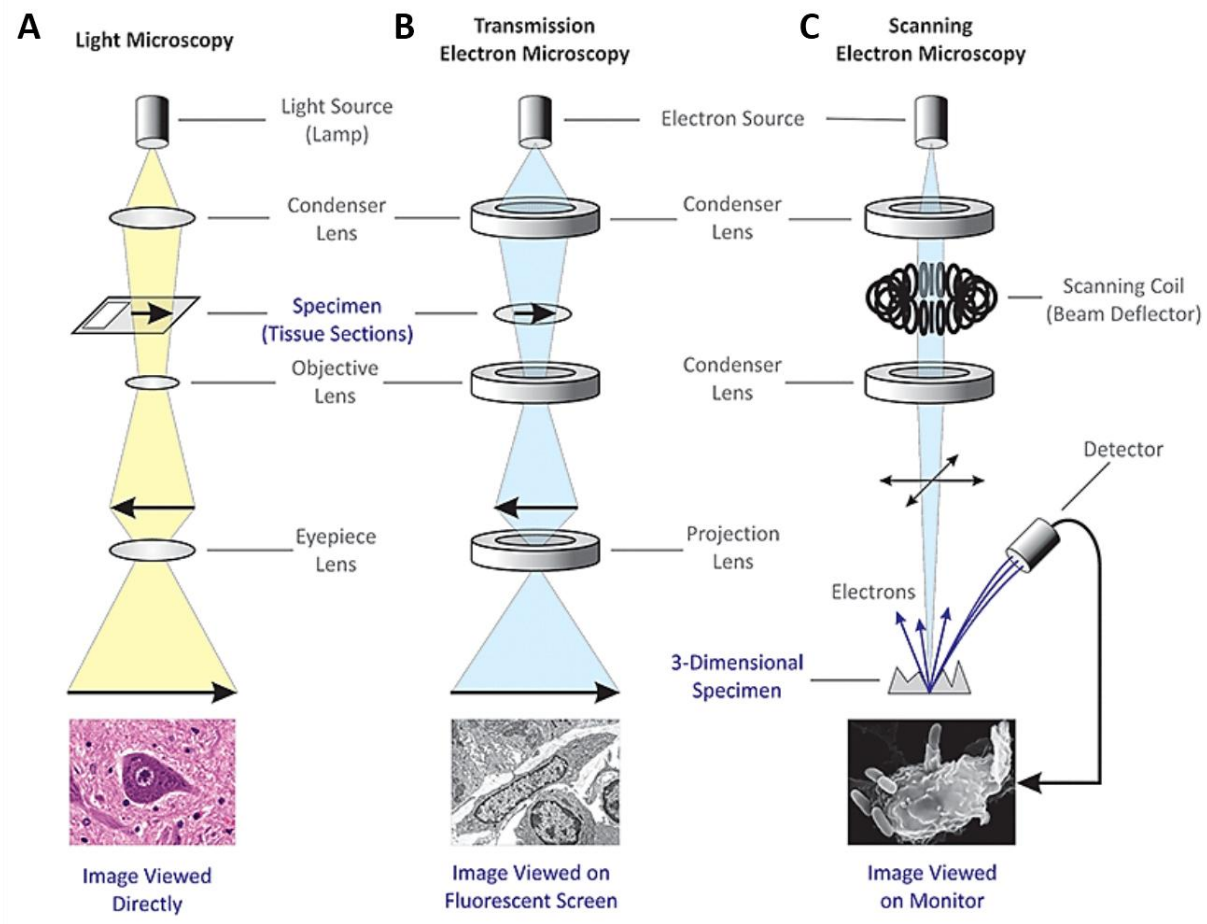

Figure 1.7.2. Comparative schemes of light and electron microscopy setups. Unlike optical light microscopy (A), where the source of illumination is a photon beam, electron microscopy uses beam of

electrons (B, C). A similar approach is used to focus both beams before and after the sample by a set of optical and electromagnetic lenses. In a TEM setup, only the elastic electrons that pass through the specimen are detected, whereas the SEM approach relies on secondary electrons from the surface of the sample. The lower line represents typical images for each setup (Introduction to Biology of Molecules and Cells, website).

The resolution power of an electron microscope can be calculated from Abbe formula [1], with assumptions that an electron has wave-like properties and its wavelength is related to their kinetic energy through de Broglie equation [2]:

[1]

where λ is the illumination wavelength, *NA* is the numerical aperture equal to n*sinθ, where *n* is the refractive index and θ is the maximal half-angle of the electron beam which enters or exits the lens.

$$\lambda e \approx$$ [2]

where *h* is the Planck's constant, m_0 is the rest mass of an electron and *E* is the energy of the accelerated electron. Thus, due to the extremely low value of the electron wavelength, the resolution of TEM can be a few angstroms. In SEM, this value can reach 2-5 nm and in case of high resolution SEM it can be even better than 1 nm.

The EM samples being extremely thin (around 50-100 nm), the conventional TEM is mostly limited to 2D imaging. 3D information can be obtained by imaging arrays of serial-sectioned 2D samples (ssTEM) in order to reconstruct the sample volume. However, this approach is time consuming and suffers from the loss of information between the sections (Spacek and Lieberman 1974). 3D imaging can be also achieved by TEM tomography, when the imaging plane is tilted along one or two axes and series of images are recorded at different angles (Baumeister, Grimm et al. 1999) in order to be computationally reconstruct the 3D volume image. This approach enables 3D visualization of ultrasmall structural details with nanometric resolution although it may suffer of lack of information from missing wedges between tilted planes and damage of samples caused by the large electron doses. In scan electron microscopy, the volume information can be accessed by combining the imaging with the ablation of the sample by Focused Ion Beam-SEM (FIB-SEM) (Orloff 1993; Heymann, Hayles et al. 2006). The best lateral resolution can be up to 6 nm (Heymann, Shi et al. 2009).

Samples for TEM microscopy require sophisticated preparation, staining and fixation. Due to their high water content, the biological samples are not resistant to the vacuum and can be

easily damaged by the electron beams. Therefore, dehydration and fixation are necessary steps in sample preparation. Moreover, biological tissues have very low electron density and produce low number of electron scattering events, and low contrast. Thus, additional staining is required. Fixation can be performed by using chemicals (glutaraldehyde and paraformaldehyde) followed by contrasting by osmium tetroxide or uranyl acetate (Gunning and Calomeni 2013) or by strong temperature decrease (cryofixation). Sometimes, these two methods of fixation can be combined for better performance. The fixed sample is embedded in different types of resin (acrylic or gelatin) and stained by heavy metals (Reynold's lead citrate or uranyl acetate) or by immunolabeling with gold beads for contrast improvement. Frozen samples do not require additional staining, because the source of contrast is the difference between water and tissue. Finally, the bulk-embedded sample is sectioned by an ultramicrotome (5-100 nm of thickness) and deposited on a metallic grid for observation.

SEM sample preparation steps are similar, but require an additional metal coating step to create a conductive layer on the sample surface. This coating enhances the generation of secondary electrons, and reduces beam penetration and thermal damage. The specimen is coated by gold, palladium, platinum, silver, or chromium via plasma sputtering.

1.7.2. Atomic Force Microscopy (AFM)

AFM is a versatile method of scanning probe microscopy, based on the measurement of forces between the probe and the atoms at the surface of the sample. AFM enables imaging under physiological conditions with molecular resolution. In a typical AFM setup, the sample is mounted on the top of a piezo-tube scanner that is positioned in extremely close proximity to the AFM tip. The motion of the piezoelectric ceramic tube is highly precise. It can move with atomic precision. The tip is mounted on the cantilever, which permits an upside-down movement. The very low spring constant of the cantilever enables the AFM to control the force between the tip and the sample surface. A focused laser light is reflected from the cantilever and detected by the photodetector. During sample scanning, the measured cantilever deflections are processed for the reconstruction of a surface topography map (Fig. 1.7.3A).

An AFM setup can operate in several modes depending on the sample-tip distance, like contact AFM, tapping mode AFM and non-contact AFM (Fig.1.7.3 B). Contact AFM mode is based on the detection of repulsive Van der Waals forces at constant cantilever deflection, thus the force between the sample and the tip is constant. In the tapping mode, the cantilever is oscillating at its resonance frequency and lightly probes the sample surface. In the non-contact mode, on the contrary, the probe does not touch the sample surface, but oscillates above the fluid

level on the surface. Contact mode has benefits of speed, but can easily damage the sample or the tip. Tapping mode provides high resolution, is suitable for dry biological samples, but has relatively slow speed. Non-contact mode is harmed by its lower resolution and operation under ultra-high vacuum. The most used technique is the tapping mode, because it is suitable for sensing soft or fragile samples and can be operated in a liquid environment.

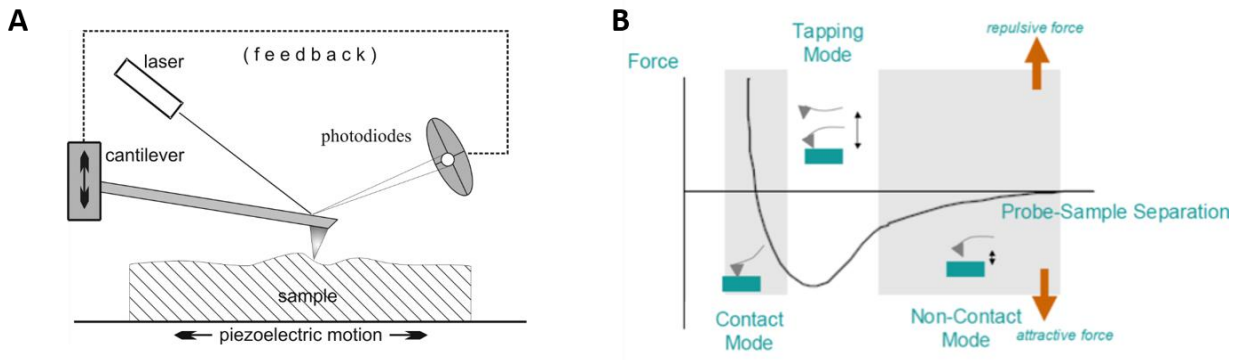

Figure 1.7.3. Basic elements of AFM and operating modes. (A) The sample is mounted on a piezoelectric controller. The deflection of the tip on the sample surface is measured by laser-photodiodes feedback and scanning systems. (B) The main interaction at short probe-sample distances is Van der Waals interaction, which can be repulsive or attractive. The type of interaction depends on the distance of the operation mode and leads to the cantilever bending.

AFM can be used for a variety of samples and does not require conductive coating like SEM. However, the resolution is limited by the sharpness and the size of the probe tip. If the tip is not ideally sharp, the resulting image represents rather the interaction of the probe with the sample surface or tip-convolution, than the true sample topology (Fig. 1.7.4). The degree to which the tip shape imposes itself is depending on the nature of the scanned surface. For flat surfaces, the degree of convolution is reduced and the tip should approximate to a hemisphere at its apex. The tip can compress soft biological samples and during the imaging under liquid conditions electrostatic effects may alter apparent heights.

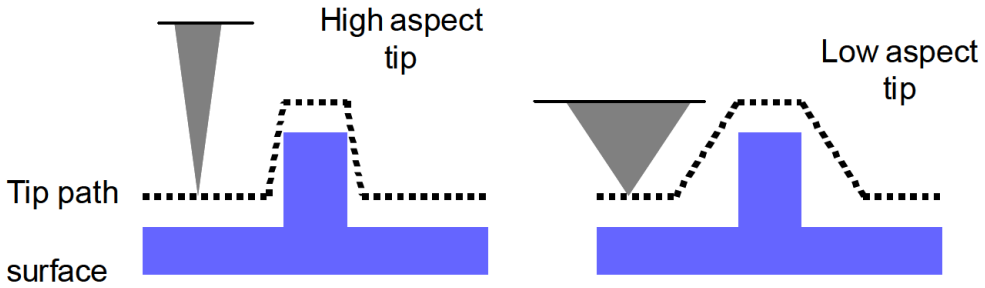

Figure 1.7.4. Influence of tip sharpness on surface sensing. The image of an object is spread by the tip profile and this process is both tip and sample dependent. As well, smaller objects will be in the shadow of tall ones and not recognized.

1.7.3. Fluorescence microscopy

Label-free methods like EM and AFM microscopy provide precise information about the morphology and spatial organization of biological objects. However, these methods are not applicable to life imaging of dynamic processes and are often limited to sensing of surface related events. Fluorescence microscopy on the contrary, presents specificity and high sensitivity. Multiple labeled cell components can be imaged simultaneously at high frame rates (up to 6000 Hz in widefield using CMOS cameras (sCMOS, Holst, 2005) or 100 Hz in confocal configuration using resonant scanners (Kirkpatrick, Chung et al. 2012). Ultra-sensitive EMCCDs enable to detect single molecules. Thus, fluorescence microscopy is a valuable tool for the investigation of biological processes.

The basic setup of a fluorescence microscope includes the source of light (mercury and xenon lamps providing a white light or lasers or LEDs that produce monochromatic illumination). The excitation light is filtered and focused to the sample by a series of optics and an objective lens. The emitted fluorescence is separated from the excitation light by a dichromatic mirror (Fig. 1.7.12) and detected by a photomultiplier or a camera (CCD or CMOS).

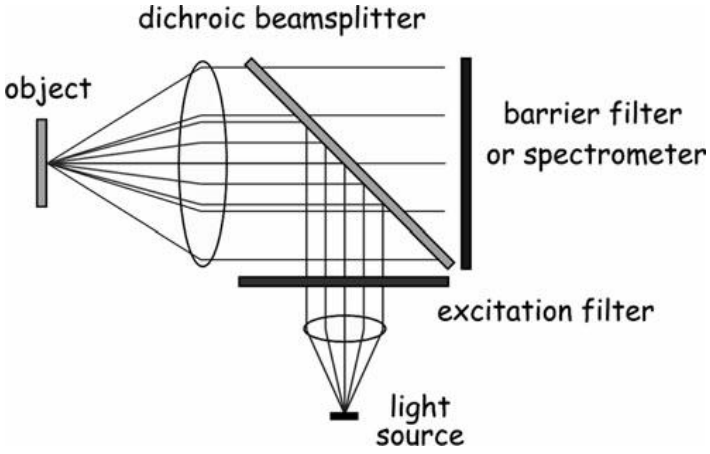

Figure 1.7.12. Scheme of the main elements of a fluorescence microscope. It is composed of light source, filters, lenses and dichroic mirror (Quercioli 2011).

Based on the setup configuration, different types of imaging systems exist: widefield, confocal and Total Internal Fluorescence illumination (TIRF). All these imaging approaches are performed in the epifluorescence configuration where the excitation and emitted light pass through the same objective. In the widefield configuration, the excitation light is focused on the rear aperture of the objective, generating a parallel beam that illuminates the specimen and produces a fluorescence signal through all the volume. Therefore, this method suffers from a relatively strong background signal from emitters outside the focal plane (Fig. 1.7.13A). In the

confocal approach, the excitation laser enters the objective as a parallel beam that is focused in a small focal volume (~250 nm in lateral and ~500 nm in axial dimension for visible light) that raster scans the sample translated by a couple of mirrors. Moreover, two pinholes introduced in the light path after the laser and before the detector, permit to reject the fluorescence signal from out-of-focus planes (Fig. 1.7.13B). Another approach to minimize the background signal is illumination of the specimen at short depth of penetration by the evanescent waves, created by the total internal reflection (TIR) phenomenon (Fig. 1.7.13C).

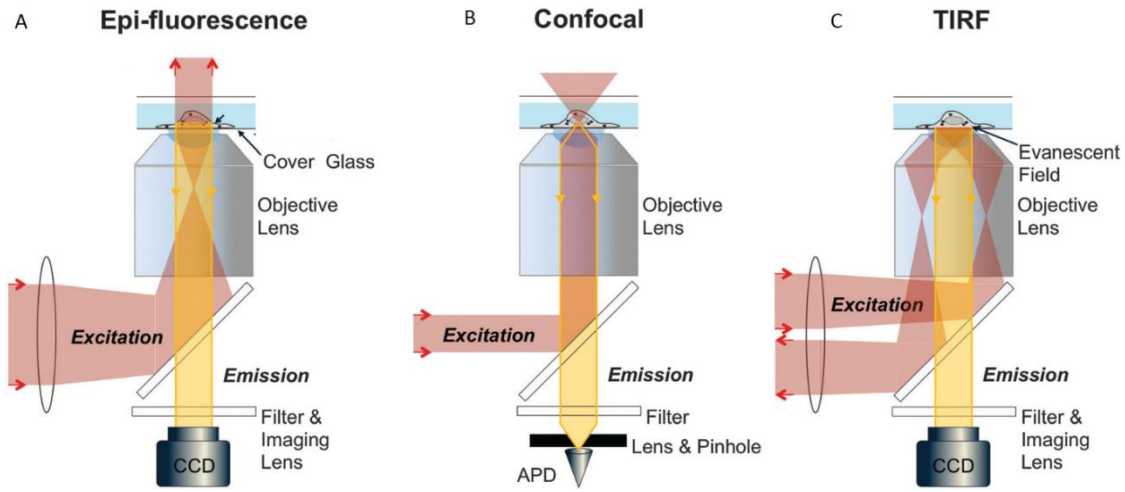

Figure 1.7.13. Mode of illumination of fluorescence microscopy setups. (A) Widefield (Epi-fluorescence) illumination excite the fluorophores in the focal volume; (B) Confocal illumination is focused on the small focal spot and performs imaging by scanning and (C) TIRF mode of illumination is collecting signal from ~200 nm depth of sample (Park, Lee et al. 2015).

TIR occurs when the incident beam of light propagates through the sample at a high angle (ensured by a high numerical aperture objective) upon the solid-liquid surface with difference of refractive indexes. This angle should be higher than the "critical angle" around 65° (for the glass-oil interface) to ensure the TIR, rather than refraction. However part of the incident light penetrates into the medium, propagates parallel to the surface and decays exponentially with the distance. This light, called evanescent wave excites the fluorophores in close proximity to the surface (up to 200 nm)(Reichert and Truskey 1990; Axelrod 2003). Thus only a thin sample layer is illuminated which strongly decreases the background signal.

Fluorescent labelling of cellular proteins

In order to generate a contrast, fluorescence microscopy requires labeling of the structure of interest. Three main labelling approaches are:

- genetic fusion to fluorescent proteins,
- specific direct binding to structures linked to organic dyes or nanoparticles
- immunolabeling.

Comparative sizes of protein of interest and potential fluorescent tags are shown in Figure 1.7.14.

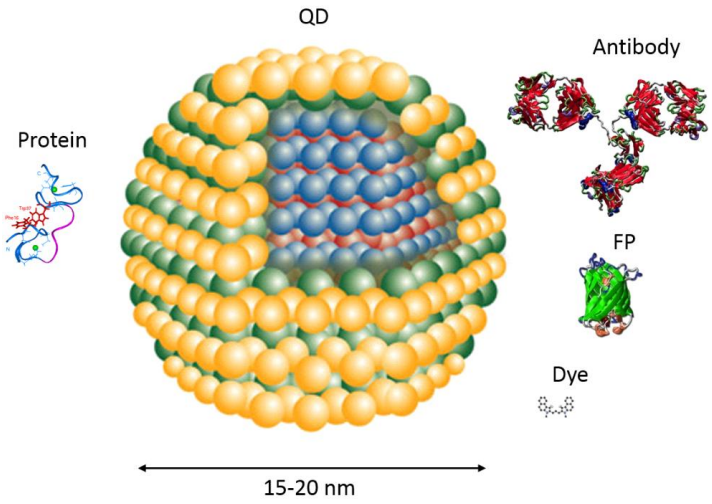

Figure. 1.7.14. Comparative sizes of common fluorescence probes and proteins of interest. Proteins of interest are in the range of sizes of few nanometers, whereas the size of a fluorescent probe can reach tens of nanometers. Fluorescent nanoparticles and Quantum Dots are even bigger.

Immunolabeling is a process of detection of a specific epitope by an antibody that is either directly labeled by a fluorescent tag, or detected by a secondary antibody conjugated to a fluorophore (indirect). In optimal conditions, this approach allows to label proteins of interest by bright and multicolor organic fluorescent molecules, gold beads or QDs. This method is mostly used to label fixed cells, which should be permeabilized to enable the antibodies to access the epitopes. The labeling can be performed on live cells in case of detecting accessible surface membrane proteins. The main drawback of this technique is that, standard protocols of immunolabeling may give a rise to various artifacts, such as nonspecific binding of antibodies, cell damage and protein extractions and/or re-localization.

Alternatively, fluorescent markers can be attached to proteins of interest through highly specific components or targeting molecules. So for example, phalloidin toxin from death cap mushroom bearing a fluorescent tag selectively binds to F-actin. However, number of such components are limited and do not cover a large variety of proteins. Other labeling approaches are based on the physico-chemical properties of dyes and specific interaction with objects, such as lipid probes and ER- (conjugate with the glyburide, sensitive to ATP-sensitive K^+ channels), mito-trackers (accumulation is dependent on the membrane potential). Lipids probes are often fluorescent analogs of natural lipids and fatty acids.

Finally, genetic fusion with fluorescent proteins (FP) or tags can mark proteins of interest. This approach ensures high labeling specificity and defined labeling stoichiometry. FPs

exist in different colors and can be expressed in bacteria, yeast and human cells. Newly developed FPs exhibit crucial changes in their spectral properties upon irradiation of specific wavelength, they are called photoactivatable fluorescent proteins (PAFPs). These proteins can switch from dark to bright state (photoactivatable) or can change the color of their emission (photoswitchable). PAFPs found a wide application in the recently developed high-resolution microscopy methods. However, compared to small organic dyes or quantum dots, FPs are limited by their low brightness, photostability and high photobleaching rate. Additionally, genetic labeling can generate some truncated products and artifacts. Moreover, their size (2-5 nm) can perturb the structure and functions of the labeled protein. Combination of a small genetic tag with an organic fluorophore seems to present an important advantage because of their smaller size and higher brightness. Genetically introduced tags can be full enzymes (SNAP-tag, CLIP-tag) or peptides (tetraCys). SNAP and CLIP tags are small (20 kDa) mutants of DNA repair protein that react specifically and rapidly with benzylguanine (BG) or benzylcytosine (BC) derivatives, respectively (Barth 2013) (Fig. 1.7.15). These tags are cell-permeable (can be used in life cells) and allow to label fusion proteins with a variety of fluorophores. Nonetheless, this approach can exhibit nonspecific reactions due to the binding to endogenous components and high background due to incomplete labelling. An efficient strategy to decrease the fluorescent background consists in using labels that are activated only upon binding to the tag on the targeted protein. Small peptide tags containing four cysteines (TC tag) can be fused to a protein of interest and then labeled by the biarsenical fluorescein derivative (FlAsH) (Griffin, Adams et al. 1998). FlAsH forms a nonfluorescent complex with ethandithiol (EDT). Upon binding to the TC motif, the EDT is replaced by the thiol groups of the cysteines and the FlAsH becomes highly fluorescent (Fig. 1.7.15). Additional multicolor variants of fluorescent biarsenical probes, such as CHoXAsH (Adams, Campbell et al. 2002; Cao, Chen et al. 2006) and the resorufin based ReAsh (Adams, Campbell et al. 2002) are the most known. FlAsH being cell permeable, can be used for live cell imaging enabling the study of cellular proteins without interfering with their activity.

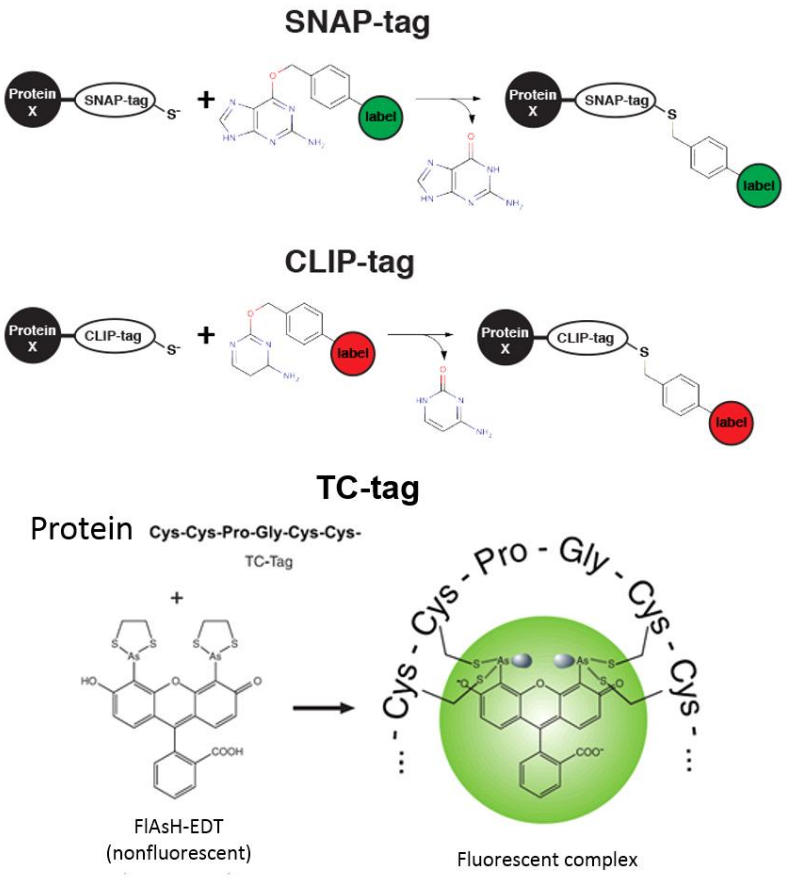

Figure 1.7.15. Pathways of labeling for genetically introduced labels. Mechanism of covalent binding of SNAP- and CLIP-tags via the interaction with BG or BC by the labels and mechanism of FlAsH labeling of TC tag trough cysteine binding (SNAP/CLIP adapted from (Kohl, Ng et al. 2014).

1.7.4. High resolution microscopy

The resolution of optical microscopes is restricted by an ultimate limit caused by the diffraction of visible light waves as they pass through the aperture and focal plane of the objective. Consequently, a microcopy image of a point object appears as a diffraction pattern, known as the Airy disk. In general, the resolving power of a microscope is defined by the Rayleigh criterion as the limit up to which two Airy disks can be seen as separate entities (Fig. 1.7.14).

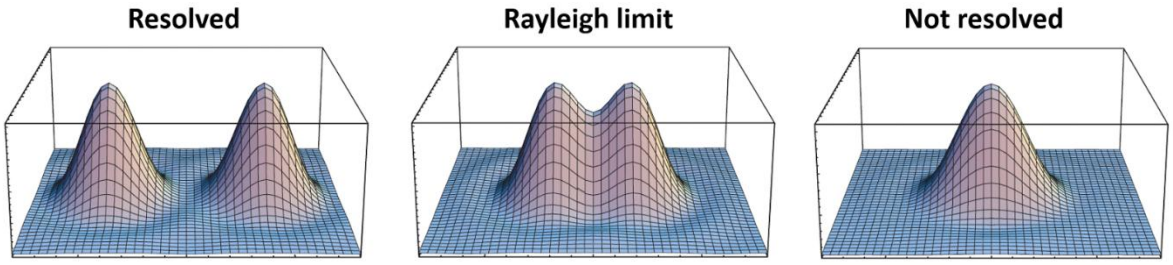

Figure 1.7.16. Graphical presentation of the Rayleigh criterion. Visualization of the Airy disks of two individual point sources of light and their intensity plot profile. Depending on the distance between the two sources, they can be resolved or not during the observation (Kubitscheck 2013).

The resolution of a microscope is defined as the distance where this limit is reached. This value can be calculated from the Abbe formula [3] for the lateral and axial dimensions:

—— —— [3]

where λ is the illumination wavelength, NA is the numerical aperture , n is the refractive index and α is the maximal half-angle of the cone of light which enters or exits the lens. Theoretical values for lateral and axial resolution at 400 nm wavelength for a high NA objective (~1.4) are ~150 and 400 nm, respectively. The image of a point object is called the Point Spread Function (PSF). The degree of PSF spreading due to diffraction and optical aberrations is a measure of the quality of the imaging system.

A number of super-resolution fluorescent microscopy (SRM) techniques have been invented during the past decades to overcome the diffraction barrier. The progress in this field was awarded by the Nobel Prize delivered in 2014 to Stephan Hell, Eric Betzig and W.E. Moerner for the development of super-resolved fluorescence microscopy.

The first attempts to increase the resolution of fluorescent microscopes concerned mainly the axial dimension. In 4Pi microscopes, the axial resolution was improved by generating an interference pattern in the focal plane by separating the excitation laser in two opposing focused laser beams (Cremer and Cremer 1978; Hell and Stelzer 1992). In combination with two-photon excitation, this method provides an improvement of the axial resolution down to 100 nm (Hänninen, Schrader et al. 1995). However, the alignment and the stability of the experimental setup was quite fastidious and 4Pi microscopy did not reach a great success in practical applications among biologists (Leung and Chou 2011).

Since this first attempt, other techniques improving the lateral and axial resolution have been developed and adapted for routine microscopy observations. Based on their general principle, the SRM techniques can be classified in two main groups:

- **deterministic approaches:** based on the modulation of the PSF size or spatial modulation of illumination. This group comprises stimulated emission depletion (STED) microscopy, reversible saturable optical linear fluorescence transitions (RESOLFT) and structured illumination microscopy (SIM, Saturated SIM);
- **stochastic** localization microcopy based on temporal modulations of the transitions between two molecular states of a fluorophore. The main representative approaches are PhotoActivation Localization Microscopy (PALM) and Stochastic Optical Reconstruction Microscopy (STORM).

Structured Illumination Microscopy (SIM)

In the SIM approach, a widefield set of images is acquired under modulated illumination and post-processed with Fourier transformation in order to access the higher frequencies in the reciprocal space. Figure 1.7.17 presents the general idea of resolution improvement. Series of low frequency images of the sample are acquired by the modulated illumination pattern. Spatial frequency mixing results in a Moiré interference pattern (Lee 1988), that contains higher frequencies which encode otherwise non-resolvable structural information. By imaging a series of these Moiré patterns as well as by rotating and translating the illumination and by subsequent computational post-processing, it becomes possible to access the higher frequency information encoded in the image and reconstruct it with a twofold improvement of the resolution. The resolution increase can be higher (50 nm) in case of illuminating the sample with a grid-like array of line-shaped maxima and minima with the emission rate depending nonlinearly on the illumination intensity (Gustafsson 2005). As a result, nonlinearity produces an effective illumination pattern with more spatial frequencies. An infinite number of harmonics theoretically corresponds to an infinite resolution. (Gustafsson 2000)(Fig.1.7.17).

This technique does not require a use of special fluorophores, it is highly sensitive and enables recording a large field of view (whole cell) in a physiological conditions. The main drawbacks of the method is that for one high-resolution image a set of 9 (15 for 3D resolution improvement) images are needed. Moreover, it suffers from the bleaching caused by the high power of illumination for direct saturation, and the long acquisition of the sets of images needed for the reconstruction of the final image. In addition, a refractive index mismatch and/or poor sample quality can induce artifacts and compromise the resolution improvement.

Nowadays, commercial SIM microscopes reach up to 30 frames per second imaging rates (Schlichenmeyer, Wang et al. 2014) Nikon N-SIM).

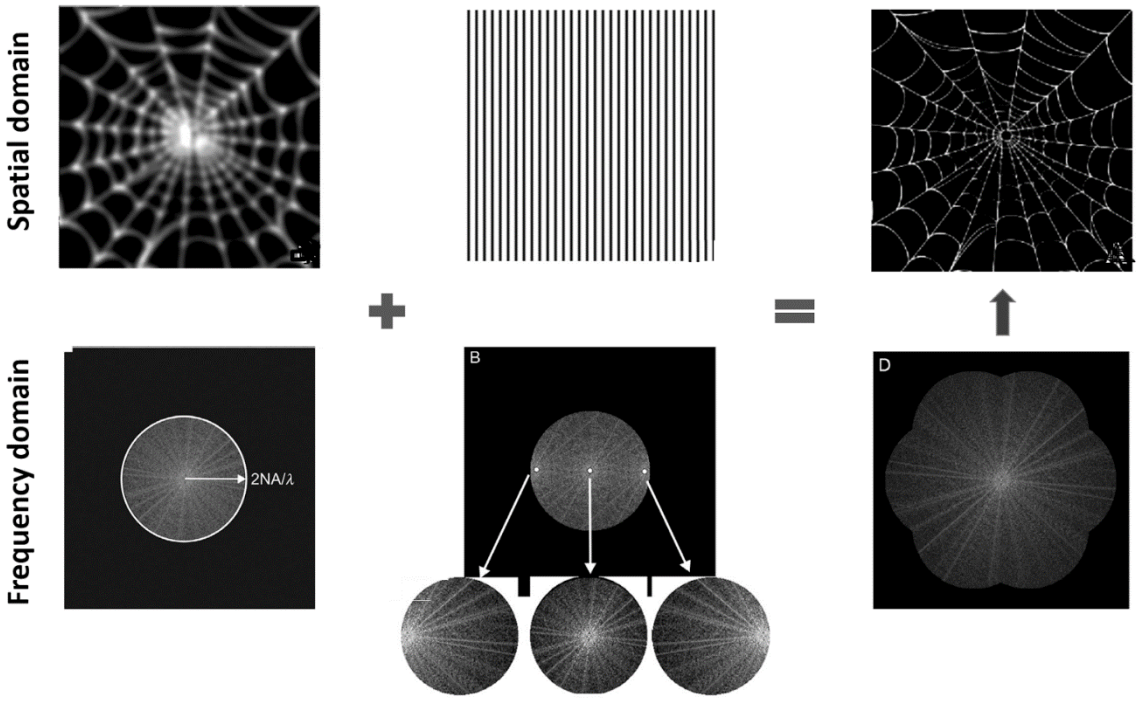

Figure 1.7.17. Resolution enhancement by structured illumination. Top line images represent a diffraction-limited image, illumination pattern and the resulting image with higher resolution. The Fourier transform of a widefield optical microscopy image in the reciprocal space is represented by the low frequencies domain image restricted by the Abbe diffraction to a circle whose radius is limited to 2NA/λ. The displacement of the illumination pattern produces three new Fourier components, which expand the observable frequency domain. Different orientations of the structured pattern produce further expansion in 3 directions of the frequency domain. Finally, the high-resolution image is reconstructed by the back transformation from the frequency to the spatial domain.

STED

STED microscopy was developed more than 15 years ago by Stefan W. Hell. The depletion principle was published in 1994 (Hell and Wichmann 1994). STED is based on the sharpening of the effective PSF by depletion of the excited state of fluorophores at the periphery of the focal spot (Fig. 1.7.18). High-resolution images are obtained by scanning the sample with this small effective PSF.

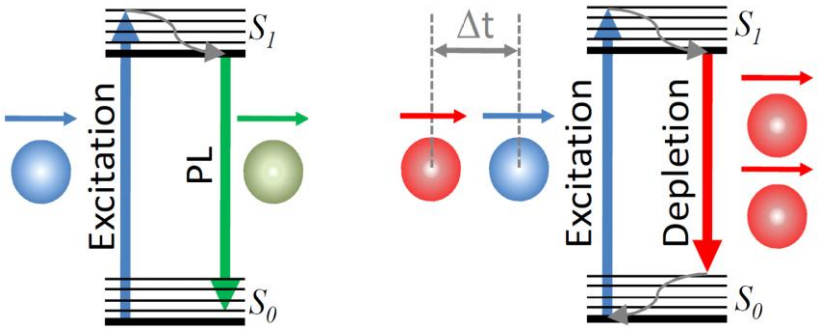

Figure 1.7.18. Molecular transitions for normal fluorescence and for stimulated emission. Normally fluorescence occurs when the excited dye is relaxed to the ground state. Simultaneous illumination of the

system by a long-wavelength light causes return of the dye to the ground state (Adapted from (Farahani, Schibler et al. 2010), and thus, causes the depletion of the excited state.

Experimentally the reduction of focal volume is achieved by using a pair of synchronized laser pulses. The first excitation laser is focused in a normal diffraction limited spot and excites the fluorophores in the sample. The depletion laser is red-shifted and doughnut shaped by an optical vortex with phase modulation (spiral phase plate or spatial light modulator) (Courtial and O'Holleran 2007). The fluorophores of the sample are excited by the first laser in the whole focal volume, but the fluorescence emission is depleted at the periphery by the doughnut shaped depletion laser, resulting in a sharpened effective focal spot. Figure 1.7.19 shows an example of a STED setup that comprises excitation and depletion lasers, phase plate, dichroic mirrors and oil objective.

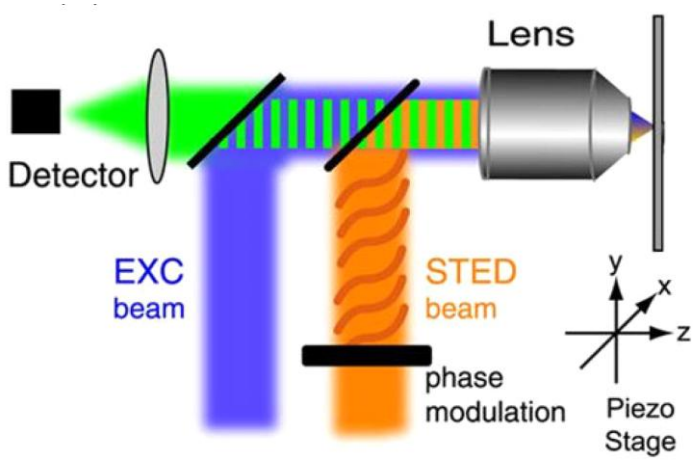

Figure 1.7.19. Basic setup of STED microscopy. It is composed of two laser beams, phase modulator, piezo stage, lenses and detector (Adapted from (Farahani, Schibler et al. 2010)).

The Resolution of the STED method (Δd) is proportional to the efficiency of the depletion that is related to the photo-physical parameters of the fluorophores and the intensity of the depletion laser. It can be calculated by the formula [4]:

[4]

where Δd is the radius of the focal spot, λ is the wavelength of the excitation laser, NA is the numerical aperture, I is the intensity of the STED laser and I_s represents the saturation intensity of the fluorophore.

Therefore, theoretically increasing the intensity of the depletion pulse will cause progressive narrowing of the focal spot infinitely. On biological samples labelled with small organic dyes, the achieved resolution is near 30 nm (Westphal and Hell 2005). For samples labeled with fluorescent proteins, it is rather 50-70 nm (Hein, Willig et al. 2008). The main

drawbacks of the STED microscope for live cell imaging is the high power of the illumination combined with scanning approach, which leads to a high level of phototoxicity.

First, STED microscopes were based on pulsed laser illumination. Continuous wave lasers (CW-STED) for both the excitation and the depletion were also proposed to simplify the setup. However, peak intensity of the CW-STED beam is lower, compare to the pulsed beam, thus resulting in the lower resolution performance (Willig, Harke et al. 2007). The combining of CW-STED and time-gating detection in the gated CW-STED (gCW-STED) (Vicidomini, Hernandez et al. 2014) solved this problem. In addition, this method of detection was earlier successfully applied with pulsed STED, where it helped to maximize the resolution performance (Galiani, Harke et al. 2012).

3D STED microscopy has been first implemented with CW-STED and provides 3.5 fold improvement of the axial and 5-8-fold increase of the lateral resolution (Willig, Harke et al. 2007). 3D STED implemented with 4Pi illumination provides 1.4-fold improvement of axial resolution (Wildanger, Medda et al. 2009). Later, the use of a circular phase mask that shapes the focal spot of the depletion laser in the axial direction gave ~90 nm axial resolution (Willig, Harke et al. 2007).

RESOLFT

RESOLFT (Hell 2007) microscopy is a generalized approach, which takes benefit from any reversible light-induced and saturable transitions between two molecular states: fluorescent **on** and dark **off** states. Different mechanisms of switching gave rise to several methods such as STED with off ground state of the fluorophore, ground-state-depletion microscopy (GSD) when the off state is a triplet state or the dark state of reversibly photoswitching fluorophores (Hofmann, Eggeling et al. 2005). Inhomogeneous illumination achieved by the interference can create zero intensity point. At low intensity of illumination, most fluorophores in the diffraction-limited area will be in the **on** state. With increase of illumination intensity, excited area can be narrowed to the small region around zero intensity spot. However, switching of the fluorophores to the dark state in the course of RESOLFT acquisition requires lower power of illumination compared to the STED. Earlier RESOLFT resolution on the FPs was 50-100 nm and was limited by the photokinetics of the proteins (Hofmann, Eggeling et al. 2005). Later was shown that RESOLFT of <40 nm resolution in living cells is compatible with enhanced reversibly switchable GFP with fatigue resistance of more than 1000 switching cycles before the 50% bleaching (Grotjohann, Testa et al. 2011)

Single Molecule Localization Microscopy

Single molecule localization microscopy techniques are based on sequential activation and precise localization of individual fluorophores in order to reconstruct high-resolution images as shown at figure 1.7.20. Among these approaches, PALM (Photoactivation Localization Microscopy) and STORM (Stochastic Optical Reconstruction Microscopy) are the most popular ones. The localization principle being the same, the main difference between PALM and STORM is in the types of fluorescent tags and the principle of activation and deactivation used. PALM (or fPALM from fluorescence PALM) was historically developed with photoactivatable fluorescent proteins, mainly with tetrameric Kaede and oligomeric EosFP (Betzig, Patterson et al. 2006). In contrast, STORM and dSTORM (direct STORM) use photoswitchable or conventional small organic dyes respectively.

Due to the diffraction limit, individual fluorophores are imaged by a light microscopy system as ~200 nm-sized spots that cannot be resolved on a densely labeled structure (more than one label per 200 nm area). To overcome this limitation, the excited fluorophores are separated temporally by stochastic activation of a small number of labels at the same time (Fig.1.7.20). The level of activation is controlled in order to have only one molecule in the "bright" state in the diffraction spot at one time, while the others are turned OFF to their "dark "state. If this condition is satisfied, their position can be precisely localized by fitting the intensity profile recorded by an ideal PSF function. In this manner, a subset of fluorophores are consecutively activated, imaged, localized and deactivated before another subset is activated and imaged. In figure 1.7.21, the PSF of individual molecules is shown as a raw image on the CCD display. Its Gaussian fit and localized position of the center of the resulting image are also shown. Iteration of the localization process allows to find the precise position of the fluorophores and to reconstruct a final high-resolution image (Betzig, Patterson et al. 2006).

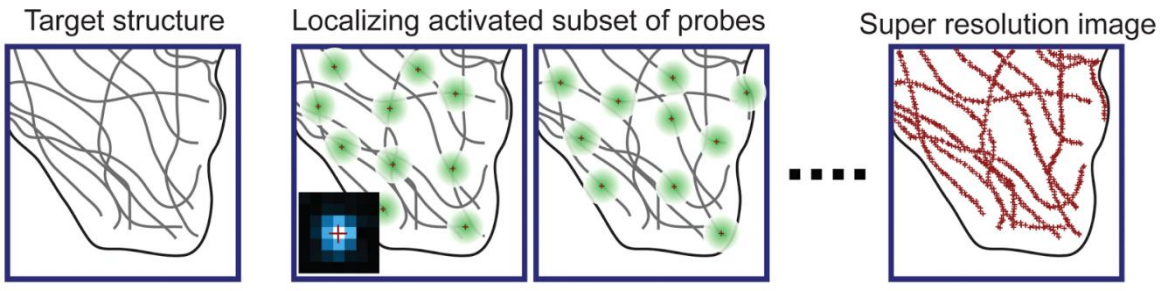

Figure 1.7.20. Principle of point-localization high-resolution microscopy. A subset of fluorophores is activated at different time points and a stack of images is recorded. Detection of the position of each fluorophore on the frame sequence provides the high-resolution image (Adapted from (Huang, Bates et al. 2009).

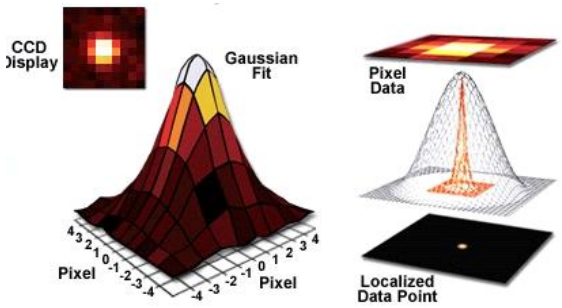

Figure 1.7.21. Single molecule localization. 3D distribution of the intensity of the PSF detected by the CCD display is fitted by a Gaussian fit to determine the center of the point source of light.

The resolution of the reconstructed image is strongly dependent on the localization precision of individual fluorophores defined as:

$$\sigma_x^2 = \frac{r_0^2 + q^2/12}{N} + \frac{8\pi r_0^4 b^2}{q^2 N^2} \qquad [5]$$

where is the standard deviation of the PSF, N is the total number of photons collected, q is the size of an image pixel, and b is the background noise per pixel. One of the main parameters is the number of detected photons from each fluorophore. If the background noise is negligible compared with the signal from the fluorophores, the error in the fitted position can be approximated by $\sigma_{x,y} \approx s/(N^{1/2})$, where s is the standard deviation of a Gaussian approximating the true PSF (approximately 200 nm for a 500 nm light) and N is the number of detected photons. In low background conditions and using bright fluorophores, a 20 nm resolution can be achieved. This resolution approaches the physical size of the immunolabelled samples.

The switching of fluorophores between two different states can be achieved by different approaches that depend on the nature of the fluorophores (Fig. 1.7.22). Photoactivatable proteins can be switched or activated from the non-fluorescent state to the bright fluorescent. This process occurs under the short pulse illumination in the violet/blue spectrum. Photoconversion on the contrast to the photoactivation permits the transition of the fluorophore from one fluorescent form to another. Photoactivation is an irreversible process, photoswitching is the process of reversible transitions between the **off** and **on** states (Fig. 1.7.22).

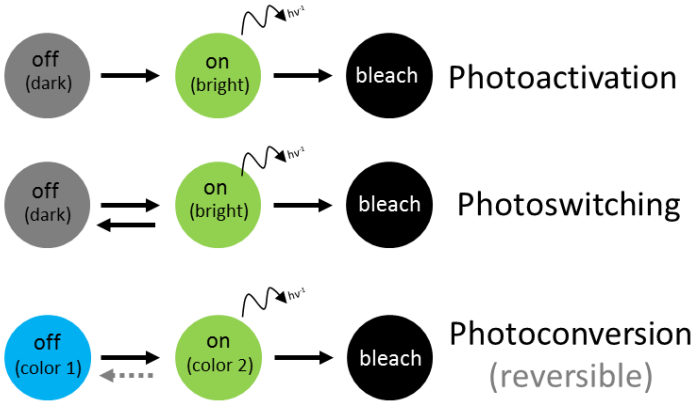

Figure 1.7.22. Mechanisms used in point localization microscopy. Photoactivation stands for the irreversible activation of dyes to the bright state with following bleaching. Photoswitching represents the transition of fluorophores between the dark and bright states until their destruction. Photoconversion indicates transitions between states with different wavelength of emission (sometimes reversible).

Depiction of some fluorescent proteins and small organic dyes with their properties is presented in the table 1 and table 2 respectively.

Table 1. Modern monomeric fluorescent proteins. Upper line for each FPs represents the parameters before the photoconversion and lower line parameters after the photoconversion.

Protein	Excitation (absorbance) maximum (nm)	Emission maximum (nm)	Quantum yield	Photoactivation light wavelength (nm)	Photo-stability	References
Photoactivatable Fluorescent Proteins						
PAGFP	400	515	0.13	405	ND	(Patterson and Lippincott-Schwartz 2002)
	504	517	0.79		Low	
PAmRFP1	(405)	ND	ND	405	ND	(Verkhusha and Sorkin 2005)
	578	605	0.08		Medium	
PAmKate	(442)	ND	ND	405	ND	(Gunewardene, Subach et al. 2011)
	586	628	0.18		High	
Photoswitchable Fluorescent Proteins						
PSCFP2	400	470	0.20	405	ND	(Chudakov, Verkhusha et al. 2004) (Chudakov, Lukyanov et al. 2007)
	490	511	0.23		Low	
Dendra2	490	507	0.5	405/488	Medium	(Chudakov, Lukyanov et al. 2007)
	553	573	0.53		High	

						(Gurskaya, Verkhusha et al. 2006)
tdEosFP	506	516	0.66	405	Medium	(Wiedenmann, Vallone et al. 2005)
	569	581	0.60		High	
mEos2	506	519	0.84	405	Medium	(McKinney, Murphy et al. 2009)
	573	584	0.66		High	
Reversibly Switchable Fluorescent Proteins						
Dronpa	(392)	ND	ND	405	ND	(Ando, Mizuno et al. 2004)
	503	518	0.85	488	Low	
rsFastLime	(384), (496)	ND	ND	405	ND	(Stiel, Trowitzsch et al. 2007)
	496	518	0.77	488	Medium	
rsEGFP	(396)	ND	ND	405	ND	(Grotjohann, Testa et al. 2011)
	493	519	0.36	488	High	
rsCherry	572	610	0.009	550	ND	(Stiel, Andresen et al. 2008)
	572	610	0.02	459	Low	

Table 2. Small organic dyes for the super-resolution microscopy.

Fluorophores	Excitation (absorbance) maximum (nm)	Emission maximum (nm)	Quantum yield	STED/Activation (nm)	References
Atto488	501	523	0.8	405/488	(Dempsey, Vaughan et al. 2011)
Cy3B	559	570	0.67	405/561	(Dempsey, Vaughan et al. 2011; Vaughan, Jia et al. 2012)
Alexa647	650	665	0.33	405/647	(Dempsey, Vaughan et al. 2011)
Cy7	747	776	0.28	495/750	(Dempsey, Vaughan et al. 2011)
FlAsH	508	528	0.49	405	(Lelek, Di Nunzio et al. 2012)

The blinking properties of the fluorophores are enhanced in the presence of reducing agents contained in special “photoswitching buffers. These buffers are in general composed of

reducing agents, such as source of thiols (cysteamine (MEA) or β-mercaptoethanol (βME)) and oxygen scavengers (GLOX system) (Aitken, Marshall et al. 2008). The concentration and precise composition of these components varies depending on the fluorophore (Dempsey, Vaughan et al. 2011; van de Linde, Krstic et al. 2011).

The effect of these reducing agents is summarized in the energy transition diagram in Figure 1.7.23. When illuminated, the molecules absorb the energy and pass from the singlet ground S0 to the first singlet excited state S1. They can reach back the ground state S0 either by a non-radiative process or by emitting fluorescence. Alternatively, inter-system crossing can lead them to a long-lived triplet state. The reducing agent favors the reduction of triplet states by reversible generation of a non-fluorescent long-lived anion (A*) corresponding to the "dark state" of the molecule. The fluorophore is turned back on by recovery of the fluorescent form by a 405 nm illumination that favors the oxidation of A*. These transitions are observed as the "blinking" of the fluorophore. It should be noted that relaxation from the triplet state is energetically coupled to the generation of singlet oxygen and reactive oxygen species that may cause photobleaching (destruction) of the fluorophore. In order to limit this process, the imaging buffers contains the GLOX or GODCAT system. This enzymatic oxygen scavenger system composed of glucose oxidase and catalase in the presence of millimolar glucose removes oxygen generating by a hydrogen peroxide that is consecutively reduced by catalase to the water (Englander, Calhoun et al. 1987).

In the case of use of fluorophores that are ultra-sensitive to singlet oxygen the imaging may be performed in a closed chamber in order or under argon atmosphere.

Interestingly recent studies reveal that many routinely used fluorescent labels can be maintained in the "blinking" state exclusively with a high power excitation, without the presence of a photoswitching buffer (ER tracker (Shim, Xia et al. 2012)), Bodipy (Bartelmess, De Luca et al. 2014)).

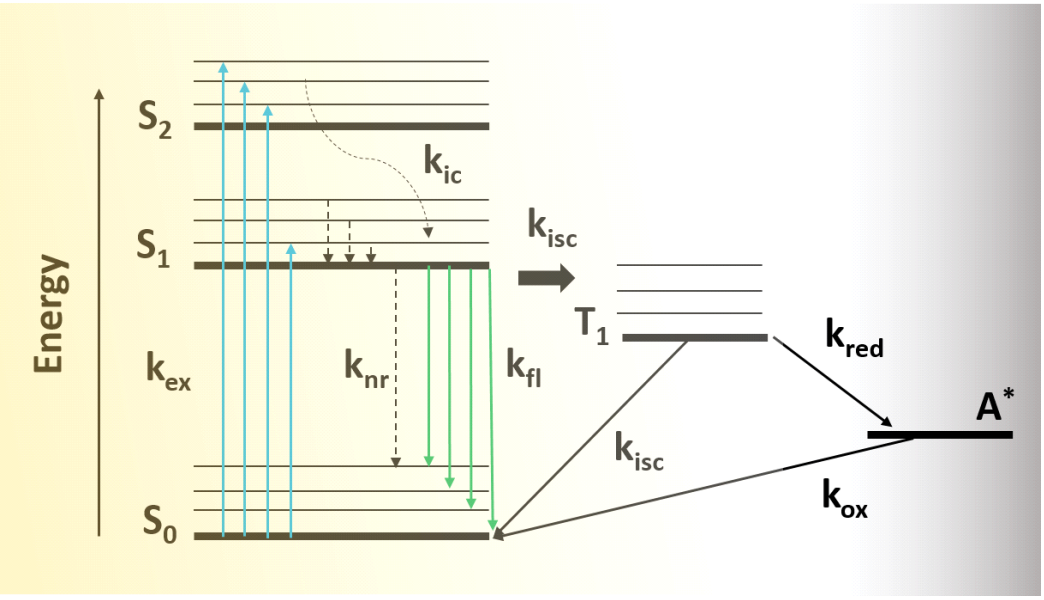

Figure 1.7.23. Energy level diagram of the photoswitching process. The fluorescent molecule is excited from the ground (S_0) to the excited single states (S_1, S_2) with k_{ex} rate. Higher excited states relax to the lower excited state S1 by internal conversion (k_{ic}). The relaxation to the ground state occurs either by emitting fluorescence (k_{fl}) or by non-radiative pathway (k_{nr}). Alternatively, the fluorophore can go to the triplet state (T_1) by intersystem crossing (k_{isc}). Presence of reducing and oxidizing agents depletes the triplet state by reduction of the fluorophore to a non-fluorescent radical anion (A^-). Radical species of the fluorophore absorb at ~400 nm. The return to the ground state by oxidation permits the reexcitation of the fluorophore and thus the cycling of the molecule between ON and OFF states, which ensures the blinking.

In a typical localization microscopy setup (widefield microscope), the activation and excitation lasers are focused by a set of lenses to and a TIRF objective on the samples. The emitted signal is separated from the excitation light by a set of dichroic mirrors and detected by a CCD camera (Fig. 1.7.24).

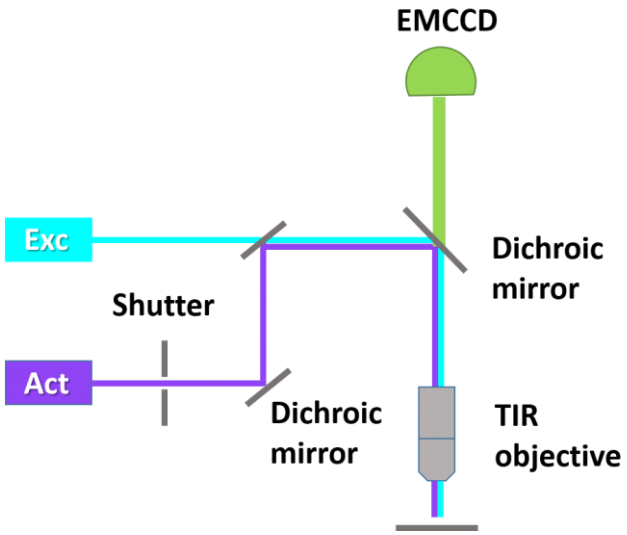

Figure 1.7.24. Basic configuration of PALM/STORM microscopy.

During the experiments, huge datasets are recorded and analyzed for the reconstruction of the final high-resolution image. The analysis is realized with the following steps:

- **preprocessing** improves the quality of images and highlights the spots by reducing the background and noise
- **detection** of the fluorescent spots often based on the intensity gradient and PSF estimation (Airy or Gaussian function are the most used for isotropic sources)
- **localization** step consists in fitting the experimental spot to the model PSF in order to retrieve the coordinates of the fluorophore
- **rendering -** visualization of the coordinates of localized fluorophores. (Most frequently used rendering approach is the histogram in which the intensity of each pixel of the final image is assigned to a number of detected blinking events).

Depending of the density of labeling and the morphology of the structures being imaged, the number of acquired images is of the order of few thousands. The stability requirement of the sample and the use of photoswitching buffers require that these techniques are the most often used for imaging of fixed samples. Even if many optimized softwares are available nowadays (Sage, Kirshner et al. 2015) for image processing and reconstruction of a HR image, image reconstruction can still take several minutes.

Localization microscopy has given rise to a bunch of new microscopy approaches such as PALM with Independently Running Acquisition (PALMIRA), Point Accumulation for Imaging in Nanoscale Topography (PAINT) and Ground State Depletion followed by individual molecules return (GDSIM).

PALMIRA permits to decrease the background signal and long image acquisition time. In this approach, digital camera runs at high speed with exposure time matching to the average on-time of the fast photoswitching fluorescent protein, like rsFastLime (Egner, Geisler et al. 2007; Stiel, Trowitzsch et al. 2007). As well, unlike PALM and STORM, PALMIRA has a simplified setup due to a single laser line used for readout and activation (Egner, Geisler et al. 2007).

In the PAINT approach, the fluorescent molecules from the solution interact transiently with sample targets and produce fluorescence only upon binding to the substrate (Sharonov and Hochstrasser 2006). These approach with sequential washing of the samples and repeatable labeling permits to obtain 10-color imaging of DNA structure (Jungmann, Avendano et al. 2014). As well, target protein labeling have been developed on the base of DNA immobilization (Jungmann, Avendano et al. 2014), peptide-based probes (Kiuchi, Higuchi et al. 2015) and antibodies (Tam, Cordier et al. 2014). Thus, fluorophores are detected from the moment of binding (start of fluorescence) until photobleaching with a localization precision around 25 nm. PAINT can be used with nonspecific membrane dyes or with specific fluorescent ligands (i. e. antibodies) (universal PAINT) (Giannone, Hosy et al. 2010).

GDSIM is another localization microscopy technique, ensured by the switching of almost all fluorophores to the dark (triplet) state by the use of a high intensity excitation. This technique provides a resolution up to 20 nm (Folling, Bossi et al. 2008).

In recent years, progresses have been made in increasing the resolution of Single Molecule Localization Microscopy techniques in the axial dimension. 3D imaging is based on spatial modifications of illumination by astigmatism or by using a two-focal plane imaging. In the first case, a cylindrical lens is introduced in the light path and produces an elliptical PSF that provides (after a careful calibration) an information about the axial position with 50 nm precision (Huang, Jones et al. 2008). Alternatively, a biplane PALM microscopy is based on a 50:50 beam splitting on the two components with different length of path (Fig.1.7.25). These components are detected on two regions of the camera and they provide information about the z coordinate of fluorophores with up to 75 nm axial localization precision (Juette, Gould et al. 2008).

The principle of controlled activation of a subset of molecules of the sample can be used for another application, and namely single particle tracking (spt). In the sptPALM approach, fluorophores are stochastically activated and imaged at a rate depending on the compromise between the resolution improvement (localization precision) and the number of frames recorded before photobleaching of the fluorophore. In each frame, the positions of the molecules are localized and the final trajectory is a result of connection positions from all the frames (Manley, Gillette et al. 2008). The main advantage of this method is that it overcomes complicated adjustments of the labeling concentration needed for the tracking experiments and the possibility to measure numerous trajectories simultaneously in one cell.

Selection of a particular high-resolution technique strongly depends on the addressed question and type of sample. Moreover, high-resolution techniques are in continuous development and HR microscopes are available commercially. Table 3 presents the main characteristics of the described above high resolution methods.

Table 3. Comparison of high-resolution microscopy techniques

Title	SIM/3D-SIM	SSIM	STED/CW-STED	PALM/ /STORM
Lateral resolution	100–130 nm	50 nm	20–100 nm	20-30 nm
Axial resolution (3D implementation)	100 nm	-	20-100 nm	20–30 nm (3D-STORM 75 nm (BP-FPALM)
Suitable dyes	Most conventional (photostable)	Photostable	Tuned for pulsed laser lines/ highly photostable stable; high depletion rate	Most conventional (photostable)
Multicolor imaging	Yes	Yes	Yes	Yes
Energy load	Medium	High	Medium-high	Medium-high
Live-cell imaging	Restricted	No	Restricted	Restricted
Postprocessing	Yes	Yes	No	Yes

1.7.5. HIV microscopy by EM and AFM

First attempts to image the HIV virus were done in the late 80s by EM using negative staining and immunolabeling methods (Filice, Carnevale et al. 1987; Pauli, Hausmann et al. 1987; Gelderblom, Özel et al. 1988). This unveiled the general structure of the virion, the envelope, the conical capsid and the position of some structural proteins (Gelderblom, Hausmann et al. 1987; Stannard, van der Riet et al. 1987). More than 20 years later the development of cryo-electron tomography allowed to preserve the intact structure of the virions and to image the position of individual viral proteins with near-atomic precision (Briggs, Grunewald et al. 2006; Meyerson, White et al. 2011; Schur, Hagen et al. 2015), (Strauss, Hammonds et al. 2015). The EM imaging of the viruses in the infected cells is intricate because of the difficulty to detect the viral cores in a heterogeneous and dense cytoplasm. Therefore, immunolabeling is the good solution for the detection of cytoplasmic viruses during the early stages of infection. On the contrary, the assembly of new virions on the plasma membrane is suitable for EM studies, because the budding particles can be easily distinguished. Numerous examples of the EM imaging of HIV-1 assembly can be found in the literature (Bharat, Castillo Menendez et al. 2014; Woodward, Cheng et al. 2015; Schur, Obr et al. 2016).

Structure

Pioneering studies of HIV-1 by EM were done on isolated and negatively stained viral particles (Stannard, van der Riet et al. 1987; Chrystie and Almeida 1988) (Fig. 1.7.25). This approach provided a general visualization of their shape and their double-layered envelopes.

Moreover, these EM images evidenced for the first time the typical conical shape of the viral core with dimensions of 130 to 30-70 nm (Chrystie and Almeida 1988). Later, ultrathin sectioning and immunolabeling were used to resolve spatial distribution of the envelope and core proteins (Gelderblom, Hausmann et al. 1987). This study showed 70 to 80 knobs made from gp120 loosely connected to the transmembrane protein gp41 distributed on the surface of viral particles. The localization of internal viral structures in this study was suffering from weak topographic accuracy but it was found that the matrix (p17/p19) covers the internal surface of the envelope and the CA protein (p24) forms the core shell. TEM on negatively stained samples was used by Ganser (Ganser, Li et al. 1999) to enlighten the assembly and the core organization of viral particles. In this pioneering work, synthetic viral cores of CA-NC (strongly resembling the authentic HIV-1 cores) were created on the base of RNA templates. This approach helped to precisely determine the angles of capsid subunits organization and to define its geometrical structure. It was proposed, that HIV-1 cores form cones by similar symmetry principles as carbon and adopt a curved p6 lattice of CA hexagons (Ganser, Li et al. 1999). These first structural data gave an insight into the general structure of HIV-1 virions and were later refined by more sophisticated EM observations, like cryo-electron tomography. This method allows creating a 3D reconstruction model of the mature, authentic HIV-1 virions with a mean diameter of nm (Briggs, Grunewald et al. 2006).

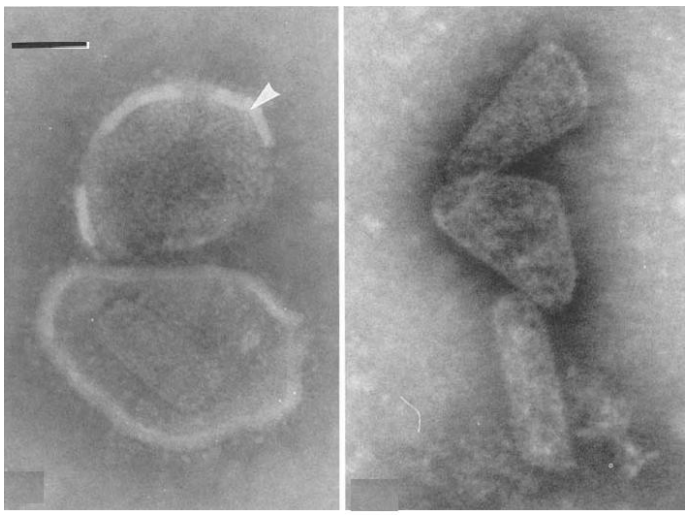

Figure 1.7.25. Negatively stained preparation of HIV-1. (A) The majority of particles revealed a pear-shaped form for the core and less particles were found with rod-shaped structures. (B) Occasionally free cores were observed (Scale bar 50 nm) (Adapted from (Chrystie and Almeida 1988).

The combination of electron tomography (ET) with cryo-fixation (Dubochet, Adrian et al. 1988), developed in late 90s permitted the study of the 3D spatial organization of HIV-1 with precision of a few angstroms. This approach enabled to uncover the spatial conformation and distribution of gp41 and gp120 Env proteins. Observations of Env trimers was also realized by

AFM microscopy. A recent cryo-ET study of Env structure in the pre-fusion conformation and stabilized by the neutralizing antibody revealed (Bartesaghi, Merk et al. 2013; Dutta, Liu et al. 2014; Lee, Ozorowski et al. 2016) that the HIV-1 Env protein is organized in trimers and undergoes conformational changes upon the binding to the cell. During these transformations between a pre-fusion and activated intermediate state, the trimeric gp41 helices serve as an anchor.

Contrary to cryo-EM, the AFM results showed no ordered arrangement of gp120 monomers on the viral surface (Kuznetsov, Victoria et al. 2003). Real-time AFM studies of the interaction of gp41 with plasma membrane revealed a strong perturbation of the negatively charged plasma membrane in the presence of gp41 (Bitler, Lev et al. 2010).

Another challenging task for electron microscopy was precise visualization the viral capsid in order to prove the model of capsid organization proposed by Ganser. This question is related to the formation of viral particles and their reorganization during maturation. Cryo-TEM imaging was performed on HIV-1 capsid assembly and rearrangement during the different steps of maturation *"in vitro"* (Zhao, Perilla et al. 2013), or using a virus like particles (VLPs) as a model (Benjamin, Ganser-Pornillos et al. 2005; Briggs, Grunewald et al. 2006). These works have showed that the Gag lattice of virus shell is composed of hexameric fullerene like structure (hexamer-hexamer spacing is 8 nm in the immature and 10 nm in the mature lattice) containing pentameric units that ensure the lattice curvature (Fig. 1.7.26).

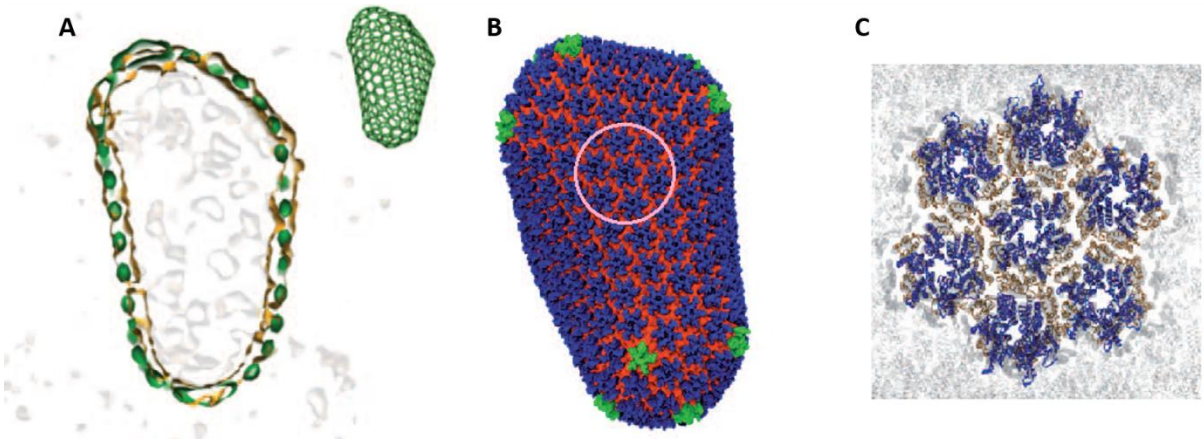

Figure 1.7.26. Viral capsid model. Fullerene-like core model made from the overlay of densities of the segmented capsid (orange contour) and the model (green) (A). 3D model of capsid organization with more than 200 hexameric (blue) and 12 pentameric units (green) (B). CA hexamers with amino-terminal (blue) and carboxyl-terminal (orange) domains (C) (Zhao, Perilla et al. 2013).

The RNPs are localized in the broad end of the viral core (Benjamin, Ganser-Pornillos et al. 2005; Briggs, Grunewald et al. 2006; Zhao, Perilla et al. 2013). The dimensions of the cap at the narrow and broad parts are ~27 and ~56 nm, respectively. The longest axis of the conical

cores spans the diameter of virions (Briggs, Grunewald et al. 2006). The stiffness of viral particles at different stages of maturation was measured by AFM. It was found that immature HIV-1 virions are 14 times stiffer than mature ones. It was hypothesized that this change of stiffness may be important for the infection efficiency (Kol, Shi et al. 2007).

Early steps of infection

HIV-1 is often transmitted through virological synapses. Viruses exploit the virological synapses that are cytoskeleton-dependent and stable adhesive junctions between immune cells that promote the direct transmission of the virus (Igakura, Stinchcombe et al. 2003; McDonald, Wu et al. 2003; Jolly, Kashefi et al. 2004).

Do et al. (Do, Murphy et al. 2014) revealed the 3D structure of the contact region and the viral transmission between infected and non-infected cells of different types (Jurkat cells, H9, cell CD4+). FIB-SEM was applied to the co-culture of infected and non-infected cells. It was observed, that CD4+T cells may wrap tightly around neighboring non-infected cells that can extend long filopodia (30-40 μm) towards the infected cells (Fig. 1.7.27). FIB-SEM approach is particularly appropriate for visualizing the virological synapses, because they can be easily damaged or lost during conventional TEM preparation.

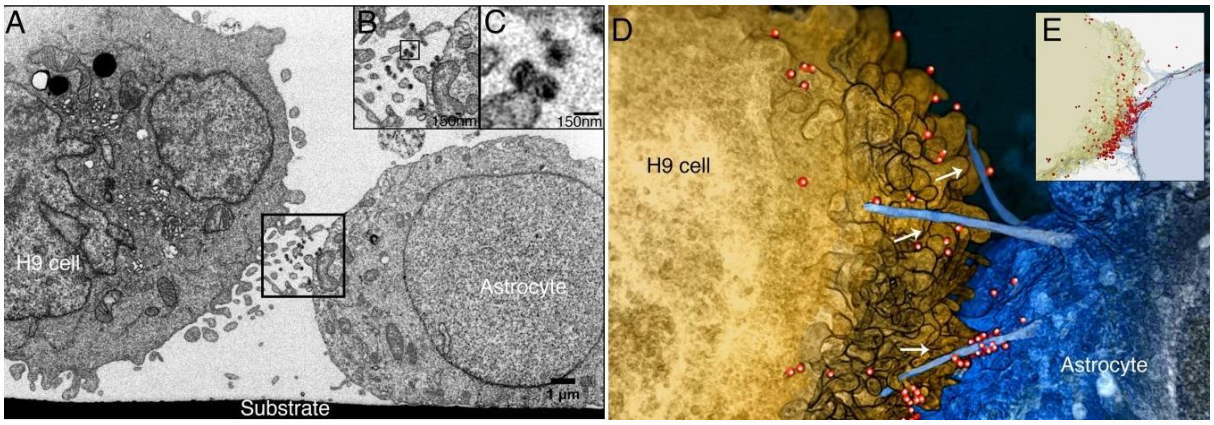

Figure 1.7.27. HIV-1 virions "surf" along membranes within the H9- astrocyte virological synapse. 2D image of an infected H9 cell and non-infected astrocyte (A, B, C); 3D rendering of FIB-SEM image stack (D) and semitransparent visualization of the same plane with dense accumulation of viruses (E) (Adapted from (Do, Murphy et al. 2014).

Electron tomography imaging of the contact zone between HIV-1 and T cells revealed the formation of a macromolecular complex between the Env and cellular receptors prior to the fusion with cell membranes. This structure called "entry claw" (Fig. 1.7.28) is composed of 5-6 Env spikes pointing towards the host cell surface (Sougrat, Bartesaghi et al. 2007).

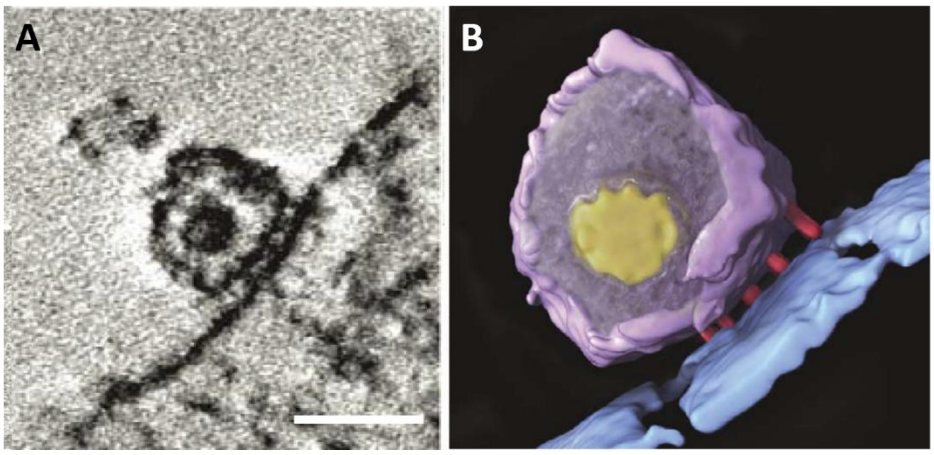

Figure 1.7.28. Visualization of HIV-1 in contact with a T cell. (A) Tomogram of the contact region between the virion and host cell (Scale bar 100 nm) and (B) 3D representation of the architecture of the contact surface with the viral envelope (magenta), contact rods (red), core (yellow), and cell membrane (blue) (Adapted from (Sougrat, Bartesaghi et al. 2007).

Cryo-EM and dSTORM showed that attachment of the virions to the surface of the host cell and their interaction with CD4 receptors triggers an expansion of the virion. The MA diameter and central capsid volume were expanded by ~8 % and 26%, respectively (Pham, Tabarin et al. 2015). These data suggest that CD4-Env interaction induces pre-entry remodeling of the viral core.

The cytoplasmic events were followed by TEM imaging of immunolabelled and negatively stained infected MT-4 cells. These experiments permitted to follow the uncoating (Arhel, Souquere-Besse et al. 2007) and nuclear entry of the viral core (Arhel, Munier et al. 2006; Monette, Pante et al. 2011; Wong, Mamede et al. 2015). Interestingly, CA shells were observed in the close proximity of the nuclear membrane and nuclear pores indicating that the uncoating process does not occur rapidly after the fusion but rather when the viral core reaches the perinuclear area. A more robust approach of SEM microscopy was applied to the nuclear membrane of cells transduced with wild type and defective DNA flap vectors, labeled by gold. TEM and SEM observations revealed the presence of CA structures near the nuclear membrane and confirmed that late uncoating events occur at the nuclear pores (Arhel, 2007). The nuclear entry of viral complexes were successfully monitored by electron microscopy. It was observed that defective viral DNA genome lacking the central DNA flap accumulates in the cytoplasm in the perinuclear region, whereas wild type ones are localized in the nuclear compartment (Arhel, Munier et al. 2006). Active transport of viral DNA into the nucleus is facilitated by interactions of HIV-1 with nucleoporins (Nup), especially with Nup62, 153 and 358 (Monette, Pante et al. 2011; Wong, Mamede et al. 2015). During the nuclear entry, the viral complex does not just use the cellular machinery to pass through the nuclear pore, but also delocalizes some nucleopore proteins (Monette, Pante et al. 2011; Wong, Mamede et al. 2015). Immunogold electron

microscopy of the isolated nuclear envelopes of T cells revealed the translocation of Nup62 and its presence in newly formed viral particles (Monette, Pante et al. 2011).

Assembly, budding and maturation

Several EM studies have been performed to enlighten the late stages of HIV-1 infection and maturation of newly formed viral particles. Figure 1.7.29 presents electron-tomography images of viral budding (A), immature particles containing round Gag shell (B) and mature viral particles with typical conical capsid containing the RTC in the broad end.

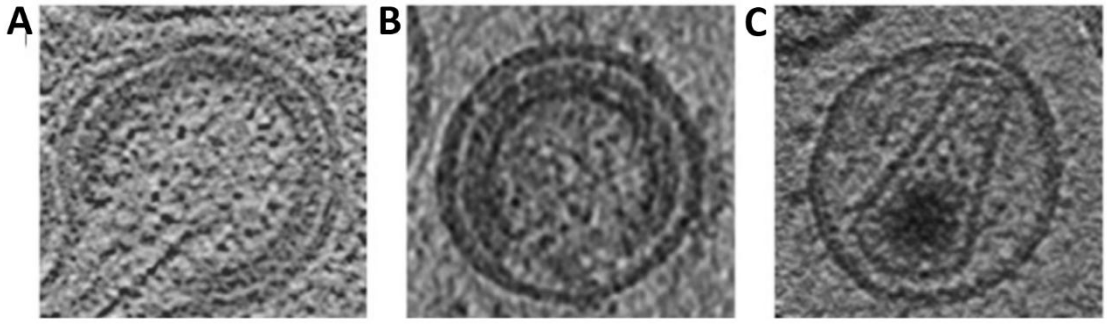

Figure 1.7.29. Cryo-electron tomograms of HIV-1. (A) Budding HIV-1 VLP. (B) Immature and (C) mature HIV-1 viral particles (Adapted from (Briggs and Krausslich 2011).

To clarify the maturation process, EM thin section micrographs of newly produced viruses (Hoglund, Ofverstedt et al. 1992) showed that formation of the viral core is related to the protease cleavage of Gag polyprotein. In immature particles, Gag molecules organized in hexamers form a shell around the RNA dimer. The curvature of the Gag lattice is promoted by small irregularly shaped gaps in immature virions and inclusions of pentameric domains in the mature capsid. The immature capsid does not present a set of disconnected motifs, but rather a continuously traceable lattice that contains one large gap corresponding probably to a scission from the plasma membrane (Wright, Schooler et al. 2007; Briggs, Riches et al. 2009; Carlson, de Marco et al. 2010; Briggs and Krausslich 2011). In the work of Carlson, new type of Gag lattice was described. This lattice is characterized by intermediate morphology and the thinner lattice, than immature ones (Fig. 1.7.10A). Interestingly, immature particles contain approximately 5000 molecules of Gag (Briggs, Simon et al. 2004), while only 1200-1500 CA molecules form the mature core (Nermut, Hockley et al. 1998; Li, Hill et al. 2000; Mayo, Huseby et al. 2003) (Fig. 1.7.30B).

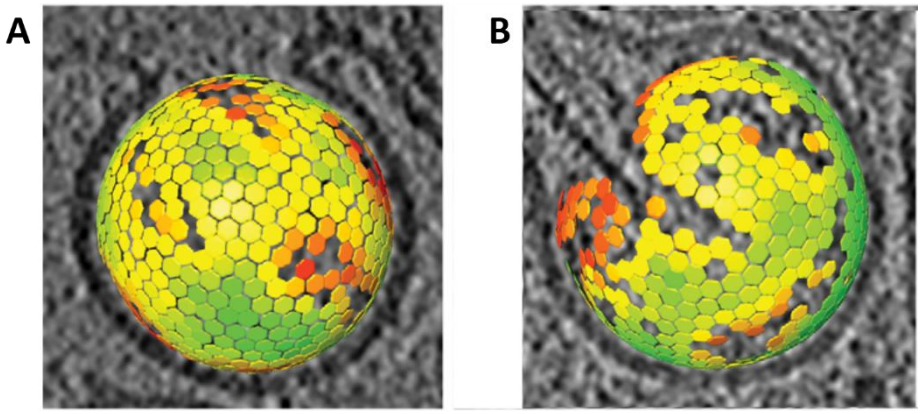

Figure 1.7.30. Budding of HIV-1 virions captured by EM. Lattice map of HIV-1 budding sites; intermediate (A) and immature lattices (B) of viral budding sites colored according to their hexagonal order from low (red) to high (green) (Adapted from (Carlson, de Marco et al. 2010).

AFM studies of HIV-1 derived VLPs and cores showed the importance of the RNA in the formation of the viral particles and showed that vRNA is a crucial factor of virion sizes polydispersity. The particles formed with vRNA are smaller and more homogeneous, than those that contain cellular RNAs (Faivre-Moskalenko, Bernaud et al. 2014) (Fig. 1.7.31).

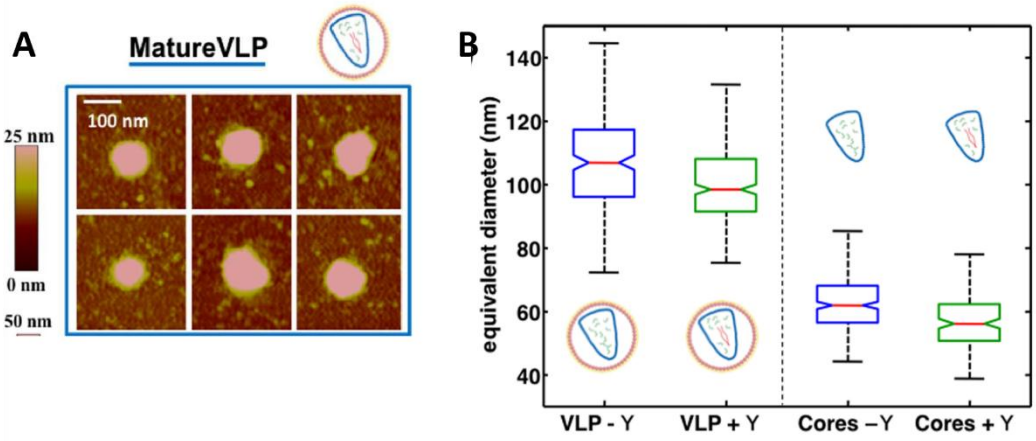

Figure 1.7.31. Influence of vRNA on virion morphogenesis. (A) AFM images of mature virus-like particles containing vRNA. (B) Box chart of equivalent diameter of VLPs and cores in the presence (+Y) and absence (-Y) of vRNA (Adapted from (Faivre-Moskalenko, Bernaud et al. 2014).

Further EM studies enlighten the role of cell components, like the endosomal sorting complexes required for transport and budding (ESCRT) or the actin filaments in the late post-infection events. The ESCRT machinery is recruited to close up the connection between the cell membrane and a new particle (Dussupt, Sette et al. 2011). Analyses of cryo-electro tomograms evidence the presence of actin filaments in close vicinity to the budding sites (Carlson, de Marco et al. 2010). Similarly, actin containing aster structures appeared on the surface of the budding sites imaged by AFM (Gladnikoff, Shimoni et al. 2009). The authors proposed that the

interaction is mediated by the NC domain of Gag, but a recent study suggested that NC is dispensable for this process (Stauffer, Rahman et al. 2014).

Mutation of the Gag polyprotein or inhibition of viral enzymes can impair the packaging of the proviral genomic material (Fontana, Jurado et al. 2015) and the budding process (Dussupt, Sette et al. 2011). Mutation of the NC region of Gag can arrest the budding process, inhibit the ESCRT recruitment and impair the vRNP incorporation (Dussupt, Sette et al. 2011; Mattei, Flemming et al. 2015). Inhibition of IN activity leads to impaired incorporation of vRNA into the mature core (Fontana, Jurado et al. 2015). Malformed particles contain vRNPs in the form of eccentric condensates that do not incorporate into the mature core.

1.7.6. HIV-1 imaging by fluorescence microscopy

HIV-1 labelling

Due to the small size of the viral particle and high concentration of viral proteins inside the virion, the labelling strategy is one of the most challenging aspects of HIV-1 imaging by fluorescence microscopy. Immunolabeling is incompatible with the observations of dynamic events. The fusion of viral proteins to fluorescent proteins presents the risk of perturbing or even losing their biological function. Staining by fluorophores may suffer from nonspecific background labelling.

The first fluorescence microscopy observations of HIV-1 viral proteins (p17, p24, gp120, Rev, Nef) were made in immune-labeled infected cells (Niedrig, Rabanus et al. 1988; Kienzle, Enders et al. 1992; Apostolski, McAlarney et al. 1993; Nottet, Janse et al. 1993). These approaches were related to HIV-1 detection (p24 recognition) in patients at the early steps of infection. Numerous monoclonal antibodies against *Gag* were produced after the discovery of virus (Chassagne, Verrelle et al. 1986; Ferns, Tedder et al. 1987), 1987). Early studies were devoted to the recognition of viral epitopes in the infected cells during the early stages of infection, such as cell binding (Niedrig, Rabanus et al. 1988; Apostolski, McAlarney et al. 1993).

The viral labeling by fusion to fluorescence proteins is fastidious because the large size of FPs ~27 kDa and the intrinsic oligomerization properties of some FPs. Moreover, the introduction of a label can affect the assembly process and dramatically change the morphology and the sizes of the produced particles (Gunzenhauser, Olivier et al. 2012; Quercioli, Di Primio et al. 2016).

Gag polyprotein labeling by genetic fusion with eGFP was first reported in the work of Perrin-Tricaud (Perrin-Tricaud, Davoust et al. 1999), where eGFP was fused to the NC domain

of Gag. The position of eGFP was chosen with regard to the function of Gag polyprotein. Insertion of eGFP at the C-terminal was incompatible with GagPol frameshifting. N-terminal localization was found to inhibit the myristol switch of MA upon membrane binding. Internal localization of eGFP at the MA domain (Muller, Daecke et al. 2004) did not perturb Gag assembly and processing, but this virus was poorly infectious. Finally, insertion of Gag between the MA and CA domains retained high infectivity without helper (WT) virus. Later, this labeling strategy was commercialized (NIH AIDS Reagents) and successfully used in numerous works (Hermida-Matsumoto and Resh 2000; Hubner, McNerney et al. 2009; Dale, McNerney et al. 2010; El Meshri, Dujardin et al. 2015).

Other eGFP fusions with viral components, like the viral protein R (Vpr) (McDonald, Vodicka et al. 2002; Campbell, Perez et al. 2007) and integrase (IN) (Albanese, Arosio et al. 2008) were developed in parallel. Successful Gag fusion to photoactivatable proteins such as PAFPs like mEos or PAmCherry (Gunzenhauser, Olivier et al. 2012; Muranyi, Malkusch et al. 2013; Prescher, Baumgartel et al. 2015) and Vpr fused to Dronpa (Lehmann, Rocha et al. 2011) has opened new perspectives for super resolution microscopy imaging of HIV-1.

In parallel, labeling systems with smaller genetic tags and fluorescent markers have been successfully implemented for HIV-1 imaging. For example, use of Gag-SNAP (SNAP-tag 20 kDa) for HR fluorescence microscopy (Eckhardt, Anders et al. 2011; Malkusch, Muranyi et al. 2013) and IN-TC (TC-tag 585 Da) for confocal (Arhel, Munier et al. 2006) and HR fluorescent microscopy have been recently reported (Lelek, Di Nunzio et al. 2012). For the imaging of nucleic acids, the viral DNA (vDNA) synthesized inside infected cells can be detected by the fluorescence in situ hybridization (FISH) approach ViewDNA (Chin, Perreira et al. 2015). An approach using alkylene-containg tags was reported for the labeling of viral cellular RNAs inside infected cells (Xu, Franks et al. 2013).

Development of the above-mentioned labelling strategies initiated a variety of microscopy studies deciphering the early and the late stages of the HIV-1 viral cycle during the last decade.

Imaging the early stages of infection

In the pioneering study by McDonald et al. HIV-1, viral particles expressing eGFP-labeled Vpr have been observed inside infected cells (McDonald, Vodicka et al. 2002). This study revealed the perinuclear localization and accumulation of HIV-1 in CD4-expressing target cells (Fig. 1.7.32A). The motility of HIV-1 viral particle revealed a curvilinear microtubule dependent movement directed towards the nucleus (Fig. 1.7.32 B). Further investigation of HIV-

1 motility in early steps of infection was done by Arhel et al. using HIV-1 particles labeled on IN by the FlAsH-TC system. This study permitted for the first time a 3D cytoplasmic tracking of pseudoviral particles inside infected HeLa cells. Movement inside the cytoplasm was observed to be microtubule or actin dependent with velocities around 0.1-1 µm/s and 0.03 µm/s, respectively. Viral complexes were found to have a directed displacement towards the nucleus followed by confined movement in the perinuclear region and diffuse motility in intranuclear region (Arhel, Munier et al. 2006).

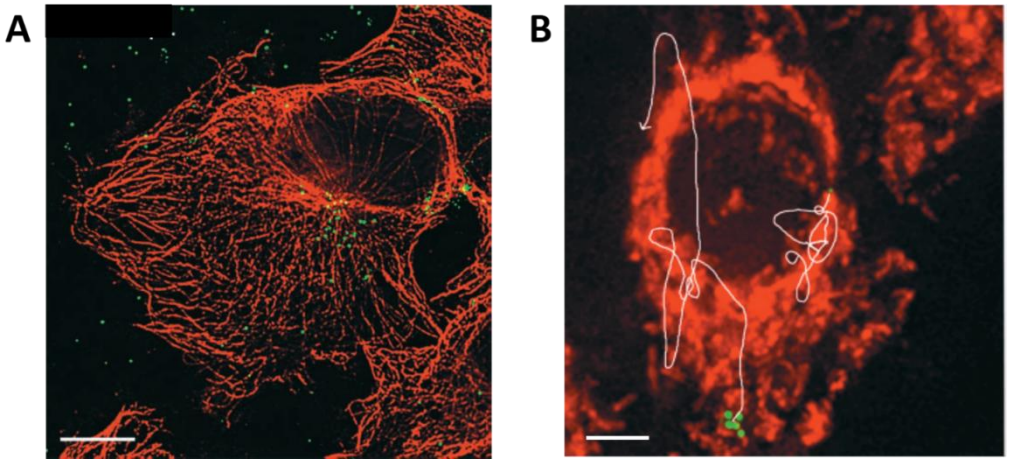

Figure 1.7.32. Intracellular motion of HIV-1. (A) After two hours of infection, the GFP-labeled viral particles (green) localize near the microtubule-organizing centers labeled by antitubulin antibodies (red) (scale bar 10 µm). (B) Trajectories of GFP–Vpr-tagged HIV particles (green) in living cells stained by the Mitotracker dye (red) (scale bar 5 µm) (Adapted from (McDonald, Vodicka et al. 2002).

The single virus tracking (SVT) method allowed visualizing the real-time interaction between HIV-1 and host cell plasma membrane. For this aim, entry-competent and replication-defective single and dual-fluorescently labeled HIV-1 derivatives have been used (Lampe, Briggs et al. 2007). These virus-like particles (VLPs) are bearing MA-eGFP and Vpr-mRFP1, or Vpr-mRFP1 alone. Dual labeling on Vpr by mRFP1 and on MA by eGFP allows distinguishing between the complete viral particles (two colors) and the cytoplasmic viral complexes lacking the matrix domain after cell fusion (one color). SVT observation on different cell lines revealed that 20% of VLPs that contacted the plasma membrane are immobilized on its surface. The majority of non-immobilized VLPs interact with membrane within contact duration following an exponential distribution with a lifetime of 20-50 ms (Endress, Lampe et al. 2008).

Dual labeling of viral particles by fluorescent proteins was also used to monitor the pathway of cellular internalization (Campbell, Perez et al. 2007). VSV-g pseudotyped virions containing Vpr-GFP and mCherry fused to a membrane targeting peptide S15 (Rodgers 2002) were used for monitoring HeLa cell infection. The loss of the S15-mCherry signal from the dual labeled particles was used as an indicator of virions that productively entered the cells. It was

observed that many virions are degraded rapidly after the endocytosis (1 hour), even if these are the pseudotyping with VSV-g. Treatment with endosome acidification inhibitor (Bafilomycin A) revealed that, acidification is required for both the cell fusion and degradation of the viruses, which failed cell entry. The Vpr-GFP signal was lost after 4 hours of infection, which was connected to the synthesis of vDNA and formation of the PIC.

Another debated question of the early HIV-1 infection is the timing and the localization of the uncoating process, as well as its relationship with the reverse transcription process and the nuclear entry. Hulme et al developed an uncoating assay based on a previously reported dual-labeling technique (Campbell, Perez et al. 2007). Authors observed that 50% of the Vpr-EGFP viral complexes inside the infected cells lose their fluorescent signal inside the cytoplasm after ~40 min of infection. This first strong decrease is followed by a progressive decay during longer times of infection with the majority of the virions uncoating up to 2 hours (Hulme, Perez et al. 2011). These results support the model of progressive uncoating during the cytoplasmic transport of RTC to nucleus and suggest the involvement of early reverse transcription products in facilitating the uncoating.

Similarly, a multicolor labeling of viral particles on MA, CA and RNAs was used for monitoring the sequential disassembly of HIV-1 (Ma, He et al. 2016). This approach combined the labeling of virions by FPs, TC tag and light-switch Ru (II) complex (O'Connor, 2009) without impairing the viral infectivity. Real-time observation of the early infection phase revealed the dynamic separation of RNAs, capsid and matrix in the middle-cytoplasm region within 60-120 min post-infection (Fig.1.7.33). These results revealed the dissociation of the capsid and matrix together from the viral RNAs with following separation of capsid and matrix from each other. This work supports the theory of a multiple-stage process of HIV-1 disassembly and gradual disintegration of the capsid in the middle cytoplasm region.

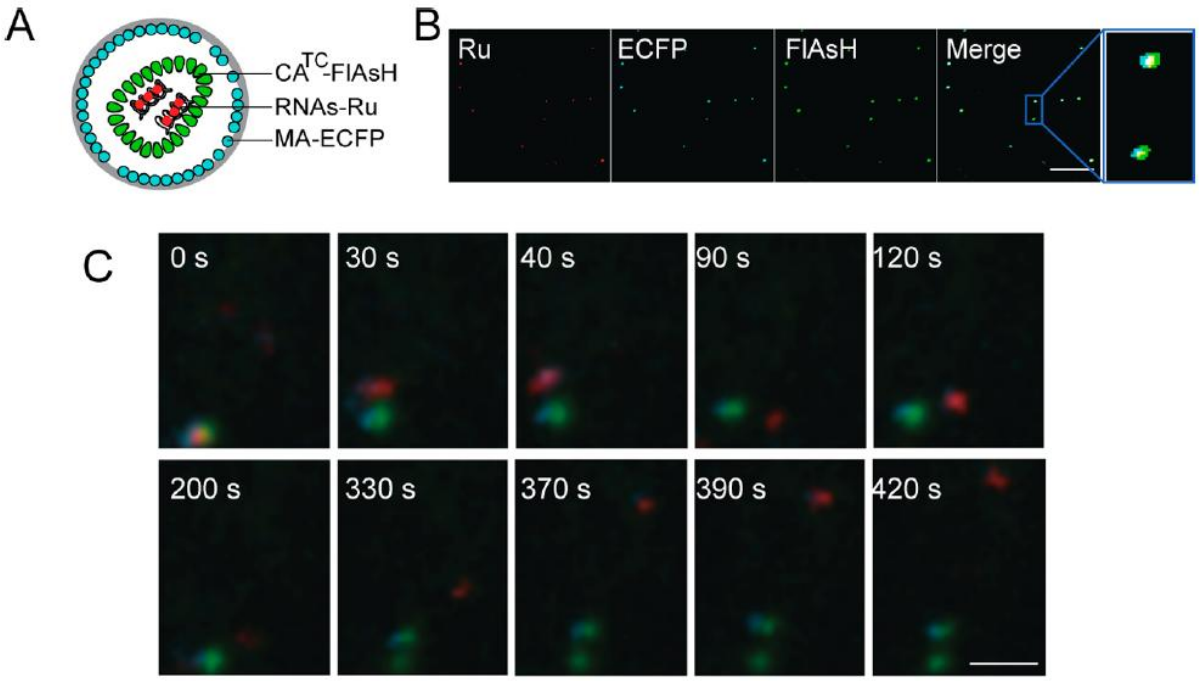

Figure 1.7.33. Multicolor labeling of HIV-1. Scheme of triple-labeled HIV-1 virion (A). Colocalization of Ru, FlAsH and ECFP (scale bar 2 μm) (B) and snapshots of the real-time dissociation of CA-TC-FlAsH, MA-ECFP and RNA-Ru (scale bar 1 μm) (C) (Adapted from (Ma, He et al. 2016).

A fluorescence-based RNA accessibility assay confirmed that uncoating is a multi-step process. The viral-associated RNA was labeled by 5-ethynyl uridine (EU) and stained with an EU-specific dye in the cytoplasm of infected cells. EU staining revealed a subtle uncoating prior to the complete dissociation of the capsid. The timing of RNA exposure is not altered after inhibition of RT. Taken together, these observations support the theory of a gradual disassembly of the capsid. A biphasic uncoating of purified cores was previously observed biochemically (Forshey, von Schwedler et al. 2002) and in the cellular context (Xu, Franks et al. 2013).

The theory of late uncoating near the nuclear pores is supported by Arhel et al (2007; 2010) who investigated the role of the DNA flap in the early steps of infection. Intact CA shells close to the nuclear pores were observed by correlative light-electron microscopy (IF on $p24^{CA}$) (Arhel, Souquere-Besse et al. 2007). These integrate CA shells were co-localized with newly synthesized viral DNA.

After uncoating, the PICs enter the nucleus through the nuclear pores. In order to enlighten the PIC intranuclear distribution, viral complexes labeled on IN, Vpr or CA were monitored (Arhel, Souquere-Besse et al. 2007; Albanese, Arosio et al. 2008; Francis, Di Primio et al. 2014; Chin, Perreira et al. 2015; Quercioli, Di Primio et al. 2016). A preferential localization of the integration sites was observed in actively transcribed DNA in low heterochromatin regions (Albanese, Arosio et al. 2008; Quercioli, Di Primio et al. 2016).

The recent development of HR fluorescence microscopy pushed the limits of the analysis to unprecedented details. Combination of click labeling of nascent viral DNA, IF and FPs with super-resolution microscopy (PALM) permitted to co-localize viral DNA, CA, NC and IN in infected cells. Detection of CA in RTC/PIC through all the cytoplasm of HeLa-derived cells is consistent with a gradual loss of CA on the way to the nucleus (Peng, Muranyi et al. 2014). Time-resolved imaging of single viruses labeled by the host-protein cyclophilin A (CypADSRed) further showed that this gradual loss of capsid in the cytoplasm and the perinuclear region is dependent on RT (Francis, Di Primio et al. 2014).

Moreover, HR microscopy permitted to visualize the morphology changes of viral particles and the recruitment of cellular structures during the early steps of infection. STED microscopy permitted to visualize the distribution of Env on the surface of mature and immature virions. While the lateral movement of Env proteins is restricted by the rigid structure of the Gag lattice in immature viruses, Env performs polarized clustering prior to contact with CD4 receptors in mature virions (Chojnacki, Staudt et al. 2012).

dSTORM imaging of CA and MA proteins upon cellular entry revealed a 236% and 160% increase of size for the capsid and matrix respectively, indicating a restructuration of the viral core soon after cellular entry (Pereira, Rossy et al. 2012). PALM imaging of IN-TC containing pseudoviruses labeled by FlAsH, combined with cluster morphology analysis permitted to distinguish different viral populations based on their morphology. Mature and immature virions were discriminated by their conical and spherical shapes, respectively. Smaller IN labeled clusters were evidenced in the nucleus as compared to the cytoplasm (Fig. 1.7.34), where IN is mainly present in intact viral cores (Lelek, Di Nunzio et al. 2012).

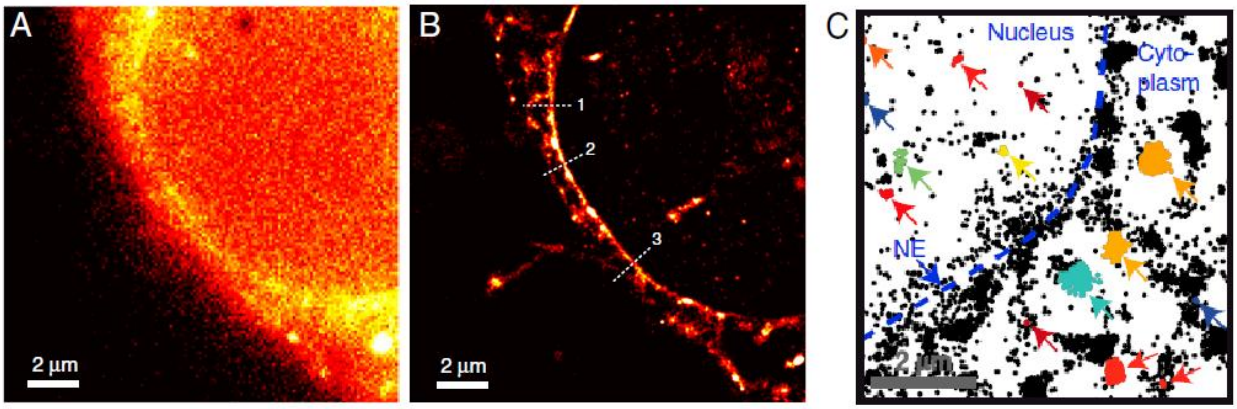

Figure 1.7.34. FlAsH-PALM imaging and analysis of HIV-1 particles labeled on IN-TC. (A) Widefield image and (B) SR reconstruction of 20,000 frames of the same region of HeLa cell infected for 2h. (C) All detected positions of FlAsH-IN clusters (multicolor arrows) (Adapted from (Lelek, Di Nunzio et al. 2012)).

Early stages of infection comprise also the nuclear entry events, which occur by active import through the nuclear pore and is mediated by the host cell nuclear pore proteins. To the date, Combination of HR microscopy and biophysical assays revealed the critical role of the nuclear basket and nucleoproteins Tpr and Nup153 in HIV-1 replication. Tpr remodels chromatin in the close proximity to the nuclear pore complex to the active state, favorable for the replication of the HIV-1. Tpr depletion was found to decrease the density of the chromatin mark H3K36me3 (Pradeepa, Sutherland et al. 2012) associated with the actively transcribed chromatin in the proximity to the nuclear basket, where occurs HIV-1 integration (Lelek, Casartelli et al. 2015).

Imaging of the late steps of HIV-1 infection

Late stages of viral infection comprise the assembly, budding, release of newly formed immature particles and maturation. Formation of new virions is ensured by the assembly of newly synthesized Gag proteins with RNA and regulatory proteins at the cellular membrane, the budding of the viral particle and the scission from the lipid membrane. Gag by itself is able to assemble into virus-like particles in the same way as the HIV-1 virus does. Gag multimerization and budding are well suited for imaging approaches. Newly assembled Gag particles were observed at the plasma membrane by STORM and PALM methods and found to be 120-140 nm in diameter (Eckhardt, Anders et al. 2011; Gunzenhauser, Olivier et al. 2012; Malkusch, Muranyi et al. 2013)(Fig. 1.7.29).

Several teams studied the dynamics of particle assembly. Measuring the diffusion parameters of individual Gag molecules at the plasma membrane by Single Particle Tracking (spt) PALM of Gag-mEos molecules showed the existence of two populations. A mobile population composed of freely diffusing Gag with an average diffusion coefficient 0.11 ± 0.08 $\mu m^2/s$ and ~1 µm path length. A second group represents immobile clusters of Gag molecules (with 100-200 nm size) trapped in VLPs at the surface of cell plasma membrane (Manley, Gillette et al. 2008).

In agreement with these results, TIRF/FRET observation of viral particles formation revealed the emergence of fast and slow Gag-GFP puncta at the plasma membrane. Co-labeling of Gag and RNA allowed monitoring the RNA docking at the plasma membrane and the assembly of new particles around RNA-Gag complexes (Jouvenet, Simon et al. 2009). Authors observed that the assembly of virions at the plasma membrane was completed in 5-6 min (Jouvenet, Bieniasz et al. 2008). A similar time rate was reported by other groups based on imaging the assembly of HIV-1 fluorescent particles lacking the Nef protein (Ivanchenko, Godinez et al. 2009). Altogether, these studies showed that individual Gag/RNA clusters emerge

rapidly at the plasma membrane and serve as nucleation sites for recruiting new Gag molecules from the cytosolic pool. Accumulation of Env was observed near the budding site but did not directly overlap with Gag suggesting that Env is recruited indirectly, possibly through the virus induced changes in the cell membrane (Muranyi, Malkusch et al. 2013) (Fig. 1.7.35).

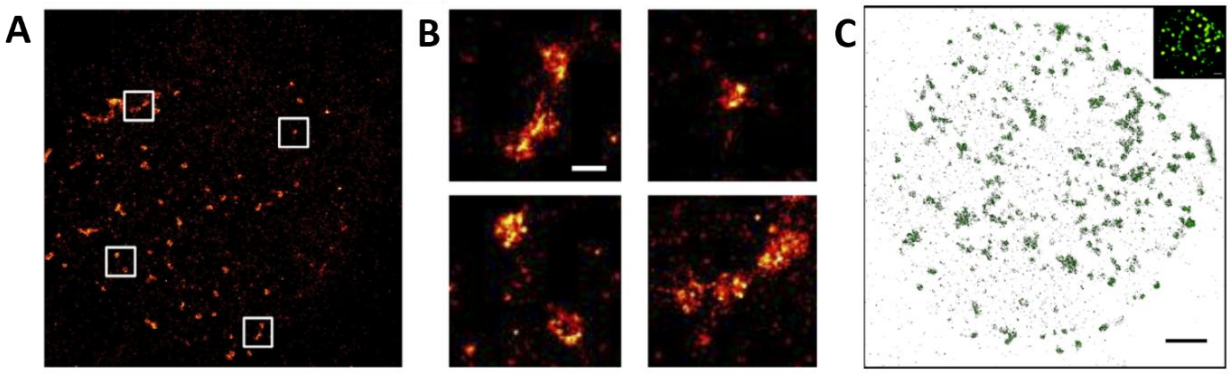

Figure 1.7.35. Visualization of Gag assembly sites. (A) dSTORM image of HIV-1 budding sites with Gag labeled by SNAP-Alexa 647 at the surface of T-cells and (B) indicated magnified regions (Scale bar 200 nm). (C) dSTORM image of Gag-SNAP-Alexa 647 expressed in A3.01 cells revealed clusters of Gag proteins at the assembly sites (Scale bar 1 µm) (Adapted from (Eckhardt, Anders et al. 2011; Malkusch, Muranyi et al. 2013)).

ESCRT plays a critical role during the budding events and the release of newly formed viral particles. ESCRT subunits were observed to localize within the head of the budding virions and to be a driving force of virion release (Van Engelenburg, Shtengel et al. 2014). It was shown that formation of new viral particles recruit the Env at the assembly sites and that this protein accumulates inside the buds (Muranyi, Malkusch et al. 2013; Van Engelenburg, Shtengel et al. 2014; Prescher, Baumgartel et al. 2015)(Fig. 1.7.36).

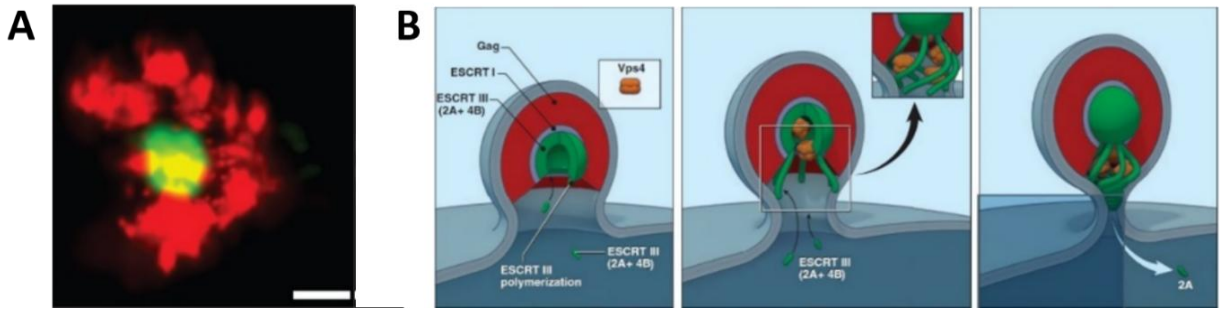

Figure 1.7.36. Recruitment of host cell proteins for budding and release. Two-color 3D SR of Gag-FLAG (red) and ESCRT-PSCFP2 (green) (A) (scale bar 50 nm) and model visualization of new Gag particle release (B) (Adapted from (Van Engelenburg, Shtengel et al. 2014)).

In conclusion, fluorescence microscopy is a valuable tool for imaging viral morphology and dynamics during infection. Recent developments in labeling strategies permitted to label different viral proteins inside the virions with minimal perturbation of the viral functions and to

visualize real-time events of viral infection. SR approaches provide visualization and analysis of infection events with high accuracy. Combination of fluorescence and electron microscopy methods creates a powerful tool for virological studies.

Research objectives

Despite the important research efforts realized during last 35 years order to establish an efficient HIV-1 antiviral treatment this virus is still unbeaten. The identification of new therapeutic targets represents still a challenging task to abolish the epidemic. Laboratory of Biophotonics and Pharmacology works since several years on the investigation of the HIV-1 infection by multidisciplinary experimental approaches. Particularly, the nucleocapsid protein NCp7 is of the great interest as a new antiviral target, due its highly conserved structure and an important role in the numerous stages during the viral life cycle. This research brought important data concerning the interactions of the NCp7 with the nucleic acids and its chaperone activity, mostly by “in vitro” studies. More recently, the Ncp7 has been studied in the cellular environment in the conditions of overexpression and using a vesicular stomatitis virus (VSV) pseudotyped HIV-1 virus.

Indeed very few studies follow the fate of NCp7 during the early stages of infection. It is known, that, NCp7, obligatory partner of the RT, participates on the reverse transcription by facilitating the two mandatory strand breaks, chaperoning synthesis of the complete viral DNA and enhances RT processivity. However the fate of the NCp7 during the transformation of reverse transcription complex (RTC) into a pre-integration complex (PIC) and its nuclear entry are still relatively unclear.

The microscopic techniques are well adapted tool to follow the virus during the different stages of infection. Electron microscopy and atomic force microscopy are used to solve the structure of virions with a resolution of a few nanometers. Optical microscopy, for its part, allows dynamic imaging under "in vivo" conditions. In addition, recent advances in this field have pushed the boundaries of spatial resolution of optical microscopes to distinguish nanometric structures. Since the size of HIV-1 is close to 100 nm, this technical advance has opened a new field allowing visualizing fine modifications linked to the reorganization of the viral particle, as well as its co-localization with the cellular partners throughout the viral cycle.

In this context, the objective of my PhD thesis is to follow the NCp7 during the early stages of the HIV-1 viral cycle. We aimed to visualize the NCp7 during the RTC-PIC remodeling and during its nuclear input by different advanced microscopy techniques, such as high-resolution fluorescence, atomic force and correlative light/electron microscopy

To follow the fate of NCp7 we used as a model the HIV-1 particles pseudotyped with the envelope protein of the vesicular stomatitis virus (VSV-G) and carrying the luciferase gene as

reporter of infectivity. In these pseudoviruses, the nucleocapsid protein or integrase is fused to a tetracysteine tag (TC) which is then labeled by the FlAsH/ReAsH fluorophores. In the first part of my work we evidenced, by quantifying the modifications of fluorescence intensity, related to a self-quenching effect of FlAsH fluorescence, a RT dependent cytoplasmic release of NCp7. In the second part the PALM/STORM (Photo-Activation Localization Microscopy/Stochastic Optical Reconstruction Microscopy) has been used to follow the intracellular distribution of NCp7 during the early stages of infection. By analyzing the cellular localization and size distribution we evaluated the effect of time and of the inhibition of RT. Finally in the third chapter we aimed to clarify the mechanism of NCp7 nuclear entry. The latter can be active within the PIC complex or passive if the protein diffuses freely through the nuclear pore. In order to settle the nuclear entry mechanism we observed firstly the effect of the inhibition of the active transport by energy depletion and secondly the co-localization of NCp7-TC with nuclear pores by electron transmission microscopy.

Finally the last chapter contains results of collaborative project between the LBP and Department of Experimental Physics of T. Shevchenko Kiev National University on the development and characterization of the luminescent semiconductor nanoclusters. These small particles adopt thermodynamically stable structure with “magic” number of atoms and have well-defined structure, which determines their specific physical and chemical properties. The nanoclusters (NCs) have extremely sharp absorption peak and are highly sensitive to the electric field. Thus clusters are highly valuable for the development of the new functional materials and markers for the microscopy. However, directly after one-pot wet chemistry synthesis NCs revealed low quantum yield and require additional modification of the surface, extremely important in case of NCs with as big fraction of atoms exposed on the surface. It is well known, that NCs have high affinity to the phosphine derivatives and the latter can passivate the surface of the NCs with following increase of the brightness. In this context, the goal of my work was to tune the properties of clusters by the additional surface ligands, hydrophobic derivatives of the phosphine: triphenylphosphine (TPP), trioctylphosphine (TOP) and tris(pentafluorophenyl)phosphine (TPFP). To perform this we synthesized the NCs and passivate them by additional ligands with following measurements of intensity within the several concentrations of ligands and in the time.

Chapter 2: Materials and methods

2.1. Cell culture

HeLa cells (ATCC reference CCL-2) are a cancer cell line, derived from metastases of a patient Henrietta Lacks with cervical cancer of uterus, who died in 1951. These cells are the first line of human immortal cells ever established. In the laboratory, these cells are used with a number of passages less than 20.

HeLa cells are cultured in 75 cm^2 flasks in the medium culture complete DMEM (Dulbecco's Modified Eagle Medium, Life Technologies Gibco® ref. 21885) supplemented with 10% FCS (fetal calf serum, Gibco® Life Technologies ref.10270-106) and a mixture of antibiotics (Penicillin 100 UI / mL and streptomycin 100 UI / mL). The cells are placed in an incubator at 37 ° C (5% CO2, 95% humidity). The cell passages are carried out every two or three days, when the cells are confluent. The cells were washed once with 3 mL of 1X PBS made from a 10X PBS (phosphate buffered saline, Biowhittaker® Lonza BE17-517Q) and detached by trypsinization, with 3 mL of trypsin solution (Lonza BE02-007E) diluted in 1X PBS for 5 min at 37 ° C. They are taken away by 7 mL of DMEM, to stop the action of trypsin, then centrifuged at 1500 rpm for 5 min. The cell pellet is then resuspended in 10 mL of complete DMEM. After counting the cells in a Mallassez cell, a determined quantity of cells is re-cultivated in a new plate containing 20 mL of complete DMEM (10^6 HeLa cells for example 3 days of culture in a flask 75 cm2).

2.1.1 Transfection

Mammalian cell transfection is a common method for the introduction of nucleic acids into eukaryotic cells. The cells were transfected by a linear polyethyleneimine (PEI) using the JetPEI® kit (Polyplus TransfectionTM). The latter is a cationic polymer that neutralizes the negative charges of the DNA phosphate backbone and condenses DNA. The polymer-DNA complexes (polyplex) can interact with the plasma membrane of cells and are then internalized by endocytosis and released in the cytoplasm. The PEI also protects DNA in the endosomes by buffering the pH. Cell transfection was performed in 6 or 12 wells plates or in µ-Slide 4-8 wells ibiTreat chambered coverslip in which a given amount of cells was seeded the day before. A round glass slide of 18 mm in diameter is placed at the bottom of each well of a 12 wells plate before adding the cells. The slide is sterilized by washing with 100% ethanol, acetone and MilliQ three times before sonication in 100% ethanol for 15 min at 80 Hz, then dried in the oven and cleaned with plasma cleaner Harrick Plasma for 5-10 min. The cells are then added and the wells

are placed in the incubator for 24 h. For each sample, two Eppendorf tubes were prepared: one containing the transfecting DNA added to a solution of 150 mM NaCl, the other containing PEI (stock solution7.5 mM) also mixed in 150 mM NaCl at a rate of 2 µL of PEI to 1 µLg DNA transfected. The PEI solution was then added to the DNA, and the mixture is vortexed and left at room temperature for 20 min, to allow the formation of PEI-DNA complexes. The content is finally deposited drop by drop on the cells in complete DMEM, which are then delivered to the incubator.

2.1.2. Energy depletion

For energy depletion HeLa cells were incubated in glucose-free Dulbecco's modified Eagle's medium containing 10% fetal bovine serum and supplemented with 10 mmol/L sodium azide (mitochondria inhibitor) and 6 mmol/L 2-deoxy-d-glucose (can't undergo glycolysis) (Sigma, St. Louis, MO). Cells seeded one day before were washed by PBS 1x and incubated with energy depletion medium for 30-60 min and then fixed by 4% of PFA at room temperature for 10 min.

2.2. Production of pseudoviral particles

2.2.1. Pseudotyping of the lentiviral vectors

Pseudotyped viruses incorporate structural proteins, which are not encoded by the viral genome. Produced pseudotyped viral particles are hybrid virions carrying envelope proteins derived from other viruses and foreign or 'transfer' genes. Pseudotyped particles do not carry the genetic material to produce additional viral envelope proteins, so the phenotypic changes cannot be passed onto progeny viral particle. Replication-defective pseudotyped particles are obtained via the use of a triple-plasmid system (Naldini, Blomer et al. 1996). These pseudoviral particles are able to 'infect' (or rather transduce) cells and thus integrate a marker gene, but they are not able to produce new viral particles. Pseudotyped lentiviral vectors are commonly used in the virus research due to their broad host cell range, higher level of safety and stability even at 37° C.

2.2.2. Vesicular stomatitis virus glycoprotein

Glycoprotein G of vesicular stomatitis virus (VSV-G) is an atypical fusion protein, which adopts pre- and post-fusion conformation depending on pH. VSV-G in the form of protrusions is

situated on the surface of bullet-like shape virions. VSV-G promotes virus attachment to specific host receptors and pH-dependent membrane fusion after cell entry. VSV-G is used for the pseudotyping of lentiviruses (notably HIV-1) (Naldini, Blomer et al. 1996; Reiser, Harmison et al. 1996). VSV-g allows virions to infect a wider cell range. It increases also the stability of viral particles, which enables their concentration by ultracentrifugation (Bartz, Rogel et al. 1996).

Lentiviruses are produced by transient transfection of 293T cells (Fig. 2.2.1). 5 x 10^6 293T cells were seeded in Petri dishes of 10 cm diameter 24h before the transfection. A total of 21 µg of DNA plasmid was used for transfection (3 µg of plasmid PMD2-G, 6 µg of plasmid pCMV_dR8.91, and 12 µg of vector transfer pSicor-luciferase). 24h after transfection, the culture medium was changed. The supernatants containing the lentiviral vectors were harvested 48 h after transfection, filtered through filters of 0.45 µm cellulose acetate (Millipore SLHV033RS) and concentrated twice by centrifugation on Vivaspin columns having a capacity of filtration of 50 kDa (Sartorius Intec, VS2031 reference). ELISA (Innotest HIV Antigen mAb, Innogenetics, 80563 Belgium reference) determined the concentration of virus p24. The viral stock is stored in aliquots of 1 mL at a -80 ° C.

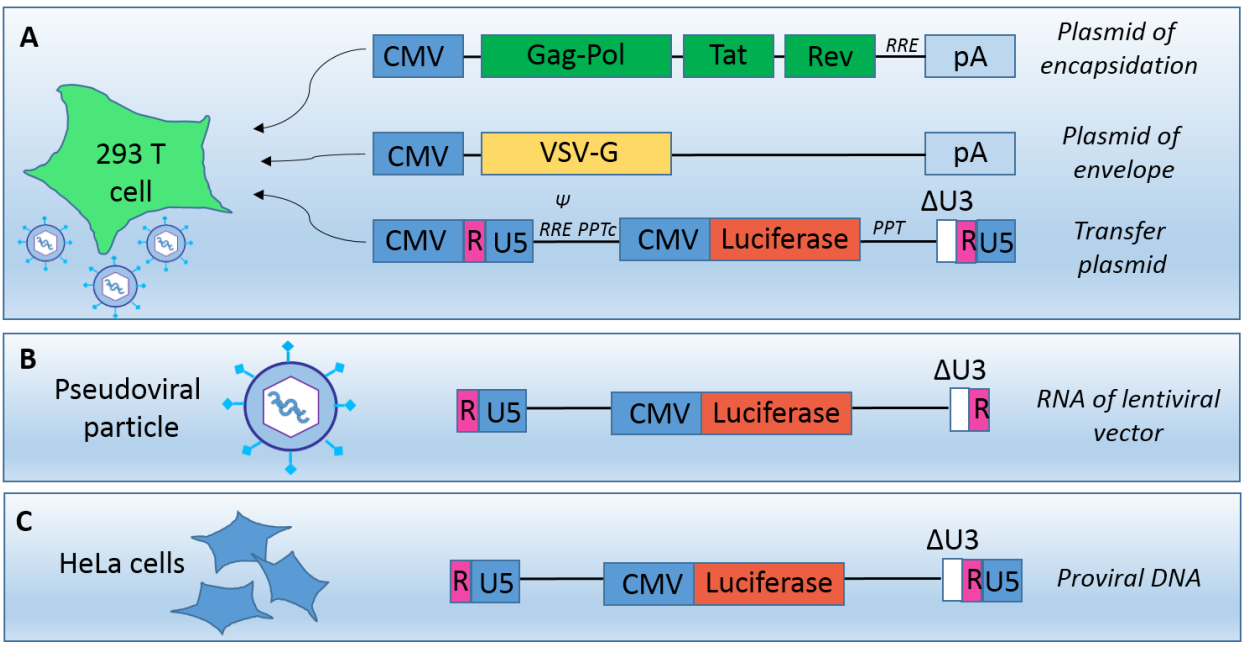

Figure 2.2.1. Production of lentiviral vectors. (A) Lentiviral vectors are produced by co-transfection of 293T cells with the packaging plasmids, envelope and transfer. The obtained lentiviral vectors (containing two strands of RNA (B)) are then transduced in HeLa cells (C) in which RNA is transcribed into proviral DNA that subsequently integrates as a provirus.

2.2.3. Tetracysteine tag conjugation

Tetracystein tag for FlAsH/ReAsH labeling is composed of six to twelve amino acids and has 0.5-1 kDa weight. Despite the low level of interference between the tag and proteins, its location can nevertheless alter the viral infectivity. Several structural and enzymatic HIV-1 proteins were efficiently tagged by TC in Pereira (Pereira, Ellenberg et al. 2011). Initially in our laboratory, TC motif was fused to the N- orC-terminus of NCp7 in the pCMV-dR8.91 plasmid used for pseudovirus production (NC-TC). The natural sites of cleavage by the viral protease were preserved by repeating the first or last 5 amino acids of the viral protein coding sequence (Pereira et al., 2011). The TC motif was also introduced at the C-terminus of integrase (IN-TC).

2.2.4. Labeling

The TC labeling reagent, FlAsH is a biarsenical derivative of fluorescein. Upon binding to the TC motif, FlAsH becomes highly fluorescent. This labeling provides different levels of brightness depending on the length of the TC tag. FlAsH can also bind non-specifically to cysteines inside the cells. Non-specific labeling and toxicity can be minimized by addition of arsenoxide antidote 1,2-ethandithhiol (EDT), which complexes more efficiently FLAsH than pairs of cysteines. In order to perform fast and efficient labeling, the addition of reducing agents triscarboxyethylphophine (TCEP) and small monothiols such as 2-mercapthoethanol (βME) is compulsory. On the other hand, excess of di- and monothiols (tens of milimolar) can decrease the specific labeling by competition with the TC tag.

We elaborated a quite effective method of labeling based on previously reported protocols for cellular and viral components (Langhorst, Genisyuerek et al. 2006; Pereira, Ellenberg et al. 2011; Lelek, Di Nunzio et al. 2012)t, 2006). Viral supernatants (1-2 µg equivalent p24 / mL) were incubated at room temperature with 0.8 mM of FlAsH EDT2 (T34561 Molecular Probes), 1 mM βME, 1 mM (TCEP) and 10 µM EDT in a total volume of 1 mL. To control the specificity of labeling, we replaced the NC-TC pseudovirus or IN-TC by the WT pseudovirus. After 1-2 h of continuous shaking, the marked pseudoviruses were purified by ultracentrifugation at 40000 rpm at 4°C for 30 min to remove unbound FlAsH. The viral particles were resuspended in 300 µl of 1X PBS (Arhel, Munier et al. 2006; Lelek, Casartelli et al. 2015) and stabilized for 20-30 min in ice.

2.3. Imaging

2.3.1. Confocal

Confocal microscopy experiments were performed on a Leica SPE II microscope equipped with a 63× oil immersion objective HXC PL APO 1.40 OIL CS and lasers with excitation wavelengths of 405, 488, 561 and 635 nm. Hoechst and FlAsH/eGFP and Rhodamine (organic NPs)/ReAsH were excited at 405 nm, 488 nm and 561 nm, respectively. The emitted fluorescence was detected by a PMT detector with a detection window of 415-450 nm, 500-600 nm and 575-700 nm for Hoechst, FlAsH/eGFP and NPs/ReAsH respectively. All cells were fixed preliminary with 4% of PFA at room temperature for 10 min, washed with PBS 1x and then imaged.

2.3.2. AFM

To characterize the size of our pseudoviral particles, we used an AFM setup developed by Pro SOLVER Nt-MDT (Moscow). The samples are probed by CSG01cantilevers with a resonance frequency of 27 kHz and a spring constant of 0.06 N / m. Fixed with 4% PFA at room temperature, the viral particles were deposited on a mica surface treated with polyethyleneimine (PEI). Measurements were performed in the tapping mode in liquid phase (1x PBS). Image acquisition was done with a resolution of 512 by 512 points with a 1 Hz scan rate.

2.3.3. CLEM

Correlative light electron microscopy requires a labeling method suitable for fluorescence imaging and electron microscopy. We used the photooxidation of ReAsH based on the protocols of Gaietta, 2011. For EM or CLEM $3x10^5$ HeLa cells were cultured on a clear or on a laser micro-patterned Aclar® support (Spiegelhalter, Tosch et al. 2010) and infected with pseudoviral particles for 6-8 hours. Cells of interest were selected, precisely located and imaged by fluorescence confocal microscopy using the confocal setup described above. For the photooxidation, cells were pre-treated in an ice-cold blocking buffer containing 10 mM potassium cyanide, 10 mM aminotriazole and 20 mM glycine in 0.1 M sodium cacodylate for 20-30 min. Directly after substitution of the blocking buffer with ice-cold solution of 10 mg/mL 3,3'-Diaminobenzidine tetrahydrochloride (DAB) in 0.1 M cacodylate buffer, cells were illuminated by a metal halide Leica EL6000 lamp with excitation filter 515/560 nm for 5-10 min

until total photobleaching of the fluorophore and appearance of precipitates in the transmission mode. Cells were imaged in the ice-cold drop of DAB solution which was changed each 5-7 min. Then, samples were washed 3-5 times for 5 min by the 0.1 M cacodylate buffer and post-treated for EM by the following procedure.

First, cells were fixed in a 0.1 M sodium cacodylate buffer containing 2% glutaraldehyde at room temperature. They were then rinsed two times with cacodylate buffer and postfixed 30 minutes in 1% osmium tetroxide in the dark on ice. After extensive rinses in distilled water, an *en bloc* staining was carried out by incubation in 1% uranyl acetate overnight at 4°C and rinsing with distilled water. Dehydration was performed in graded series of ethanol solutions (50%, 70%, 90% and 3x 100% ; quickly rinsed and incubated during 10 min each on ice) , to be then embedded with epoxy resin (50% in ethanol overnight, and 2x 100% 2 hours). The blocs were finally polymerized at 60°C for minimum 48 hours. Ultrathin serials sections (60-80 nm) of the precise region of interest were cut with a Leica ultracut UCT. Sections were examined under a Philips CM12 transmittion electron microscope (CM12, Philips; FEI Electron Optics, Eindhoven, the Netherlands) operated at 80 kV and equipped with an Orius 1000 CCD camera (Gatan, Pleasanton, USA) (Fig. 2.3.1).

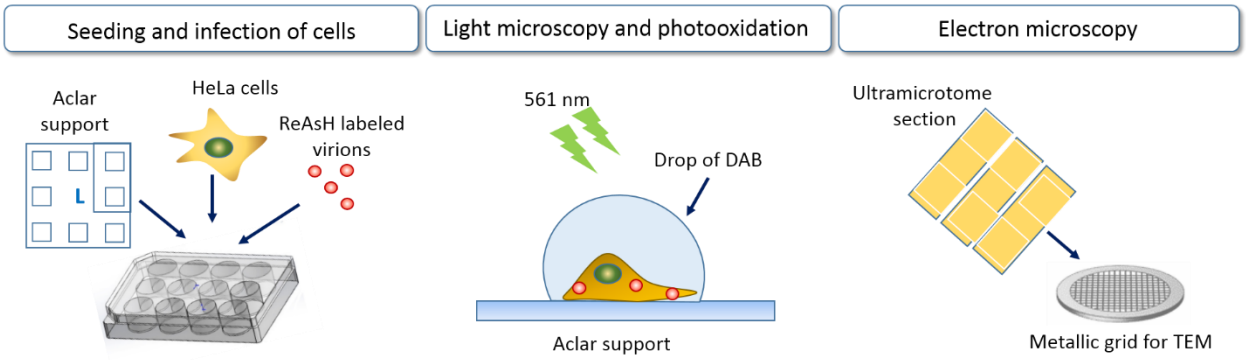

Figure 2.3.1. Procedure of CLEM microscopy with photooxidation. A low number of cells seeded on the aclar support were infected with labeled pseudoviral particles, then imaged, before being photooxided, and finally post-treated for TEM.

2.4. PALM

2.4.1. Sample preparation

Two types of samples were prepared, namely free pseudoviral particles on treated coverslips and infected HeLa cells. Both types of samples were prepared on 18 mm coverslips that were previously cleaned by the following procedure. Washed 3 times with ethanol, acetone

and distilled water, coverslips were sonicated for 10-15 min in ethanol. Then, dried coverslips were treated in Harrick Plasma cleaner for 5-10 min. For deposition of free virions, coverslips were additionally covered with a) poly-L-lysine (Sigma) incubated for 15-20 minutes at 37° C, then washed with sterile water 3 times and dried for 2 hours; b) bovine fibronectin (Invitrogen) (100 µg/ml) incubated for 30 min at 37° C, then coverslips were washed by PBS and dried for 30 min before fixation. Viruses were incubated on the treated coverslips 30 min before fixation with 4% PFA at room temperature. In the case of infected cells, the cells seeded the day before, were incubated with pseudoviral particles for at least 45 min (ED experiments). Then cells were washed with PBS 1x and fixed by 4% PFA at room temperature (2 hours of incubation) or after a time equal to the time of incubation.

The two component photoswitching buffer (Lelek, 2012) consisted of the GLOX system (~10-15% glucose, 0.5 mg/mL glucose oxidase and 0.04 mg/mL catalase all Sigma) and a source of thiols (1mM βME, Sigma). The presence of oxygen was strongly reduced by the use of depression slides with working volume of 100 µL, where coverslips were tightly sealed by two-component silicon glue Twinsil® (Fig.2.4.1).

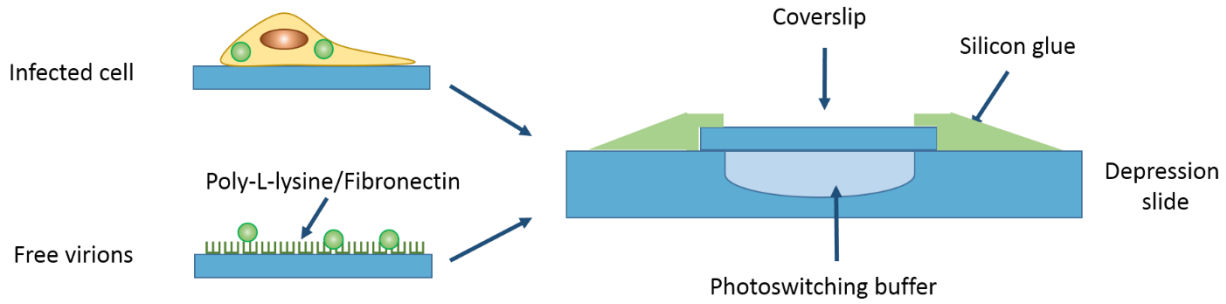

Figure 2.4.1. Sample preparation for FlAsH-PALM. Free viral particles have been deposited on the pre-treated with Poly-L-Lysine or fibronectin coverslips, whereas infected cells have been deposited on the non-treated coverslips; in the next step, coverslips with were sealed with silicon glue on a depression slide with photoswitching buffer inside the reservoir.

2.4.2. PALM

First, optimization experiments were performed on the Leica SR GSD setup equipped with 488 (300 mW), 532 (500 mW), 642 (500 mW) and 405 (30 mW) nm lasers. 18x18 µm images were acquired in the GSD mode through the Leica HCX PL APO 100/1.47 objective on the SuMo stage with Suppressed Motion technology for minimizing drifts.

Later, TIRF/PALM microscopy was performed on a home-built setup based on an Olympus IX-71 inverted microscope with a high NA TIRF objective (Apo TIRF 100 x, oil, NA 1.49, Olympus). Samples were illuminated with laser diodes at 405 and 488 nm (both

15 W cm^{-2}, Spectra Physics). The fluorescence emission was detected on an electron multiplying CCD digital camera (ImagEM, HAMAMATSU) with a pixel size of 106 nm and an exposure time of 100 ms. A stop Line Notch Filter 488 nm (Semrock) and a 488 nm longpass filter (Semrock) were used to filter the FlAsH fluorescence signal. Preview images were acquired at low power followed by "bleaching" to the dark state with max power for a few minutes. PALM acquisition was performed under continuous illumination at 488 nm (~60 mW) and 405 nm (~3 mW).

2.4.3. Data treatment

7000-15000 frames videos were obtained for each 18x18 µm or 27x27 µm region of interest (ROI) (depending on setup).

High-resolution images were reconstructed by using ThunderSTORM plugin for ImageJ software (Ovesny, Krizek et al. 2014) (Fig. 2.4.2). Wavelet filter was used for the filtering of raw images and integrated Gaussian PSF methods for localization. We chose a histogram approach for the rendering of the final image. In this method, the intensity of each pixel corresponds to the number of detected blinking events. Visualization of the final image was performed by the histograms approach with a pixel size 20 nm, defined according the Nyquist-Shannon's criterion. This criterion or sampling theorem states that used sampling interval (pixel size of SR image) is not greater than one-half the size of the smallest resolvable feature of the optical image (in our case ~40-50 nm clusters inside the nucleus).

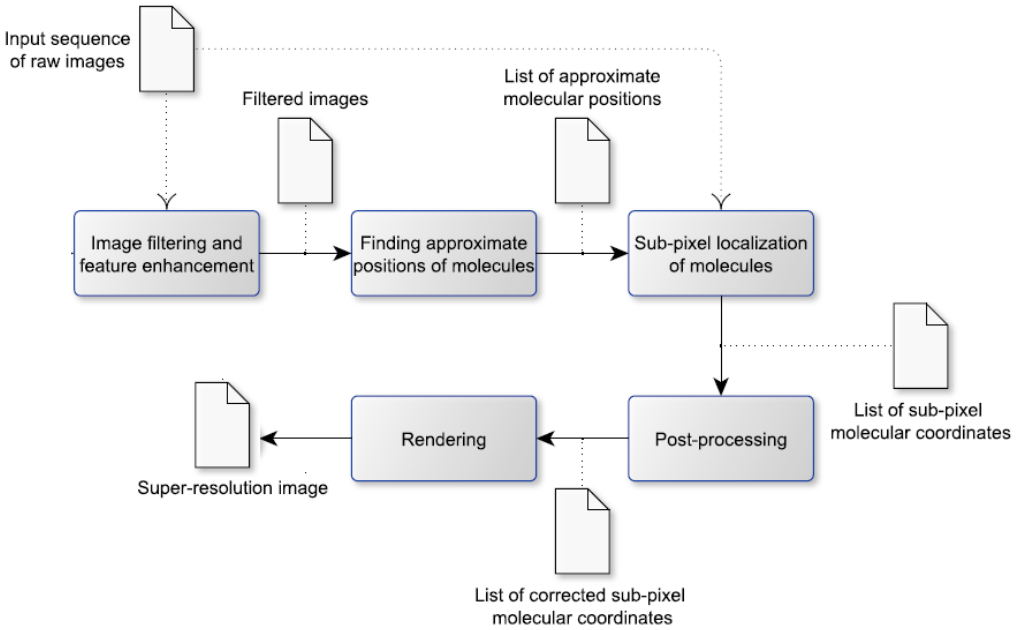

Figure 2.4.2. Schematic representation of data processing for single molecule localization microscopy by ThunderSTORM.

2.4.4. Analysis

The localization precision was calculated by the ThunderSTORM plugin ImageJ according to the precise formula (1a) or roughly estimated by the (6b):

[6]

where σ is the standard deviation of the point spread function, *a* the size of the camera pixel (pixel size/magnification), *b* the background noise and *N* the number of photons, calculated according to:

[7]

EMgain is the electron multiplier gain; QE is the quantum efficiency of the camera, RID is the raw integrated density of the pixel intensity under the PSF and the conversion factor relates the number of Analog to Digital Units (ADU) and recorded number of electrons.

The size of the detected objects was estimated as the full width half maximum (FWHM) by fitting the intensity plot profile with a 2D Gaussian function (Fig. 2.4.3.) [8].

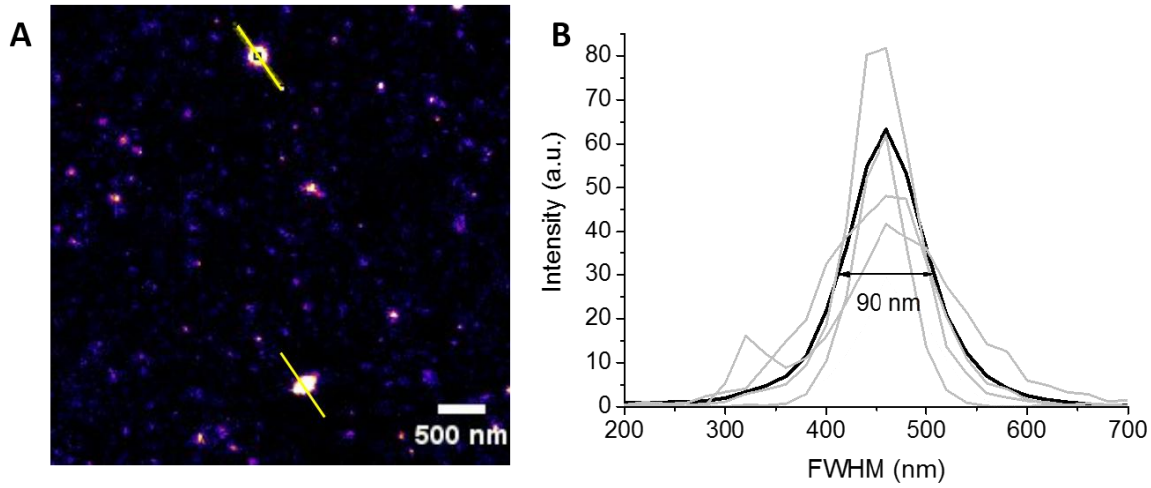

Figure 2.4.3. Size estimation of detected particles. (A) High resolution image of free viral particles with lines across the virions (ImageJ ROI manager); (B) Intensity values across the lines (gray) and average value of 5 measurements (black). The FWHM on the intensity plot profiles is defined as the size of the detected virions.

[8]

Where y_0 base, x_c center, A area under the curve, and w is FWHM.

For a better evaluation of the particle sizes, additional macros in ImageJ have been applied to plot profiles specified manually.

Chapter 3: Results

3.1. Cytoplasmic Release of NCp7 proteins from the HIV-1 viral cores during the early steps of infection

3.1.1. Introduction

We are interested in the laboratory into the protein NCp7 as a therapeutic target for new antiretroviral drugs due to its multiple functions and highly conserved sequence between different viral strains. Within the frame of this work, we have been interested in investigating the fate of the protein during the early steps of viral infection.

Early steps of infection comprises the steps from cell recognition to integration of the viral DNA into the host genome. After receptor recognition and cell fusion, the viral core is released in the cytoplasm where uncoating and reverse transcription (RTion) occurs. During the RT processes, the genomic RNA is copied into viral DNA (vDNA) and the viral core is reorganized into the preintegration complex (PIC). This complex is ready to enter the nucleus, where integration of viral genome is performed. Despite the large amount of data from in vitro studies, the investigation of these processes in infected cells is complicated and provides sometimes controversial results, probably due to the numerous concurrent processes taking place.

Viral core comprises a shell of p24 proteins around the viral genome associated with 1500-2000 NCp7 molecules. Enzymatic proteins (reverse transcriptase (RT), integrase (IN) and protease (PR)) and viral protein r (Vpr) are also present. NCp7 protein is well known for its nucleic acid chaperone activity and is critical for the proper annealing of RNA during RTion (Saadatmand and Kleiman, 2012) as well as for the obligatory strand transfers (Darlix et al, JMB, 2011). The presence of NCp7 retained inside the PIC is debated. In PIC, NCp7 can bind dsDNA either non-specifically (Tanchou, 1998; Poljak, 2003) or specifically through sequences such as the DNA flap (Mirambeau, 2007). Around 200 molecules of IN are present inside the viral core. This enzymatic protein is required for viral integration and was found inside the nucleus of infected cells. Moreover, IN contains nuclear localization signals that should help importation in the nucleus by active transport. Thus IN should be present inside the PIC until the integration step and was chosen in our studies as a reference component of the PIC.

Uncoating and RTion are key steps in the early steps of infection. Recently, several models of uncoating were proposed: fast uncoating directly after inoculation (Burkinsky, 2004; Dvorin, 2003), gradual loss of capsid during the transport to the nucleus (Warrilow, 2009) and late uncoating in the perinuclear region (Arhel, 2007; Yamashita, 2007). Regardless the proposed

uncoating mechanism, a strong connection with reverse transcription was established. Whereas in the first model uncoating triggers RTion, the second assumes a simultaneous loss of capsid and viral transformation, while the third one emphasizes that the intact viral core is crucial for effective RTion. The precise composition in proteins of the PIC as well as the mechanisms responsible for the nuclear entry are still debated (Suzuki, 2007).

As a model system for investigating the early steps of the viral life cycle, HIV-1 pseudoviral particles expressing NCp7 or IN conjugated to tetracystein (TC) tags have been chosen. These particles can be produced with different loads of the tags. In the case of 100% load, high concentration of fluorophores (~100 mM) in the confinement space causes a strong self-quenching effect. Thus, a decrease of fluorophore density or an increase in the distance between molecules prevents the self-quenching and increases the intensity of fluorescence.

Based on *in vitro* studies (Lyonnais, 2013) RTion is assumed to be responsible for the dismantling of the nucleocapsid and release of NCp7 molecules. In order to prove this hypothesis in cellular infection study, RT was inhibited by AZT (azidothymidine or zidovudine), a thymidine analogue from the nucleoside reverse-transcriptase inhibitor (NRTI) family that selectively inhibits the RT (Furman, 1986) in the 50-500 nM range (Mitsuya, 1985).

The objective of the first part of the work was to follow the RT-dependent release of TC-tagged NCp7 labeled by FlAsH from the viral complexes in the infected cells. The concept was proved on viral particles containing different percentages of tagged molecules. The release of NCp7 molecules was shown from the evolution of the fluorescence intensity during the time course of infection. As expected, the release of NCp7 was considerably decreased by AZT, which blocks Reverse Transcription.

3.1.2. Publication

Cytoplasmic Release of NCp7 proteins from the HIV-1 viral cores during the early steps of infection

Sarwat Zheib[a], Iryna Lysova[a], Eleonore Réal, Romain Vauchelles, Halina Anton, Yves Mély

Laboratoire de Biophotonique et Pharmacologie, UMR 7213 CNRS, Université de Strasbourg, Faculté de Pharmacie, Illkirch, France

[a] *contributed equally to the work*

Abstract:

The HIV-1 nucleocapsid protein (NCp7) is a small protein that plays an important role as a chaperone of nucleic acids in the viral replication cycle. Its mechanism and properties have been widely studied *"in-vitro"* using model systems, but data about its fate in the early steps of the viral life cycle in conditions reflecting a real infection are still missing. In this report, we used infectious HIV-1 pseudoviruses bearing NCp7 proteins fused to a tetracystein (TC) tag, specifically labeled by a biarsenical fluorescein derivative (FlAsH) to monitor these proteins in infected cells during the early stages of infection. Interestingly, using pseudoparticles with defined ratios of TC-tagged to non-tagged NCp7 proteins, we found that the fluorescence intensity of these particles decreased when the percentage of TC-tagged proteins increased. This fluorescence decrease is the result of the strong fluorescence quenching consecutive to the close proximity of the FlAsH-labelled TC-tagged NCp7 proteins in the viral complex. Therefore, the fluorescence intensity of individual viral complexes in infected cells appears as an appropriate parameter to reveal changes in the amount of NCp7 molecules in the particles with time. Interestingly, we observed a dramatic fluorescence increase of the individual viral complexes in infected cells at 6 and 14 h post-infection. In contrast, the fluorescence intensity of pseudoviruses containing TC-tagged integrase was constant with time. Therefore, the observed fluorescence increase is likely related to the cytoplasmic release of NCp7 molecules from the viral complexes, which decreases the strong fluorescence quenching resulting from the high concentration of tagged NCp7 molecules initially present in the viral cores. This dequenching effect is significantly reduced when reverse transcriptase is inhibited, showing that NCp7 release is connected to vDNA synthesis. A spatial analysis further showed that NCp7-TC release is more pronounced when approaching the perinuclear space, where the capsid disassembly is thought to

be completed. Our data evidence for the first time, the cytoplasmic release of NCp7 during the remodeling of the reverse transcription complex (RTC).

Introduction:

During the early stages of infection, the viral core enters into the cytoplasm of the host cell and the reverse transcriptase initiates the synthesis of the viral DNA genome. As a result, the viral complex undergoes a transformation from a ribonucleoprotein (RNP) complex into the reverse transcription complex (RTC) and then finally into the preintegration complex (PIC). This transformation is thought to be associated with an important rearrangement of the viral structure that involves a set of viral and cellular proteins. However, the precise timing and composition of the complexes during the viral complex maturation is still debated (Arhel, 2010, Warrilow, 2009).

The initial RNP complex or 'nucleocapsid' comprises notably the viral protein r (Vpr), integrase (IN), reverse transcriptase and the viral RNA dimer coated by more than 2000 molecules of NCp7 (Thomas and Gorelick, 2008). According to a recently proposed model based on "in-vitro" experiments, the NCp7 molecules may be progressively released from the RTC during the synthesis of the viral DNA (Lyonnais, 2013). This hypothesis is based on the lower affinity of NCp7 for double stranded DNA as compared to the single stranded genomic RNA, as well as on the dilution of the content of the viral complex on disassembly of the capsid core. However, this release has not been evidenced so far "in cellulo", in conditions mimicking the real infection.

To reach this objective, we used in this study VSV-pseudotyped HIV-1 viruses (LVs) expressing NCp7 or IN proteins fused to a TC tag, and luciferase as a reporter gene. These LVs constitute models for the early steps of infection and can be selectively labeled on the TC-tagged proteins by the arsenical fluorescein analogue FlAsH. To evidence the release of NCp7 proteins from the viral complexes, we used the fact that the high concentration of NCp7-TC (~100 mM based on the NCp7 to RNA volume (De Marco, 2010)) in the RNP should cause strong self-quenching of the fluorescence of label. This strong quenching was clearly evidenced by comparing the fluorescence intensity of pseudoviruses expressing various ratios of TC-tagged to non-tagged NCp7 molecules. Interestingly, we observed a strong increase of fluorescence intensity when the ratio of NCp7-TC/NC decreased. Therefore, a progressive release of NCp7 during reverse transcription should cause a progressive fluorescence intensity increase of the viral complexes. In line with our assumption, by monitoring the fluorescence intensity of individual FlasH-labelled viral complexes expressing NC-TC or IN-TC, we observed a strong

fluorescence increase from 2 to 14 h post infection with NCp7-TC, but not with IN-TC. Finally, this loss of quenching with time was abolished in the presence of 3'-azido-3'-désoxythymidine (AZT), a specific inhibitor of reverse transcriptase, indicating that the release of NCp7 molecules was dependent on reverse transcription. Moreover, the highest intensities of the viral complexes were observed in the perinuclear region, suggesting the release of NCp7 mainly occurs prior to the nuclear entry. Overall, our data show for the first time the RT-dependent cytoplasmic release of NCp7 molecules during the early stages of HIV-1 infection.

Materials and methods:

Cell culture

HeLa and 293T cells were cultured in Dulbecco's modified Eagle medium supplemented with 10% fetal calf serum (Invitrogen Corporation, France) at 37°C in a 5% CO_2 atmosphere.

Production of vectors and viruses:

The plasmids were cloned according to Perreira et al.(Pereira, Ellenberg et al. 2011) The protease cleavage sites were conserved by duplicating the 5 first and last amino acids of the mature protein coding sequence (Pereira, Ellenberg et al. 2011) .

HIV-1 pseudotyped viruses were prepared following a protocol based on Arhel et al. 2006 and Lelek et al 2012 (Arhel, Genovesio et al. 2006; Lelek, Di Nunzio et al. 2012) . 293T cells were co-transfected by pMD2-G, pCMV_dR8.91 and the transfer vector pSicor-luciferase using jetPEI® (PolyPlus transfection, France) according to supplier's recommendations. 24 h post transfection, the culture medium was replaced by serum free medium. The cell supernatant was collected 48 h post transfection. It was filtered through 0.45 µm low binding filters (Millipore, France) in order to eliminate large cellular debris and was further concentrated by centrifugation in Vivaspin collection tubes with a cutoff of 50 kDa (Sartorius, Intec, France).

The concentration of p24 antigen was measured by a p24 ELISA test (Innotest HIV Antigen mAb, InnoGenetics, Belgium). The aliquots of viral particles were stocked at -80°C.

The infectivity of the pseudoviruses was measured by luciferase luminescence 24 h after infection. HeLa cells were plated in triplicate for each type of pseudovirus in 96-well dishes and infected with equivalent amounts (0.5-11 ng) of p24 viral antigen mixed with 8 µg/mL polybrene solution in DMEM. After 24 h, the cells were washed with PBS and lysed using a cell culture lysis buffer (Promega, France) supplemented with 0.5 % Triton-X100 during 20 min at room temperature. Luciferase activity was measured by using a luciferase assay (Promega, France)

according to supplier's recommendations by using a Berthold TriStar luminometer (LB941, Berthold Technologies, Germany).

For the production of particles with different fractions of TC-tagged and WT NCp7 proteins, a mixture of vector plasmids coding for the two proteins was used for transfection.

FlAsH labeling of the pseudoviruses

The viral supernatants (containing 0.5 – 1 μg of p24) were labeled at room temperature with 0.8 μM FlAsH-EDT2 (Molecular Probes, France), 1 μM beta-mercaptoethanol, 1 μM Tris (2 carboxyethyl) phosphine (TCEP) and 10 μM 1,2-ethanedithiol in a total volume of 1 mL of serum free medium. The unbound fluorophores were washed out by an ultracentrifugation step (100 000g during 30 min at 4°C) and viruses containing pellets were resuspended in 200 μL of PBS and deposited on HeLa cells cultured on poly-L-lysine coated cover glasses, or in Ibi-Treat 4 well chambers (μ-Dish IBIDI, Germany). After 2 h of infection at 37°C, the cells were washed in PBS and incubated for additional 6-14 h at 37°C. The samples were stained by 1 μM Hoechst 33342 during 10 min and fixed with 4% PFA during 10 min at room temperature.

For the imaging of isolated particles, labelled pseudoviruses were resuspended in PBS after the ultracentrifugation step and deposited on poly-L-lysine or fibronectin coated glass cover slips. After 30 min, the samples were fixed with 4% PFA.

Fluorescence Microscopy

TIRF microscopy was performed on a home built setup based on an Olympus IX-71 inverted microscope with a high-numerical aperture (NA) TIRF objective (Apo TIRF 100 x, oil, NA 1.49, Olympus). Samples were illuminated with a 488 nm laser diode (15 W cm^{-2}, Spectra Physics). The fluorescence emission was detected on an electron multiplying CCD digital camera (ImagEM, HAMAMATSU) with a pixel size of 106 nm and an exposure time of 100 ms. A stop Line Notch filter 488 nm (Semrock) and a 488 nm long pass filter (Semrock) were used to filter the FlAsH fluorescence signal.

Confocal microscopy experiments were performed on a Leica SPE microscope equipped with a 63× oil immersion objective (NA = 1.2). Hoechst and FlAsH were excited with 405 nm and 488 nm lasers, respectively. The emitted fluorescence was detected by a PMT detector with a detection window of 415-450 nm and 500-600 nm for Hoechst and FlAsH, respectively.

Image processing and analysis

The image processing and analysis were carried out using a ImageJ software (Schneider, Rasband et al. 2012). To quantify the fluorescence intensity of the FlAsH-labelled pseudoviruses, the images were first thresholded in order to isolate the fluorescent spots and a particle analysis function was used to identify their borders. The coordinates were saved in RIO manager and applied to the initial image to measure the mean fluorescence intensity of the spots. In each experiment, the measurements were realized on 10-13 images per condition and three independent experiments were performed in order to confirm the observations.

Spatial analysis of the intensity of the fluorescent spots was performed by using a home-built macro for ImageJ software (Schneider, Rasband et al. 2012). In a first step, the images of the blue and green channel representing the nucleus (DNA labeled by Hoechst) and the FlAsH-labelled viral particles, respectively were separated. The autofluorescence signal of the green channel was used to generate a mask of the cell contours and the shape of the nucleus was detected automatically on the binary image after thresholding the Hoechst channel. The macro generated then automatically concentric regions around the nucleus and detected the number and mean intensity of the green particles in each region. The threshold values and the thickness of the concentric crowns were setup up by the user.

Results:

1. Virus design, production and infectivity tests

NCp7 being a relatively small protein (7 kDa) endowed with a highly conserved structure and key functions, its fusion to a fluorescent tag can cause a loss of viral infectivity. To avoid this, we used the very small tetracystein tag (6 amino acids) in combination with FlAsH, a biarsenical fluorescein based label (Griffin, Adams et al. 1998; Adams, Campbell et al. 2002). Besides its small size, this labeling system presents the key advantage that the fluorescent label is added only after the production step minimizing perturbations that could occur during the assembly process. The TC tag (CCRECC) was inserted at the C-terminal end of NCp7 (Fig. 1A). The infectivity of the pseudoviruses, as measured by the luciferase activity on HeLa cells 24 h post infection, was fully preserved when only 10% of NCp7 molecules were tagged or when the TC tag was inserted at the C-terminus of the IN (Fig. 1B). Even when 100% of the NC molecules were tagged by TC, the pseudoviruses remained infectious, showing an infectivity that still corresponded to 40% of that of the control pseudoviruses with no tagged proteins. The effect of FlAsH labeling on pseudovirus infectivity on HeLa cells was also evaluated by comparing the luciferase activity after infection by FlAsH-labeled pseudoviruses with that obtained with the same pseudoviruses that underwent the labeling procedure in the absence of

FlAsH. Figure 1C shows that the binding of FlAsH to the TC tag reduces the infectivity of the pseudoviruses by an additional 20%.

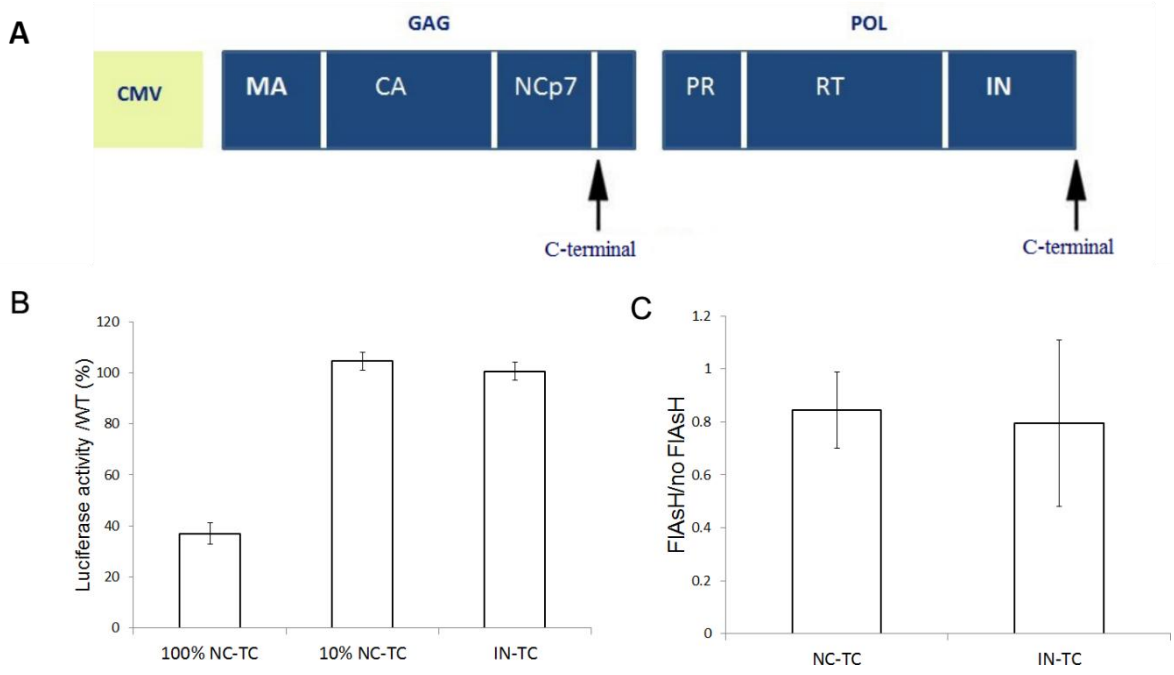

Figure 1: Influence of the FlAsH-TC system on the viral infectivity. (A) Scheme of plasmids coding for TC-tagged NC and IN proteins. (B) Effect of the TC tag on pseudovirus infectivity. The luciferase activity in HeLa cells of TC-containing pseudoviruses relative to WT pseudoviruses is reported 24 h post-infection. Noticeably, when the infection was performed in the presence of 1 µM of 3'-azido-3'-désoxythymidine (AZT), a specific inhibitor of reverse transcriptase, the activity of luciferase did not exceed 1% of the control samples (data not shown). (C) Effect of FlAsH binding on pseudovirus infectivity. The luciferase activity in HeLa cells 24 h after infection with FlAsH-labeled pseudoviruses was compared to that obtained using pseudoviruses that underwent the labeling procedure in the absence of FlAsH.

For imaging experiments, HeLa cells were incubated with the labeled pseudoviruses during 2 h, then washed and incubated in the complete medium for 2 to 14 h. The cells were fixed and imaged by confocal microscopy. Typical images are shown in figure 2. Intense fluorescent spots are observed in the cytoplasm and sometimes in the nucleus of the infected cells (Fig 2 A, B). Intensity plot profiles of 100 intracellular fluorescent spots measured in 20 different infected cells were fitted by a Gaussian function. The average FWHM value was 300 +- / 35 nm (Figure 2 C), which is near the theoretical diffraction limit of the microscope. Therefore it can be assumed that the majority of the intracellular spots correspond to single viral particles. Cells infected with pseudoviruses that do not contain any TC tag, show a low intense labeling probably due to the non-specific binding of FlAsH to the cysteine residues of viral proteins. Both the fluorescence intensity and density of the labeled particles are significantly lower as compared to the TC-containing pseudoviruses shown in Figure 2 A,B, confirming the specificity of the FlAsH labeling. Interestingly, no fluorescent spot was detected in HeLa cells infected with viral particles that underwent the labeling procedure without adding the FlAsH fluorophore (Figure 2

F-G). Moreover, autofluorescence of non-infected cells was negligible in our experimental conditions.

Taken together, our data show that HIV-1 pseudoviruses expressing NCp7-TC and IN-TC proteins labeled by FlAsH are infectious and can be imaged in infected cells by fluorescence microscopy. These particles were further used as a model system for the study of the intracellular fate of NCp7 during the early stages of HIV-1 infection.

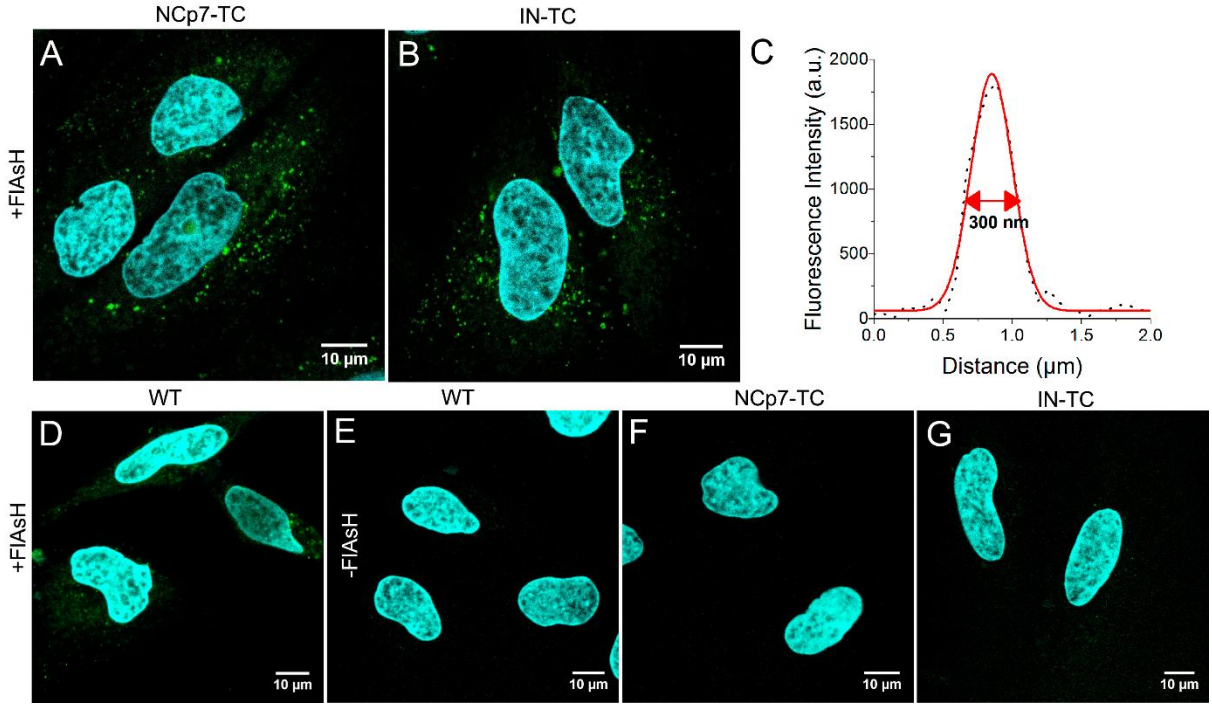

Figure 2: Confocal images of HeLa cells infected with pseudoviruses expressing (A, F) 100% NCp7-TC, (B, G) IN-TC and non-tagged (D, E) NCp7 labeled with (A, B, D) or without (E, F, G) FlAsH. The nuclei were stained by Hoechst. (C) Intensity plot profile of a typical intracellular fluorescent spot fitted by a Gaussian function. Mean value of 100 measurements FWHM= 300 +/- 35 nm.

2. Fluorescence quenching in FlAsH-labelled pseudoviruses expressing NCp7-TC

In mature HIV-1 virions, the RNA dimer is coated by more than 2000 molecules of NCp7 (Darlix, Godet et al. 2011). The size of the capsid core being approximately 50-100 nm (Briggs, Grunewald et al. 2006), the local concentration of NCp7 inside the HIV-1 virion is in the millimolar concentration range. At such a high concentration, we hypothesized that the emission of the fluorescein based FlAsH fluorophores should be strongly reduced, due to self-quenching effects (Weinstein, Yoshikami et al. 1977; Chen and Knutson 1988; Walter 1988; Walter 1988; Walter 1988). In order to check whether a concentration-dependent FlAsH quenching occurs in the NCp7-TC pseudoviruses, we simultaneously transfected HeLa cells with plasmids coding for tagged and non-tagged NCp7 in order to produce pseudoparticles where the fraction of tagged NCp7 was either 10%, 50% and 100%. The produced pseudoparticles were then labeled by FlAsH dyes, deposited on fibronectin-coated coverglasses, fixed in 4% PFA and imaged by a

TIRF microscope in order to compare their fluorescence intensity. According to our hypothesis (Fig. 3A), a decrease of TC-bound FlAsH concentration should reduce the fluorescence self-quenching of FlAsH and result in an increase of the fluorescence emission. Consequently, pseudoviruses containing lower proportions of tagged NCp7 proteins should emit a stronger fluorescence signal.

Typical images are shown in figure 3B. The WT virus with non-tagged NCp7 proteins showed a significantly lower fluorescence intensity those with TC tagged proteins, confirming the specificity of labeling (Fig. 3B). The intensity of 500 fluorescent spots was measured and the distribution was represented in the box plot shown in Figure 3C. Interestingly, the fluorescence of the viral particles increases when the fraction of TC-tagged proteins decreases (mean fluorescence intensity values are 3400+/-650 for 100% NCp7-TC, 4300+/-700 for 50% NCp7-TC and 5650+/- 900 for 10% NCp7-TC particles). Assuming that all pseudoparticles contain the same number of NCp7 proteins, it results that the number of NCp7-TC proteins and thus, the number of FlAsH bound probes in pseudoparticles expressing 100% NCp7-TC is respectively 2 and 10 times higher than in pseudoparticles expressing 50% and 10% NCp7-TC. Therefore, taking into account this difference in the number of FlAsH probes, it results that the FlAsH fluorescence in the particles expressing 100% NCp7-TC is quenched by a factor of 2.5 and 17, as compared to pseudoparticles expressing 50% and 10% NCp7-TC, respectively. These results confirm that FlAsH fluorescence quenching occurs at high concentrations of tagged NCp7 proteins.

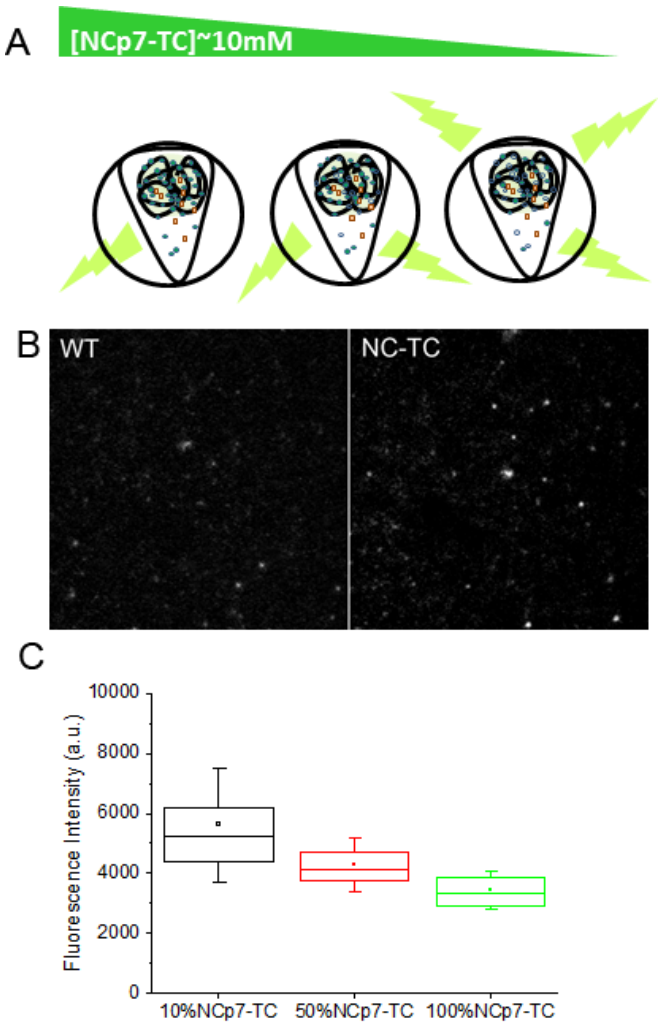

Figure 3: Evidence of fluorescence self-quenching in FlAsH-labeled pseudoviruses expressing TC-tagged NCp7 proteins. (A) Scheme illustrating the FlAsH fluorescence self-quenching in the viral core. The fluorescence emission is thought to decrease when the concentration of FlAsH bound to TC-tagged NCp7 proteins is increasing. (B**)** Typical TIRF images of FlAsH labeled pseudoviruses expressing either WT NCp7 proteins or TC-tagged NCp7 proteins. (C) Box chart representing the fluorescence intensity of pseudoviruses as a function of the percentage of TC-tagged NCp7 proteins. The box shows intervals containing 25-75% of the values, whiskers represent the SD, the lines and the squares correspond to the median and the mean values, respectively (N=500).

3. Self-quenching of FlAsH fluorescence in infected cells.

In a next step, we checked whether the differences in the fluorescence intensity of pseudoviruses expressing different fractions of tagged NCp7-TC proteins are preserved during infection. Pseudoviruses expressing 100%, 50% and 10% TC-tagged NCp7 proteins were incubated with HeLa cells during 2 hours. After the washing step, the cells were incubated in the complete medium during 3 additional hours and fixed with 4% PFA. Cells were then imaged by confocal microscopy and optical sections in the middle of the cells were chosen for the analysis.

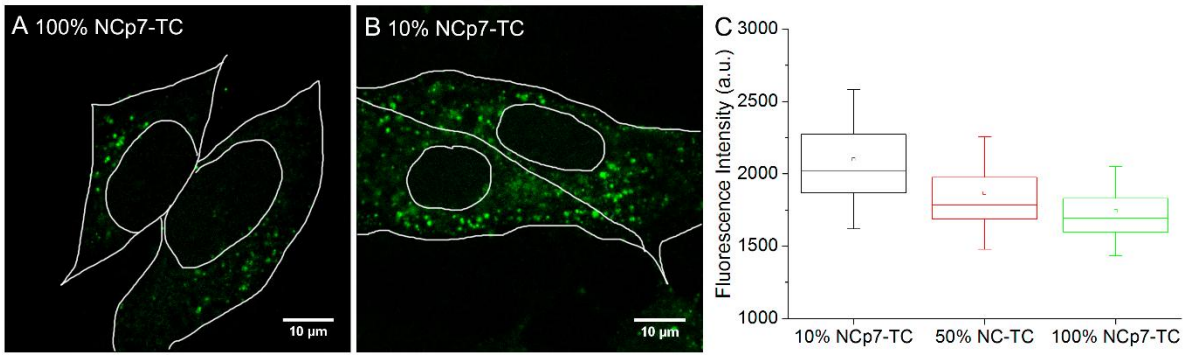

Figure 4: Self-quenching of FlAsH-labeled pseudoviruses in infected cells. Confocal images of cells infected with FlAsH-labelled pseudoviruses containing 100% (A) and 10% (B) of NCp7-TC. (C) Box chart representing the fluorescence intensity of the cytoplasmic spots in cells infected with pseudoviruses containing 10%, 50% and 100% of NCp7-TC proteins (N>1000). Mean values: 1750 +/- 200 for 100% NCp7-TC, 1900 +/- 200 for 50% NCp7-TC and 2100+/-230 for 10% NCp7-TC.

The mean intensity of 1000 fluorescent spots in 20-30 different cells was measured and the distribution of the values is shown in figure 4D. As with the free pseudoviruses, we observed a fluorescence intensity increase related to a decrease of the fraction of TC-tagged NCp7 proteins and consequently, the concentration of bound FlAsH molecules. Thus, our data suggest that changes in the NCp7-TC concentration in the viral particles could be evidenced by monitoring their fluorescence intensity within infected cells.

4. Dequenching of FlAsH fluorescence during the time course of infection

In order to monitor the possible concentration changes of FlAsH-labeled NCp7-TC molecules in pseudoviruses during the early steps of infection, HeLa cells were incubated with pseudoviruses expressing 100% NCp7-TC and labeled by FlAsH during 2 hours, washed and then, further incubated in the complete medium for different times (0, 8 and 16 hours). Afterwards, the cells were fixed, stained with Hoechst and imaged by confocal microscopy. Typical images (Figure 5A) show intense fluorescent spots all over the cytoplasm and sometimes in the nucleus of infected cells. We next counted the average number of viruses detected in the infected cells (Figure 5B). While for the WT control, we could detect on the average only 10 spots per cell independently on the incubation time, significantly higher numbers of spots were observed for cells infected with pseudoviruses expressing NCp7-TC/FlAsH. Moreover, the number of these intracellular spots increased with time, likely due to a progressive internalization of the pseudoviruses.

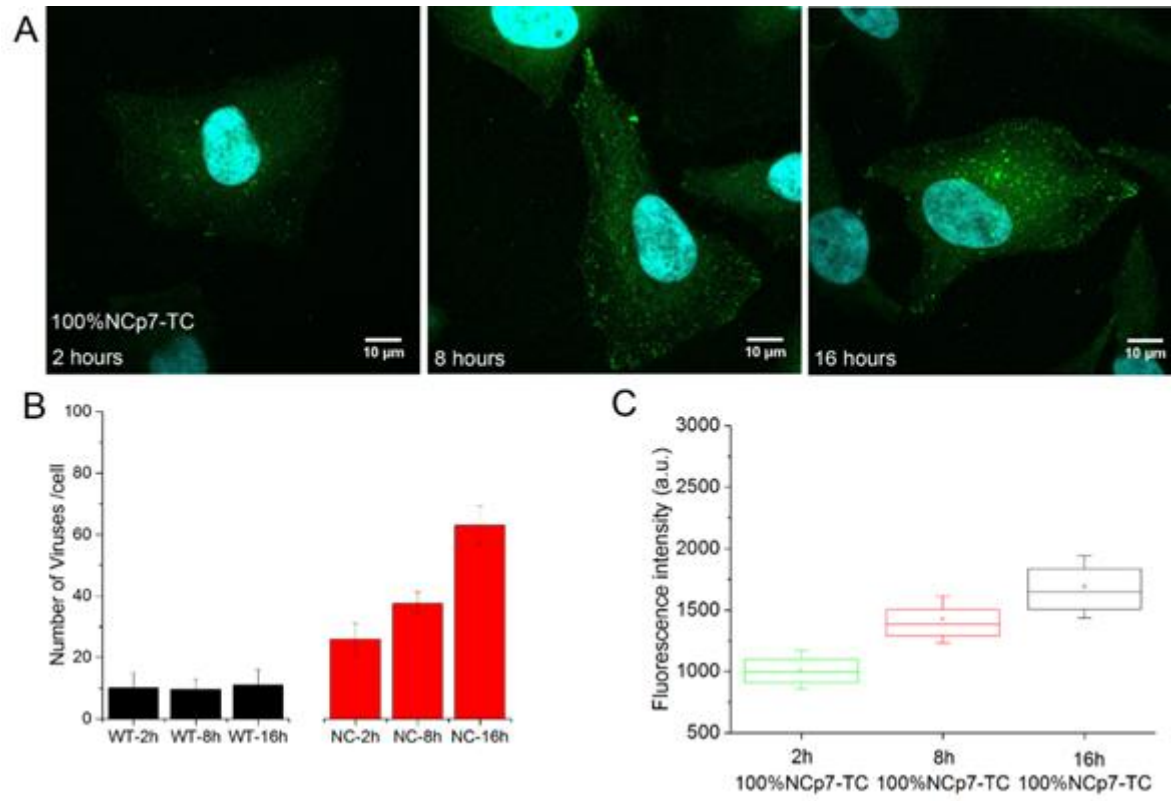

Figure 5: Time-dependence of the fluorescence intensity of FlAsH-labeled pseudoviruses expressing NCp7-TC proteins during infection. (A) Typical Images of HeLa cells infected by NCp7-TC/FlAsH pseudoviruses at 2, 8 and 16 hours post-infection. (B) Time evolution of the average number of particles detected per cell for FlAsH-labeled pseudoviruses expressing WT NCp7 or 100% NCp7-TC. Time evolution of the mean fluorescence intensity of 1000-2000 fluorescent spots detected in 30-40 cells at each time point for pseudoviruses expressing (C) 100% NCp7-TC (mean fluorescence intensity values: 1000+/- 150 at 2 h, 1400+/-200 at 8 h and 1700+/-200 at 16 h).

In parallel, a significant increase of the mean fluorescence intensity of the FlAsH-labeled pseudoviruses expressing 100% NCp7-TC was observed as a function of time (Fig. 5C). This increase may be related to the fluorescence dequenching resulting from a decrease in concentration of the NCp7-TC/FlAsH complexes in the viral core, due to their release in the cytoplasm..

Taken together, our results evidence a time-dependent increase of the FlAsH fluorescence in the viral complexes containing NCp7-TC proteins. We interpret these observations by the increase of the interfluorophore distance between FlAsH molecules that may result from the release of the NCp7-TC bound FlAsH molecules from the viral complex and the remodeling of the viral complex.

Dependence of FlAsH dequenching on the reverse transcription process

To further confirm that the observed time-dependent fluorescence increase observed with FlAsH-labeled pseudoparticles is related to the release of NCp7-TC, we determined the dependence of the fluorescence changes on the reverse transcription process. Indeed, as the

release of NCp7 is thought to be partly related to the conversion of the single-stranded RNA which binds NCp7 with good affinity into DNA duplexes which bind NCp7 with low affinity, inhibition of reverse transcription should partly prevent the release of NCp7 molecules. To this end, HeLa cells were infected by FlAsH-labelled pseudoviruses expressing 100% NCp7-TC in the presence of AZT, a specific inhibitor of reverse transcriptase. Comparison of the confocal images of infected cells in the absence (Figure 6A) and in the presence (Figure 6B) of AZT, indicated that AZT did not significantly perturb the intracellular distribution of the viral particles. In contrast, in line with our expectations, AZT considerably reduced the time-dependent fluorescence increase of the viral particles (compare Figures 6C and D), confirming that the release of NCp7 molecules in relationship with the reverse transcription process is likely responsible for the fluorescence intensity changes of the viral particles.

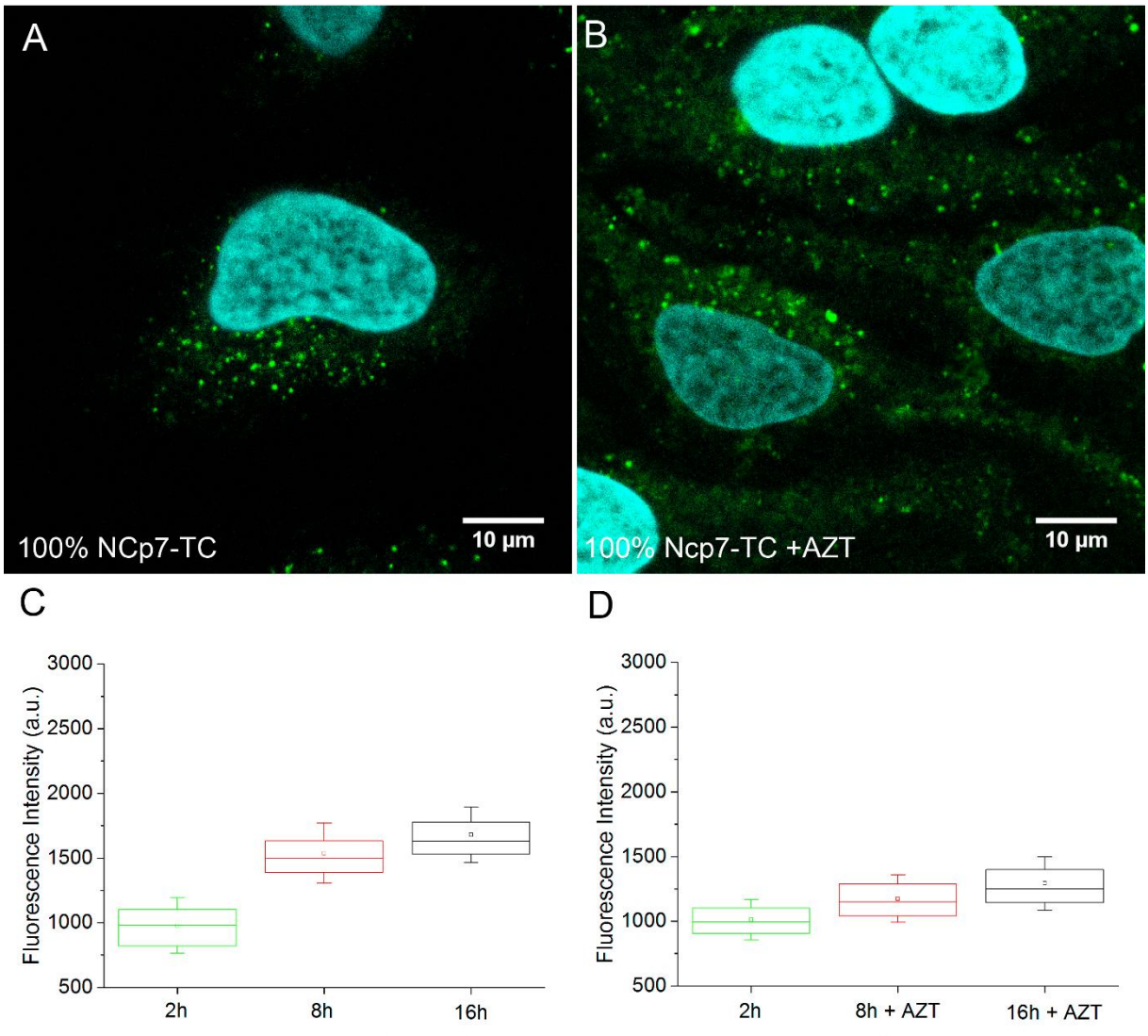

Figure 6: Effect of AZT on NCp7 release. (A,B) Confocal images of HeLa cells infected by FlAsH-labeled pseudoviruses expressing 100% NCp7-TC in the absence (A) and in the presence (B) of 1 µM AZT. (C, D) Time evolution of the mean fluorescence intensity of 1000-2000 fluorescent spots detected in 30-40 cells for each time point in the absence of AZT (C, mean fluorescence intensity values: 1000+/-150 at 2 h, 1400+/-200 at 8 h and 1700+/-200 at 16 h) and in the presence of 1 µM AZT (D, mean fluorescence intensity values: 1000+/-150 at 2 h, 1150+/-200 at 8 h and 1300+/-200 at 16 h).

5. Spatial analysis of the intensity of the FlAsH-labeled particles

In a next step, our objective was to determine if the release of NCp7 proteins occurs at a specific cellular location in the cytoplasm. To reach this aim, we analyzed the dependence of the fluorescence intensity of FlAsH-labeled pseudoviruses expressing 100% NCp7-TC at 2 and 14 h post-infection as a function of their distance to the nuclear envelope using a home-made Image J macro (Figure 7A). This macro created concentric crowns with adjustable thickness around the nucleus and provided the mean intensity of the fluorescent spots in each crown. At 2 h post infection, the intensity of the spots was found to be homogeneous all over the cytoplasm. At 16 h post infection, the fluorescence intensity of the pseudoviruses significantly increases when the particles get closer to the nucleus, suggesting that the release of NCp7 occurs mainly in the vicinity of the nucleus.

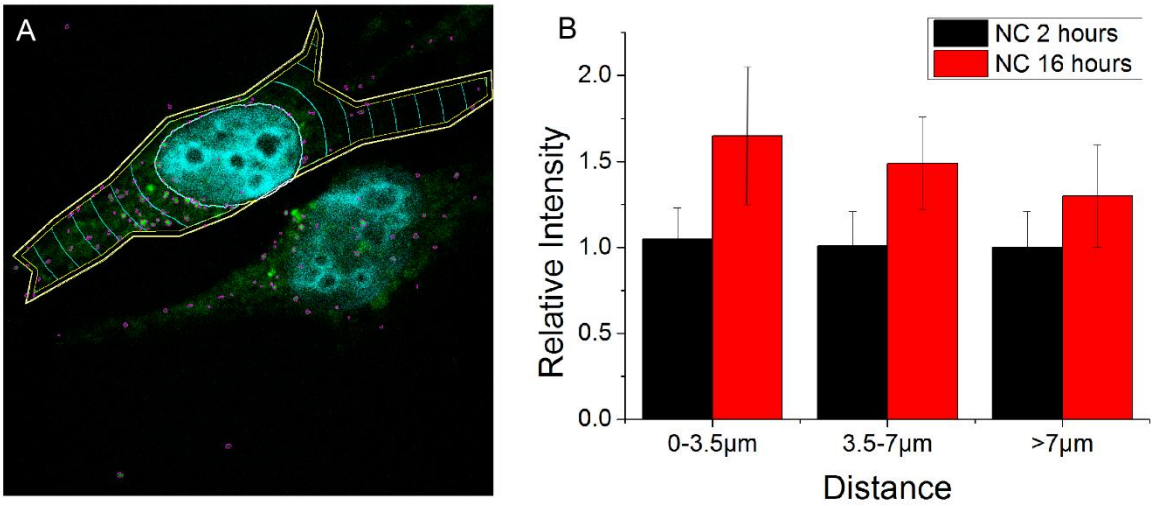

Figure 7: Spatial analysis of the pseudovirus fluorescence intensity. (A) Representative analyzed cell. A macro was used to divide the cell in concentric crowns. The distance between consecutive crowns was set to 3.5 µm. The nucleus is detected automatically through the Hoechst fluorescence. The contours of the cells are drawn manually based on the cell autofluorescence. (B) Mean intensity of the fluorescent spots detected at different distances from the nuclear envelope. The value in the regions distant by more than 7 µm from the nucleus and at 2 h post infection was taken as 100% for the normalization. The relative increase at 2 h is 1% and 5% for the regions 3.5-7 µm and 0-3.5 µm, respectively. At 16 h post-infection, the fluorescence intensity increase represents 31% in the regions >7 µm, 48% in the 3.5-7 µm region and 65% near the nucleus.

Discussion:

To investigate the intracellular fate of HIV-1 NCp7 proteins in the context of infected cells, we have produced HIV-1 pseudoviruses expressing NCp7 proteins with a small tetracystein tag fused to their C-terminus. The pseudoviruses were labeled by the fluorescein derivative FlAsH. Importantly, the pseudoviruses were still infectious, showing 40% of the infectivity of the pseudoviruses expressing non tagged NCp7 proteins, indicating that the tag is

small enough to preserve the activity of this highly conserved protein endowed with key functions all over the viral life cycle. Due to the binding of the FlAsH dyes to the TC tags, the pseudoviruses expressing NCp7-TC proteins could be perceived as clearly visible fluorescent spots of size below the diffraction limit in the cytoplasm of HeLa cells infected by these pseudoviruses.

By measuring the fluorescence intensity of the free pseudoparticles simultaneously transfected with plasmids coding for tagged and non-tagged NCp7, so that the fraction of tagged NCp7 varies from 10% to 100%, we evidenced a quenching of FlAsH fluorescence that increases with the fraction of tagged NCp7. This was not unexpected, as fluorescein-based molecules have been described to undergo self-quenching effects at millimolar concentration (Weinstein, Yoshikami et al. 1977; Chen and Knutson 1988; Walter 1988; Walter 1988; Walter 1988). This quenching results from a combination of dimerization process (only monomers being fluorescent), monomer-monomer and monomer-dimer energy transfer and collisional quenching (Chen and Knutson 1988). As this quenching is highly dependent on the local concentration of the dye, this property is used to monitor various processes such as the release of encapsulated molecules from liposomes, membrane permeation or changes in water volume in vesicles and cells (Chen, Pearce et al. 1988; Ye, Shi et al. 1989; Wang, Shi et al. 1991; Mojzisova, Bonneau et al. 2009).

By monitoring the intensity of individual FlAsH labeled pseudoviruses expressing 100% NCp7-TC in infected cells, we evidenced a significant increase in their fluorescence with time. This increase is not caused by any cellular or environmental modification since it was not observed for pseudoviruses expressing IN-TC. Moreover, this increase was abolished by AZT, a specific inhibitor of reverse transcriptase. These observations are in line with a previous established model describing a release of NCp7 molecules during the RTC to PIC conversion. Indeed, transcription of ssRNA into dsDNA is thought to cause a dissociation of an important fraction of NC molecules from the RTC complexes (Lyonnais, Gorelick et al. 2013), due to the lower affinity of NCp7 for dsDNA as compared to ssRNA (Mirambeau, Lyonnais et al. 2006; Mirambeau, Lyonnais et al. 2007; Darlix, Godet et al. 2011). Several studies highlighted the relationship between the biological role of NCp7 molecules and their density on RNA. The initial presence of a high number of NCp7 molecules on the viral RNA dimer enabling its full coating is thought to play an essential protective role inhibiting an early onset of reverse transcription (Racine, Chamontin et al. 2016). Then, when the NCp7:nucleotide ratio decreases, the protein role likely switches from genome protection to reverse transcription chaperoning (Darlix, Godet et al. 2011). In agreement with this hypothesis, our data indicate a release of

NCp7 proteins from the viral cores at 8 and 16 h post infection, where reverse transcription is thought to be mainly completed (Hulme, Perez et al. 2011; Chin, Perreira et al. 2015). In contrast, as only limited release of NCp7-TC proteins occurred in the presence of AZT, our data further validate the close relationship between reverse transcription and NCp7 release. This close relationship is further illustrated by our observation that NCp7 is released all over the cytoplasm in line with the data of Chin et al. showing that vDNA synthesized during reverse transcription was distributed through the whole cytoplasm at 8 and 12 h post infection (Chin, Perreira et al. 2015).

The release of NCp7 –TC molecules during the RTC remodeling might be also related to the uncoating process that should facilitate the dissociation of the bound NCp7 molecules as result the the dilution of the capsid content. Of course, the disassembly of the capsid will also favor the escape of the free NCp7 molecules from the viral complex. However, the timing of the capsid disassembly and its relationship to reverse transcription remains elusive. Based on the protective role of the capsid core for the viral genome in the cytoplasm (Gao, Wu et al. 2013; Lahaye, Satoh et al. 2013; Rasaiyaah, Tan et al. 2013) together with the role of the CA protein in the nuclear import of the PIC (Matreyek and Engelman 2011; Schaller, Ocwieja et al. 2011; Bichel, Price et al. 2013; Di Nunzio, Fricke et al. 2013; Matreyek, Yucel et al. 2013; Bhattacharya, Alam et al. 2014) and its presence in the nucleus (Peng, Muranyi et al. 2014; Hulme, Kelley et al. 2015), a model of "late" uncoating was suggested according to which the conical capsid core remains complete until the virus docks to the nuclear envelope (Arhel, Souquere-Besse et al. 2006; Arhel 2010). Moreover, RT and IN were reported to cooperatively stabilize the core, and RT inhibition was reported to delay uncoating (Hulme, Perez et al. 2011; Yang, Fricke et al. 2013). Therefore, the onset of reverse transcription should lead to the dissociation of RT from its core stabilizing interactions and initiate the uncoating process (Zhu, Dobard et al. 2004). Based on these observations, the latest models propose a partial remodeling of the capsid core leading to some degree of uncoating in the cytoplasm before completion of reverse transcription (Hulme, 2011; Yingxin, 2016). Moreover, part of the capsid likely remains attached to the viral complex, mediating the nuclear entry and determining the integration site in the nucleus (Campbell and Hope 2015). In our study, the analysis of the fluorescence intensity of FlAsH-labeled pseudoparticles as a function of the distance from the nucleus indicated that NCp7 release occurs all over the cytoplasm, but appears more efficient in the vicinity of the nucleus. These data are consistent with a progressive release of NCp7 molecules that accompanies the maturation of the viral complexes on their journey towards the nucleus. Moreover, as the inhibition of reverse transcription by AZT is thought to prevent the initiation of

the uncoating process, this may further explain the poor release of NCp7 molecules from the viral complexes in the presence of the drug.

In conclusion, the intracellular imaging of HeLa cells infected by VSV-pseudotyped HIV-1 viruses expressing FlAsH-labeled NCp7-TC proteins, used as a model system for mimicking the early steps of infection, showed the cytoplasmic release of NCp7 molecules from the viral complexes during their journey to the nucleus. This release increases with time and is inhibited by AZT, indicating that NCp7 molecules are released during or after vDNA synthesis. Our data further indicated that NCp7 molecules are preferentially released close to the nucleus, where the capsid disassembly should be completed. Besides giving fundamental information, the imaging approach that we developed might be used to clarify the mechanism of action of specific NCp7 inhibitors and inspire the design of new therapeutic strategies.

References

Adams, S. R., R. E. Campbell, et al. (2002). "New biarsenical ligands and tetracysteine motifs for protein labeling in vitro and in vivo: synthesis and biological applications." J Am Chem Soc **124**(21): 6063-6076.

Arhel, N. (2010). "Revisiting HIV-1 uncoating." Retrovirology **7**: 96.

Arhel, N., A. Genovesio, et al. (2006). "Quantitative four-dimensional tracking of cytoplasmic and nuclear HIV-1 complexes." Nat Methods **3**(10): 817-824.

Arhel, N. J., S. Souquere-Besse, et al. (2006). "Wild-type and central DNA flap defective HIV-1 lentiviral vector genomes: intracellular visualization at ultrastructural resolution levels." Retrovirology **3**: 38.

Bhattacharya, A., S. L. Alam, et al. (2014). "Structural basis of HIV-1 capsid recognition by PF74 and CPSF6." Proc Natl Acad Sci U S A **111**(52): 18625-18630.

Bichel, K., A. J. Price, et al. (2013). "HIV-1 capsid undergoes coupled binding and isomerization by the nuclear pore protein NUP358." Retrovirology **10**: 81.

Briggs, J. A., K. Grunewald, et al. (2006). "The mechanism of HIV-1 core assembly: insights from three-dimensional reconstructions of authentic virions." Structure **14**(1): 15-20.

Campbell, E. M. and T. J. Hope (2015). "HIV-1 capsid: the multifaceted key player in HIV-1 infection." Nat Rev Microbiol **13**(8): 471-483.

Chen, P. Y., D. Pearce, et al. (1988). "Membrane water and solute permeability determined quantitatively by self-quenching of an entrapped fluorophore." Biochemistry **27**(15): 5713-5718.

Chen, R. F. and J. R. Knutson (1988). "Mechanism of fluorescence concentration quenching of carboxyfluorescein in liposomes: energy transfer to nonfluorescent dimers." Anal Biochem **172**(1): 61-77.

Chin, C. R., J. M. Perreira, et al. (2015). "Direct Visualization of HIV-1 Replication Intermediates Shows that Capsid and CPSF6 Modulate HIV-1 Intra-nuclear Invasion and Integration." Cell Rep **13**(8): 1717-1731.

Darlix, J. L., J. Godet, et al. (2011). "Flexible nature and specific functions of the HIV-1 nucleocapsid protein." J Mol Biol **410**(4): 565-581.

Di Nunzio, F., T. Fricke, et al. (2013). "Nup153 and Nup98 bind the HIV-1 core and contribute to the early steps of HIV-1 replication." Virology **440**(1): 8-18.

Gao, D., J. Wu, et al. (2013). "Cyclic GMP-AMP synthase is an innate immune sensor of HIV and other retroviruses." Science **341**(6148): 903-906.

Griffin, B. A., S. R. Adams, et al. (1998). "Specific covalent labeling of recombinant protein molecules inside live cells." Science **281**(5374): 269-272.
Hulme, A. E., Z. Kelley, et al. (2015). "Complementary Assays Reveal a Low Level of CA Associated with Viral Complexes in the Nuclei of HIV-1-Infected Cells." J Virol **89**(10): 5350-5361.
Hulme, A. E., O. Perez, et al. (2011). "Complementary assays reveal a relationship between HIV-1 uncoating and reverse transcription." Proc Natl Acad Sci U S A **108**(24): 9975-9980.
Lahaye, X., T. Satoh, et al. (2013). "The capsids of HIV-1 and HIV-2 determine immune detection of the viral cDNA by the innate sensor cGAS in dendritic cells." Immunity **39**(6): 1132-1142.
Lelek, M., F. Di Nunzio, et al. (2012). "Superresolution imaging of HIV in infected cells with FlAsH-PALM." Proc Natl Acad Sci U S A **109**(22): 8564-8569.
Lyonnais, S., R. J. Gorelick, et al. (2013). "A protein ballet around the viral genome orchestrated by HIV-1 reverse transcriptase leads to an architectural switch: from nucleocapsid-condensed RNA to Vpr-bridged DNA." Virus Res **171**(2): 287-303.
Matreyek, K. A. and A. Engelman (2011). "The requirement for nucleoporin NUP153 during human immunodeficiency virus type 1 infection is determined by the viral capsid." J Virol **85**(15): 7818-7827.
Matreyek, K. A., S. S. Yucel, et al. (2013). "Nucleoporin NUP153 phenylalanine-glycine motifs engage a common binding pocket within the HIV-1 capsid protein to mediate lentiviral infectivity." PLoS Pathog **9**(10): e1003693.
Mirambeau, G., S. Lyonnais, et al. (2007). "HIV-1 protease and reverse transcriptase control the architecture of their nucleocapsid partner." PLoS One **2**(7): e669.
Mirambeau, G., S. Lyonnais, et al. (2006). "Transmission electron microscopy reveals an optimal HIV-1 nucleocapsid aggregation with single-stranded nucleic acids and the mature HIV-1 nucleocapsid protein." J Mol Biol **364**(3): 496-511.
Mojzisova, H., S. Bonneau, et al. (2009). "Photosensitizing properties of chlorins in solution and in membrane-mimicking systems." Photochem Photobiol Sci **8**(6): 778-787.
Peng, K., W. Muranyi, et al. (2014). "Quantitative microscopy of functional HIV post-entry complexes reveals association of replication with the viral capsid." Elife **3**: e04114.
Pereira, C. F., P. C. Ellenberg, et al. (2011). "Labeling of multiple HIV-1 proteins with the biarsenical-tetracysteine system." PLoS One **6**(2): e17016.
Racine, P. J., C. Chamontin, et al. (2016). "Requirements for nucleocapsid-mediated regulation of reverse transcription during the late steps of HIV-1 assembly." Sci Rep **6**: 27536.
Rasaiyaah, J., C. P. Tan, et al. (2013). "HIV-1 evades innate immune recognition through specific cofactor recruitment." Nature **503**(7476): 402-405.
Schaller, T., K. E. Ocwieja, et al. (2011). "HIV-1 capsid-cyclophilin interactions determine nuclear import pathway, integration targeting and replication efficiency." PLoS Pathog **7**(12): e1002439.
Schneider, C. A., W. S. Rasband, et al. (2012). "NIH Image to ImageJ: 25 years of image analysis." Nat Methods **9**(7): 671-675.
Walter, B. (1988). Ann.Phys (Leipzig) **34**: 518-533.
Walter, B. (1988). Ann.Phys (Leipzig) **34**: 502-517.
Walter, B. (1988). Ann.Phys (Leipzig) **34**: 316-326.
Wang, Y. X., L. B. Shi, et al. (1991). "Functional water channels and proton pumps are in separate populations of endocytic vesicles in toad bladder granular cells." Biochemistry **30**(11): 2888-2894.
Weinstein, J. N., S. Yoshikami, et al. (1977). "Liposome-cell interaction: transfer and intracellular release of a trapped fluorescent marker." Science **195**(4277): 489-492.
Yang, Y., T. Fricke, et al. (2013). "Inhibition of reverse transcriptase activity increases stability of the HIV-1 core." J Virol **87**(1): 683-687.
Ye, R. G., L. B. Shi, et al. (1989). "Functional colocalization of water channels and proton pumps in endosomes from kidney proximal tubule." J Gen Physiol **93**(5): 885-902.
Zhu, K., C. Dobard, et al. (2004). "Requirement for integrase during reverse transcription of human immunodeficiency virus type 1 and the effect of cysteine mutations of integrase on its interactions with reverse transcriptase." J Virol **78**(10): 5045-5055.

3.2. High resolution imaging of NCp7 in the context of pseudoviral infection

3.2.1. Introduction

The size of HIV-1 viral particles is approximately 2-fold smaller than the diffraction limit of classical photonic microscopes. Thus, in order to properly image virions, the use of high resolution (HR) microscopy techniques is a natural choice. However, these new techniques require a labeling with fluorophores presenting specific and well defined photophysical properties. The use of TC/FlAsH for HR microscopy was so far reported only once, using PALM technique (Photoactivation Localization Microscopy) (Lelek, Di Nunzio et al. 2012). This technique is based on sequential switching of the fluorophores in the on (bright) state and their precise localization before turning them back into the dark (off) state. The high resolution image is then reconstructed from the localizations of the individual fluorophores of the sample (Betzig, Patterson et al. 2006; Briggs, Grunewald et al. 2006). The requirements for a "good" fluorophore for this type of microscopy is high photostability, high quantum yield, and appropriate on/off rate (Dempsey, Vaughan et al. 2011). In general fluorescein based fluorophores are rather poor candidates and despite the published protocol for FlAsH-PALM imaging, the optimization of the experimental conditions was tedious and time consuming.

The parameters to adjust were:

- The composition of the switching buffer that contains an oxygen scavenging system and a source of primary thiols. The oxygen scavenger is typically composed of glucose, glucose oxidase and catalase that remove oxygen from the medium in order to reduce the photobleaching of the fluorophore by oxygen reactive species (ROS). Sources of primary thiols, such as β-mercaptoethanol (βME) or mercaptoethylamine (MEA) favor the switching of the fluorophore into its dark state. We have tried several compositions of the switching buffer in order to find the optimal composition.
- Mounting of the sample: the main constraint for the mounting of the sample in our case was the presence of oxygen. PALM/STORM experiments are often performed in a closed chamber in the presence of oxygen above the switching buffer. In the case of FlAsH, the photobleaching is extremely fast, so we have tried different types of chambers. We also replaced air with argon prior imaging, but finally the best way to minimize oxygen was to

use depression slides. The sample on the coverslip is fixed to the cavity filled with the switching buffer and all the air is evacuated upon the mounting.

- Power of the laser illumination: The blinking (transitions between on and off states) of the FlAsH is favored by the continuous illumination of a high-intensity laser (488 nm) combined with an activation laser (405 nm). The intensity of both lasers should be high, in the range of 50-100 mW. We tested two different microscopes (GSD system by Leica and custom made TIRF microscopy setup), both equipped with respectively 300 mW and 100 mW 488 lasers and 50-100 mW 405 nm laser to observe the blinking of FlAsH.

After a careful optimization and numerous preliminary experiments, we succeeded to set up the experimental conditions allowing the PALM/STOM imaging of FlAsH/TC labeled HIV-1 pseudoviruses.

3.2.2. PALM imaging of free HIV-1 pseudoviruses

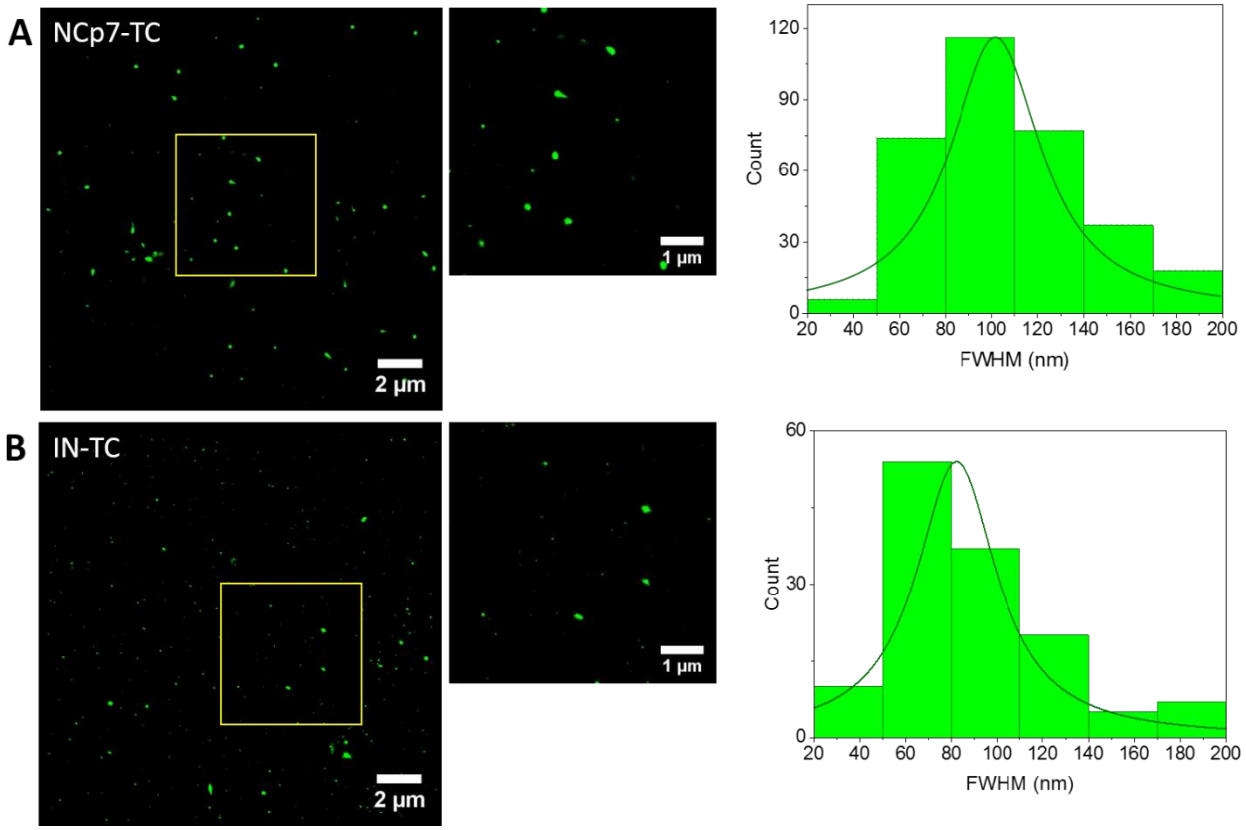

Figure 3.2.1. PALM images and size distribution of FlAsH-labeled free viral pseudoparticles expressing NCp7-TC (A) or IN-TC (B). For each type of particles, 18x18 µm PALM images and their size distributions (bin size 30 nm) fitted by the Lorentz curve are provided. Bin size 30 nm.

In order to validate our experimental approach, FlAsH-labelled pseudoviruses expressing NC-TC or IN-TC were deposited on Poly-L-lysine or fibronectin coated cover glasses, fixed and imaged with PALM microscopy. After an initial bleaching period, the FLAsH dyes started to

blink and stacks of ~10,000 images were acquired at 10 Hz frame rate. In average 500-700, photons were detected during the ON state of the fluorophore giving a localization precision of ~20 nm. The reconstructed high-resolution images, shown in figure 3.2.1 contain numerous fluorescent spots. The intensity threshold was established at a value of 8, so that only pixels with higher intensity (corresponding to localizations containing more than 8 blinks) were considered for the analysis. The intensity profiles of the spots were fitted with a Gaussian function and the FWHMs were measured in order to estimate their size. The histograms of the size distribution of 150-300 spots corresponding to FlAsH-labeled NCp7-TC of IN-TC containing HIV-1 pseudoviruses are represented in figure 3.2.1. The distributions were rather large, showing average values of 110 +/- 50 nm and 90 +/- 35 nm for NCp7 and IN, respectively. These values matched well the sizes of the viral particles reported in the literature as well as those measured by AFM and EM in this work.

TEM and AFM size measurements of free pseudoviral particles

In the previous chapter, the TC tag was shown to decrease the infectivity of the pseudoviral particles expressing 100% NC-TC by 60%. As tags and genetically fused labels can change the size of the virions, we performed AFM and TEM measurements on the NCp7-TC expressing pseudoviral particles to confirm the size data of the NCp7-TC/FlAsH PALM approach. Negative staining TEM was performed on a suspension of NCp7-TC expressing viruses fixed by 4% PFA, deposited on the grid and stained by uranyl citrate. Particles with mean size of 90 +/- 25 nm were observed on TEM micrographs (Fig. 3.2.2 A). AFM images of NCp7-TC expressing and wild type (WT) viral particles were obtained in liquid phase with 1 nm precision. Purified viral particles were resuspended in a 4 % PFA solution of PBS 1x and imaged in a drop of PBS 1x. A typical AFM image of the free virions is presented in Figure 3.2.2 C. Narrow distributions of sizes with mean values of 77 +/- 8 nm and 75 +/- 15 nm were observed for the NCp7-TC expressing and WT virions, respectively. These sizes are in the line with the previously published sizes 80-100 nm of WT particles (Parr-Brownlie, Bosch-Bouju et al. 2015), revealing that the tag does not modify the size of the particles. The dispersity of the detected sizes by the different techniques is likely related to the shrinkage and the slight deformation of the viral particles due to the fixation and additional treatments. Taken together our TEM and AFM data are in the line with the FlAsH/PALM data and previous results, revealing minimal perturbation because of the introduction of the TC tag.

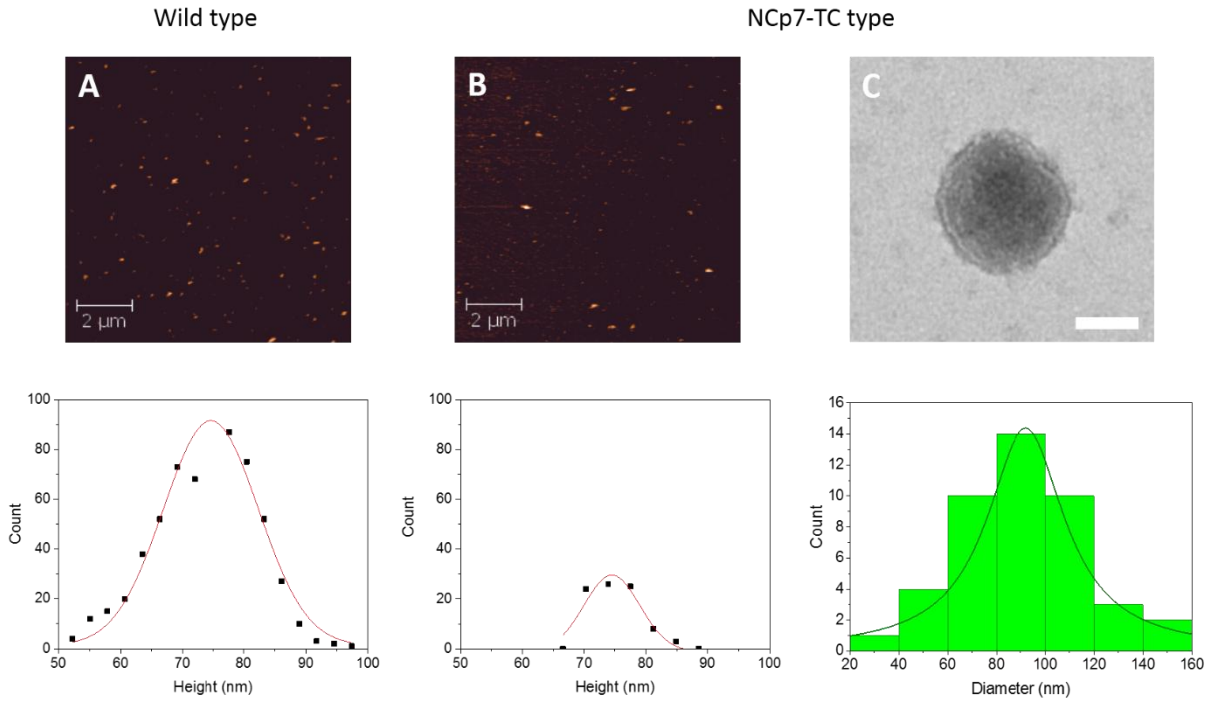

Figure 3.2.2. TEM and AFM imaging of pseudoviral particles. (A), (B) AFM images of wild type and NCp7-TC viral particles deposited on mica treated by PEI (scale bar 2 µm) and size distributions; (C) TEM micrograph of an individual NCp7-TC virion (scale bar 50 nm) and size distribution of 44 detected particles fitted by Lorentz curve.

3.2.3. PALM imaging of HIV-1 pseudoviruses in infected cells.

In a next step, we imaged the TC-containing pseudoviruses directly in infected HeLa cells. Compared to the images on the coverslips, these experiments were complicated by the high fluorescence background of the cells, accentuated by the excitation provided by the activation UV laser. The average localization precision was thus decreased to 25 nm.

3.2.3.1. Preliminary experiments of PALM imaging of TC-FlAsH pseudoviruses in HeLa cells

FlAsH/PALM imaging in cellular environment presents several complications. Firstly, due to its low photostability and brightness, the FlAsH fluorophore is not particularly adapted for long acquisition under strong illumination conditions. Secondly, in presence of the reducing buffer and activated by the UV irradiation, the cellular fluorophores may also pass in the "blinking" regime similar to FlAsH. Since the intensity of FlAsH is low as compared to "good" STORM fluorophores, a particular attention should be paid to the reconstruction and analysis. Finally, during the labeling process, the WT virus was found to contain also a small amount of FlAsH molecules nonspecifically bound to the cysteine residues present in the viral proteins. As

shown in the previous chapter, the fluorescence signal of these viruses is low when observed by "classical" microscopy, but becomes non-negligible when imaged by PALM.

In order to validate the FlAsH imaging of HIV-1 pseudoviruses in infected cells, a series of preliminary experiments was performed. Figure 3.2.3A shows epifluorescence images of non-infected HeLa cells as well as images of HeLa cells infected by WT particles and particles expressing NC-TC. Similarly, to our confocal observations, few autofluorescent spots are visible in the cytoplasm of non-infected cells. Several low intensity fluorescent spots are visible in cells infected with the WT virus while cells infected with NC-TC-containing viruses contain numerous strongly fluorescent particles in the cytoplasm. During PALM imaging in all three conditions, the initial bleaching phase was followed by an equilibrium state in which the individual fluorophores switched between their bright and dark states, but their time profiles were significantly different. In non-infected cells, the blinking was present in all cells leading to a low diffuse signal in the reconstructed images. A typical time trace of the fluorescence intensity measured in the location highlighted in the image, corresponding to one of the autofluorescent spots is presented in figure 3B. Only three strong peaks (intensity above 1500) are present showing that the autofluorescent molecules most probably, NADPH, or FAD along with flavins and flavoproteins, and tryptophan (Aubin, 1979) are not sufficiently activated to create high-resolution images of the cellular vesicles. In the cells containing the WT virus, the blinking was more pronounced, because of the presence of FlAsH. However, as shown on the intensity time trace figure 3.2.3B, the blinking was significantly attenuated after 5000 frames and the reconstructed high resolution histograms contained only few spots (average size of 95 +/- 27 nm) with an amplitude above 10 blinks (Fig. 4.2.4. A). On the contrary, in cells infected with TC-containing viruses, the blinking persisted to up to 10000 frames (time trace in figure 3.2.3 B) and numerous spots (with size of 105 +/- 22 nm) were reconstructed in the HR images (Fig. 3.2.4B). The average amplitude of the Gaussian fit of the spot intensity profile (25+/- 13) blinks thus significantly more than the WT one (Fig. 3.2.4B). Taken together these preliminary experiments enabled us to validate the protocol of the PALM imaging of TC/FlAsH labeled viral proteins in the cellular context. In the next steps, we investigated the cellular distribution of these viral models with time in physiological conditions and in conditions of reverse transcription inhibition on order to give insight on the fate of NCp7 during the early steps of the HIV-1 infection.

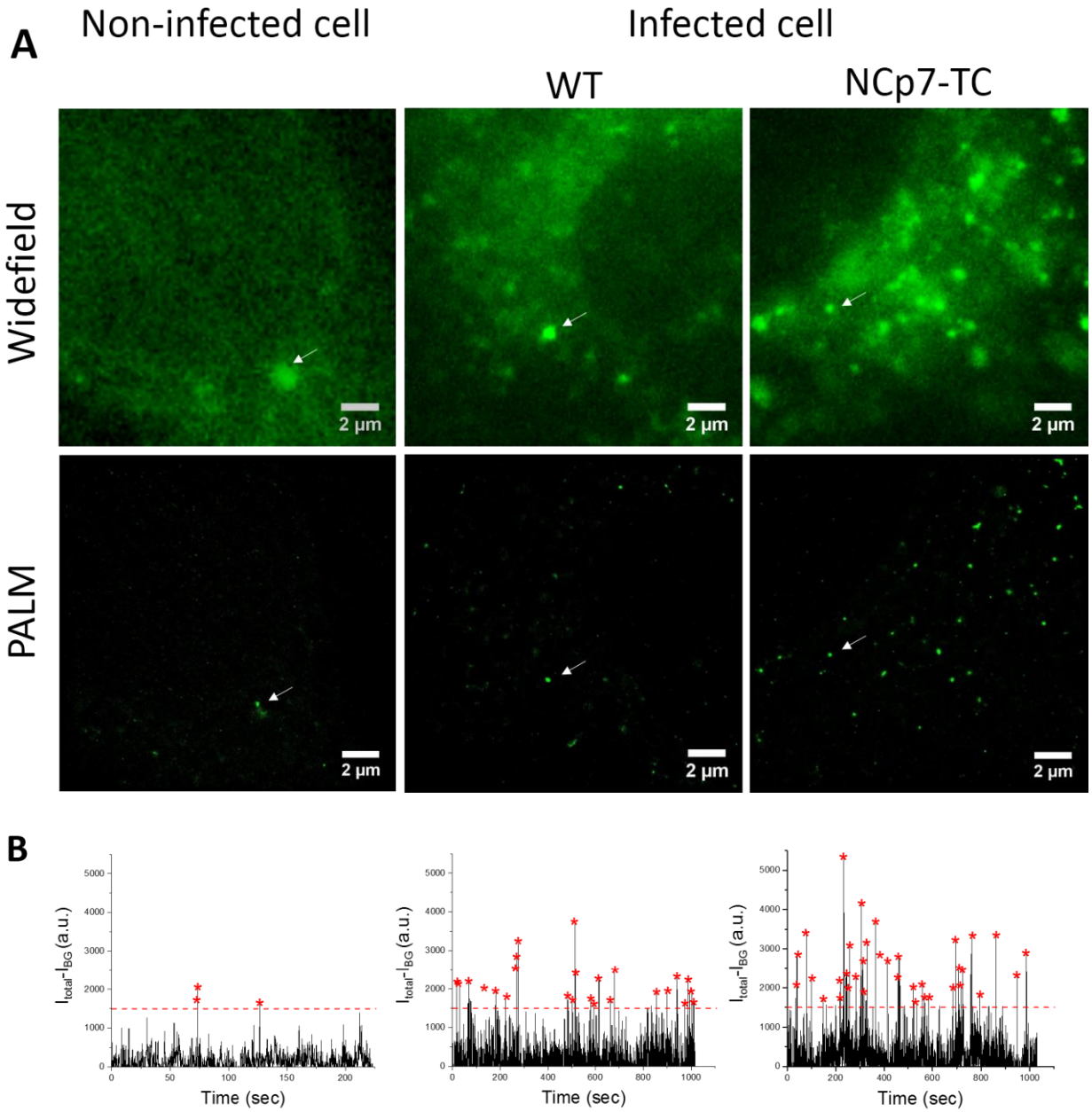

Figure 3.2.3. PALM imaging of non-infected cells and of cells infected by labeled WT and NC-TC containing pseudoviral particles. Widefield and PALM images of non-infected and infected cells (A) revealed autofluorescent, non-specific and specific fluorescent puncta (B) Time-traces of the fluorescent puncta (white arrows) where the peaks of intensity > 1500 (with already subtracted background) represent the effective blinking events (red asterisks).

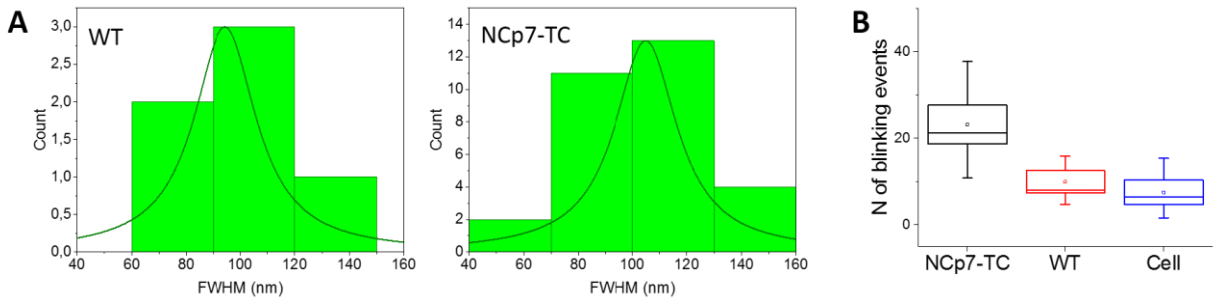

Figure 3.2.4. Size and intensity analysis of the pseudoparticles detected by PALM. (A) Size distributions of WT and NC-TC expressing particles fitted by the Lorentz function. (B) Box chart resuming the distribution of the amplitude of the Gaussian fitting the fluorescent spots in the reconstructed histograms. Box chart representing the 5-95% of data (whisker), with the standard deviation (box), the mean (square) and median (line) values.

3.2.3.2. Intracellular distribution of NCp7 during the early stage of infection

Next, the FlAsH-labeled NCp7-TC and IN-TC pseudoviruses were imaged in infected cells at 8 h post infection. To this end, HeLa cells were incubated in PBS containing FlAsH labelled pseudoviruses for 2 h, then the cells were washed twice with PBS and incubated in complete medium during additional 6 h, fixed in 4% PFA and imaged. According to the literature and our previous experiments, after 6-8 h of infection, the RT and uncoating processes should be completed (at least in a part of viruses) and some viral cores should reach the nucleus. In all experiments, the IN-TC viruses were used as a control since IN is known to stay in the viral complex from the cellular entry until the integration step.

HR images of HeLa cells infected by NCp7-TC/FlAsH and IN-TC/FlAsH containing pseudoviruses are show in figure 3.2.5 A and B, respectively. Their average size in the cytoplasm is 110 +/- 40 nm and 110 +/- 40 nm for NCp7-TC and IN-TC containing complexes, respectively. These values are slightly bigger than the size of the isolated particles. This can be related to the experimental conditions (higher fluorescent background causing lower localization precision compared to the imaging of viral particles on a coverslip), or also to the remodeling of the viral complex in the cytoplasm. Similar size increase upon cellular entry has been described for particles immunolabelled on matrix or capsid proteins (Pereira, Rossy et al. 2012). On the contrary, Lelek et al. observed a cytoplasmic decrease in the size of IN-TC containing complexes. (Lelek, Di Nunzio et al. 2012). In all cases, the size distribution of the cytoplasmic complexes was found to be quite disperse, likely as a result of the different remodeling states of individual particles. Therefore the precision of the measurements is questionable and does not provide clear conclusions.

Both types of pseudoviruses were also found inside the nucleus of infected cells. In agreement with the results of Lelek et al., the size of the IN-TC/FlAsH containing complexes inside the nucleus was found to be 50 +/- 10 nm. Similar sizes were found with NCp7-TC/FlAsH pseudoviruses, but with a somewhat wider distribution. This drastic decrease in size of the viral complexes upon their nuclear entry evidences their reorganization in order to facilitate their passage through the nuclear pore. This is the first evidence of the intranuclear presence of NCp7 in the viral complexes. This finding supports the importance of the biological role of NCp7 during the nuclear steps of the viral lifecycle and notably, its potential role in the integration process (Carteau, Batson et al. 1997; Gao, Gorelick et al. 2003; Poljak, Batson et al. 2003; Thomas, Gagliardi et al. 2006).

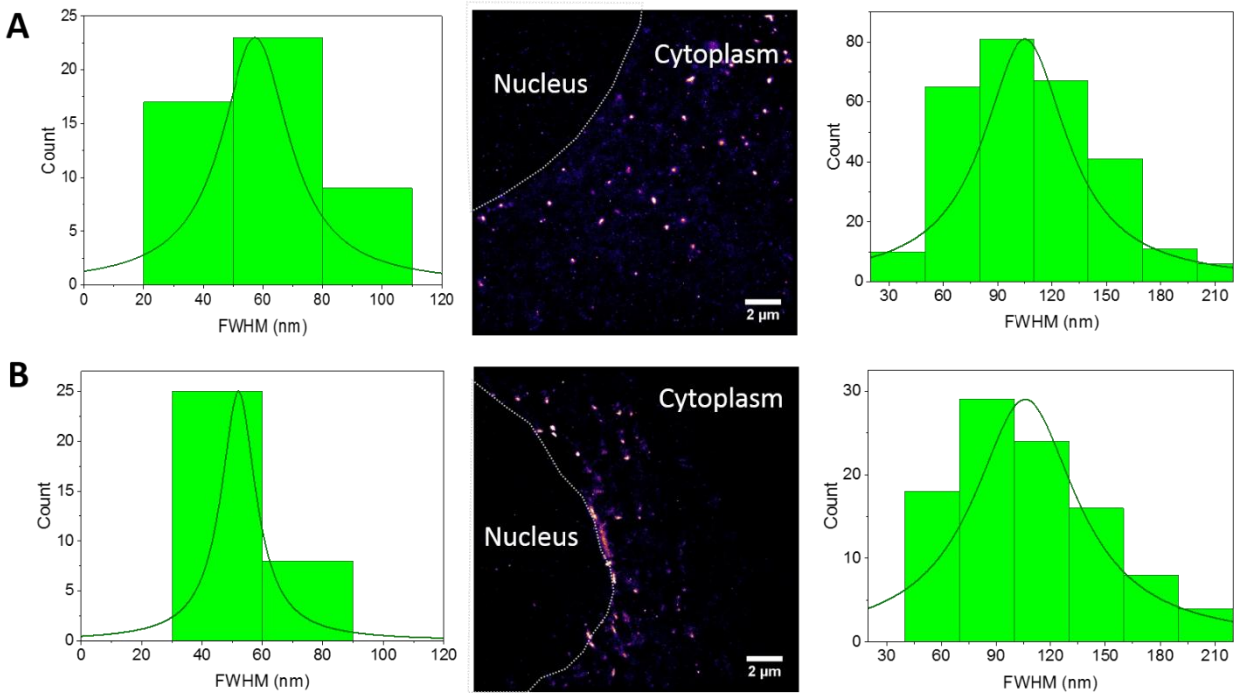

Figure 3.2.5. PALM imaging of FlAsH-labeled NCp7-TC and IN-TC containing complexes in infected cells. HR image of 18x18 µm ROIs in HeLa cells infected by the FlAsH-labeled pseudoviral particles expressing NCp7-TC (A) and IN-TC (B). Colors in the image represent the intensity distribution of pixels from low (dark purple) to high (white). Size distributions inside the nucleus (left graphs) and cytoplasm (right graphs) are fitted by a Lorentz function. Bin size 30 nm.

3.2.3.3. Effect of the labeling density

In the previous chapter, we observed the dequenching of FlAsH when decreasing the NCp7-TC fraction in the labeled pseudoviruses. Herein, we used these partially labeled viral particles for HR imaging. HeLa cells were infected with FlAsH-labelled pseudoviruses containing either 100% or 10% of TC-tagged NCp7 proteins for 2 h. Then, the viral particles were removed and the cells were washed twice with PBS, before being incubated in complete

medium during additional 6 h. After fixation, the samples were imaged by PALM under oblique illumination. HR images obtained after reconstruction are shown in figure 3.2.6. In both cases, 10% NCp7-TC and 100% NCp7-TC, the fluorescent spots corresponding to the viral particles are present in the cytoplasm and in the nucleus of infected cells.

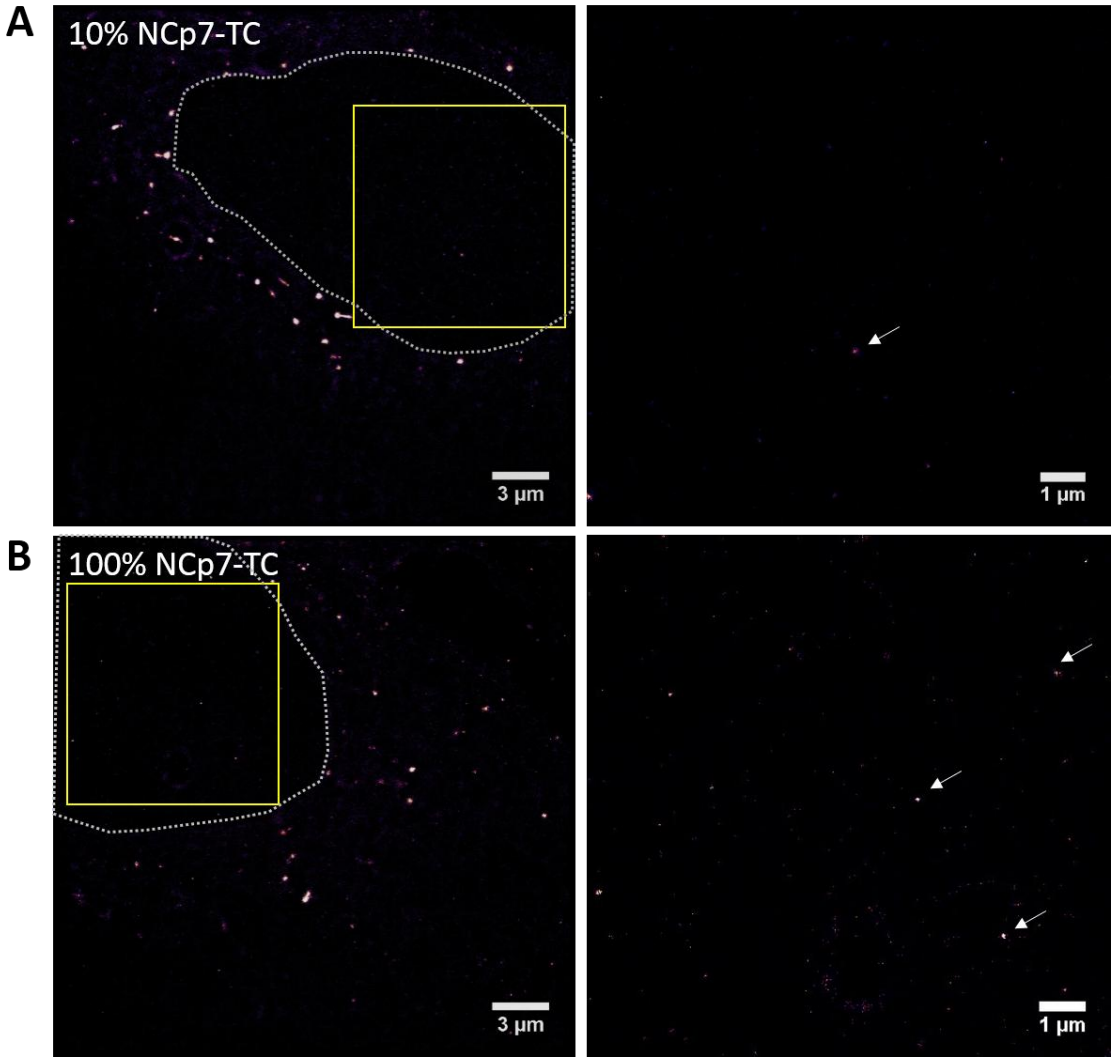

Figure 3.2.6. PALM images of HeLa cells infected with FlAsH-labeled pseudoviruses containing 10% and 100% NCp7-TC. In both conditions, the fluorescent spots corresponding to the viral complexes are present in the cytoplasm and in the nucleus (arrows) of the infected cells. Dotted line indicates the nucleus area.

Analysis of the size distribution of 300 intracellular spots in 10 different cells for each condition did not show any significant difference in the cytoplasmic populations. In agreement with previous observations, the average size of the complexes was 125+/-25 nm and 130 +/- 30 nm for 10% and 100% NCp7-TC, respectively (Fig. 3.2.7).

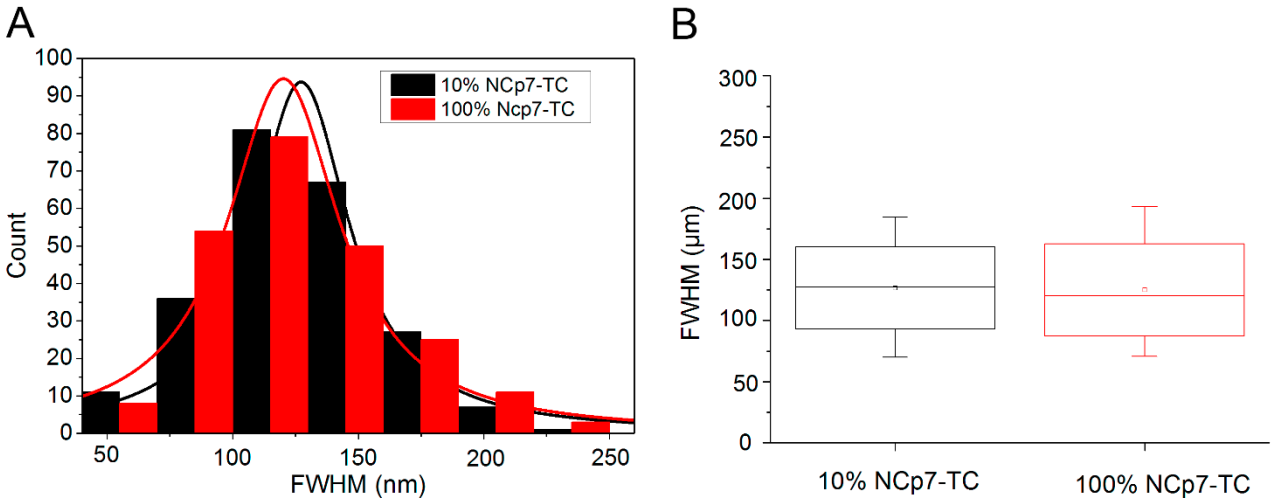

Figure 4.2.7. **Sizes of the cytoplasmic NCp7 clusters.** (A) Size distribution of detected particles fitted by Lorentz. (B) Box chart representing the 5-95% of data (whisker) with the standard deviation (box); the mean (square) and median (line) values.

On the contrary, significant differences were observed in the nuclear compartment. Globally, the density of detected nuclear clusters is lower in the case of infection with 10% labeled viruses compared to 100% NCp7-TC (Fig. 3.2.8A). Moreover, as shown in figure 3.2.8B, the size of the nuclear clusters is somewhat lower (mean value 60 +/-15 nm) for viruses containing 10% of labeled protein compared to 100% labeling (mean value 70 +/- 20 nm). If we consider that an important fraction of NCp7 molecules is released from the RTC before or during its transformation to PIC, it is conceivable that at the lower labeling density, the main part of the fluorescently labeled NCp7 is released in the cytoplasm and the nuclear complexes that contain few or no labeled proteins are detected with a smaller size or non-detected at all. Therefore these observations are fully in agreement with the hypothesis of the release of a part of NCp7 molecules before entering the nucleus.

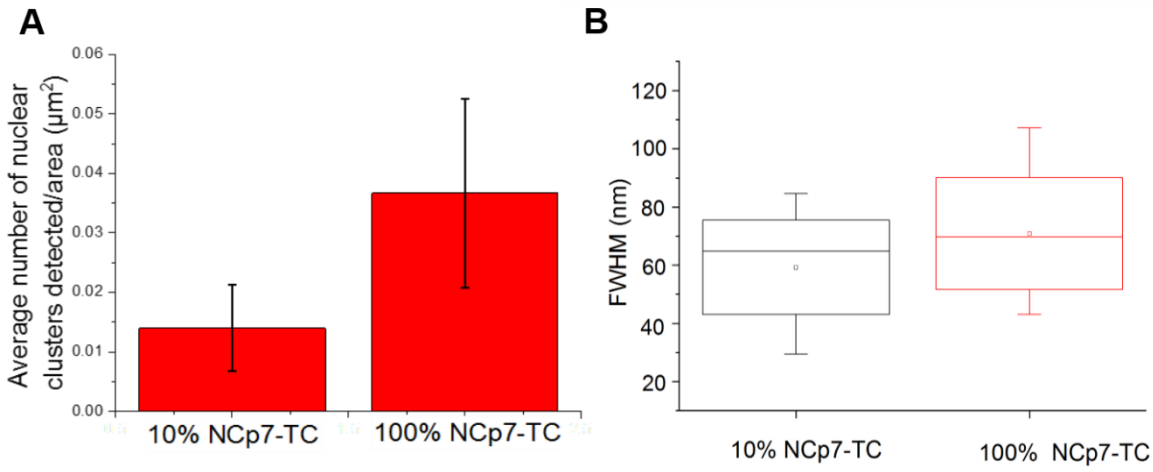

Figure 3.2.8. **FlAsH-labeled NCp7-TC containing clusters detected in the nucleus.** (A) Average number of nuclear NCp7-TC clusters (per nucleus area) and (B) box chart of size distribution: 5-95% of data (whisker), with the standard deviation (box); the mean (square) and median (line) values.

Taken together, the HR imaging of cells infected with HIV-1 pseudoviruses containing 10% and 100% of FlAsH labeled NCp7-TC protein, and notably the analysis of the nuclear NCp7-TC clusters are in line with our previous observations indicating a cytoplasmic release of this protein prior to the nuclear internalization step.

3.2.3.4. Distribution of the pseudoviruses during the time course of the infection

Distribution of the NCp7-TC containing particles during the time course of the infection

In a next step, we have analyzed by PALM the intracellular distribution of NCp7-TC containing particles with time. For this purpose, HeLa cells were infected during 2 h and either fixed or incubated during additional 14 h in the presence of virus free medium. Figure 3.2.9 shows typical images of the infected cells after 2 and 14 h of infection.

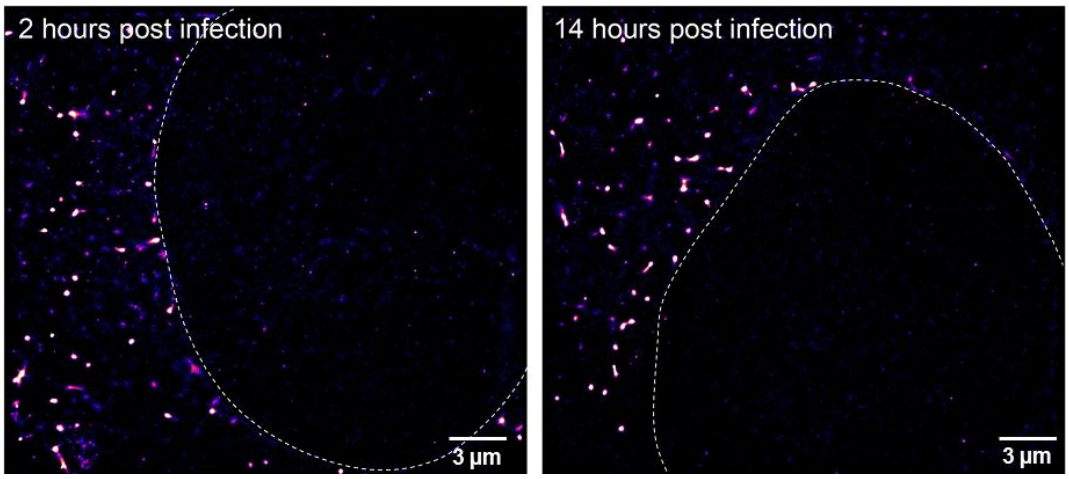

Figure 3.2.9. PALM images of HeLa cells infected with pseudoviruses expressing 100% NCp7-TC labelled with FlAsH after 2 and 14 h of infection. 25x25 µm HR images of infected cells were reconstructed from ~10,000 frames. Pixel size 20 nm.

As shown in figure 3.2.9, intense fluorescent spots corresponding to FlAsH-labeled NCp7 molecules in RTC are present in the cytoplasm of the infected cells. In agreement with previous observations, the approximate size of the NCp7-containing complexes is 100-120 nm (Fig. 3.2.10). The analysis of the size distribution of 500 cytoplasmic spots revealed that the size slightly decreases after 14 h of infection. This decrease might reflect the remodeling of the viral cores in the cytoplasm related to the RT and uncoating processes.

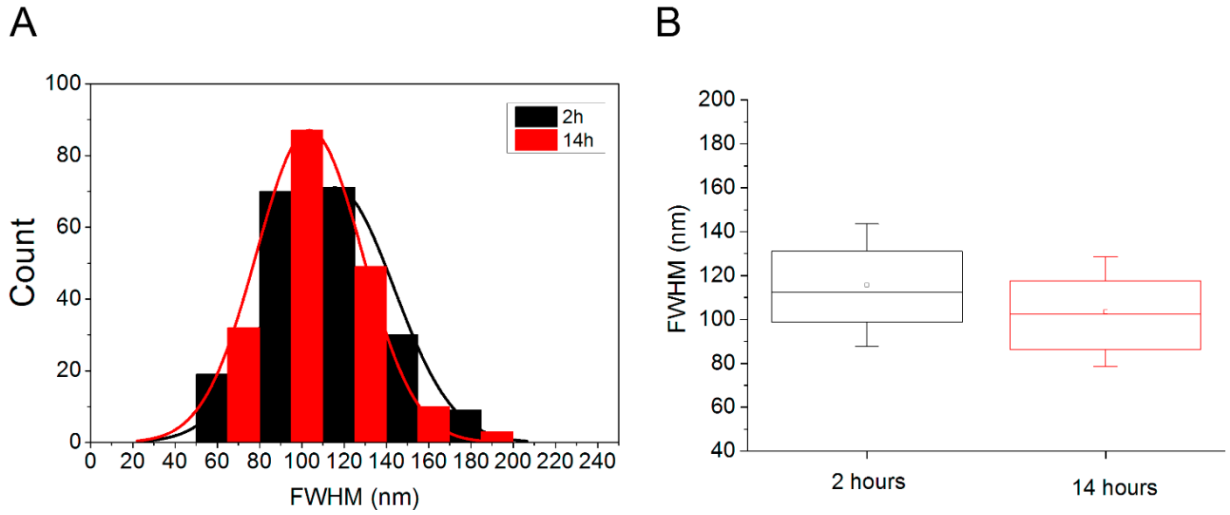

Figure 3.2.10. Size distribution of the FlAsH-labeled NCp7-TC containing pseudoparticles in the cytoplasm of infected HeLa cells in the time course of infection. (A) Histogram and (B) box chart of sizes of viral particles detected in the cytoplasm of 20 different cells. Mean value for 2 h is 115 +/- 25 nm and 100 +/- 20 nm at 14 h post infection. Comparison of the size distribution at 2 and 14 h by the chi square test: p = 0,00011 revealed significant differences between the two times.

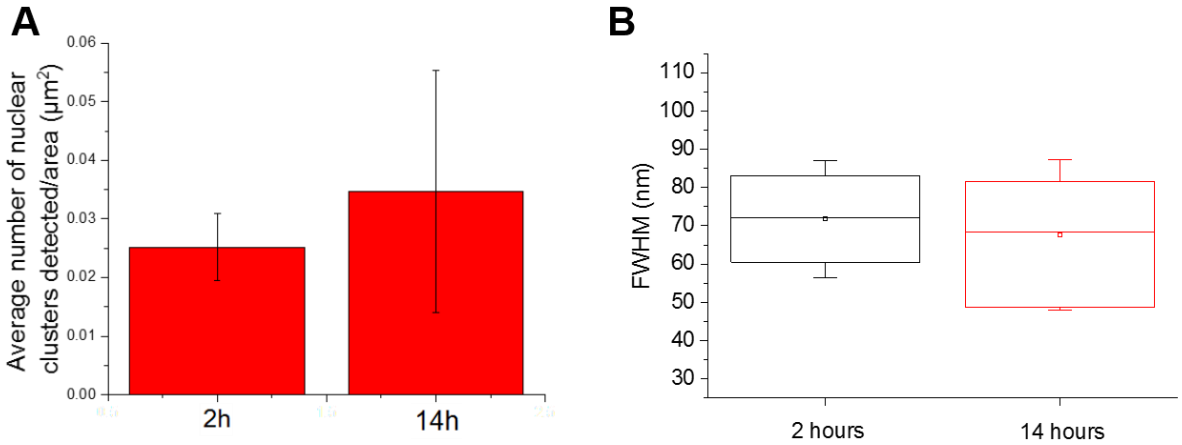

Figure 4.2.11. FlAsH-labeled NCp7-TC containing clusters detected in the nucleus at 2 and 14 hs of infection. (A) Average density of detected particles and (B) box chart representation of the size distribution. Mean value is 72 +/- 10 nm and 70 +/- 20 nm at 2 and 14 h post infection, respectively.

Interestingly, already at 2 h post infection the first viral particles have reached the perinuclear space and a few NCp7-TC containing clusters are present in the nucleus. The density of intranuclear clusters does not significantly change at 14 h (Fig. 3.2.11A). The mean size of the nuclear NCp7-TC/FlAsH clusters is approximately 70 nm and stays constant with time (Fig. 3.2.11B). This observation is in agreement with the results of Lelek et al. who observed similar nuclear FlAsH-labeled IN-TC containing clusters in the nucleus of infected HeLa cells.

Distribution of the FlAsH-labeled Integrase-TC expressing pseudoparticles during the time course of the infection

The time course of infection was also studied using the IN-TC expressing pseudoviruses. In agreement with previous observations, the IN-TC-containing viral complexes are distributed in the cytoplasm and in the nucleus of infected cells as shown in figure 3.2.12.

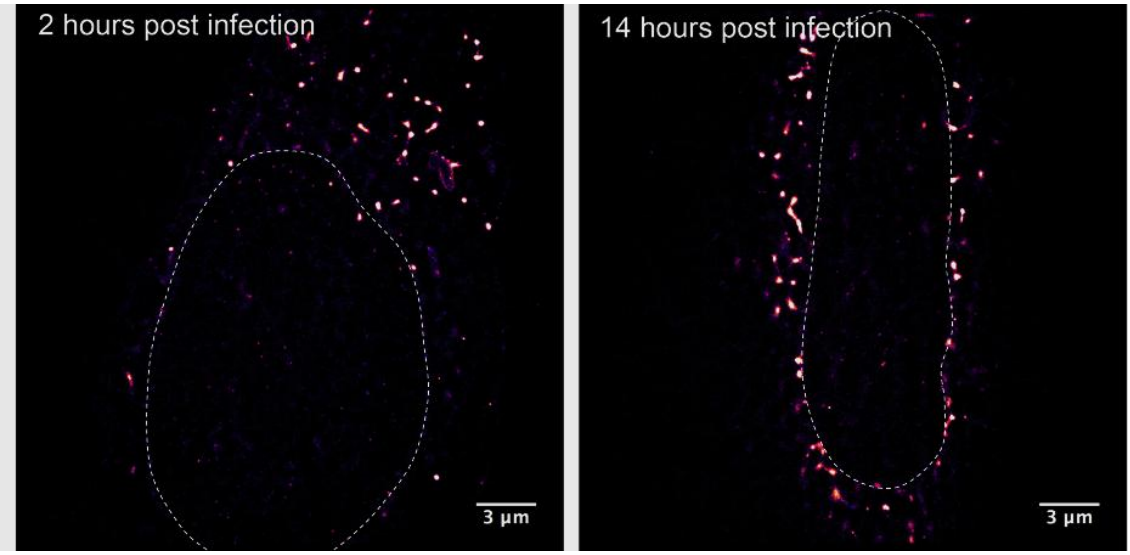

Figure 3.2.12. High resolution images of HeLa cells infected with IN-TC pseudoviruses labeled with FlAsH. 25x25 µm ROIs of 4% PFA fixed cell imaged on TIRF setup. Dotted line indicates the nucleus area.

At 2 h post infection the particles are distributed homogeneously in the cytoplasm. At 14 h, they become more concentrated around the nucleus, with numerous clusters docked at the nuclear envelope. The size distribution shown in figure 3.2.13 shows no decrease with the time of infection for the IN-TC-containing complexes.

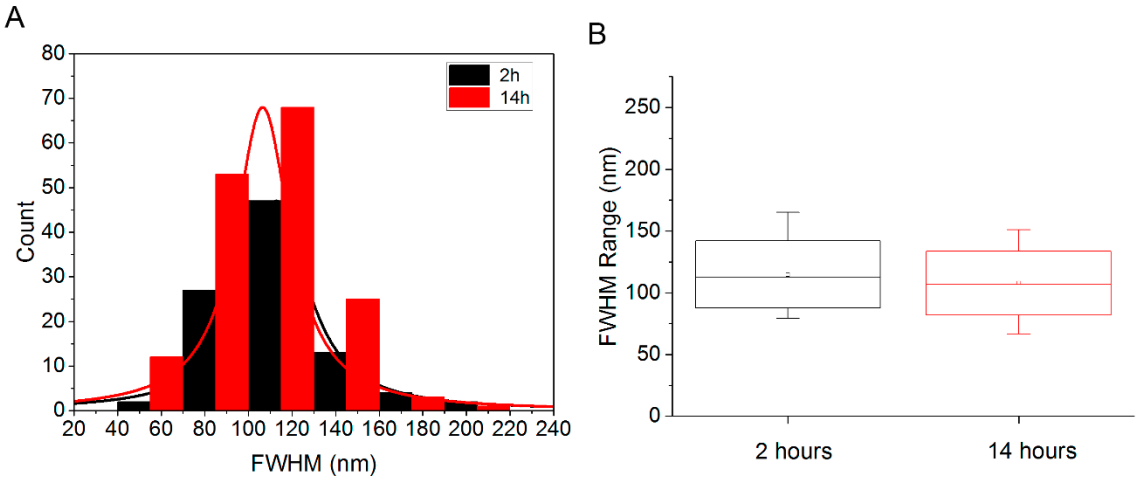

Figure 3.2.13. Sizes of IN-TC/FlAsh viral particles in the cytoplasm. (A) Histogram and (B) box chart of the size distribution with mean value for 2 h is 115 +/- 25nm and 110 +/- 25 nm at 14 h post infection. Comparison of the size distribution at 2 and 14 h by chi square test: p=0,058, do not show a difference between two populations.

Intranuclear spots are present after 2 h of infection (Fig. 3.2.14). Their size is comparable to the size of NCp7-TC containing viral complexes and corresponds also to the sizes reported by Lelek (Lelek, 2012). Interestingly at 14 h, the nuclear complexes are less frequent and are bigger (Fig. 3.2.14), probably due to the dissociation of the viral complexes after the integration of the DNA into the host cell genome. Alternatively, if we suppose that the integration is relatively fast and the lifetime of the nuclear viral complexes is short it is possible that the bigger nuclear spots that we observe correspond to the defective integration sites.

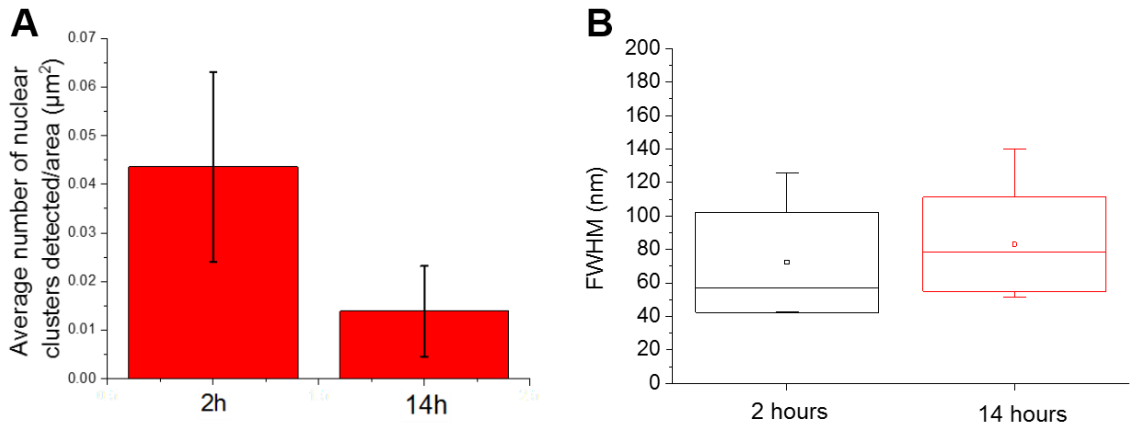

Figure 3.2.14. FlAsH-labeled IN-TC containing complexes detected in the nucleus for 2 and 14 h of infection. (A) Average density of detected particles and (B) box chart of the size distribution with mean value for 2 h is 70+/- 20 nm and 85 +/- 25 nm at 14 h post infection.

Comparison of the cellular distribution of NCp7-TC and IN-TC containing pseudoviruses revealed that already after 2 h of infection both types of particles are present in the nucleus. This indicates that the early steps of infection are relatively fast and that 2 h are sufficient for the first viruses to escape from the endosomes, synthetize the viral DNA, to be uncoated and enter into the nucleus. The size of the nuclear clusters is comparable for both types of viruses. Similarly, at 14 h post infection the signal from the nuclear compartment is weaker and the average number of nuclear clusters decreases, which might be related to the dissociation of the viral complexes once the integration is achieved.

In the cytoplasm, the complexes of TC-labeled viral proteins showed a diffuse localization at 2 h post infection. They become more concentrated in the perinuclear area at 14 h. The RTCs containing FlAsH labelled NCp7-TC showed a slight size decrease with time. We hypothesized that this decrease might be related to the remodeling of the viral complexes during the reverse transcription and in the case of NCp7 also to its partial release. In order to confirm this assumption, we analyzed the effect of the inhibition of reverse transcription on the time evolution of TC-labeled pseudoviruses.

3.2.3.5. Effect of RT inhibition on the cellular distribution of pseudoviruses

Effect of RT inhibition on the cellular distribution of NCp7-TC-containing complexes

In the next step we studied the effect of the inhibition of RT on the cellular distribution of the NCp7-TC and IN-TC in the HeLa cells. The cells were infected during 2 h then washed twice and incubated during additional 14 h in complete medium containing 1 μM AZT a specific inhibitor of RTase. After fixation by 4% PFA, the cells were imaged by PALM. Typical images of the intracellular distribution of NCp7-TC at 2, and 14 h post infection and 14 h infection in presence of AZT are shown in figure 3.2.15.

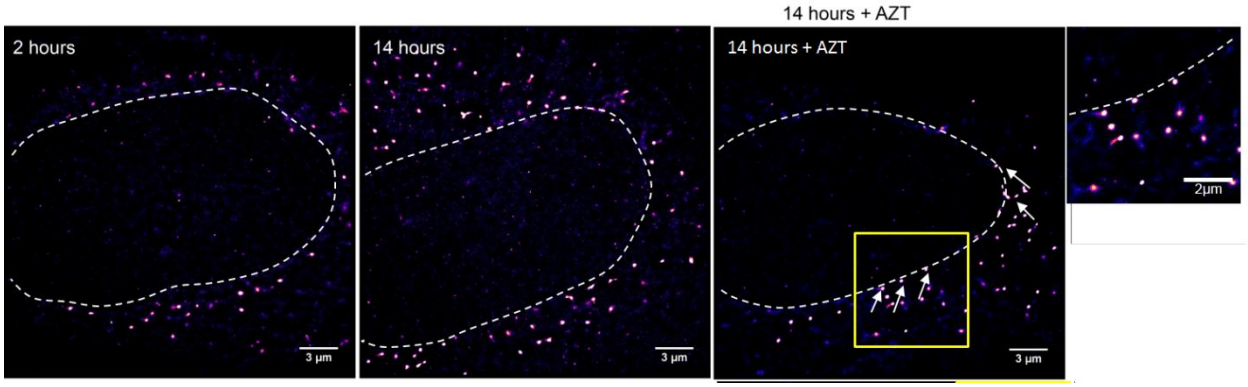

Figure 3.2.15. Influence of RT inhibitor on intracellular distribution of NCp7-TC. 25x25 μm HR images of the HeLa cells infected by pseudoviral particles containing 100% of NCp7-TC/FlAsH during 2 and 14 hours in presence or in absence of AZT. IN-TC/FlAsH clusters (white arrows) revealed significant perinuclear localization (zoomed region) after 14h of infection in the presence of the AZT.

NCp7-TC clusters were again observed in the cytoplasm and the nucleus of the infected cells. The size distribution of the cytoplasmic complexes in Fig 3.2.15 was 115+/- 30 nm and 105+/- 25 nm at 2 h and 14 h post infection, respectively. In the case of inhibition of RT by AZT, the size was 110+- 30 nm (Fig. 3.2.16). Interestingly, numerous NCp7-TC clusters are present at the nuclear envelope (Fig. 3.2.15, zoomed region) showing that the cytoplasmic transport is not perturbed and the RTCs reach the perinuclear space independently of RT progression.

However, in the presence of AZT, the nuclear NCp7-TC spots were detected only in 40% of the imaged cells indicating that the translocation though the nuclear pore is limited in the absence of RTC to PIC transformation. These observations indicate that the inhibition of the RT clearly perturbs the viral lifecycle and the non-transcribed RNA does not enter the nucleus, even if some exceptions were observed (in these cells the nuclear density of the NCp7-TC/FlAsH clusters and their size were not significantly different from the control samples, see figure 3.2.17). The nuclear signal might arise from the PICs that escaped RT inhibition and

accomplished the DNA synthesis during the first 2 h of infection before addition of AZT, or alternatively, from RTCs that succeeded to enter the nucleus in spite of the RT inhibition. In order to confirm these results it is necessary to deepen this study by analyzing a larger number of infected cells, modifying the time of infection and/or the RT inhibitor.

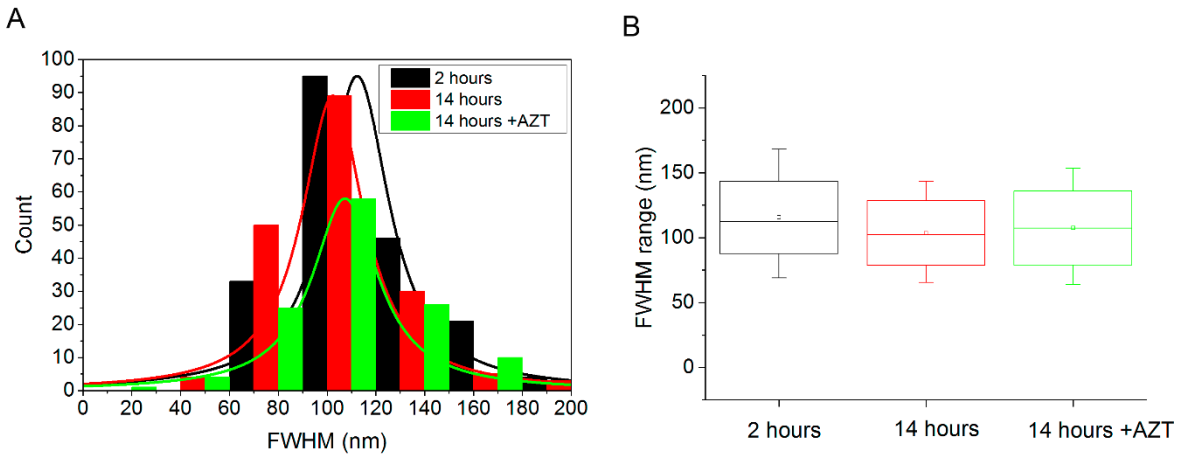

Figure 3.2.16. Histogram and box chart of the size distribution of NCp7-TC containing viral particles in the cytoplasm. Mean value is 115 +/- 30 nm at 2 h p.i. and 105 +/- 25 nm at 14 h p. i. and 110+-/30 nm 14 h p.i. in the presence of AZT. Comparison of the size distribution at 2 h and 14 h by chi square test: p=0,0023. Difference of size populations for 2 h and 14 h in the presence of AZT is not significant.

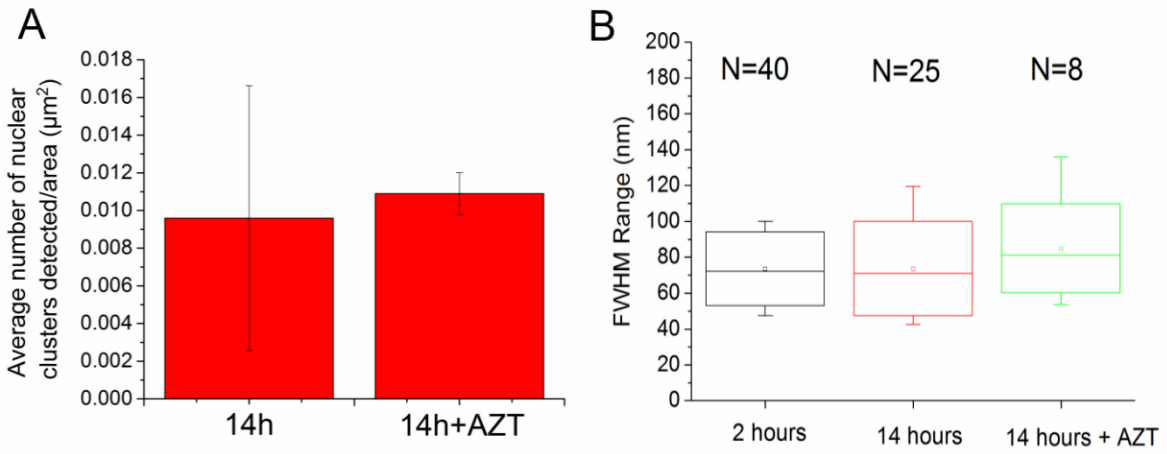

Figure 3.2.17. Nuclear localization of NCp7-TC-containing complexes in the presence of AZT. (A) Density of the detected clusters in the presence of 1 mM AZT after 14 h of infection. (B) Box chart representation of the size distribution of nuclear NCp7-TC containing particles detected in 7 cells with a mean value for 2 h is 70+/- 20 nm, 80 +/- 25 nm at 14 h p. i. and 85+/-25 for 14 h p.i. in presence of AZT.

Effect of RT inhibition on the cellular distribution of Integrase-TC

The effects of RT inhibition were then observed in the same experimental conditions in HeLa cells infected with IN-TC/FlAsH containing pseudoviruses. The PALM images of the cells infected during 2 h, 14 h and 14 h in the presence of AZT are shown in figure 4.2.18. The IN-TC containing complexes are distributed in the cytoplasm and in the nucleus of infected cells. Inhibition of RT caused a decrease of the nuclear internalization, and the accumulation of IN-TC containing clusters at the nuclear membrane (Fig. 3.2.18 C).

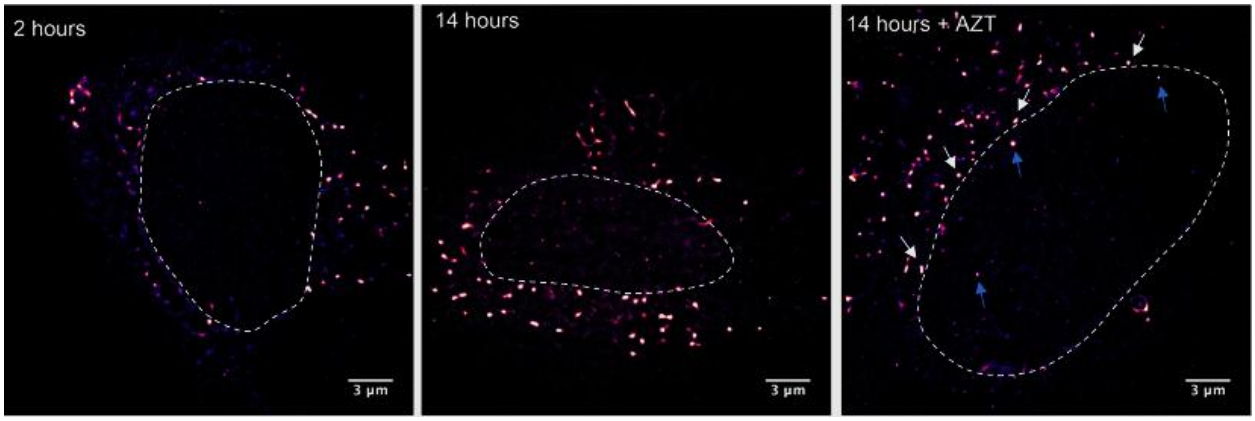

Figure 3.2.18. Influence of RT inhibition on the intracellular distribution of IN-TC containing clusters. 25x25 µm PALM images of HeLa cells infected by 100% IN-TC/FlAsH containing pseudoviruses during 2 and 14 h in presence or in absence of AZT. Additionally to the perinuclear accumulation (white arrows) also observed for the NCp7-TC containing clusters, IN-TC clusters were found in the nuclear region (blue arrows).

The average size of the cytoplasmic clusters corresponds to previous observations (Fig. 3.2.19). By comparing the average values, the average cluster diameter does not seem to vary significantly with time and in the presence of AZT. However, the sizes need to be evaluated more accurately to get a more solid conclusion.

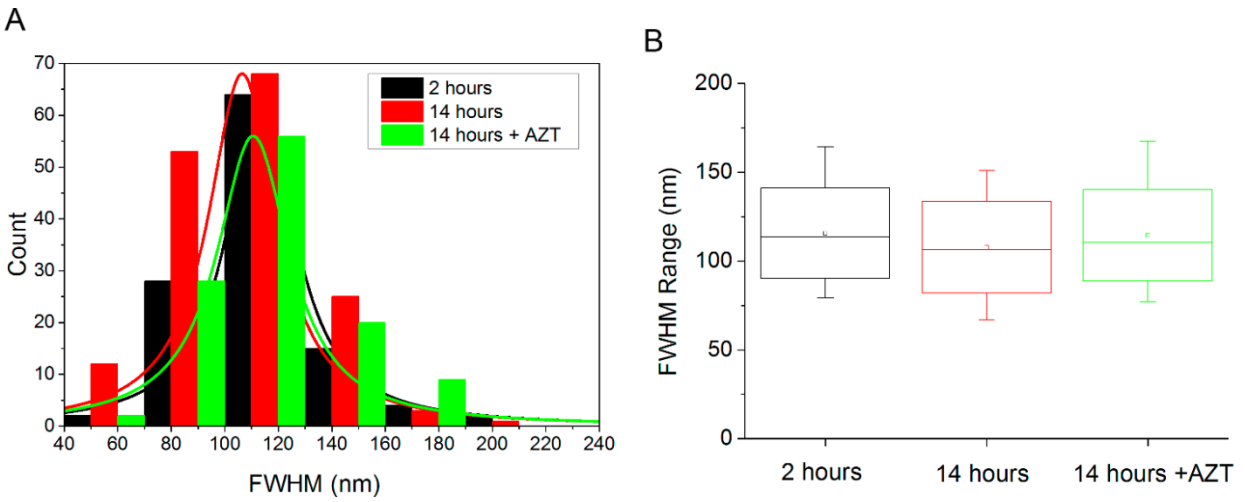

Figure 3.2.19. Histogram (A) and the box chart (B) of the size distribution of IN-TC/FlAsh viral particles in the cytoplasm. Mean value for 2 hours is 115+/-25 nm, 107+/-23 nm at 14 hours post infection and 114+/-25 14 hours p.i. in presence of AZT. Comparison of the size distribution at 2 and 14 hours by chi square test: p=0,046.

As in the case of NCp7-TC containing clusters, the inhibition of RT causes an important decrease of number of nuclear IN-TC complexes with the appearance of some clusters in the nuclear space (Fig. 3.2.20). The mean value increased from 85 +/- 25 nm to 135+/-35 nm and the measured values are highly dispersed as shown by the whisker size. These observations reinforce the hypothesis presented for NCp7-TC containing clusters that aberrant RTCs might enter the nucleus but are not able to properly create an integration site.

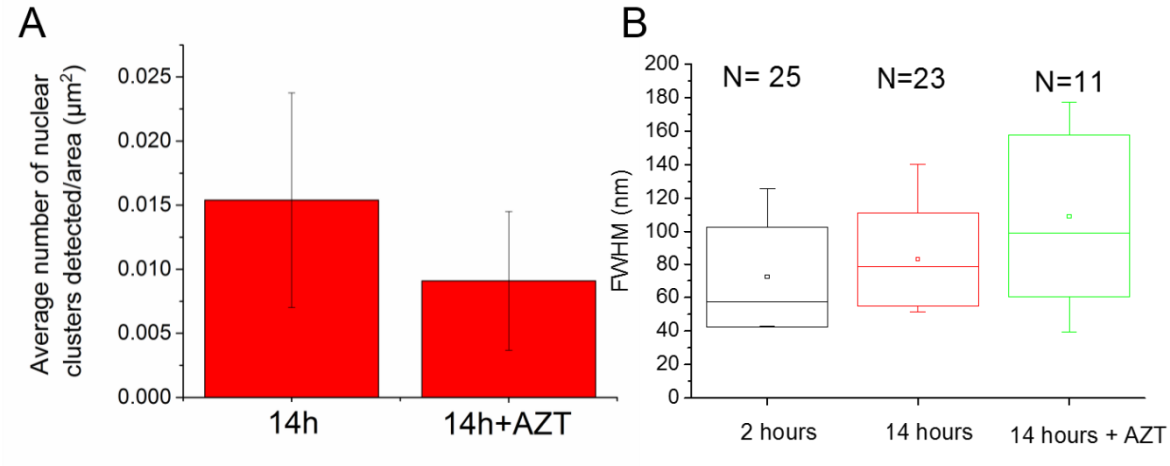

Figure 4.2.20. Nuclear IN-TC/FlAsH containing particles. (A) Average number of clusters per nucleus area. (B) Box chart representation of the size distribution of particles detected in 7 cells. Mean value is 70+/- 20 nm at 2 h, 85 +/- 25 nm at 14 h post infection and 135+/-35 nm for 14 h p.i. in presence of AZT.

3.2.4. Discussion and conclusions

Discussion

During the early stages of the HIV-1 viral lifecycle, the nucleocapsid protein NCp7 is playing a crucial role as a chaperone of nucleic acids. In the mature virion, the RNA dimer is highly condensed and stabilized by more than 2000 NCp7 molecules (Thomas and Gorelick 2008) forming the reverse transcription complex (RTC). During viral DNA synthesis by reverse transcriptase, the RTC remodels and becomes the preintegration complex (PIC), responsible for the transport of the viral genome into the nucleus and its integration into the host cell DNA. The presence of NCp7 in the PIC and its implication in the nuclear steps of the viral cycle remain unknown. Our data (chapter IV.1) confirmed the RT-dependent cytoplasmic release of NCp7 molecules. In this chapter, we used high resolution microscopy imaging in order to follow the NCp7-TC/FlAsH containing viral particles during infection and compare their distribution to IN-TC/FlAsH containing viral particles. Since IN is in the viral complex during the whole early phase of infection (from cell penetration until integration of viral DNA in the nucleus), these pseudoviruses are considered as a relevant model to follow the genome containing viral complexes (RTC and then PIC).

After initial setting of experimental parameters, we succeeded to obtain high resolution images of TC-containing HIV-1 pseudoviruses labeled by FlAsH either deposited on a coverslip or directly in infected cells. The size of detected spots ranged between 80 and 100 nm (for the viral particles deposited on the coverslips) and 100-120 nm for the pseudoviruses imaged in the infected HeLa cells. This increase might be explained by the lower localization precision due to the higher background signal when imaging cells, but also to the remodeling of the viral cores after cellular entry. A similar size increase was observed by dSTORM imaging of MA and CA proteins (Pereira, Rossy et al. 2012). Clusters of both IN and NCp7 proteins were also detected in the nucleus. This observation is not surprising for IN-TC as reported by Lelek et al. (Lelek, Di Nunzio et al. 2012). In contrast, evidence of the nuclear presence of NCp7 in the viral context is rare (Zhang and Crumpacker 2002). Comparison of 10% and 100% labeled NCp7-expressing pseudoviruses revealed a significant decrease of nuclear NCp7-TC clusters in the case of lower labeling confirming the cytoplasmic release of a fraction of NCp7-TC molecules.

The study of the time course of infection has shown a size decrease of the NCp7-TC and IN-TC containing complexes that may witness the remodeling of the viral core during reverse transcription. In agreement with this hypothesis, this size decrease was absent when RT was inhibited by AZT. The HR images of infected cells show also that at 2 hours post infection the viral particles are distributed homogeneously in the whole cytoplasmic region while at 14 hours

post infection, the pseudoviruses are more concentrated in the perinuclear space. We propose two explanations for this observation. Firstly, it is possible that the viruses terminate in close proximity of the nuclear envelope some processes, such as reverse transcription or uncoating that require time. Secondly, they may represent defective viruses that fail in uncoating or in other processes necessary for the structural remodeling preceding the nuclear entry and thus, they accumulate at the nuclear envelope. The fact that this accumulation is accentuated in presence of AZT plays in favor of the second hypothesis, but most probably, the increased number of viruses docked at the NE results from both phenomenon.

As soon as 2 h post infection both NCp7 and IN proteins are present in the nuclear clusters, and the density of nuclear spots decreases at 14 h post infection. It is conceivable that the nuclear complexes detected at 2 h post infection correspond to viral particles that did not yet proceed to the integration step. At 14 h post infection, the integration process is well running and the probability to detect nuclear complexes in the course of the integration (prior to their disassembly) is lower. As NCp7-TC/FlAsH imaging revealed similar results than integrase (size decrease upon nuclear entry, timing of appearance of first nuclear spots and reduction of the density of nuclear spots 14 h post infection) we can hypothesize that the nuclear NCp7-TC clusters represent the fraction of NCp7 molecules that stayed bound to the viral DNA after reverse transcription and followed the nuclear internalization within the PIC. However it should be noted that that these observations do not exclude the possibility that the nuclear NCp7-TC-FlAsH clusters correspond to released NCp7 molecules that entered the nucleus via passive diffusion and accumulate at a specific location – for example the nucleoli. Presented data give only a first insight in these processes and open a new perspectives for the study of the possible role of NCp7 in the nuclear steps of HIV-1 infection.

In the next step, we have studied the effect of RT inhibition in order to see how it modifies the distribution and sizes of the viral complexes in cells. It is known that inhibition of RT impairs the nuclear import of viral complexes (Arhel, Souquere-Besse et al. 2007; Arhel 2010). Accordingly, incubation of infected cells in presence of AZT, a specific RT inhibitor caused a reduced number of nuclear IN-TC/FlAsH spots. Moreover, the rare nuclear clusters detected were significantly bigger with a larger dispersion of sizes indicating that these are most probably aberrant viral complexes. In the case of NCp7-TC, the results were less clear. Since 60% of images cells did not show any nuclear NCp7-TC clusters, while the other 40% contained the same density of nuclear spots as the control samples. These observations suggest that the latter correspond to PICs that entered into the nucleus prior to the addition of AZT (first 2 h of infection) but did not succeeded the integration, or to aberrant mid-products of reverse

transcription that entered into the nuclear space in spite of the defects in the remodeling step. Alternatively, they may represent NCp7 molecules that quit the RTC (independently of reverse transcription) and diffused freely to the nucleus where they accumulated on some specific locations. Indeed, specific interactions between NCp7 and ribosomal proteins have been described (Anton, Taha et al. 2015; Mekdad, Boutant et al. 2016) and the nucleoli are a location of strong accumulation of NCp7 when overexpressed in transfected cells (Lochmann, Bann et al. 2013; Anton, Taha et al. 2015; Yu, Lee et al. 2016).

Conclusions

Taken together, high resolution PALM imaging of the intracellular distribution of NCp7-TC/FlAsH containing pseudoviruses provided a first insight on the fate of the NCp7 protein during the early steps of infection. Comparison with the data concerning IN-TC-containing RTC and PIC trafficking showed important similarities, namely in respect with the size modifications upon cell entry and nuclear internalization. However, discrepancies on the effect of RT inhibition on the nuclear entry need further elucidation by complementary experiments. Evidently, some experiments need to be repeated in order to increase the sampling and allow a more precise data analysis. Next, simultaneous dual color imaging of NCp7 with other viral proteins or the viral genome would be of major interest to further identify the nature of the nuclear NCp7 clusters.

3.3. Mechanism of NCp7 nuclear entry

3.3.1. Introduction

Active Ran-dependent transport of viral genome into the nucleus of host cell

The nuclear entry and integration of viral DNA into the host cell genome represent a crucial stage of viral infection. Nuclear pore complexes (NPC) mediate nuclear entry of HIV-1 preintegration complex.

NPCs are large protein complexes localized on the double membrane of the nuclear envelope. These complexes are responsible for the nucleo-cytoplasmic traficking. The NPCs contain 30 different proteins or nucleoporins (Nups), organized in 8-fold symmetry in three main domains: the nuclear basket, the central pore and the cytoplasmic filaments (Fig. 3.3.1) (Rout and Aitchison 2000; Cronshaw, Krutchinsky et al. 2002).

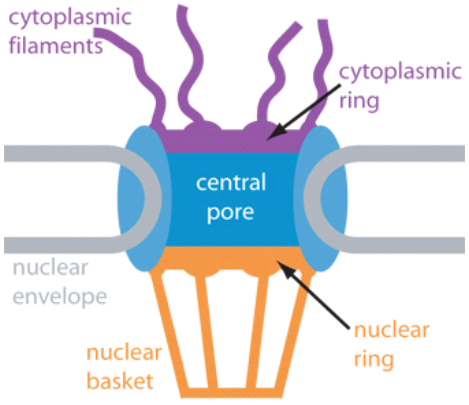

Figure 3.3.1. Schematic illustration of nuclear pore complex cross section. Size of NPC is about 120 nm. The diameter of the channel is ~5 nm with 45 nm depth. (NIH center for macromolecular modeling & informatics)

Small molecules pass through the central pore of NPCs by passive diffusion (Suntharalingam and Wente 2003). In contrast, the nuclear import of macromolecular complexes (>40kDa) requires active transport mechanism (Fahrenkrog and Aebi 2003). The translocation of cargo molecules through the NPC is conditioned by a specific transport signal - nuclear localization sequence (NLS) or nuclear export sequence (NES) that targets them into or out of the nucleus. These sequences are recognized by highly selective transport factors (importins or exportins), most of which come from the family of karyopherins. Retroviruses, especially HIV-1 are using two importin proteins, namely importin- (Popov, Rexach et al. 1998) and importin-β (Gallay, Hope et al. 1997). The importin-cargo complex docks on the NPC and interacts with the Nups that facilitate its translocation through the central canal. Formation and dissociation of

importin-cargo complex is regulated by interaction with the GTPase Ran, which adopts different conformations depending on GTP or GDP binding.

Active import of macromolecules inside the nucleus starts from the binding of the transport receptors to the phenylalanine glycine (FG) domains of the nucleoporins (Terry and Wente 2009). After the transport across the central canal, the complex is dissociated inside the nucleus during the conversion of RanGDP to RanGTP by the action of the nuclear protein RCCC1 (Ribbeck, Lipowsky et al. 1998). The complex of importin and RanGTP is translocated back to the cytoplasm where it dissociates and GTP is hydrolyzed to GDP. RanGDP bound to the nuclear transport factor NTF2 is transported back to the nucleus compartment by a non-energy dependent transport (Ribbeck, Lipowsky et al. 1998). In this manner a constant gradient of GTP is created across the nuclear envelope (NE) with RanGDP predominantly in the cytoplasm and RanGTP inside the nucleus (Gorlich and Kutay 1999; Madrid and Weis 2006). During the export, a cargo containing NES binds to exportin and RanGTP. This complex is exported to the cytoplasm via the central canal and dissociates. RanGTP binds GTPase activating protein (GAP) that hydrolyzes of GTP to GDP for successful restoration of the RanGDP inside the nucleus (Fig. 3.3.2). Inhibition of GTP hydrolysis aborts the transport events and causes undocking of the cargo-transport factor –Ran complex from the initial binding site. ATP depletion induces the absence of RanGTP (Melchior, Guan et al. 1995) and inhibition of the energy-dependent NLS-mediated import due to the blocking of oxidative phosphorylation or/and glycolysis (Richardson, Mills et al. 1988).

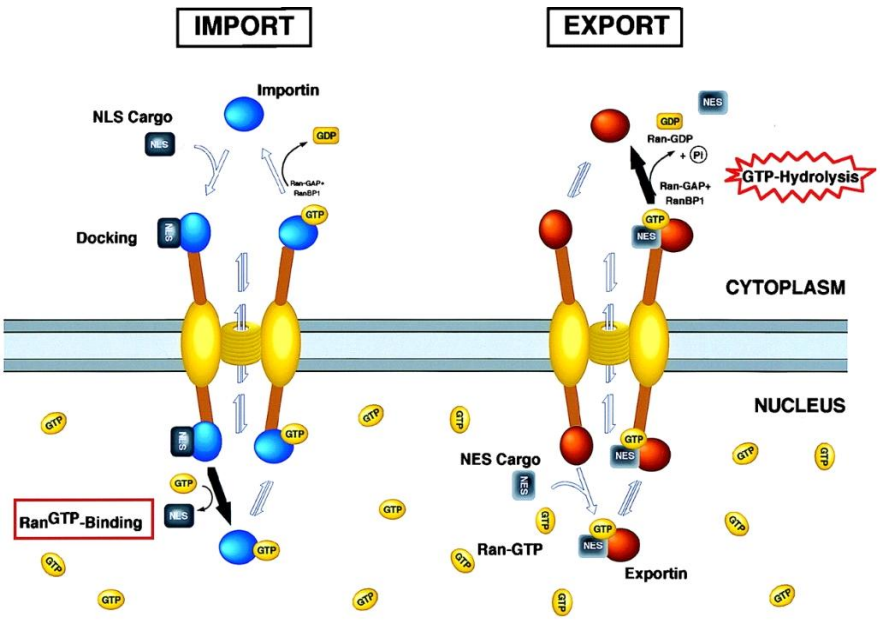

Figure 3.3.2. Schematic illustration of nucleocytoplasmic transport. Translocations (import and export) of materials through the nucleopore involves interactions between the transport receptors (mostly karyopherins), cargo and Nups.

The nuclear internalization of PIC occurs through the active import pathway (Bukrinsky, Sharova et al. 1992). However, the mechanism underlying the nuclear entry of PIC is so far inconclusive and several viral proteins such as IN, Vpr, MA and CA containing NLS may play a role during nuclear internalization (see part 1.4. Viral life cycle in Introduction section) (Fig. 3.3.3) (Suzuki and Craigie 2007).

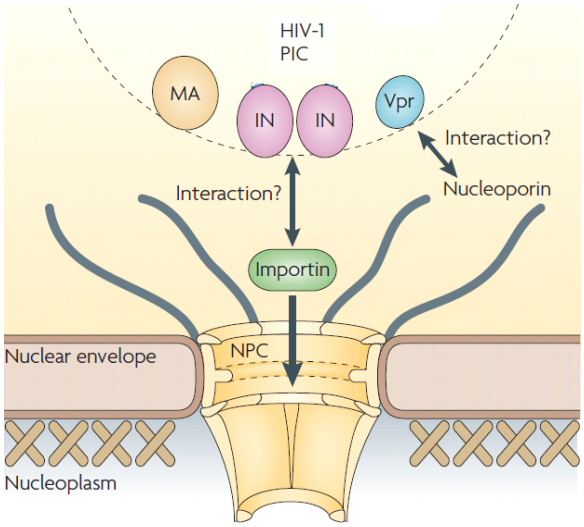

Figure 3.3.3. HIV-1 NLS containing proteins and PIC nuclear import. MA, Vpr and IN are thought to be karyophilic determinants of nuclear import facilitating the active nuclear import, whereas the Vpr and IN interact also with Nups (Suzuki and Craigie 2007).

Vpr and IN contain non-canonical NLS sequences, compared to the MA ones, which has GKKKYKLKH domain similar to the canonical monoparties basic-type NLS (Bukrinsky, Haggerty et al. 1993; Gallay, Swingler et al. 1995). It was shown in some works, that disruption of this region lead to the nuclear accumulation of viral cDNA in non-dividing cells but not in the dividing (von Schwedler, Kornbluth et al. 1994). In the conditions of overexpression, Vpr accumulates at the NPCs (Balliet, Kolson et al. 1994; Vodicka, Koepp et al. 1998) and IN that localizes inside the nucleus (Petit, Schwartz et al. 1999; Pluymers, Cherepanov et al. 1999) on the contrary MA was not found to have nuclear localization (Depienne, Roques et al. 2000). These localizations are consistent with their functions: MA is targeting PICs to the nucleus (Freed, Englund et al. 1995), Vpr mediates the interactions with Nups and importins (Jenkins, McEntee et al. 1998) and IN is essential for DNA integration (Gallay, Swingler et al. 1995). Interestingly, due to its capacity to destabilize the lipid membranes, it was proposed that Vpr might mediate nuclear entry by disruption of the nuclear envelope leading to direct access of PIC to the nucleus (de Noronha, Sherman et al. 2001). Several studies have shown that CA is also involved in the nuclear import (namely by the interactions with the Nups), despite the fact that CA is not karyophilic and is partly dissociated from the RNP complexes (Dismuke (Yamashita and Emerman 2004; Dismuke and Aiken 2006).

Upon viral nuclear internalization, NPC complexes undergo significant compositional changes. Dislocation of Nups, without disruption of NE integrity were reported (Monette, Pante et al. 2011). More than 10 different Nups from all three regions are involved in the entry of HIV-1 complex inside the nucleus (Brass, Dykxhoorn et al. 2008; Konig, Zhou et al. 2008). The more important ones are Nup358, Nup98, Nup153 and Nup62. At the nuclear entry stage, the viral preintegration complex (PIC) is partially uncoated. The interactions of HIV-1 core with Nup153 seem to play an important role in the nuclear internalization of the PIC (Lee, Ambrose et al. 2010; Di Nunzio, Fricke et al. 2013). Integration of the cDNA in the host chromosome is mediated by Nup62, Nup153 and Nup98 (Di Nunzio, Danckaert et al. 2012).

Mechanism of nuclear entry of NCp7

In the previous chapter, we have shown that already 2 hour post infection the NCp7 is present in the nucleus and that this presence depends on the reverse transcription process. Moreover, when RT is inhibited, the NCp7-TC complexes accumulate at the nuclear envelope, as it is the case for IN-TC localized in PIC. These observations indicate that at least a fraction of the NCp7 molecules stay bound to PIC during the nuclear entry step. However, NCp7-TC is a small molecule that can diffuse though the central channel of nuclear pores, therefore we performed additional experiments to enlighten the mechanism of the nuclear internalization pathway of NCp7.

Effect of nuclear import inhibition on the cellular distribution of HIV-1 Integrase and NCp7

To further enlighten the nuclear entry mechanism of NCp7, we attempted to evaluate the efficiency of its nuclear internalization in conditions where the active nuclear import is inhibited by energy depletion. This was achieved by incubating HeLa cells in glucose-free Dulbecco's modified Eagle's medium containing 10% fetal bovine serum and supplemented with 10 mM sodium azide (mitochondria inhibitor) and 6 mM 2-deoxy-d-glucose (that cannot undergo glycolysis) (Sigma, St. Louis, MO). It should be noted that energy depletion of the cell perturbs many physiological processes (notably the active transport via the microtubule network that is hijacked by pseudoviruses to reach the nuclear envelope). Therefore, a particular attention was paid to properly set up the experimental conditions and interpret the obtained results. Comparison of the active nuclear import inhibition on the efficiency of nuclear internalization of NCp7 with the one of IN-TC (known to enter the nucleus with the PIC (Gallay, Hope et al. 1997; Woodward and Chow 2010)) provides a first insight into the mechanism of NCp7 nuclear internalization process.

3.3.2. Preliminary experiments

The energy depletion may severely harm the cellular functions and lead to the cell death when prolonged for more then 60-90 minutes. Therefore, prior to real experiments, it was necessary to optimize the experimental conditions concerning the timing of the infection process.

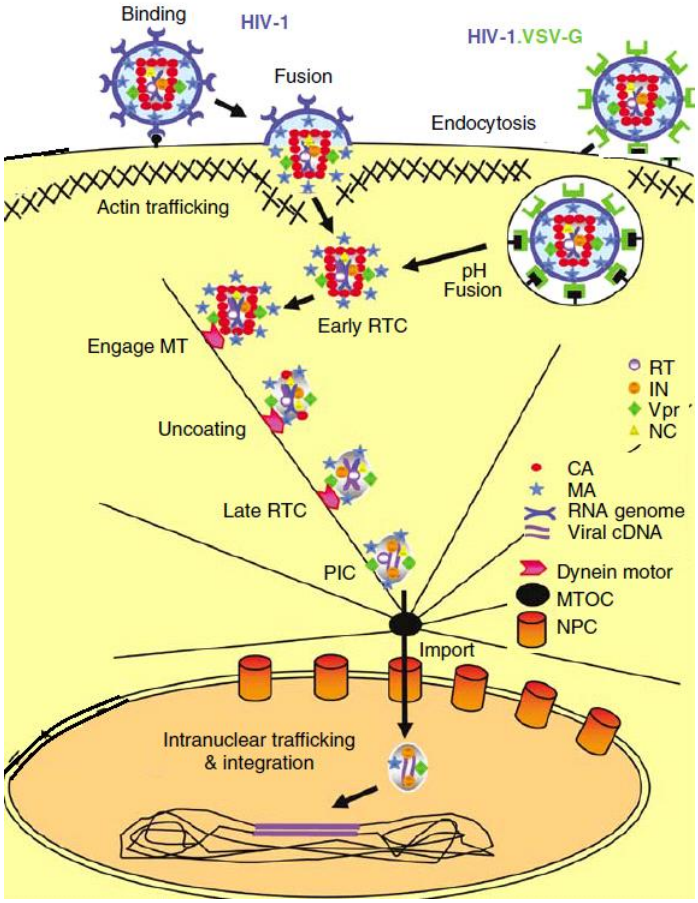

Figure 3.3.4. Early steps of retroviral infection. Internalization pathways of HIV-1 and pseudotyped by VSV-g HIV-1 particles. Fusion of viral particles with cell membrane starts by the recognition and docking of the viruses to the CD4 receptors, whereas HIV-1 VSV-g pseudoparticles enter the cell by endocytosis (Anderson and Hope 2005).

As shown in figure 3.3.4, pseudoviruses enter the cytoplasm by endocytosis, due to their pseudotyping by VSV glycoprotein. The viral particles rapidly escape from the endosomes and are transported to the perinuclear area by the microtubule network. Prior the infection experiments, it was necessary to determine the experimental conditions in which the viral particles would have enough time to enter the cell and attain the nuclear envelope before the "switching off" of the active nuclear import. Obviously, the nuclear internalization is related to the viral lifecycle, and the timing of the nuclear entry is conditioned by complex processes involving viral and cellular proteins. In our previous experiments, we observed that 2 hours of infection are sufficient for the first viral complexes to enter the nucleus. Therefore, we decided to realize energy depletion experiments as a first cue in elucidating the internalization process.

Prior to performing infection experiments, we studied the effect of energy depletion on:

- the cytoplasmic transport (from the cell surface to the perinuclear region) of polymer nanoparticles (NPs), used as a model
- the extinction of active nuclear import using eGFP-NLS as a model.

As a first approach to define the timing of the transport of endocytosed nanoparticles from the plasma membrane to the nuclear envelope, we first incubated HeLa cells in the presence of fluorescent nanoparticles (Reisch, Didier et al. 2014) during 30 minutes either in complete or energy depletion medium (EDM). As shown in figure 3.3.5A this incubation time was sufficient for the NPs incubated in physiological conditions to reach the perinuclear space, while they stayed docked at the plasma membrane in energy depleted cells. In a next step, HeLa cells were incubated 30 minutes in complete medium and additional 30 minutes in complete or EDM medium. In both cases, the NPs entered the cells and reached the perinuclear area (Fig. 4.3.5B). Therefore, taking into account exclusively the timing of the cytoplasmic transport, 30 minutes are sufficient for the cargos transported via microtubules to reach the perinuclear area.

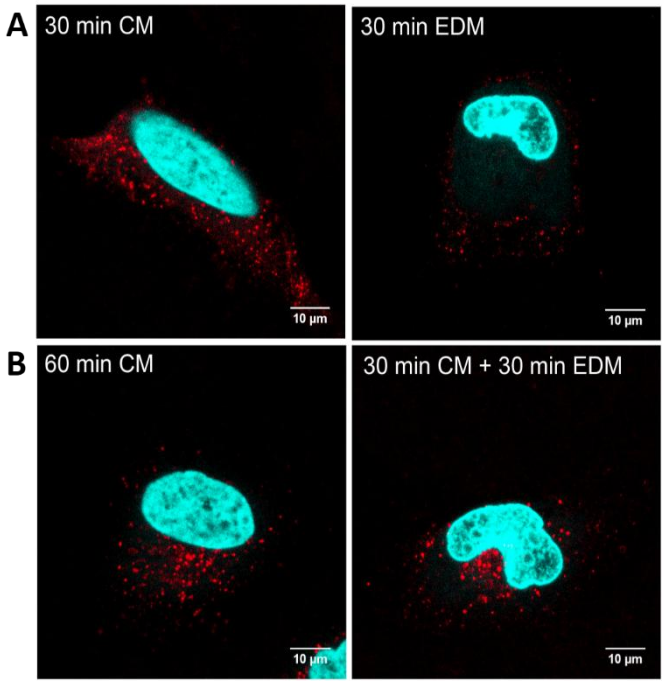

Figure 3.3.5. Effect of energy depletion on the intracellular transport of organic NPs. (A) Confocal images of HeLa cells incubated with NPs in complete medium (CM) or energy depletion medium (EDM) for 30 min. (B) Confocal images of HeLa cells incubated in physiological conditions for 30 min and additionally incubated for the same time in CM or EDM. Nucleus is stained by 1µM Hoechst.

In a next step, in order to check the efficiency of active nuclear import inhibition by energy depletion, we quantified the redistribution of eGFP-NLS in HeLa cells after 30 minutes of incubation in EDM. HeLa cells were transfected with plasmids coding for either eGFP or

eGFP-NLS and observed by confocal microscopy 24 hours post transfection. Figure 3.3.6A shows in its first line typical images of eGFP and eGFP-NLS cellular distribution. eGFP is homogeneously distributed in the whole cell while eGFP-NLS is mainly localized in the nucleus. The ratio of the average fluorescence intensity measured in the nucleus and in the cytoplasm is 1.4 +/-0.2 and 4.3 +/- 1.4 for eGFP and eGFP-NLS, respectively. (Fig. 3.3.6B). After 30 minutes of incubation in an energy depletion medium, the eGFP expressing cells remained unaffected (I_{nuc}/I_{cyt} = 1.2 +/- 0.1) while the strong contrast of the fluorescence signal between nuclear and cytoplasmic compartment in eGFP-NLS expressing cells vanished. Indeed, the I_{nuc}/I_{cyt} ratio decreased down to 1.6 +/- 0.4. These results clearly demonstrate the efficiency of energy depletion on the active nuclear import after 30 minutes of incubation in the energy depletion medium.

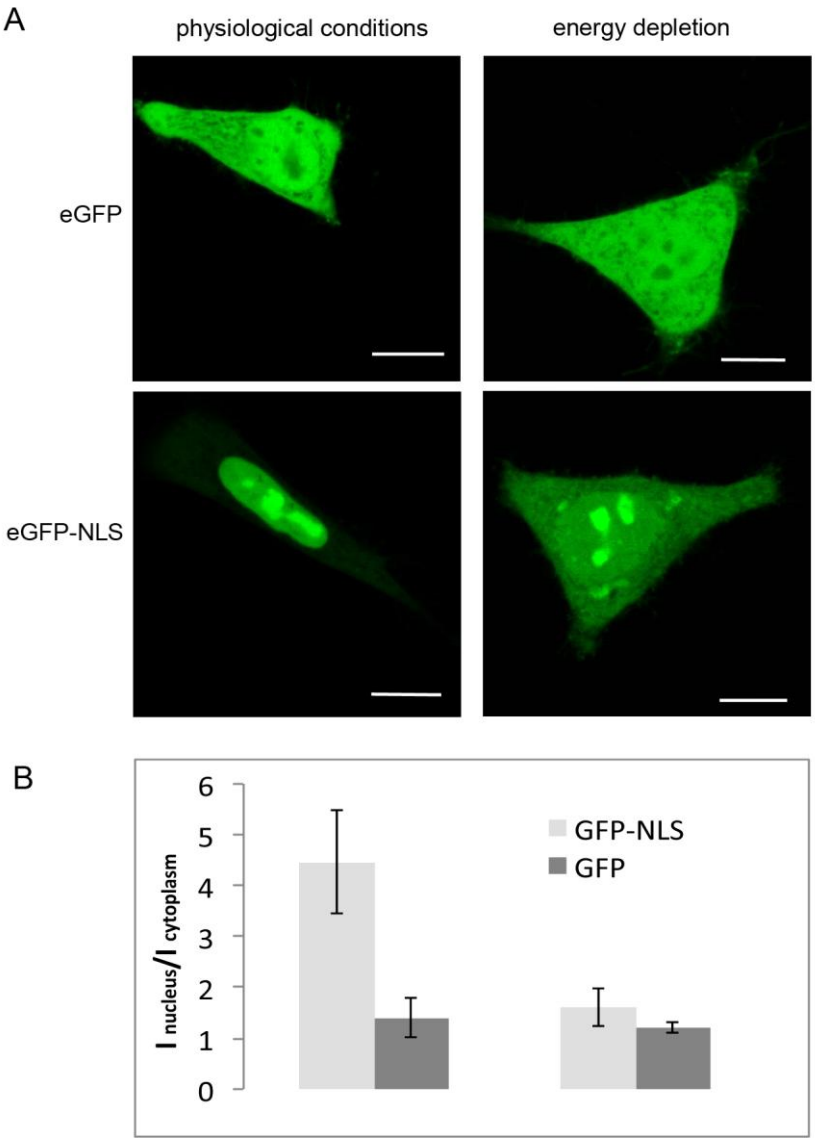

Figure 3.3.6. Effect of energy depletion on the efficiency of the active nuclear import (A) Confocal images of HeLa cells expressing eGFP or eGFP fused to the nuclear localization signal (eGFP-NLS) incubated in normal medium or after 30 minutes of incubation in energy depletion medium. (B) Effect of energy depletion on the ratio of the fluorescence intensity between nucleus and cytoplasm of eGFP and eGFP-NLS expressing cells. Measurements were realized on 10 cells for each condition. Scale bar 10 µm.

These results showed that i) 30 minutes are sufficient for the endocytosed NPs to reach the perinuclear area and that ii) EDM causes rapidly the arrest of endocytosis and microtubule-mediated cytoplasmic transport. The active nuclear import is stopped after 30 minutes of energy depletion. Thus, 30 minutes of incubation in complete medium followed by 30 minutes of incubation in an energy depletion medium represents the minimal timing allowing the pseudoviruses to reach the perinuclear areas and to stay blocked in the proximity of the nuclear pores. Since the model used is strongly simplified, we decided in order to take into account the infection process to extent the incubation times up to 45-60 minutes in the ED experiments with the pseudoviruses.

3.3.3. Intracellular distribution of the viral complexes in energy depleted cells

Intracellular distribution of the IN-TC in energy depleted cells

In order to validate our experimental approach, the effect of energy depletion was first studied using the viral complexes labeled on IN since this protein is well-known for being internalized in the nucleus via active transport within the PIC (Bukrinsky, Sharova et al. 1992). HeLa cells were incubated in presence of FlAsH labeled IN-TC viral complexes during 60 min in serum free DMEM medium. Then after the washing step, the cells were kept for the same period in the complete (Control condition) or energy depletion medium (EDM). After fixation with 4% PFA during 10 min at room temperature, cells were imaged by PALM microscopy. Typical images are presented in figure 7.

In control samples, labeled IN-TC complexes were found in the cytoplasm and the nucleus of infected cells (Fig. 3.3.7A). In energy depleted cells (Fig. 3.3.7B), lower amounts of complexes are present in the nuclear compartment and fluorescent puncta frequently accumulate at the nuclear envelope (70% of ED cells). These observations confirm that during first 60 minutes of infection the viral particles that enter the cells have enough time to reach the perinuclear region and to dock to the nuclear envelope (probably at the level of nuclear pores). Figure 3.3.8A represents the number of IN-TC/FlAsH clusters per nucleus area calculated for 17 cells in 2 independent experiments. Our results show that energy depletion decreased by ~54% the density of IN-TC/FLAsH nuclear clusters in the nucleus. Similarly, the ratio of cytoplasmic to nuclear clusters is almost 2 fold higher for energy-depleted cells (Fig. 3.3.8B).

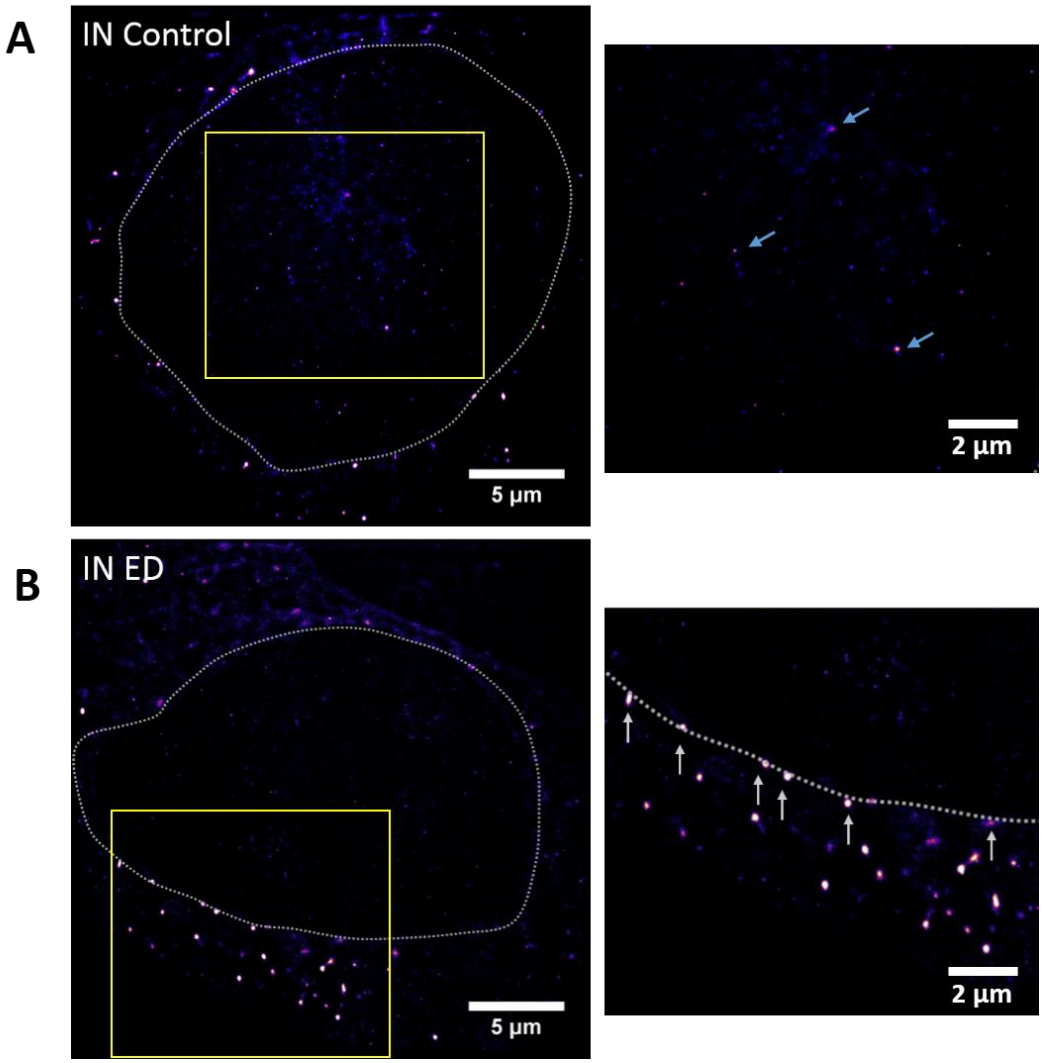

Figure 3.3.7. Influence of energy depletion on the intracellular localization of IN-TC/FlAsH complexes. PALM images of infected HeLa cells in physiologic (Control) (A) and energy depletion (ED) conditions. (B). Zoomed region of A represents nuclear IN-TC/FlAsH clusters detected after 120 min of infection (white arrows). Zoomed region of B shows bright IN-TC/FlAsH clusters (blue arrows) in the perinuclear region. The dotted line highlights the nuclear envelope.

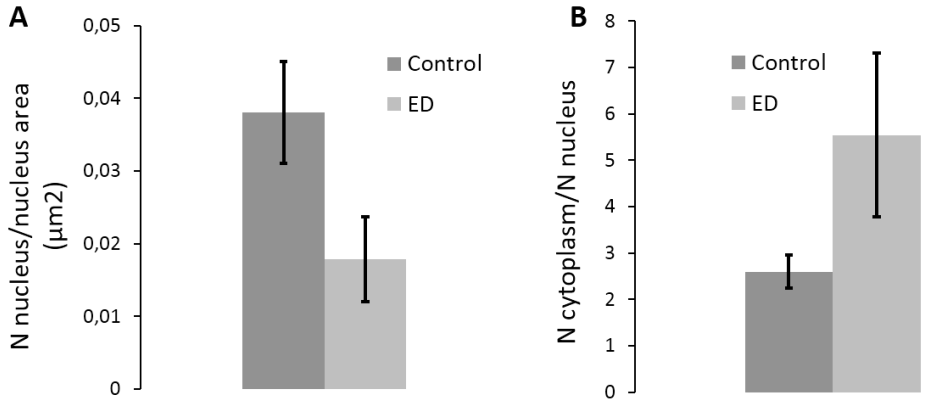

Figure 3.3.8. IN-TC complexes in the nuclear compartment (A) Density of IN-TC/FlAsH clusters in the nucleus and (B) ratio between number of complexes inside the cytoplasm and inside the nucleus. T-test of density: p=0.00014, difference is significant.

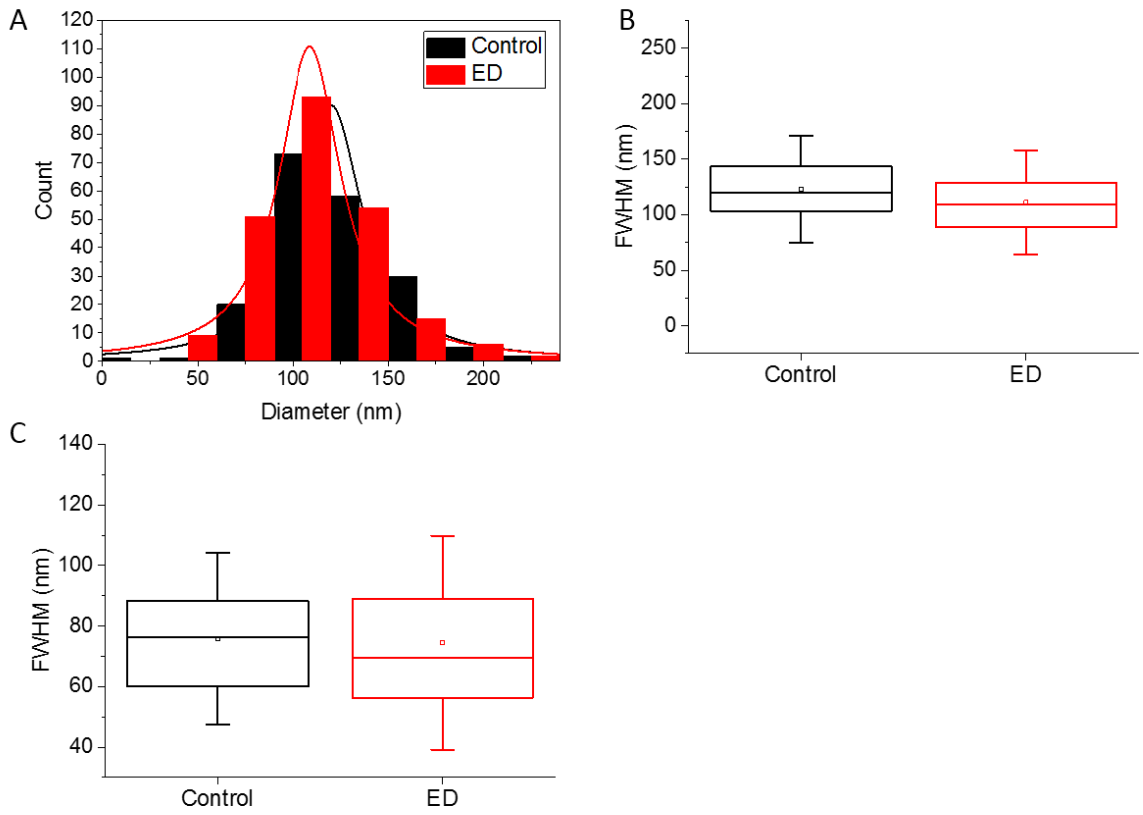

Figure 3.3.9. Effect of energy depletion on the size of IN-TC/FlAsH complexes in infected cells. (A) Histogram (bin size 30 nm, fit by Lorentz curve) and box chart presentation of clusters detected in the cytoplasm (B) and in the nucleus (C). Box chart of clusters represents intervals containing 25-75% of the values, whiskers represent the SD, line and the squares correspond to the median and the mean value respectively.

As shown in figure 3.3.9, the size distribution of the cytoplasmic and nuclear particles was not significantly influenced by the ED process. The mean values are 120 +/- 30 nm and 110+/- 30 nm in the cytoplasm for the control and ED cells respectively and 75 +/- 20 nm in the nucleus for both samples.

Taken together, our data show that energy depletion efficiently inhibits the nuclear import of PIC and validate our experimental approach. In the next step, we used this approach to evaluate the role of the active nuclear import in the nuclear internalization of NCp7-TC/FlAsH.

Intracellular distribution of NCp7 proteins in energy depleted cells

The same experimental protocol was applied to HIV-1 pseudovirus containing FlAsH labeled NCp7-TC. In line with the aforementioned control experiments, we observed fluorescent spots in the cytoplasm and in the nucleus of infected cells (Fig. 3.3.10A). The density of the nuclear NCp7-TC/ FlAsH clusters corresponds well to the density of IN-TC/FlAsH clusters (0.04 part/μm^2). Similarly, to IN-TC/FlAsH complexes, we observe a strong perinuclear accumulation

of fluorescent spots with an overall bigger number of complexes inside the cytoplasm in energy depleted cells (Fig. 3.3.10B). The effect of energy depletion on the nuclear localization of NCp7 is lower compared to integrase with a 30% reduction of the number of NCp7-labeled complexes per nuclear area (Fig. 3.3.11A). However, this decrease is at the limit of significance (p= 0,0559) which indicated that probably an alternative process to the active import is implicated. The ratio between cytoplasmic and nuclear complexes is 2 fold higher in ED conditions compared to control cells as in the case of IN (Fig. 3.3.11B) witnessing the blocking of the NCp7-TC containing complexes in the perinuclear area.

The size distribution of the cytoplasmic complexes is comparable with mean values of 100+/- 30 nm for both physiologic and ED conditions (Fig. 3.3.12A). In contrast, the nuclear clusters are ~20% bigger in ED conditions (mean size 65 +/- 20 nm and 80 +/- 27 nm for control and ED cells, respectively (Fig. 3.3.12C)). This increase might be related to the nuclear internalization process. Indeed if part of NCp7 molecules enter the nucleus by passive diffusion they might preferentially accumulate at some specific location such as in the nucleoli or bind to ribosomal proteins.

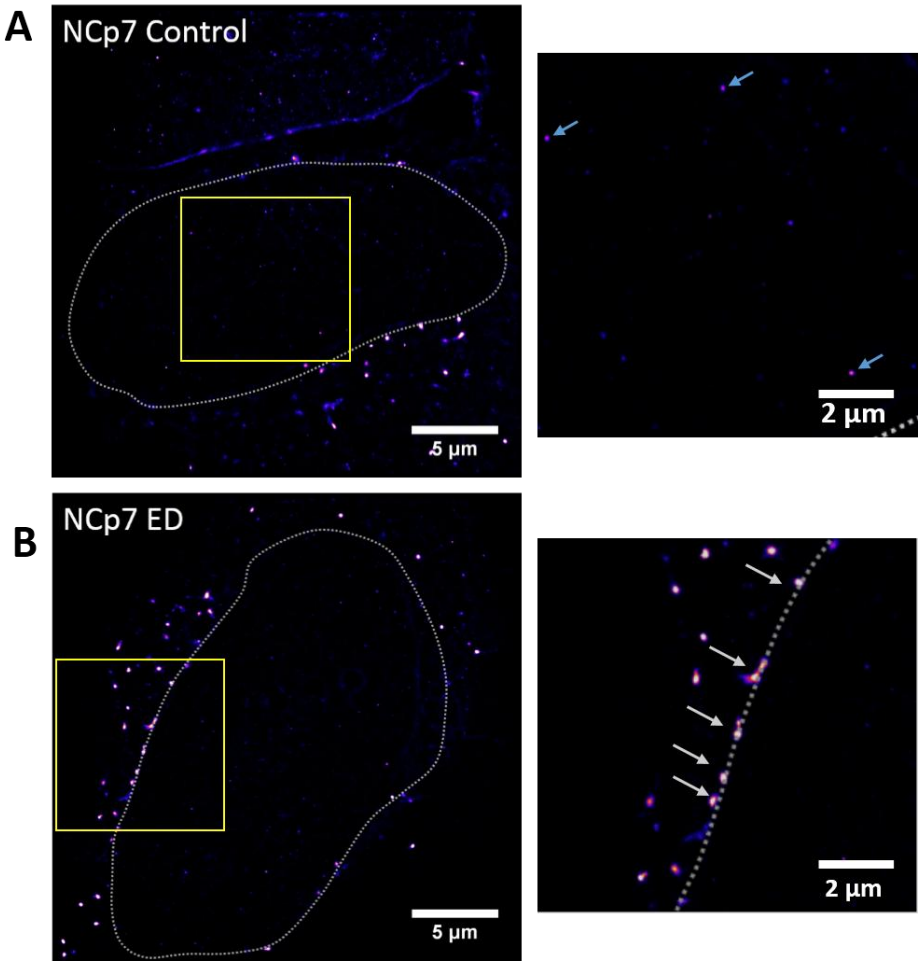

Figure 3.3.10: Influence of energy depletion on the intracellular localization of NCp7-TC/FlAsH labeled pseudoparticles. (A) PALM images of the 25x25 µm ROIs of HeLa cells infected by the NCp7-TC/FlAsH for physiological (Control) and (B) energy depletion (ED) conditions. Zoomed regions revealed nuclear localization of NCp7 after 120 min of infection in Control sample (A) and strong perinuclear localization in ED condition (B).

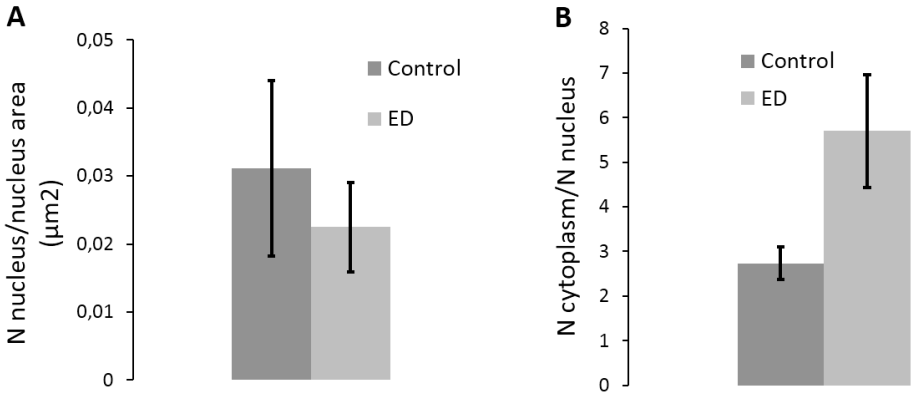

Figure 3.3.11. Quantification of labeled NC complexes inside the nuclear compartment. (A) Number of detected viral complexes per nucleus area (p-value = 0.0559) and (B) ratio between the numbers of complexes found in cytoplasm *vs* nucleus.

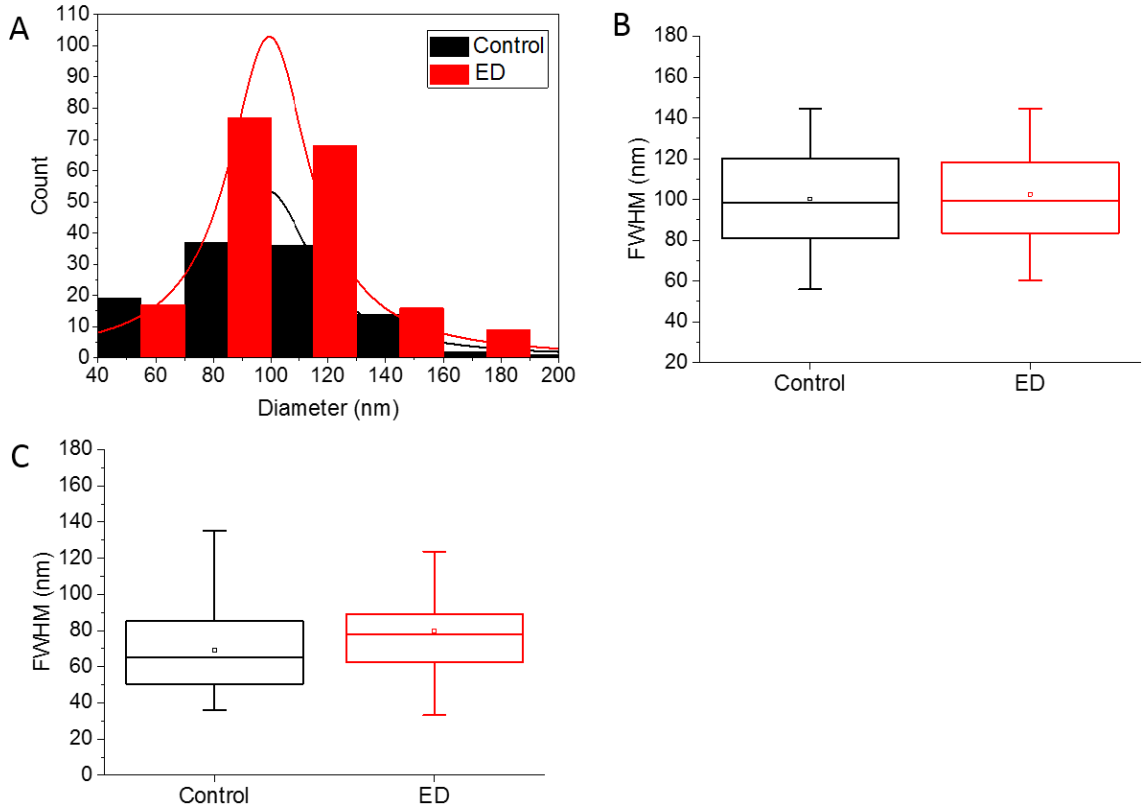

Figure 3.3.12. Influence of energy depletion on the size of NCp7-TC/FlAsH complexes in infected cells. (A) Histogram (bin size 30 nm, fit by Lorentz curve) and box chart presentation of clusters detected in the cytoplasm (B) and the nucleus (C). Box chart with intervals containing 25-75% of the values, whiskers represent the SD. The line and the squares correspond to the median and the mean value, respectively.

3.3.4. Imaging of NCp7 at the nuclear envelope

Energy depletion experiments have shown that inhibition of the active nuclear import causes a decrease of the number of nuclear NCp7-TC/FlAsH complexes and that at least a fraction of NCp7 molecules might be internalized via active nuclear import. In this chapter, we aimed to image the NCp7-TC clusters at the nuclear envelope. For this purpose, we first quantified the co-localization of NCp7-TC/ReAsH with the nuclear pore complexes by confocal microscopy. Next, the presence of NCp7 labeled RTC in the perinuclear area was imaged by correlative light-electron microscopy.

Co-localization with nucleopores: confocal observation

HeLa cells were transfected by Nup153-3eGFP and Nup214-3eGFP (Ellenberg, Siggia et al. 1997). It was shown that the low expression of these fusion proteins does not perturb the biological function of the NPCs. Then, transfected HeLa cells were infected by ReAsH labeled IN-TC (positive control) or NCp7-TC viral complexes or incubated with fluorescent

nanoparticles (negative control) for 6-8 h. The samples were washed with PBS, fixed by PFA 4% and imaged by two color confocal microscopy. Typical images are shown in figure 3.3.13A. As shown in the insert, the red spots representing the viral complexes or nanoparticles are localized both in proximity and distant from the NPCs (green spots). The level of colocalization was calculated as a fraction of yellow spots for the total number of red spots measured in 20 cells, with 150 detected viruses at the nuclear envelope. Obtained values shown in figure 13B are 22 +/- 5% for IN-TC, 20 +/- 3% for NCp7-TC and ~13+/- 6% for NP. (Fig. 3.3.13). Co-localization levels of IN and NCp7 are comparable independently on the NUPs labelling, indicating that a portion of the NCp7 molecules is probably still attached to the PIC when they are about to enter the nucleus.

In order to further image these NCp7-TC complexes located near the nuclear pores, we applied a correlative light-electron microscopy approach.

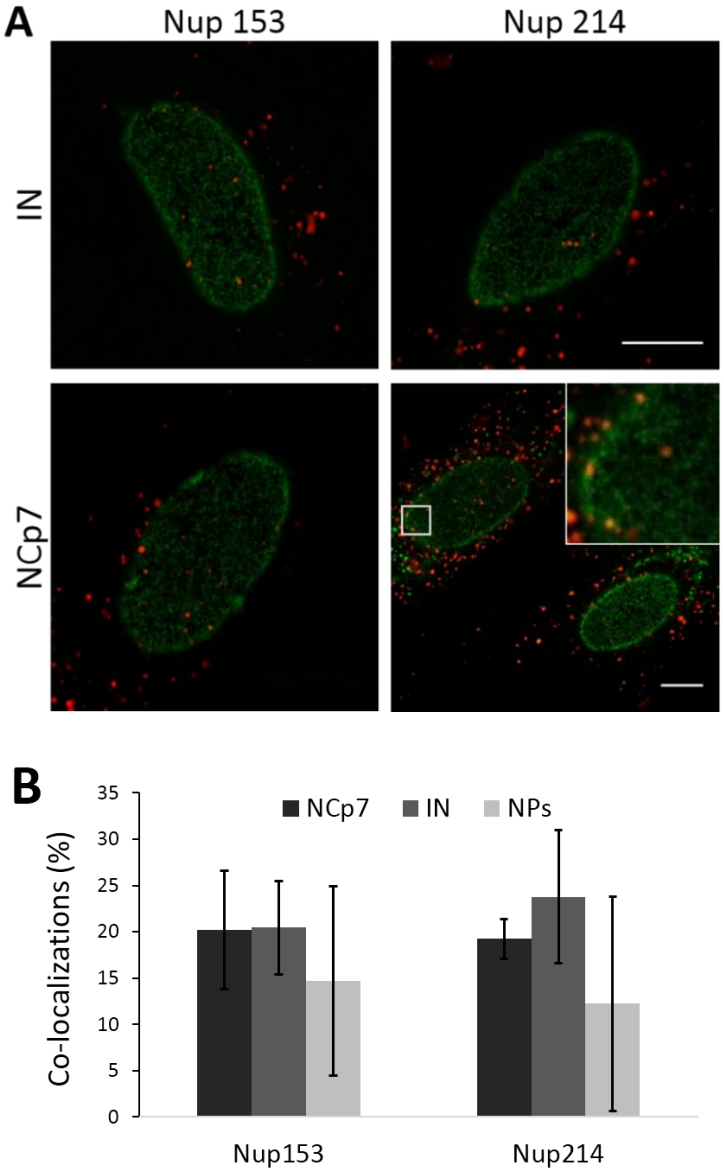

Figure 3.3.13. Co-localization of viral complexes with nucleopores. (A) Confocal images of HeLa cells infected for 8h with HIV-1 labeled on TC-tagged IN/NCp7 by ReAsH (red) and Nups labeled by EGFP (green) Scale bar 10 µm. (B) Percentage co-localizations of NCp7/IN-TC, NPs and Nup153 and Nup214 calculated from 10 cells for each condition.

3.3.5. CLEM

3.3.5.1. Proof of concept

Correlative light electron microscopy (CLEM) is an experimentally complex approach that enables to visualize the same structure by light and electron microscopy. One of the specific requirements of this approach is the need of a label suitable for both techniques. ReAsH, a biarsenical derivative of resorufin is a fluorophore that can be used for the oxidation and polymerization of 3,3-diaminobenzidine tetrahydrochloride (DAB), generating an electron dense product in the close proximity of ReAsH-TC (Gaietta, Giepmans et al. 2006). The principle of

the photooxidation reaction is shown in figure 4.3.14. The excited fluorophore passes to the triplet state that is energetically coupled to the generation of singlet oxygen from the molecular oxygen. The singlet oxygen then photo converts the DAB producing an oxidized DAB polymer around the ReAsH-TC complex. The crucial parameter in the photooxidation process is the intersystem crossing rate. As this parameter is inversely proportional to the fluorescence quantum yield, many bright fluorescent compounds are not suitable for photooxidation labeling. ReAsH is well suited as it is enough bright for light microscopy and it can produce a high output of singlet oxygen (Sosinsky, Giepmans et al. 2007) (Fig. 3.3.14).

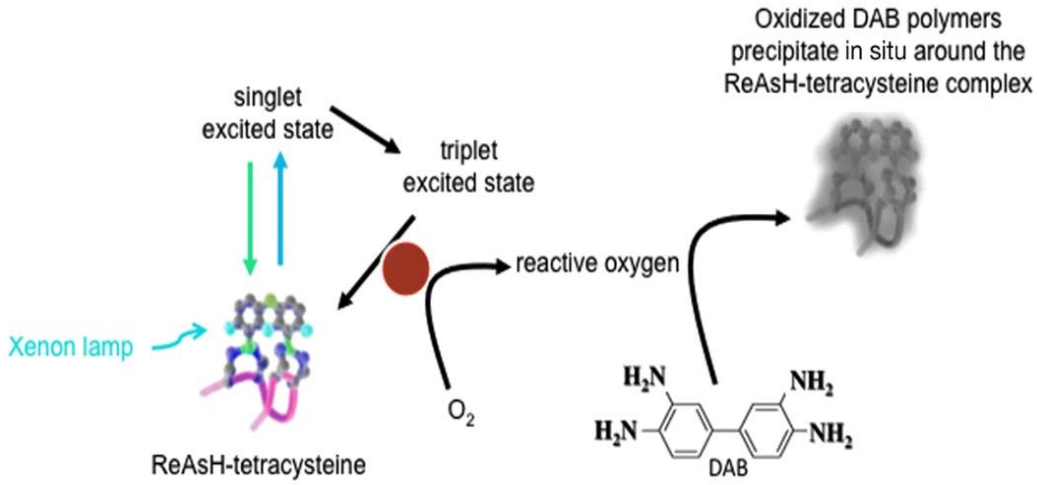

Figure 3.3.14. ReAsH-triggered photoconversion of DAB. The dye specifically bound to the TC tag is excited by the light source, which triggers the production of reactive oxygen species. These species cause then the oxidation and polymerization of DAB, generating a water-soluble precipitate in close proximity to the ReAsH-TC complexes. Brownish DAB polymer is rendered electro dense upon treatment with osmium tetroxide, as well non-treated product is electron-opaque (Maranto 1982; Gaietta, Deerinck et al. 2011).

In order to observe by CLEM the ReAsH-labeled viral complexes in the infected cells we adapted the DAB photooxidation protocol described by the group of Gaietta (Gaietta, Deerinck et al. 2011). Cells were deposited on a custom gridded ACLAR film support suitable for TEM sample preparation (Jimenez, Van Donselaar et al. 2010; Spiegelhalter, Tosch et al. 2010) and infected by ReAsH labeled NCp7-TC containing HIV-1 pseudoviruses during 6-8 hours. After fixation, the cells were imaged by confocal microscopy. The samples were then incubated for 30 minutes on ice with blocking buffer in order to minimize the non-specific oxidation of DAB by mitochondrial enzymes (Deerinck, Martone et al. 1994; Gaietta, Deerinck et al. 2002). The low temperature permits to minimize spontaneous non-specific oxidation of DAB. The photooxidation was then performed by illumination at maximum power of the argon lamp (Leica SPE microscope excitation filter 515/560 nm detection for 10-15 min in the presence of a drop of fresh cold DAB solution (Fig. 3.3.15)).

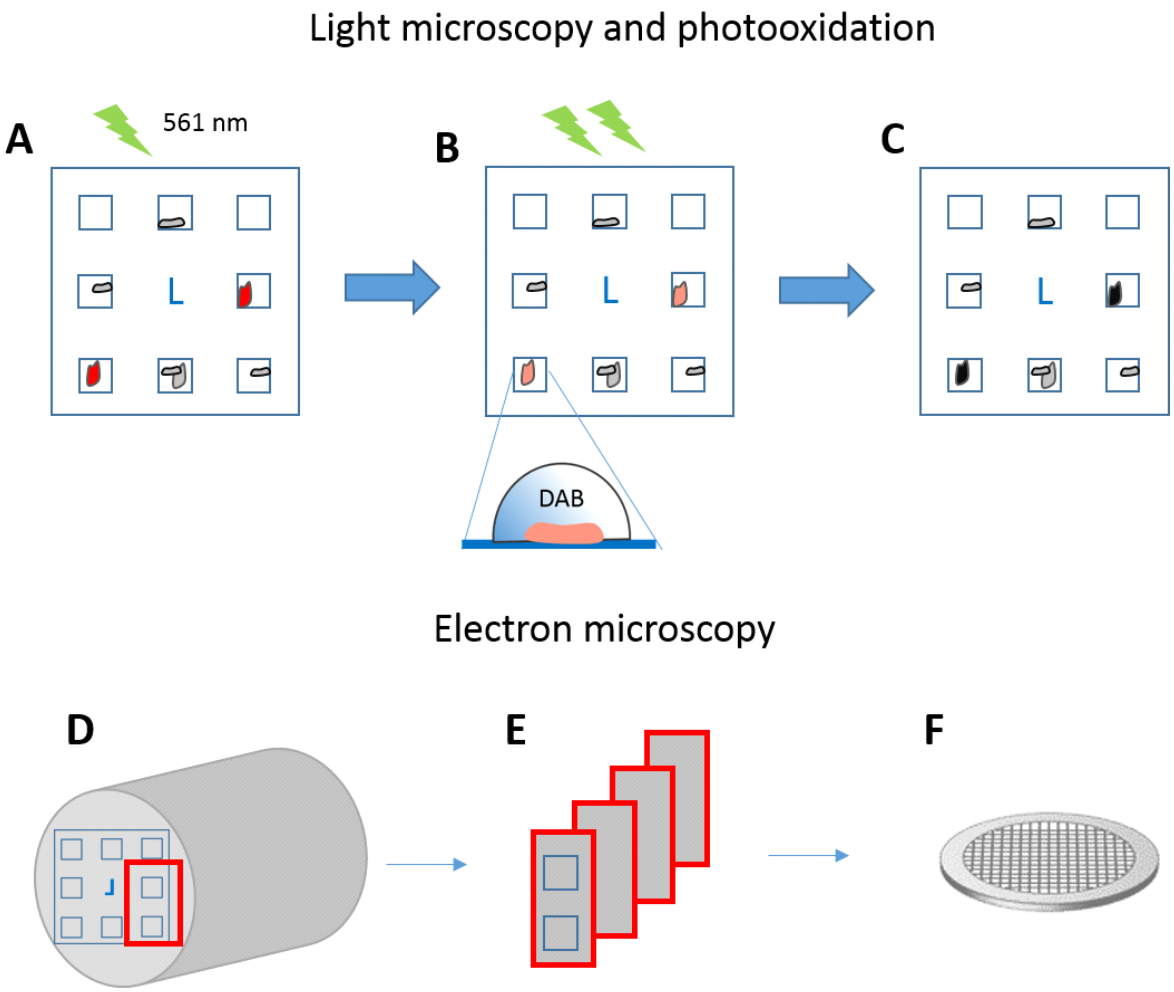

Figure 3.3.15. CLEM technique. Light microscopy and photooxidation of HeLa cells infected by NCp7-TC/ReAsH-containing pseudoparticles. Deposition and infection of HeLa cells on the ACLAR film (A). Imaging of cells inside the squared regions by confocal microscopy (B). Next, cells pre-treated with blocking buffer containing potassium cyanide were illuminated in the ROIs by the high power lamp in the presence of a drop of DAB solution (C). Electron microscopy: additional fixation by osmium tetroxide, dehydration and resin embedding (D), ROIs with photooxidied cells are cut into 80 nm slices by an ultramicrotome (E) and deposited on the grid for TEM observation (F).

Specimens were imaged on transmission mode before and after photooxidation in order to verify the presence of a DAB precipitate (Fig.3.3.16). Infected cells showing a fluorescent signal of labeled viral complexes gave after photooxidation a dense brownish precipitate of DAB (Fig. 3.3.16, A, B). Non-infected cells used as a control showed only light diffuse precipitation, probably caused by oxidation of DAB by the cellular peroxidase.

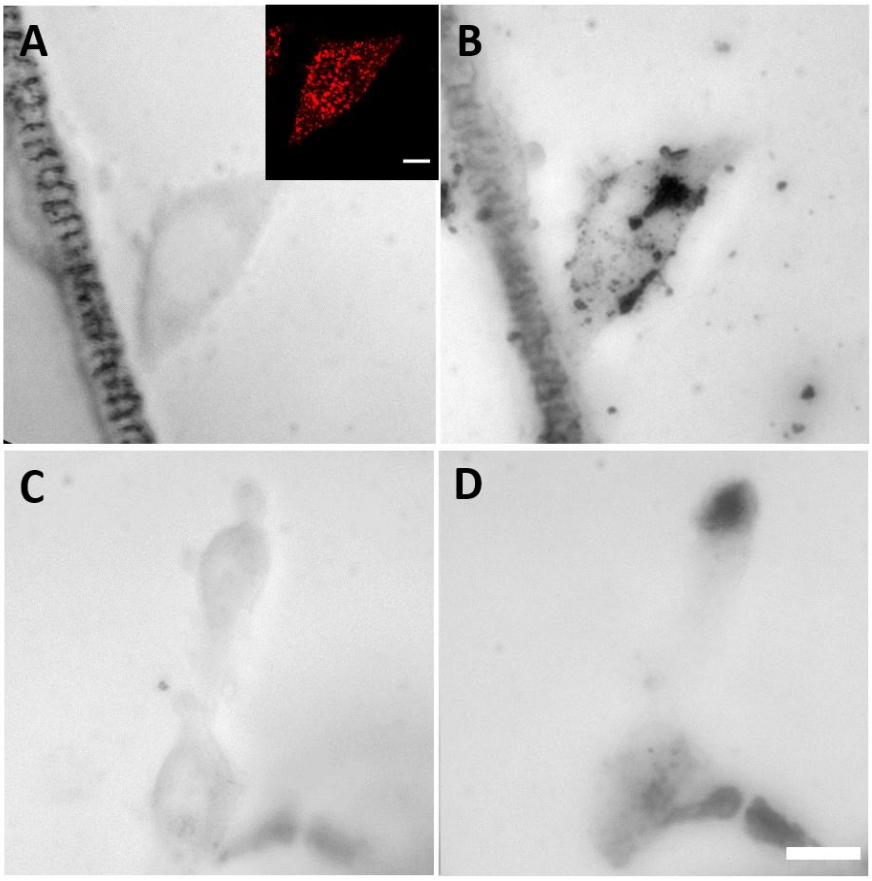

Figure 3.3.16: Photooxidation of DAB in the presence of ReAsH. DAB photooxidation was performed on infected (A, B) and non-infected control cells (C, D). Images of the cells before (A, C) and after (B, D) the photooxidation process. The inserts show a light microscopy image of the cells. Dense dark precipitate appeared in the infected cell after illumination (B). Diffuse light precipitate was observed also in control (non-infected) cells after illumination (D). Scale bar 10 µm.

Cells prepared for TEM observations (additional fixation by osmium tetroxide, dehydration and resin embedding) were then imaged under the electron microscope. Figure 3.3.17 shows the corresponding cells in confocal and electron microscopy. Dark spots are present in the cytoplasm of infected cells (Fig. 3.3.17B). Some of them correspond to the fluorescent spots observed in confocal image (Fig. 3.3.17C). Obviously, the confocal image contains more spots. This can be explained by the difference in the sample volume imaged. Indeed, the sample slice thickness for TEM is 80 nm, while the fluorescence signal is collected from a 0.5 µm focal depth. In control samples (Fig. 3.3.17 D, E, F), only weak autofluorescence can be observed and TEM images did not show any small dark puncta but only a few big dark aggregates.

In conclusion, these experiments showed that the ReAsH induced photooxidation of DAB provides labeling of the viral complexes by generating dense precipitates that can be observed in TEM.

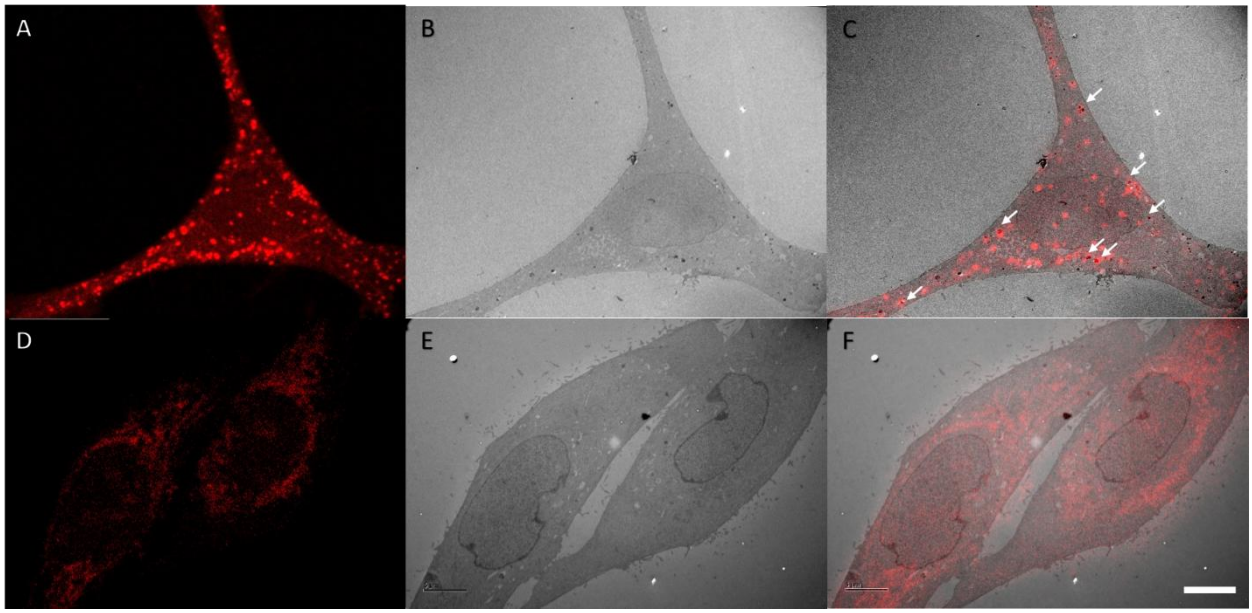

Figure 3.3.17. CLEM observation of cells infected by ReAsH-labeled NC-TC containing pseudoparticles. Fluorescence microscopy image of an infected HeLa cell (A), TEM image of the same cell (B) and merge of the two images (C). White arrows in merge image (C) indicate the regions where the spots from fluorescence and TEM images are superimposed. Fluorescence (D), TEM (E) and merge (F) images of control non-infected cells. No speckles were observed. Scale bar 10µm.

3.3.5.2. TEM observations of NCp7-TC/ReAsH

TEM micrographs of HeLa cells infected by HIV-1 containing NCp7-TC/ReAsH revealed the presence of different types of cytoplasmic vesicles densely marked by DAB precipitates. The superimposition of confocal and TEM images was not trivial due to the distortion of the samples during the fixation and dehydration step. However, we were able to find good correspondence between the fluorescent and DAB puncta (Fig. 3.3.18).

Viral particles with sizes ranging between 100 to 400 nm (majority around 200 nm) were found through all the cytoplasm, near the nucleus and in the close proximity to NPC (Fig. 3.3.18). No precipitate was observed in the nucleus. The average size of the HIV-1 RTC is around 100 nm, but we assume that during the photooxidation process, the generated singlet oxygen may diffuse in the environment and oxidize the DAB polymers further away from the ReAsH localization. Therefore, we suggest that dark spots with blurred edges and diameter approaching 200 nm may correspond to individual cytoplasmic RTCs. The giant vesicles of 300-400 nm size contain often a number of smaller black puncta about 60-80 nm (Fig. 3.3.18, A,D). We suppose that these are viral particles not released from the endosomes. Similarly, small black puncta found inside the membrane vesicles may correspond to viral particles trapped in the

cellular vesicles. (Fig. 3.3.19A, orange arrow). Finally, dark spots with homogeneously distributed precipitates and blurred edges without membrane can be free viral complexes (Fig 3.3.18 D, G). Typical free or vesicular viral particles are shown in figure 3.3.19.

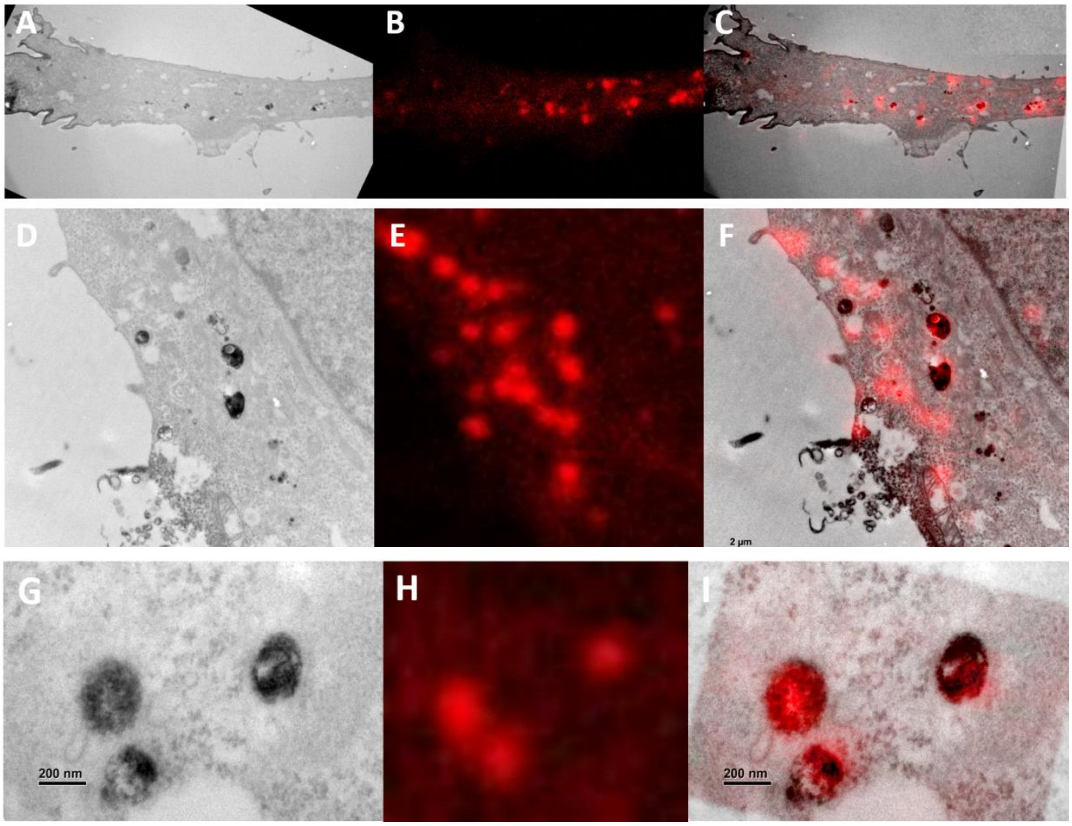

Figure 3.3.18. CLEM of ROIs inside an HIV-1 infected cell. TEM micrographs of the cytoplasmic region of an infected HeLa cell (A, D, G), confocal images of the corresponding ROIs (B, E, H) and merged images (C,F, I).

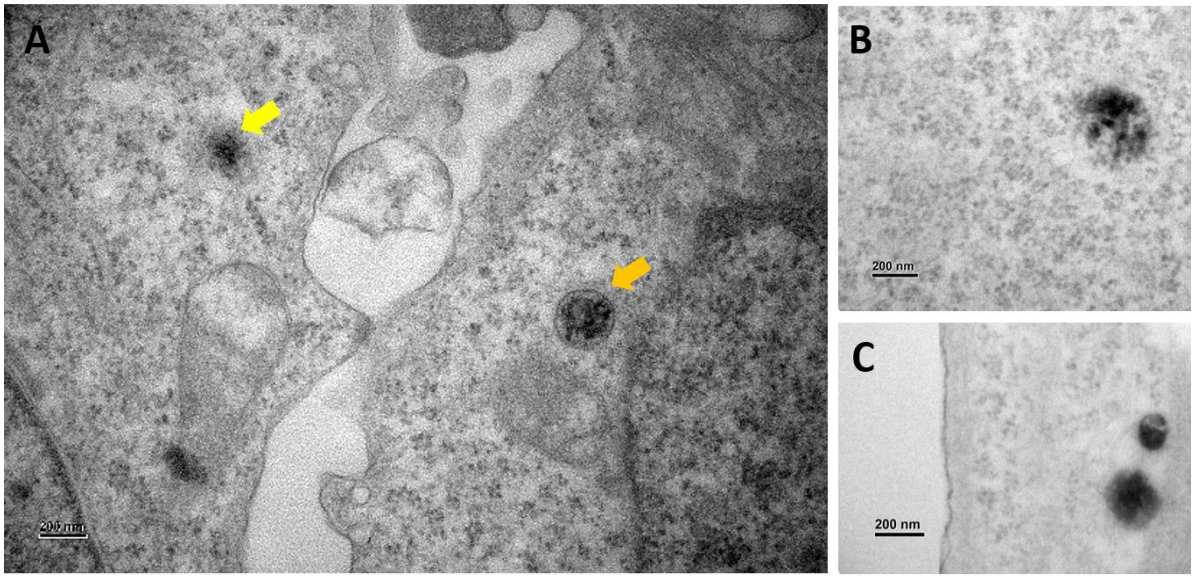

Figure 3.3.19. TEM micrograph of HeLa cells infected for 8 h by HIV-1 viral particles. (A) DAB precipitates of free (yellow arrow) and endosome-trapped (orange arrow) viral complexes. Membrane-free puncta present (B) dotted pattern and (C) homogeneous distribution of DAB precipitates.

Interestingly, in the cytoplasm we observed ReAsH/NCp7-TC containing complexes in the proximity of the microtubules (Fig. 3.3.20). These may represent the RTC that are being transported to the nuclear area.

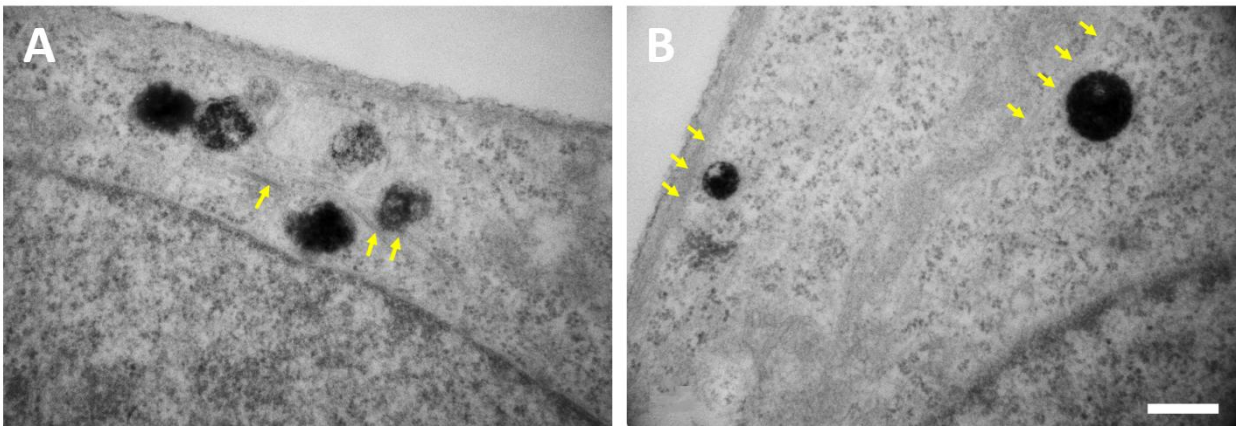

Figure 3.3.20. Co-localization of viral complexes and microtubules. Numerous free and endosome-trapped viral complexes were found in close proximity to cytoskeleton fibers (yellow arrows).

In the perinuclear area, numerous dark speckles with sizes ~200 nm were found in close proximity to the nuclear envelope and also near the nuclear pore complexes (Fig. 3.3.21). In some speckles were observed darker regions, which can correspond to capsid structures (Fig. 3.3.22).

Taken together, these observations confirm the co-localization of NCp7-TC containing complexes with the nuclear pores. It seems that a significant fraction of NCp7 molecules

(necessary to efficiently photoconvert the DAB) is still present in the viral complexes when they dock at the nuclear envelope.

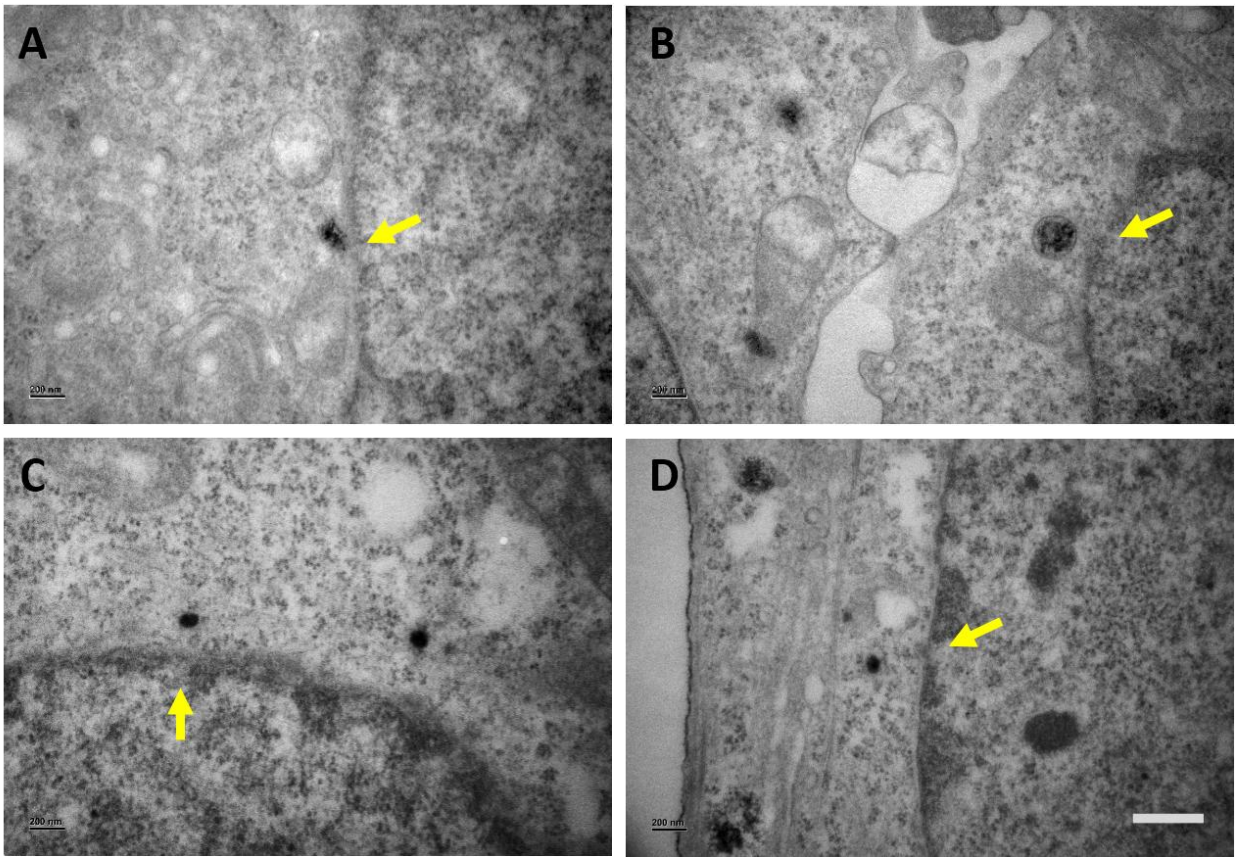

Figure 3.3.21. Labeled viral complexes in the perinuclear region. After 6-8 h of infection, numerous viral complexes were observed near the nucleus envelope, in close proximity to nuclear pores. Yellow arrows indicate the nuclear pores. Scale bar 400 nm.

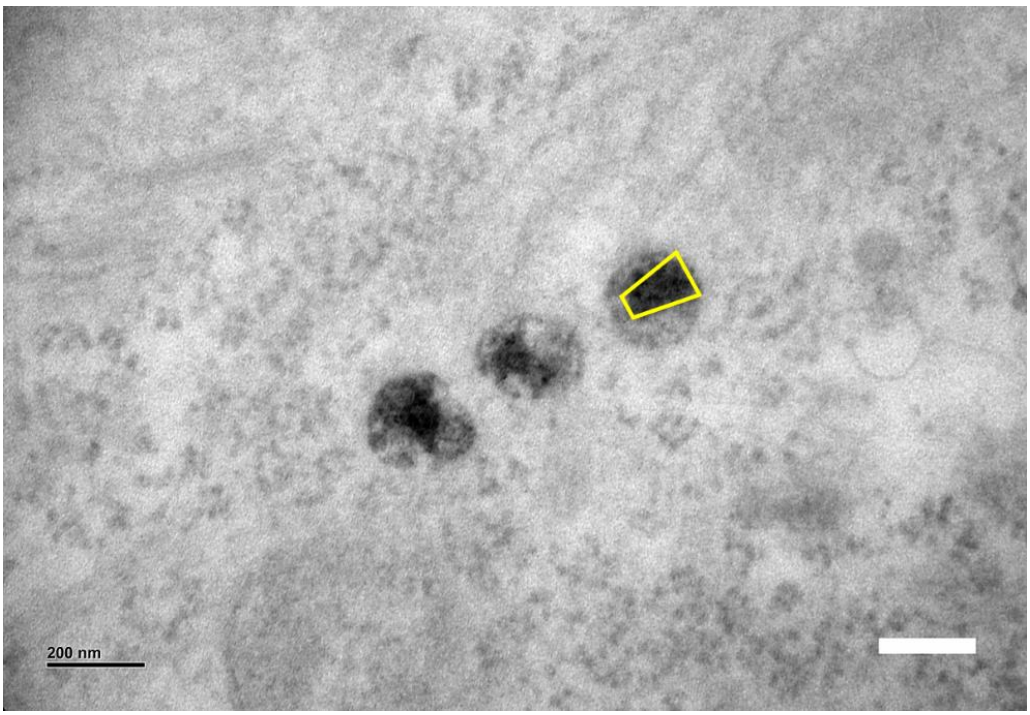

Figure 3.3.22. Capsid labeled by DAB precipitation. Free viral complexes found in the cytoplasm periphery revealed dense accumulation of inhomogeneous DAB precipitation in a capsid-like shape. Scale bar 200 nm.

3.3.6. Discussion and conclusions

Discussion

The HIV-1 VSV-G pseudotyped virus follows the same process of cellular internalization than the wild- type vesicular stomatitis virus. This virus enters the host cell via clathrin-mediated endocytosis (Matlin, Reggio et al. 1982; Sun, Yau et al. 2005) and is released in the cytosol due to a decrease of intravesicular pH (White, Matlin et al. 1981; Gruenberg and Maxfield 1995; Carneiro, Bianconi et al. 2002). The time rate of these processes is extremely fast, a half time of 2-3 min being required for the fusion with the cellular plasma membrane (Le Blanc, Luyet et al. 2005; Johannsdottir, Mancini et al. 2009) and 15-20 min for the cytoplasmic release from the endosomes (Mire, White et al. 2010). This timing is conserved for the pseudotyped HIV-1 (VSV-g) particles (Aiken 1997).

Free HIV-1 complexes are then transported towards the nucleus. During this transport, the RTC is transformed into the integration competent PIC that is internalized into the nuclear compartment. The timing of these processes takes up to 24 hours for the main part of virions. However as observed in our previous experiments and in agreement with the results reported by

Lelek (Lelek, Di Nunzio et al. 2012), it is possible to detect the first nuclear IN-TC clusters already 2 hours post infection.

In order to elucidate the mechanism of nuclear entry of NCp7, the efficiency of its nuclear internalization was quantified in conditions where the active nuclear import was inhibited by energy depletion of the infected cells. For this purpose, HeLa cells were infected and kept for one hour in serum free medium. Then, the medium was replaced by an energy depletion medium. Our preliminary experiments have shown that 30 min of incubation in ED medium are sufficient to inhibit completely the nuclear import. In order to validate this experimental approach, the experiments were in the first step realized with IN-TC containing viral particles.

HIV-1 integrase remains as a PIC member in the pool of viral proteins that are imported in the nucleus by the active pathway. Moreover, bearing an NLS this protein potentially participates on the nuclear import via interactions with the NUPS (Woodward and Chow 2010). Thus, in order to validate our experimental protocol of energy depletion, we observed the effect of the energy depletion on the efficiency of nuclear import of IN. The results show that 1 h incubation of infected cells in ED medium caused a 54% decrease of the density of nuclear IN-TC spots and a 50% increase of cytoplasmic/nuclear IN-TC containing particles. These findings validate the experimental conditions used and the same protocol was applied for NCp7-TC containing pseudoviruses. In this case, the effect was less pronounced though still present. The 30 % decrease of the number of NCp7-containing complexes internalized inside the ED cells and 2-fold increase of the ratio of cytoplasmic to nuclear complexes confirmed that NCp7 enters, at least partly into the nucleus by active transport. However, an alternative pathway of passive NCp7 internalization cannot be excluded. The larger sizes of the NCp7 nuclear complexes may result from the individual NCp7 molecules internalized by diffusion on nucleic acids or interacting with nuclear complexes.

In a next step, we compared the co-localization of IN-TC- and NCp7-TC-containing complexes with the nuclear pore complexes at the plasma membrane. As mentioned previously, NCp7 can diffuse to the nucleus as a free molecule or alternatively it could be internalized bound to PIC. In order to settle the nuclear internalization pathway for NCp7 molecules, we compared the level of co-localization of IN and NCp7 with NPCs in HeLa cells infected with HIV-1 pseudoviruses. In our experimental conditions and due to a fast photobleaching of the ReAsH labels, it is impossible to detect a single labeled molecule. Hence, we assume that the fluorescent spots observed in the red channel are either clusters of NCp7 molecules bound to RNA in the RTC or a pool of NCp7 molecules that might stay in the PIC after reverse transcription. Our

results showed that the level of the co-localization was comparable for both viral proteins indicating that the NCp7 might be present in the PIC docked to the nuclear pore. In contrast, the intracellular distribution of organic NPs taken as controls revealed an absence of co-localization with NPCs, due to their non-specific pathway of internalization and trapping in endosomes.

Finally, we imaged the intracellular NCp7-TC/ReAsH clusters by CLEM microscopy. The combination of light and electron microscopy presents the advantage of specific functional labeling (TC-ReAsH) and nanometric resolution of TEM. This approach permits to observe the intracellular distribution of viral particles by confocal fluorescence microscopy and the cell ultrastructure by TEM. Despite the limited diffusion of the DAB precipitates, free viral complexes were easily detected in the cytoplasmic compartment as black spots of ~200 nm. Moreover, this method of labeling permits to visualize free and endosome-trapped viral complexes and in some cases capsid like structures inside them, likely as a result of delayed reverse transcription. To our knowledge, we have for the first time applied the DAB photooxidation protocol to TC-ReAsH labeled viral complexes in CLEM. Only cytoplasmic viral complexes have been visualized by the present method. Possibly, the decrease of the number of NCp7-TC/ReAsH molecules in the viral complexes prior to the nuclear entry limits their detection in the nucleus. Consequently, due to the fast bleaching of fluorophores, nuclear viral complexes were not detected by confocal microscopy and the lack of produced oxygen species may prevent dense DAB precipitation for TEM detection. However, numerous dark puncta of viral complexes were observed in the close proximity of the nuclear envelope and NPCs, which is in the good agreement with confocal observation.

Conclusions

A significant number of NCp7 molecules is still present in the viral complexes when they dock to the nuclear pores. Interestingly, the nuclear localization is decreased by depletion of the active nuclear import indicating that part of the NCp7 molecules enters the nucleus being bound to PIC. However, as the effect of ED was more pronounced for IN-TC, our results do not exclude a partial entry of NCp7-TC molecules by passive diffusion. Moreover, CLEM observation revealed that a large number of NCp7-TC molecules are still present in the viral complexes before the nuclear entry and that viral complexes are localized in close proximity to the nuclear pores responsible for active import.

Chapter 4: Conclusions and perspectives

The main objective of my work was to investigate the fate of the HIV-1 nucleocapsid protein NCp7 during the early steps of infection by means of optical and electron microscopy. In order to reach this objective, we used VSV-g pseudotyped HIV-1 pseudoviral particles expressing NCp7 or IN fused to a tetracystein tag as a model. The insertion of this small tag preserves the infectivity and size of the virions. TC tags were labeled with biarsenical fluorophores, which can be used for both optical and electron microscopy. Using this powerful model system and state-of-the-art microscopy techniques, we enlightened the reverse transcription-dependent release of the NCp7 molecules prior to the nuclear import of the pre-integration complexes and investigated the mechanism of NCp7 nuclear internalization.

In order to prove the NCp7 release during reverse transcription *in cellulo*, we used the effect of fluorescence self-quenching of dyes at high concentration. As an extremely high number of NCp7 molecules ~2000 cover the RNA dimer in viral particles, the local concentration of TC tags reaches tenths of millimolar. At this concentration, FlAsH molecules are in the close proximity leading to a self-quenching of fluorescence. Therefore, a decrease of fluorophores concentration increases the distance between the dyes, which reduces the quenching effect and increases the brightness of the viral particles. As a proof of concept, the intensity of the viral particles containing 10%, 50% and 100% of NCp7-TC was measured on coverslips and inside infected cells. A strong fluorescence increase was observed with decreasing NCp7-TC content, confirming the self-quenching effect. Next, a progressive fluorescence intensity increase of intracellular 100% NCp7-TC particles was observed with time. Moreover, this increase was related to reverse transcription, suggesting that it is related to the remodeling of the viral complex during the DNA synthesis (during the reverse transcription, RNA compaction changes causing the modification of distances between the NCp7 molecules) and/or to progressive release of NCp7 protein from the viral core. Finally, the measurements of the fluorescence intensity as a function of the distance of the viral particles from the nucleus showed that the NCp7 molecules are mainly released in the perinuclear area. Taken together, our results confirm the hypothesis of a RT-dependent cytoplasmic release of NCp7 molecules near the nucleus.

To further confirm the release of NCp7 from the viral particles inside the infected cells, Fluorescence Lifetime Imaging Microscopy (FLIM) experiments may be performed. This imaging technique produces images, based on the values of the fluorescence lifetimes calculated from the exponential decay rate of the fluorescence detected in the pixels. As self-quenching of dyes reduces the fluorescence lifetime, FLIM imaging of the infected cells can provide an

information on the spatial localization of the different types of viral particles (densely labeled compacted RNA vs. DNA covered with less NCp7). Realizing the measurements at different times of infection can provide information about the timing and the cellular localization of RT-dependent RTC remodeling. However, FLIM measurements require high number of photons emitted from individual fluorophores. Therefore, photostable fluorophores would be more suitable for this method, than FlAsH.

Several hypothesis have been developed about the relation between these two processes: in the first model uncoating proposed to be required for the formation of the RTC; second model describes the gradual loss of the capsid during the RT process; finally, third model suggest the presence of the intact capsid all the way to the nucleus and uncoating prior the nuclear entry(Fassati and Goff 2001; Iordanskiy, Berro et al. 2006; Arhel, Souquere-Besse et al. 2007; Arfi, Lienard et al. 2009; Hulme, Perez et al. 2011). Thus, monitoring of the release of NCp7 by fluorescence dequenching of FlAsH can be combined with the labeling of capsid proteins for investigating the relationship between the uncoating and RT processes.

Finally, the tool enabling to monitor the RT via the NCp7 release can be further used to study the mechanism of HIV-1 inhibitors. Several promising NCp7 inhibitors are being developed in the laboratory (Grigorov, Bocquin et al. 2011; Avilov, Boudier et al. 2012; Mori, Nucci et al. 2014). This approach might help to enlighten their mechanism of action and to show which step of the viral cycle they perturb.

As the size of HIV-1 viral particles (around 100 nm) is far below the diffraction limit of optical microscopes, we applied high-resolution localization microscopy technique (PALM/STORM) to monitor the intracellular distribution of viral complexes containing TC-tagged NCp7 or IN. This allowed us for the first time to visualize intranuclear NCp7-TC/FlAsH clusters. The intranuclear density of clusters was strongly decreased for virions expressing 10% of labeled NCp7, confirming the probable release of NCp7 proteins from PIC prior to nuclear entry. Interestingly, the first intranuclear clusters were observed for the NCp7-TC and IN-TC labeled viral complexes within 2 hours of infection. It means that for some viruses the early steps of infection may be accomplished extremely quickly. It should be noted that we do not know if these clusters correspond to PICs. Therefore, this question should be studied in a next step by monitoring the co-localization of NCp7 with other PIC proteins and/or with the viral genome. After 14 hours of infection, the size of the intranuclear IN-TC complexes increased and their number decreased, which may be caused by the dissociation of the viral complexes after integration. The size increase of the puncta might be also explained by the fact that they correspond to defective integration sites. However, this size increase was not observed for

NCp7-TC labeled intranuclear complexes. The presence of AZT clearly perturbed the nuclear internalization of both IN and NCp7. The NCp7-TC labeled nuclear clusters were found only in 40% of cells and showed a size increase, suggesting that RT inhibition blocks the release of NCp7 and its nuclear internalization. However, the presence of nuclear NCp7 clusters in several AZT-treated cells might indicate an alternative nuclear entry.

Similarly, a smaller number of IN-TC clusters with bigger size and size dispersion have been found inside the nucleus in the presence of AZT, which supports the theory of nuclear entry of some aberrant PICs, which cannot create appropriate integration sites. Taken together, our first HR microscopy results provide the early insights into the intracellular distribution of NCp7 in the course of infection. However, more data is required to provide the solid statistical significance. As well, localization precision of the ~25 nm inside the cell may slightly influence the results of statistical analysis of the size modifications. Thus, more observations are needed for the comparisons of highly dispersed populations and their analysis.

We evidenced NCp7 inside the nucleus by high-resolution microscopy. Previously, the role of NCp7 in integration (Poljak, Batson et al. 2003) was investigated *in vitro,* revealing that NCp7 basic residues and zinc fingers stabilize the IN at the LTR ends of vDNA and promote the formation of a viral complex ready for integration. However, the presence of NCp7 in PIC and its role during the integration was not confirmed *in cellulo.* The presence of IN inside the nucleus within the PIC is required for the integration step. In order to prove the presence of the NCp7 inside the PIC, IN and NCp7 could be co-localized by dual-color immunolabelled IN and NCp7-TC/FlAsH high-resolution microscopy. However, labeling of IN in viral complexes already labeled on NCp7-TC by FlAsH in infected cells can be used several complications. The immunolabeling protocol (and notably the permeabilization step) may influence the integrity of the TC tag and properties of FlAsH. Similarly, the viral DNA could be labeled via fluorescence in situ hybridization (FISH) or by click labeling the fluorophore with an azide group (5-ethynyl-2'-deoxyuridine (EdU)) (Salic and Mitchison 2008; Peng, Muranyi et al. 2014). Thus, a protocol combining several labelling approaches should be carefully optimized prior to imaging experiments. To finalize this study, the nuclear presence of NCp7 should be confirmed by additional methods, such as immunoprecipitation. NCp7 can for instance be immunoprecipitated with host cell partners for entry like Nup153, Nup358 and histone H3K36me3, associated with integration sites.

Next, we would like to define the nuclear internalization pathway for NCp7. The protein can enter the nucleus by an active nuclear import within the PIC or by passive diffusion, both through the nuclear pore complex (NPC). Moreover, it was shown in our laboratory that NCp7

alone or in complex with nucleic acids can bind with high affinity to negatively charged lipid membranes and destabilize the lipid bilayer (Kempf, Postupalenko et al. 2015). Therefore, by perturbing lipid membranes, NCp7 could enable a transient nuclear envelope disruption and translocation of NCp7 to the nucleus independently of the nuclear pore complexes.

HIV-1 is thought to enter into the nucleus of non-dividing cells mainly via an active import mediated by nucleopores (Bukrinsky, Sharova et al. 1992). Accordingly, depletion of active nuclear import caused a decrease by 54% of the intranuclear density of IN clusters in HeLa cells. For NCp7 the decrease was more moderate, being around 30%. Moreover, for both types of clusters a strong perinuclear localization and an increase of the ratio of cytoplasmic to nuclear clusters inside ED cells were observed. These results indicate, that inhibition of the active import strongly perturbs the nuclear internalization of the viral complex, but do not prevent the NCp7 entry via the diffusion pathway.

. In order to obtain a more pronounced difference (if it is the case) between normal infection and infection in energy-depleted cells, the number of intranuclear clusters should be studied at longer times post infection, when more viral complexes reach the nuclear compartment. It would also enlighten the timing of the turnover of entry, integration and complex dissociation cycles.

Since several Nups are involved in the viral nuclear import, visualization of the labeled NCp7/IN viral complexes in cells expressing Nup153-eGFP and Nup214-eGFP has been done by confocal microscopy. Significant co-localizations were observed for both types of clusters with Nup214 and Nup153. These observations suggest the presence of a pool of NCp7 molecules in the PIC when the latter is docked on the nuclear envelope.

The density of NPCs on the nuclear envelope is very high, therefore when imaged by optical microscopy several pores can overlap because of the resolution limit and the co-localization of viral particles and the NPC can be biased. These limitations can be overcome by transmission electron microscopy. Therefore, we imaged NCp7-TC/ReAsH clusters in cells by the CLEM technique combining confocal microscopy and TEM. We observed free and endosome-trapped viral complexes. In agreement with the hypothesis of a microtubule-dependent transport of HIV-1 from the cell periphery towards the nucleus, viral particles were observed near the cytoskeleton filaments. In the perinuclear area, viral complexes were found in close proximity to nucleopores and sometimes dark capsid like structures were observed near the NPCs confirming the hypothesis that a significant number of NCp7 molecules stays with PIC until the nuclear docking. This observation is in agreement with the hypothesis of late

uncoating prior to nuclear entry proposed by Arhel et al (Arhel, Souquere-Besse et al. 2007). It should be noted, that NCp7-TC/ReAsH viral complexes have been observed by TEM only inside the cytoplasm. This could be explained by the low density of the labeled proteins in the nucleus. Additionally, low-density DAB precipitates can be masked by the dense chromatin inside the nucleus.

Altogether our data showed that an important fraction of NCp7 molecules is released from the RNP during reverse transcription but a pool of nucleocapsid proteins remains inside the PIC at least until its docking at the nuclear pore complexes. Therefore, we suggest that NCp7 proteins enter the nucleus within the PIC via active nuclear import. However, entry via passive diffusion of free NCp7 molecules cannot be completely excluded. Moreover, the presented method of monitoring reverse transcription by the release of NCp7 proteins can be used for antiviral drug development.

Chapter 5: Another works

5.1. Tuning luminescent properties of CdSe nanoclusters by phosphine surface passivation

Introduction

As a student on co-direction between the University of Strasbourg and Taras Shevchenko National university of Kiev, I was participating in the development of the new fluorescent labels for biological imaging based on semiconductor nanoclusters. These small (<2 nm) and photostable nanoparticles exhibit extremely sharp absorption peak and high sensitivity to the environment. However, they have low quantum yield (QY) and require additional functionalization prior to imaging application. Thus, main objective of the project was to develop post-synthesis shell for the stabilization and improvement of NPs QY.

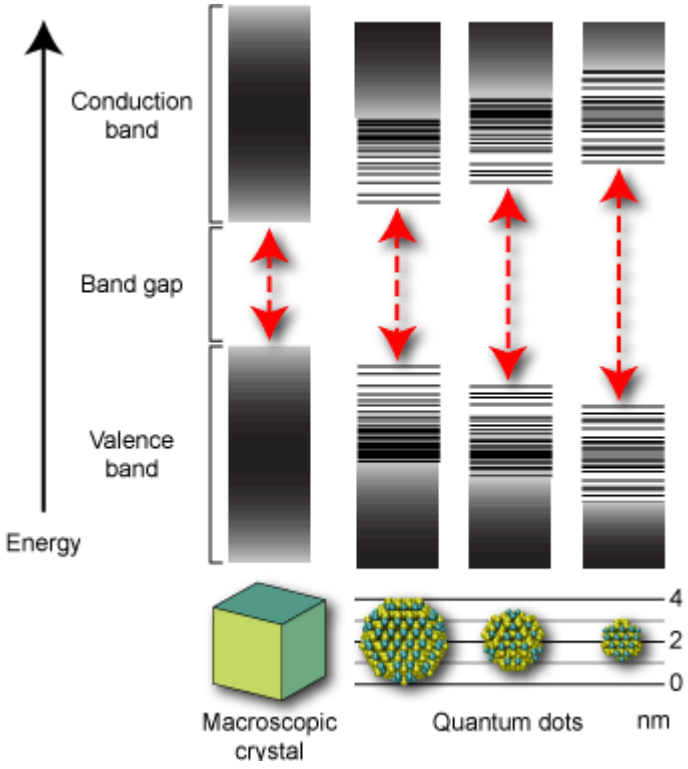

Figure 5.1.1. Quantum confinement in semiconductors. Energy levels of electrons in semiconductors are arranged into a number of bands of energy (Bulk matter/Macroscopic crystal). "Band gap" energy is defined for the energy difference between the top of valence band and the bottom of the conduction band. Transitions of electron between this two bands are sometimes permitted, sometimes not and requires certain amount of energy. Confinement energy depends on the size of NPs and can be tuned during the synthesis. Within the decrease size of NPs band gap energy is growing and spectrum of particles shifts to the blue region. Thus discrete wave function of QDs as molecule can be constructed from the individual atoms orbitals of Highest Occupied Molecular Orbital (HOMO) (Valence band) and Lowest Unoccupied Molecular Orbital (LUMO) (Conduction band).

Semiconductor nanoparticles (group of II-VI, IV-VI, III-V elements) are parts of matter which have at least one dimension less than 50 nm and exhibit quantum confinement. This size-

dependant effect occurs when size of the object is less or equal to the Bohr diameter (strong confinement) of exciton, formed by the bound couple of electron hole. Due to the quantum confinement in semiconductors band gap becomes larger with decreasing size and additional kinetic energies of electrons and holes appeared as energy levels at the edges of conduction and valence bands (Fig.1). Thus, energy of absorption and emissions are changed and can be easily tuned by the change of size. CdSe nanoparitcles are the most studied due to its tuned emissions which covers whole visible spectrum. These particles are stable, bright, extremely photostable and are used in diodes, photovoltaic devices and as labels for biological imaging (Kim, Garcia de Arquer et al. 2015)(Michalet, Pinaud et al. 2005).

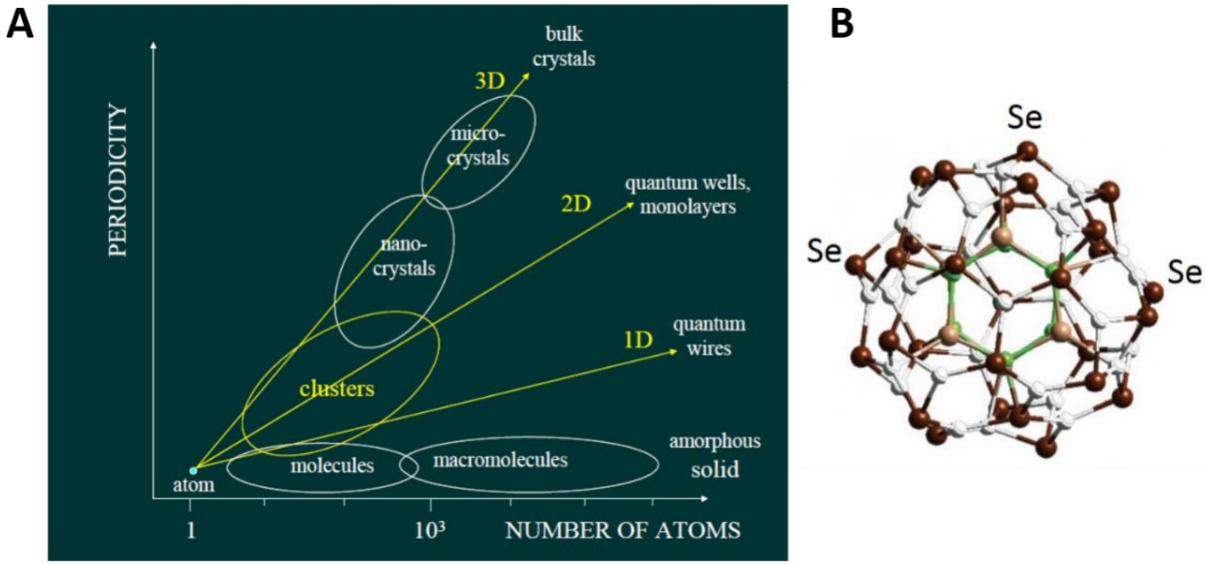

Figure 5.1.2. Nanoclusters. (A) Classification of structures with regard to the periodicity and number of atoms; (B) Calculated structure of the CdSe33 nanocluster.

We are particularly interested in the 'magic-sized' nanoclusters. Cluster structures exhibit lack of periodicity (nanocrystals) and sometimes are comprised from the bigger number of atoms, compare to molecules (Fig.2). As well bigger fraction of the atoms on the surface makes them highly sensitive to the passivation of surface and to the environment. Highly thermodynamically stable structures made from some discreet numbers of atoms or 'magic numbers'. Whereas 'magic-size' clusters have high rate of occurrence during the synthesis. These particles exhibit extreme stability, small size (1.5-2nm) and can be produced in macroscopic amounts with narrow size distribution.

Macroscopic amount of $CdSe_{33}$ and $CdSe_{34}$ nanoclusters produced by the two-phase water-toluene synthesis are capped by the long-chain aliphatic amines. However, this capping agent exhibit high affinity to the atoms of Cd, whereas surface Se atoms remained unbound. Thus, Se dangling bounds create the trap states and lead to the non-radiative recombination and

possible to low QY. Therefore, surface passivation, especially capping of Se atoms is a key to the stabilization and improved brightness. Based on the previous works of synthesis and post-treatment of NPs phosphine derivatives have been chosen as additional surfactant known for the high affinity to the Se. In the following study we used triphenylphosphine(TPP), trioctylphosphine (TOP) and tris(pentafluorophenyl) phosphine (TPFP) as additional capping agents for CdSe NCs.

5.2. Publication

Methods and Applications in Fluorescence

RECEIVED
4 June 2016

REVISED
13 October 2016

ACCEPTED FOR PUBLICATION
18 October 2016

PUBLISHED
25 November 2016

PAPER

Tuning luminescent properties of CdSe nanoclusters by phosphine surface passivation

Iryna Lysova[1,2,3], **Halina Anton**[2,3], **Igor Dmitruk**[1] **and Yves Mely**[2]

[1] Taras Shevchenko National University of Kyiv, 64/13, Volodymyrska Str., Kyiv 01601, Ukraine
[2] Laboratoire de Biophotonique et Pharmacologie, UMR 7213 CNRS, Université de Strasbourg, Faculté de pharmacie, 74 route du Rhin, 67401 ILLKIRCH Cedex, France
[3] These authors equally contributed to the work.

E-mail: igor_dmitruk@univ.kiev.ua

Keywords: semiconductor nanoclusters, phosphines, spectroscopy

Abstract

Appropriate surface ligands are required for tuning the physicochemical and photophysical properties of nanoclusters (NCs). These surface ligands are especially critical for passivating the small $(CdSe)_{33,34}$ NCs where the majority of atoms are at the NC surface. In this study, triphenylphosphine (TPP), trioctylphosphine (TOP) and tris(pentafluorophenyl)phosphine (TPFP) have been tested as capping agents for alkylamine-coated CdSe NCs. TPP and TOP compounds are found to increase the quantum yield of photoluminescence (PL) from 0.15% to 0.6% and 0.53%, respectively, and to preserve this increased PL with time, probably by preventing charge leakage as a result of their binding to Se atoms. Since no dramatic change in the shape of NCs' PL spectrum occurs after surface treatment, both the exciton band and the low-energy broad band in magic NCs are thought to describe the intrinsic luminescence properties of the NCs. As a result, the PL increase due to Se passivation is thought to be mainly caused by a decrease in the efficiency of the NC nonradiative pathways.

Introduction

Nanosize semiconductor structures possess unique physical and chemical properties. Decreasing the size of the crystals to a few nanometers results in quantum confinement and changes in the energy levels. Semiconductor nanoclusters (NCs) which form thermodynamically stable structures with well-defined 'magic numbers' of atoms [1, 2] are of particular interest. These NCs 1–2 nm in diameter present a specific core-cage structure different from the bulk that determines their physical and optical properties [3]. In particular, $(CdSe)_{33}$ and $(CdSe)_{34}$ NCs display typical sharp blue and UV absorption peaks and photoluminescence (PL) in the blue to green part of the spectrum [4].

Several synthesis protocols have been proposed for the production of stable monodisperse populations of magic-sized NCs. One-pot synthesis of $(CdSe)_{33}$ and $(CdSe)_{34}$ capped by decylamine in a two-phase water-toluene system at room temperature under atmospheric conditions has been published [3, 5]. Aqueous synthesis of a highly monodisperse colloidal solution of magic-sized CdSe NCs capped by L-cysteine has also been described [4]. Moreover, dodecylamine-capped NCs with larger sizes in nonanoic acid at 100 °C–200 °C under inert atmosphere [6] were also synthesized. At the surface of these capped NCs, amine or sulfhydryl groups bind to Cd atoms [7]. In contrast, selenium (Se) atoms are not passivated, so that their free electron pair can act as a dangling bond which can easily bind an ion or active molecule from the solution and act as an effective hole trap on the NC surface. These trap states of exposed Se atoms are thought to be responsible for the very low PL quantum yield of NCs [8, 9]. Consequently, the PL emission could be enhanced by passivating the surface Se states with appropriate ligands [7, 10–12]. In line with this hypothesis, an increase of the PL of the NCs has been obtained by addition of trioctylphosphine oxide (TOPO) and phosphonic acid ligands that bind to Se atoms during synthesis [13]. Likewise, an increase of the brightness of NCs can also be achieved by the post-synthesis addition of triphenylphosphine (TPP) to polyethylene glycol thiolate- or alcylamine-capped NCs in organic solvents [7, 10]. A bright blue exciton emission in extremely small CdSe nanoparticles was reported in [7], but the applied treatment resulted in a change of the structure and formation of nanocrystals.

© 2016 IOP Publishing Ltd

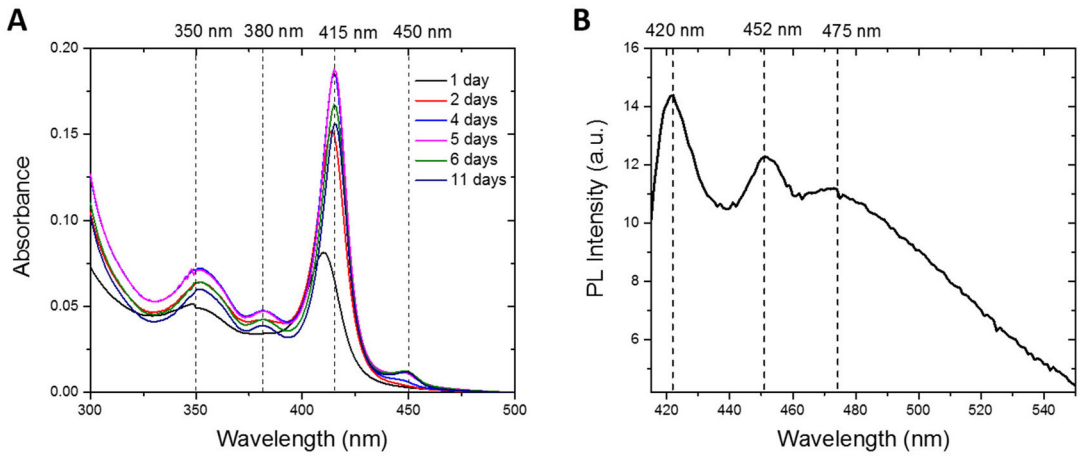

Figure 1. Absorption (A) and emission (B) spectra of NC synthesized in toluene. The absorption spectra were recorded at different times post-synthesis.

In this context, the aim of this work was to quantify the effect of the post-synthetic surface passivation of $(CdSe)_{33,34}$ in toluene on NC PL. We chose three different phosphine containing ligands—TPP, tris(pentafluorophenyl)phosphine (TPFP) and trioctylphosphine (TOP)—for their capacity to bind to the Se atoms on the NC surface and reduce the trap states in this way. We prepared magic-sized NCs in toluene and monitored their optical properties immediately after the addition of the ligands and with time. Our data showed that the post-synthesis addition of TOP and TPP increased the PL quantum yield by a factor of four and prevented its strong drop with time. In contrast, the addition of TPFP had only a limited effect.

Experimental section

Materials

Se powder (Se > 99%), cadmium sulfate ($CdSO_4 * 8/3H_2O$), sodium sulfite (Na_2SO_3), alkylamines (octylamine), TPP, TPFP, toluene and methanol were purchased from Sigma Aldrich. TOP was purchased from Alfa Aesar. Pure water with 18.2 MΩ·cm resistivity at 25 °C was used for the preparation of the solutions.

One-pot synthesis

A precursor of Se (0.05 M) is prepared by mixing 100 mg Se powder (99.9%) with 478 mg of Na_2SO_3 powder (99%) in water at 80 °C–90 °C under magnetic stirring. $CdSO_4$ (0.15 M) salt solution is prepared freshly in water. For the final mixture, reagents are added in the following order: 2 mL of octylamine, 10 mL of pure methanol, 19 mL of water, 1 mL of Se precursor and 10 mL of cadmium precursor. Up to 30 min are allowed between each chemical/solution addition to ensure better mixing. Directly after adding the last component, the stirring is stopped and 30 mL of toluene is added gently without mixing. The final solution is kept up to 10 d at room temperature in order to obtain stable and optically mature clusters.

Mixtures of phosphine derivatives and 200 μL of cluster solution are prepared freshly before the measurements and are diluted 40 times in toluene to obtain samples with absorbance <0.05 at 405 nm. The final phosphine concentrations in the cuvette range between 0.5–5mM.

Optical measurements

UV–vis spectrometry of CdSe nanoparticles in suspension before and after adding phosphine derivatives is performed with a UV–Vis–NIR spectrophotometer Agilent Cary 4000. In addition, the PL of these particles is recorded with a HORIBA FluoroMax-4 Spectrofluorometer. For all measurements in cuvettes, samples are diluted 40 times with toluene. The excitation wavelength is 405 nm.

The PL quantum yield (QY) of the magic-sized CdSe NCs is determined using 7-(diethylamino) Coumarin-3-carboxylic acid (DEAC) in methanol as a reference (QY $\Phi_{REF} = 0.04$) [14]. The solutions of DEAC are diluted with methanol to obtain an absorbance smaller than 0.1 at 405 nm. The PL spectra are measured at room temperature with an excitation wavelength of 405 nm and the integrated emission intensity of NCs (E_{NC}) is compared with the integrated intensity of DEAC emission (E_{REF}). The quantum yield of NCs is then calculated using equation (1):

$$\Phi_{NC} = \left(\frac{E_{NC}}{E_{REF}}\right) \times \left(\frac{A_{REF}}{A_{NC}}\right) \times \left(\frac{n_{NC}^2}{n_{REF}^2}\right) \Phi_{REF}, \quad (1)$$

where A_{REF} and A_{NC} are the absorbances at the excitation wavelength (405 nm), n_{NC} and n_{REF} are the refraction indexes of toluene and methanol, respectively.

Results and discussion

Maturation of the CdSe NCs in toluene

Formation of the CdSe NCs is monitored by UV–Vis absorption spectroscopy (figure 1(A)). Several hours after adding the last component, an absorption spectrum specific for $(CdSe)_{33,34}$ appears [3] with a

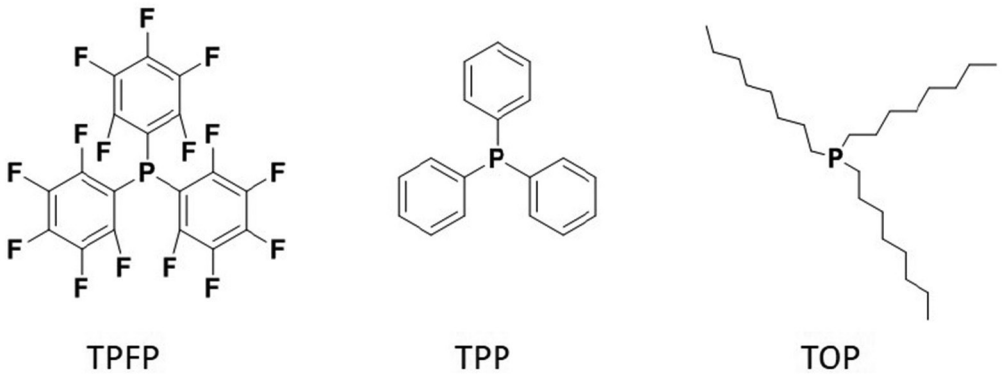

Figure 2. Structures of TPFP, TPP and TOP capping agents.

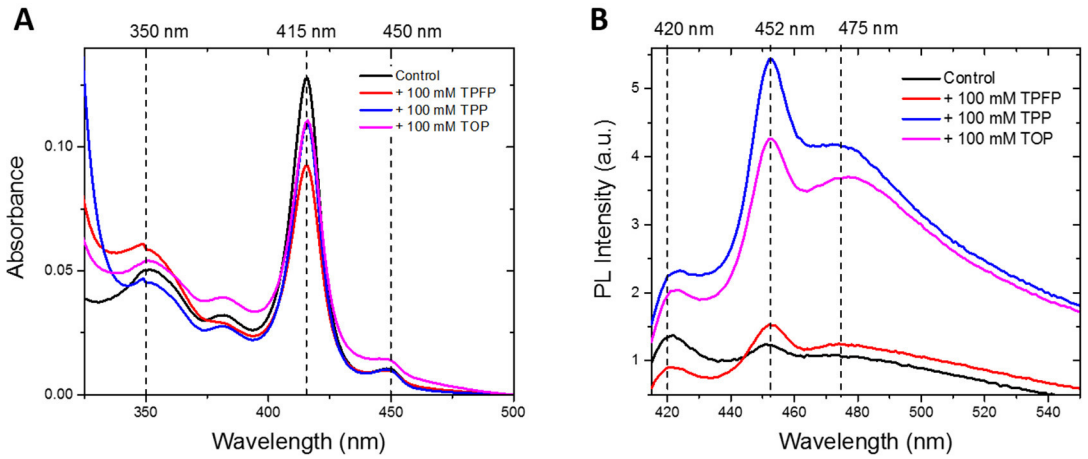

Figure 3. Absorption (A) and PL spectra (B) of octylamine-capped CdSe NCs in the presence of different phosphines.

peak at 410 nm that increases and sharpens with time, evidencing the growth and maturation of the NCs. In addition, the position of this peak red-shifts with time to 415 nm. Peaks at 350 nm and 380 nm corresponding to the excited states of excitons in $(CdSe)_{33,34}$ NCs follow similar trends with time [4]. After 5 d, a small band appears at 450 nm, indicating the formation of larger clusters [2, 15] or nanoplatelets [16, 17]. At the same time, the absorbance of the NCs slightly drops, but then remains stable for several weeks. The estimation of cluster size can be done using an empirical relation between the CdSe NPs diameter and the exciton peak position [5, 18]. For particles with an absorption peak at 415 nm, we can expect about ~1.2 nm size. But we are aware that this estimate is only approximate since it is based on experimental data for crystalline nanoparticles, while magic NCs have a different structure. After 4–5 d of maturation, the NCs emit a weak PL (figure 1(B)) with two sharp peaks at 420 nm and 452 nm corresponding to the absorption peaks 415 nm and 450 nm [17] and a broad band at 475 nm likely due to the recombination of excitons at the low energy surface states of these NCs [4] or to the internal relaxation of excitons in the magic NCs.

Effect of phosphines on NC PL

In the next step, we test the effects of the surface passivation of CdSe NCs by three different phosphines (TPP, TPFP and TOP) (figure 2) as additional capping agents. Phosphines are widely used in the synthesis of semiconductor nanocrystals [19–24].

Figure 3 shows the changes in the absorption (A) and PL (B) of octylamine-capped NCs, induced by the phosphines added at 100 mM. In all three cases, the absorption of the 415 nm peak is slightly reduced as compared to the control NCs, probably indicating a slight dissociation of the $(CdSe)_{33,34}$ NCs. The absorption band at 450 nm stays stable except with TOP, where a slight increase is observed. Transformation of the 415 nm peak into the 450 nm peak in this case suggests that NCs aggregate into dimers or nanoplatelets, as reported in [25]. Since no further shift of the 450 nm peak is observed, the formation of CdSe nanoplatelets looks more likely [26]. Overall, the absorption spectra of NCs are only slightly modified by phosphines. In contrast, more dramatic effects are observed on the PL, which is increased by all phosphines. The PL QY value of pure NCs is extremely low, being 0.15%, in line with previous reports [8, 13]. In the presence of 100 mM TPFP, TPP, and TOP, the QY values increase to 0.2%,

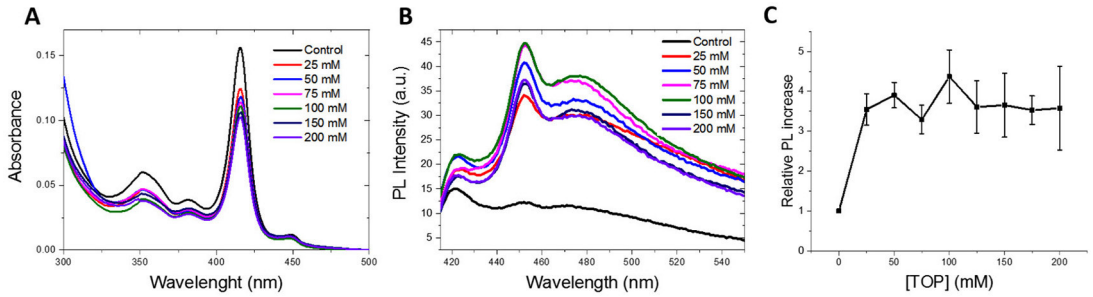

Figure 4. Absorption (A), PL spectra (B), and relative PL increase at 452 nm (C) of octylamine-capped CdSe NCs in the presence of TOP. The relative PL increase is defined with respect to the PL of the NCs in the absence of TOP.

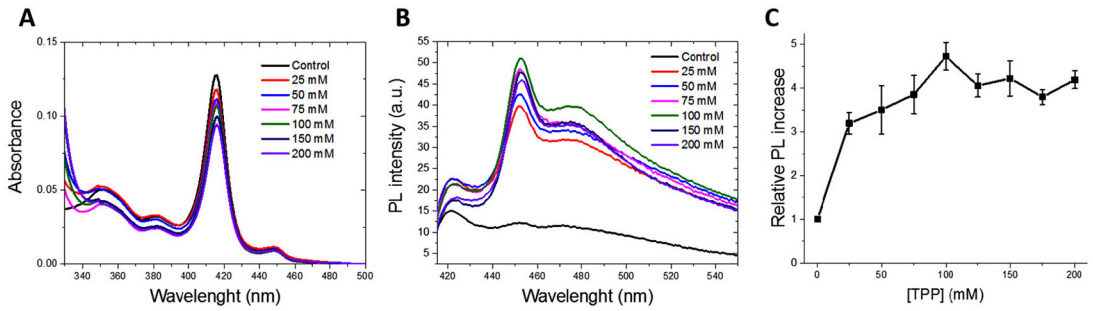

Figure 5. Absorption (A) and PL spectra (B), and relative increase of PL intensity at 452 nm (C) of octylamine-capped CdSe NCs in the presence of TPP. The relative PL increase is defined with respect to the PL of the NCs in the absence of TPP.

0.6%, and 0.53%, respectively. This increase appears to be mainly related to the large increase of the broad band at 475 nm, which has been related to the surface properties of the NCs [27–29]. Therefore, our data confirm that the binding of phosphines to the Se atoms at the NC surface can decrease the ability of Se atoms to create nonradiative trap states, which in turn results in a PL increase. Thus, among the possible causes of quantum yield increase, namely, a decreased efficiency of nonradiative pathways, an increased efficiency of radiative pathways, or a redirection of the excitation between radiative and nonradiative pathways, the first one seems the most likely.

Next, in order to disclose the best ligand to cluster ratio in terms of brightness enhancement, we add 25–200 mM phosphines to the clusters in toluene. For all TOP concentrations, a slight decrease in the absorption peaks at 350 and 415 nm is observed (figure 4(A)), but with no changes in the peak positions. Thus, all the tested concentrations of TOP only moderately affect the NC structure. In contrast, TOP causes a large increase in PL with a sharpening of the PL spectrum (figures 4(B) and (C)). A nearly four fold increase in PL intensity at 452 nm relative to the control sample (without TOP) is already observed at the lowest TOP concentration tested, and does not change at higher TOP concentrations (figure 4(C)), indicating that the lowest concentration (25 mM) already provides the full effect. TOP is a very good donor of electrons and, due to its alkyl chain, can easily access the Se atoms at the surface of the octylamine capped NCs. By donating electrons, TOP is thought to remove the dangling bonds at the NC surface, and thus increase the PL.

The effect of TPP on NCs is similar to that of TOP, with a slight decrease in the absorption spectra (figure 5(A)) and a strong PL increase (figure 5(B)) in the presence of increasing TPP concentrations. The highest effect is observed at 100 mM (figure 5(C)), indicating a slight shift in concentration in respect to TOP. This shift may likely be due to the lower electron donor ability of TPP in respect to TOP, so that a higher concentration of TPP is needed to remove the Se dangling bonds at the NC surface.

Figure 6 shows the effect of TPFP on the spectral properties of NCs. Upon TPFP addition to the NC solution, the absorption of the main 415 nm peak decreases by 30% and then stays stable. The PL of the cluster solution shows an initial drop likely due to the corresponding drop in the absorbance at the excitation wavelength, followed by a significant increase. The relative enhancement, as compared to the control sample and corrected for the decrease in the absorbance at 405 nm, reaches a factor of only 1.4 for 200 mM TPFP concentration (figure 6(C)), indicating that TPFP is less efficient than TOP and TPP in removing the Se dangling bonds at the NC surface.

The photophysical properties of NCs in the presence of phosphines have also been monitored with time. To this aim, we perform a first series of experiments, where phosphine is added to the stock solution of NCs, and then diluted 40 times. Measurements are done at $t = 0$, 30, 120 and 240 min, after dilution and

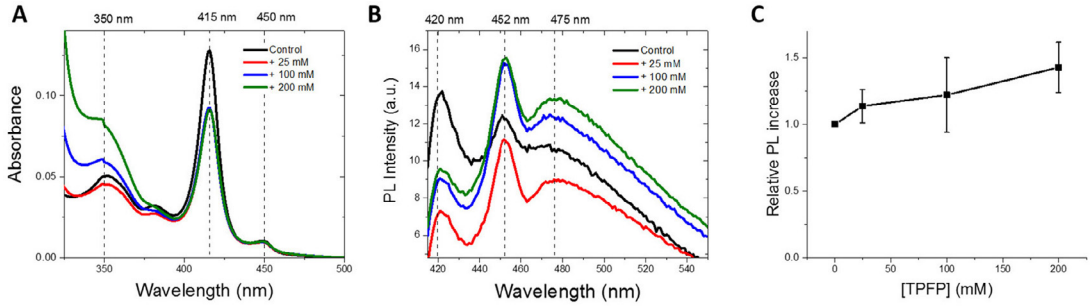

Figure 6. Absorption (A) and PL (B) spectra of octylamine-capped CdSe NCs in the presence of different concentrations of TPFP. (C) Relative PL intensity increase of NCs treated with TPFP relative to the control at 452 nm and corrected for the drop of absorbance at 405 nm excitation wavelength.

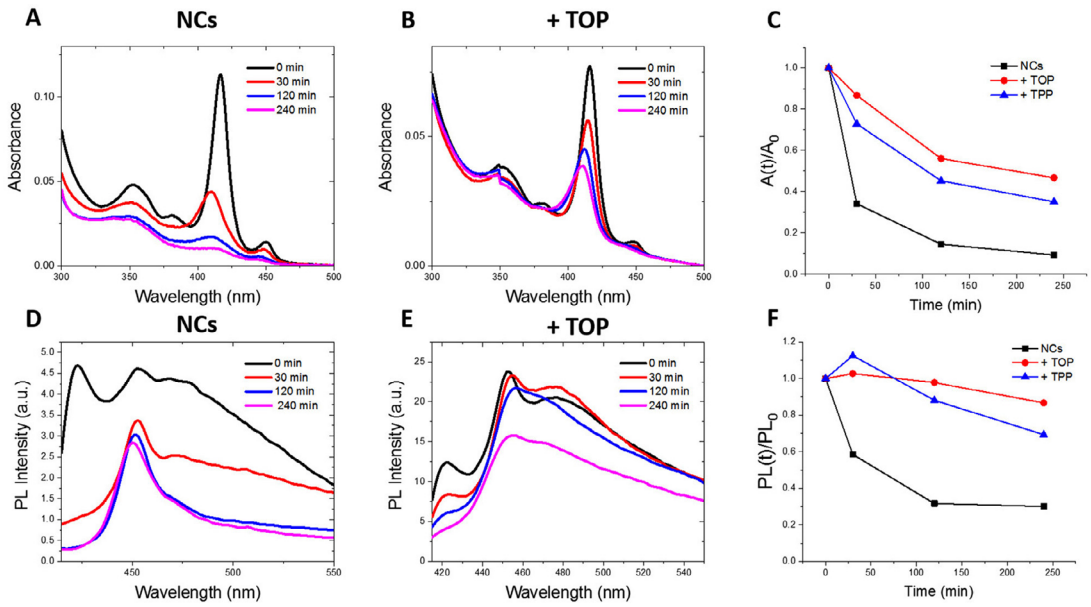

Figure 7. Absorption and PL spectra of diluted samples of octylamine-capped CdSe NCs without ((A) and (D)) or with additional capping with 75 mM TOP ((B) and (E)), and time dependence of the absorbance at 415 nm (C) and PL at 475 nm (D) of NCs without or with additional TOP and TPP capping. In (C) and (F), the absorbance at 415 nm and intensities at 475 nm are compared with the values at $t = 0$.

compared with measurements on control samples in the absence of phosphines.

On the control samples, we observe a strong time-dependent decrease in the 415 nm absorption peak accompanied by a blue-shift of this peak, suggesting that NCs may be destabilized by the dilution and dissociate with time (figure 7(A)). The dissociation of NCs is confirmed by the disappearance of the 420 nm peak and the broad band at 475 nm in the PL spectra (figure 7(D)).

Interestingly, the decrease in absorbance and the shift of the 415 nm peak is much less pronounced when the NCs are capped by TOP (figures 7(B) and (C)), suggesting that the phosphines stabilize the NCs structure and/or provide better isolation of the CdSe core from the solution. Similarly, the changes in the PL spectra at both the 420 nm and 475 nm band (figures 7(E) and (F)) are much less pronounced and slower than in the absence of phosphines, confirming that the reaction with TOP slows down NC dissociation. Very similar data are obtained when NCs react with TPP, suggesting that TOP and TPP similarly stabilize the NCs (figures 7(C) and (F)).

In the next step, the samples have been prepared with a slightly different protocol, in which the phosphine solutions are added to NC stock solution, kept in contact for 30, 120 and 240 min and then diluted just before absorption and PL measurements. Using this protocol, the absorbance remains constant for both TOP and TPP treatment between 30 and 120 min (figure 8(A)), indicating the limited dissociation of NCs. For PL spectra, both phosphines lead to an immediate increase in PL as compared to the control. Particularly, they cause a dramatic growth of intensity of the 452 nm peak and low-energy broad band, with just a slight growth of the 420 nm peak. The increase of the 452 nm peak, as well as the dependence of this peak on the phosphine concentration (figure 4(B)), are consistent with an aggregation of the magic NCs into nanoplatelets and efficient passivation of Se dangling bonds at

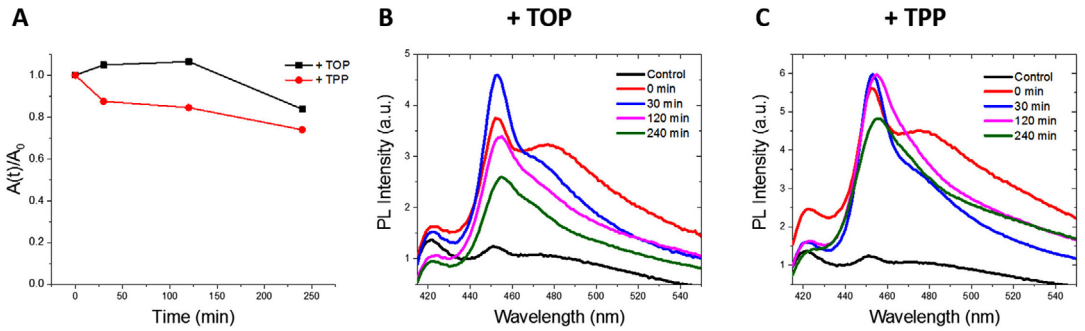

Figure 8. Time dependence of the absorption (A) and PL spectra ((B) and (C)) of phosphine-capped NCs. (A) Absorbance at 415 nm of NCs relative to their absorbance at time $t = 0$. Emission spectra at 0, 30, 120 and 240 min after addition of TOP (B) and TPP (C).

the surface of nanoplatelets and magic NCs. For TOP, a further increase in the 452 nm peak accompanied by a decrease of the low-energy emission is observed after 30 min, suggesting that the formation of nanoplatelets continues. After 120 min and 240 min, a continuous decrease in PL is observed, indicating that the effect of passivation of Se atoms decreases with time. One possible interpretation is that NCs are further converted into nanoplatelets but their oxidation decreases the PL.

For TPP, we observe similar but more moderate changes with time, suggesting that in concentrated solutions, TPP shows a stronger protecting effect than TOP. This may be due to the higher reduction potential of TOP as compared to TPP. Indeed, the TOP molecules bound to the Se atoms at the NC surface may be rapidly oxidized in TOPO and lose their beneficial effect.

For several applications, it is desirable to dry the nanoparticles in order to dissolve them in other solvents or mix them with other compounds, such as polymers. However, this is very challenging with very small nanoparticles, which are prone to aggregate and undergo structural changes. A few attempts were made [7], but XRD data indicate that the structure of the NCs after such treatment changed to a crystalline one. That is why we dealt with nanoparticles in colloid solution only and performed all treatments at room temperature in order to preserve the original core-cage structure of the magic CdSe NCs.

Conclusions

We have investigated the effect of the post-synthetic addition of three different phosphines on the stability and optical properties of octylamine-capped CdSe NCs in toluene. Our results show that passivation of the NC surface by all three phosphines provides a PL enhancement, likely by preventing leakage of the charges from the NCs as a result of their binding to Se atoms. TPFP is less efficient, probably due to the steric hindrance of its aromatic rings that reduces the accessibility of the phosphine reactive group. The effect of TOP and TPP is more pronounced, giving a four-fold increase in PL QY, but we do not observe any decrease of intensity of the low-energy 475 nm band or substantial increase of the exciton band at 420 nm after phosphine passivation of Se dangling bonds on the surface. This suggests that, unlike crystalline nanoparticles, both the exciton band and the low-energy broad band in magic NCs are probably related to the intrinsic luminescence properties of the NCs, or that the low-energy band is caused by surface traps not connected with Se dangling bonds. Thus, the low-energy band of the magic NCs may be at least in part the result of internal relaxation processes not connected with surface traps. As a consequence, the increase of PL due to Se passivation is thought to be caused by a decrease in the efficiency of NC nonradiative pathways. Furthermore, the stability of NCs in time has been studied in diluted and concentrated samples. On dilution, passivation decreases the rate and extent at which the NCs dissociate. In concentrated solutions, TPP preserves the PL of NCs with time more efficiently than TOP, probably as a result of its lower oxidation rate. Overall, our data show that among the three phosphines tested, TPP provides the best NC surface passivation.

Acknowledgments

This work was supported by Labex NIE, CNRS and University of Strasbourg. IL had a fellowship from the French Embassy in Ukraine.

References

[1] Ptatschek V, Schmidt T, Lerch M, Müller G, Spanhel L, Emmerling A, Fricke J, Foitzik A H and Langer E 1998 Quantized aggregation phenomena in II–VI-semiconductor colloids *Ber. Bunsenges. Phys. Chem.* **102** 85–94

[2] Romanyuk V R, Dmitruk I M, Barnakov Y A, Belosludov R V and Kasuya A 2009 Ultra-stable nanoparticles in *A*(II)*B*(VI) (*A*(II) = Cd, Zn; *B*(VI) = S, Se, Te) compounds *J. Nanosci. Nanotechnol.* **9** 2111–8

[3] Kasuya A *et al* 2004 Ultra-stable nanoparticles of CdSe revealed from mass spectrometry *Nat. Mater.* **3** 99–102

[4] Park Y S *et al* 2010 Aqueous phase synthesized CdSe nanoparticles with well-defined numbers of constituent atoms *J. Phys. Chem.* C **114** 18834–40

[5] Bacherikov Y Y D, Davydenko M O, Dmytruk A M, Dmitruk I M, Lytvyn P M, Pro-kopenko I V and Romanyuk V R 2006 CdSe nanoparticles grown with different

chelates *Semicond. Phys. Quantum Electron. Optoelectron.* **9** 75–9
[6] Kudera S *et al* 2007 Sequential growth of magic-size CdSe nanocrystals *Adv. Mater.* **19** 548–52
[7] Dolai S *et al* 2014 Isolation of bright blue light-emitting CdSe nanocrystals with 6.5 kDa core in gram scale: high photoluminescence efficiency controlled by surface ligand chemistry *Chem. Mater.* **26** 1278–85
[8] Schreuder M A, McBride J R, Dukes A D, Sammons J A and Rosenthal S J 2009 Control of surface state emission via phosphonic acid modulation in ultrasmall CdSe nanocrystals: the role of ligand electronegativity *J. Phys. Chem.* C **113** 8169–76
[9] Kippeny T C *et al* 2008 Effects of surface passivation on the exciton dynamics of CdSe nanocrystals as observed by ultrafast fluorescence upconversion spectroscopy *J. Chem. Phys.* **128** 084711–7
[10] Lawrence K N, Dolai S, Lin Y H, Dass A and Sardar R 2014 Enhancing the physicochemical and photophysical properties of small (<2.0 nm) CdSe nanoclusters for intracellular imaging applications *RSC Adv.* **4** 30742–53
[11] Yang P, Tretiak S and Ivanov S 2011 Influence of surfactants and charges on CdSe quantum dots *J. Cluster Sci.* **22** 405–31
[12] Landes C F, Braun M and El-Sayed M A 2001 On the nanoparticle to molecular size transition: fluorescence quenching studies *J. Phys. Chem.* B **105** 10554–8
[13] Cossairt B M and Owen J S 2011 CdSe clusters: at the interface of small molecules and quantum dots *Chem. Mater.* **23** 3114–9
[14] Chatterjee A and Seth D 2013 Photophysical properties of 7-(diethylamino)coumarin-3-carboxylic acid in the nanocage of cyclodextrins and in different solvents and solvent mixtures *Photochem. Photobiol.* **89** 280–93
[15] Dukes A D, McBride J R and Rosenthal S J 2010 Synthesis of magic-sized CdSe and CdTe nanocrystals with diisooctylphosphinic acid *Chem. Mater.* **22** 6402–8
[16] Joo J, Son J S, Kwon S G, Yu J H and Hyeon T 2006 Low-temperature solution-phase synthesis of quantum well structured CdSe nanoribbons *J. Am. Chem. Soc.* **128** 5632–3
[17] Wang Y Y *et al* 2014 The magic-size nanocluster (CdSe) (34) as a low-temperature nucleant for cadmium selenide nanocrystals; room-temperature growth of crystalline quantum platelets *Chem. Mater.* **26** 6318
[18] Murray C B, Norris D J and Bawendi M G 1993 Synthesis and characterization of nearly monodisperse CdE (E = sulfur, selenium, tellurium) semiconductor nanocrystallites *J. Am. Chem. Soc.* **115** 8706–15
[19] Jiang Z J and Kelley D F 2010 Role of magic-sized clusters in the synthesis of CdSe nanorods *ACS Nano* **4** 1561–72
[20] Morris-Cohen A J, Frederick M T, Lilly G D, McArthur E A and Weiss E A 2010 Organic surfactant-controlled composition of the surfaces of CdSe quantum dots *J. Phys. Chem. Lett.* **1** 1078–81
[21] Newton J C *et al* 2012 Low-temperature synthesis of magic-sized CdSe nanoclusters: influence of ligands on nanocluster growth and photophysical properties *J. Phys. Chem.* C **116** 4380–9
[22] Peng Z A and Peng X G 2001 Formation of high-quality CdTe, CdSe, and CdS nanocrystals using CdO as precursor *J. Am. Chem. Soc.* **123** 183–4
[23] Talapin D V, Rogach A L, Kornowski A, Haase M and Weller H 2001 Highly luminescent monodisperse CdSe and CdSe/ZnS nanocrystals synthesized in a hexadecylamine-trioctylphosphine oxide-trioctylphospine mixture *Nano Lett.* **1** 207–11
[24] Zanella M, Abbasi A Z, Schaper A K and Parak W J 2010 Discontinuous growth of II–VI semiconductor nanocrystals from different materials *J. Phys. Chem.* C **114** 6205–15
[25] Liu Y H, Wang F D, Wang Y Y, Gibbons P C and Buhro W E 2011 Lamellar assembly of cadmium selenide nanoclusters into quantum belts *J. Am. Chem. Soc.* **133** 17005–13
[26] Ithurria S and Dubertret B 2008 Quasi 2D colloidal CdSe platelets with thicknesses controlled at the atomic level *J. Am. Chem. Soc.* **130** 16504–5
[27] Amin V A *et al* 2015 Dependence of the band gap of CdSe quantum dots on the surface coverage and binding mode of an exciton-delocalizing ligand, methylthiophenolate *J. Phys. Chem.* C **119** 19423–9
[28] Teunis M B, Dolai S and Sardar R 2014 Effects of surface-passivating ligands and ultrasmall CdSe nanocrystal size on the delocalization of exciton confinement *Langmuir* **30** 7851–8
[29] Bowers M J, McBride J R and Rosenthal S J 2005 White-light emission from magic-sized cadmium selenide nanocrystals *J. Am. Chem. Soc.* **127** 15378–9

List of references

(1981). "Pneumocystis pneumonia--Los Angeles." MMWR Morb Mortal Wkly Rep **30**(21): 250-252.

Abd El-Wahab, E. W., R. P. Smyth, et al. (2014). "Specific recognition of the HIV-1 genomic RNA by the Gag precursor." Nat Commun **5**: 4304.

Adams, S. R., R. E. Campbell, et al. (2002). "New biarsenical ligands and tetracysteine motifs for protein labeling in vitro and in vivo: synthesis and biological applications." J Am Chem Soc **124**(21): 6063-6076.

Aduri, R., K. T. Briggs, et al. (2013). "Molecular determinants of HIV-1 NCp7 chaperone activity in maturation of the HIV-1 dimerization initiation site." Nucleic Acids Res **41**(4): 2565-2580.

Aiken, C. (1997). "Pseudotyping human immunodeficiency virus type 1 (HIV-1) by the glycoprotein of vesicular stomatitis virus targets HIV-1 entry to an endocytic pathway and suppresses both the requirement for Nef and the sensitivity to cyclosporin A." J Virol **71**(8): 5871-5877.

Aitken, C. E., R. A. Marshall, et al. (2008). "An oxygen scavenging system for improvement of dye stability in single-molecule fluorescence experiments." Biophys J **94**(5): 1826-1835.

Albanese, A., D. Arosio, et al. (2008). "HIV-1 pre-integration complexes selectively target decondensed chromatin in the nuclear periphery." PLoS One **3**(6): e2413.

Aldovini, A. and R. A. Young (1990). "Mutations of RNA and protein sequences involved in human immunodeficiency virus type 1 packaging result in production of noninfectious virus." J Virol **64**(5): 1920-1926.

Alfadhli, A., T. C. Dhenub, et al. (2005). "Analysis of human immunodeficiency virus type 1 Gag dimerization-induced assembly." J Virol **79**(23): 14498-14506.

Alvizo, O., S. Mittal, et al. (2012). "Structural, kinetic, and thermodynamic studies of specificity designed HIV-1 protease." Protein Sci **21**(7): 1029-1041.

Amarasinghe, G. K., R. N. De Guzman, et al. (2000). "NMR structure of the HIV-1 nucleocapsid protein bound to stem-loop SL2 of the psi-RNA packaging signal. Implications for genome recognition." J Mol Biol **301**(2): 491-511.

Anderson, J. L. and T. J. Hope (2005). "Intracellular trafficking of retroviral vectors: obstacles and advances." Gene Ther **12**(23): 1667-1678.

Ando, R., H. Mizuno, et al. (2004). "Regulated fast nucleocytoplasmic shuttling observed by reversible protein highlighting." Science **306**(5700): 1370-1373.

Anton, H., N. Taha, et al. (2015). "Investigating the cellular distribution and interactions of HIV-1 nucleocapsid protein by quantitative fluorescence microscopy." PLoS One **10**(2): e0116921.

Ao, Z., K. D. Jayappa, et al. (2012). "Contribution of host nucleoporin 62 in HIV-1 integrase chromatin association and viral DNA integration." J Biol Chem **287**(13): 10544-10555.

Apostolski, S., T. McAlarney, et al. (1993). "The gp120 glycoprotein of human immunodeficiency virus type 1 binds to sensory ganglion neurons." Ann Neurol **34**(6): 855-863.

Arfi, V., J. Lienard, et al. (2009). "Characterization of the behavior of functional viral genomes during the early steps of human immunodeficiency virus type 1 infection." J Virol **83**(15): 7524-7535.

Arhel, N. (2010). "Revisiting HIV-1 uncoating." Retrovirology **7**: 96.

Arhel, N., A. Genovesio, et al. (2006). "Quantitative four-dimensional tracking of cytoplasmic and nuclear HIV-1 complexes." Nat Methods **3**(10): 817-824.

Arhel, N., S. Munier, et al. (2006). "Nuclear import defect of human immunodeficiency virus type 1 DNA flap mutants is not dependent on the viral strain or target cell type." J Virol **80**(20): 10262-10269.

Arhel, N. J., S. Souquere-Besse, et al. (2006). "Wild-type and central DNA flap defective HIV-1 lentiviral vector genomes: intracellular visualization at ultrastructural resolution levels." Retrovirology **3**: 38.

Arhel, N. J., S. Souquere-Besse, et al. (2007). "HIV-1 DNA Flap formation promotes uncoating of the pre-integration complex at the nuclear pore." EMBO J **26**(12): 3025-3037.

Avilov, S. V., C. Boudier, et al. (2012). "Characterization of the inhibition mechanism of HIV-1 nucleocapsid protein chaperone activities by methylated oligoribonucleotides." Antimicrob Agents Chemother **56**(2): 1010-1018.

Axelrod, D. (2003). "Total internal reflection fluorescence microscopy in cell biology." Methods Enzymol **361**: 1-33.

Bacharach, E., J. Gonsky, et al. (2000). "The carboxy-terminal fragment of nucleolin interacts with the nucleocapsid domain of retroviral gag proteins and inhibits virion assembly." J Virol **74**(23): 11027-11039.

Balliet, J. W., D. L. Kolson, et al. (1994). "Distinct effects in primary macrophages and lymphocytes of the human immunodeficiency virus type 1 accessory genes vpr, vpu, and nef: mutational analysis of a primary HIV-1 isolate." Virology **200**(2): 623-631.

Barraud, P., J. C. Paillart, et al. (2008). "Advances in the structural understanding of Vif proteins." Curr HIV Res **6**(2): 91-99.

Barre-Sinoussi, F., J. C. Chermann, et al. (1983). "Isolation of a T-lymphotropic retrovirus from a patient at risk for acquired immune deficiency syndrome (AIDS)." Science **220**(4599): 868-871.

Bartelmess, J., E. De Luca, et al. (2014). "Boron dipyrromethene (BODIPY) functionalized carbon nano-onions for high resolution cellular imaging." Nanoscale **6**(22): 13761-13769.

Bartesaghi, A., A. Merk, et al. (2013). "Prefusion structure of trimeric HIV-1 envelope glycoprotein determined by cryo-electron microscopy." Nat Struct Mol Biol **20**(12): 1352-1357.

Barth, S. (2013). "The SNAP-tag technology - a versatile tool with many applications." Curr Pharm Des **19**(30): 5404-5405.

Bartz, S. R., M. E. Rogel, et al. (1996). "Human immunodeficiency virus type 1 cell cycle control: Vpr is cytostatic and mediates G2 accumulation by a mechanism which differs from DNA damage checkpoint control." J Virol **70**(4): 2324-2331.

Basanez, G. and J. Zimmerberg (2001). "HIV and apoptosis death and the mitochondrion." J Exp Med **193**(4): F11-14.

Batisse, J., S. Guerrero, et al. (2012). "The role of Vif oligomerization and RNA chaperone activity in HIV-1 replication." Virus Res **169**(2): 361-376.

Baumeister, W., R. Grimm, et al. (1999). "Electron tomography of molecules and cells." Trends Cell Biol **9**(2): 81-85.

Benjamin, J., B. K. Ganser-Pornillos, et al. (2005). "Three-dimensional structure of HIV-1 virus-like particles by electron cryotomography." J Mol Biol **346**(2): 577-588.

Berg, J. M. and Y. Shi (1996). "The galvanization of biology: a growing appreciation for the roles of zinc." Science **271**(5252): 1081-1085.

Berglund, J. A., B. Charpentier, et al. (1997). "A high affinity binding site for the HIV-1 nucleocapsid protein." Nucleic Acids Res **25**(5): 1042-1049.

Berkhout, B. (1996). "Structure and function of the human immunodeficiency virus leader RNA." Progress in nucleic acid research and molecular biology **54**: 1-34.

Berkowitz, R., J. Fisher, et al. (1996). "RNA packaging." Curr Top Microbiol Immunol **214**: 177-218.

Betzig, E., G. H. Patterson, et al. (2006). "Imaging intracellular fluorescent proteins at nanometer resolution." Science **313**(5793): 1642-1645.

Bharat, T. A., L. R. Castillo Menendez, et al. (2014). "Cryo-electron microscopy of tubular arrays of HIV-1 Gag resolves structures essential for immature virus assembly." Proc Natl Acad Sci U S A **111**(22): 8233-8238.

Bharat, T. A., N. E. Davey, et al. (2012). "Structure of the immature retroviral capsid at 8 A resolution by cryo-electron microscopy." Nature **487**(7407): 385-389.

Bhattacharya, A., S. L. Alam, et al. (2014). "Structural basis of HIV-1 capsid recognition by PF74 and CPSF6." Proc Natl Acad Sci U S A **111**(52): 18625-18630.

Bichel, K., A. J. Price, et al. (2013). "HIV-1 capsid undergoes coupled binding and isomerization by the nuclear pore protein NUP358." Retrovirology **10**: 81.

Bieth, E., C. Gabus, et al. (1990). "A study of the dimer formation of Rous sarcoma virus RNA and of its effect on viral protein synthesis in vitro." Nucleic Acids Res **18**(1): 119-127.

Bitler, A., N. Lev, et al. (2010). "Kinetics of interaction of HIV fusion protein (gp41) with lipid membranes studied by real-time AFM imaging." Ultramicroscopy **110**(6): 694-700.
Bleck, M., M. S. Itano, et al. (2014). "Temporal and spatial organization of ESCRT protein recruitment during HIV-1 budding." Proc Natl Acad Sci U S A **111**(33): 12211-12216.
Bourbigot, S., N. Ramalanjaona, et al. (2008). "How the HIV-1 nucleocapsid protein binds and destabilises the (-)primer binding site during reverse transcription." J Mol Biol **383**(5): 1112-1128.
Bouyac-Bertoia, M., J. D. Dvorin, et al. (2001). "HIV-1 infection requires a functional integrase NLS." Mol Cell **7**(5): 1025-1035.
Braaten, D., E. K. Franke, et al. (1996). "Cyclophilin A is required for an early step in the life cycle of human immunodeficiency virus type 1 before the initiation of reverse transcription." J Virol **70**(6): 3551-3560.
Brass, A. L., D. M. Dykxhoorn, et al. (2008). "Identification of host proteins required for HIV infection through a functional genomic screen." Science **319**(5865): 921-926.
Briggs, J. A., K. Grunewald, et al. (2006). "The mechanism of HIV-1 core assembly: insights from three-dimensional reconstructions of authentic virions." Structure **14**(1): 15-20.
Briggs, J. A. and H. G. Krausslich (2011). "The molecular architecture of HIV." J Mol Biol **410**(4): 491-500.
Briggs, J. A., J. D. Riches, et al. (2009). "Structure and assembly of immature HIV." Proc Natl Acad Sci U S A **106**(27): 11090-11095.
Briggs, J. A., M. N. Simon, et al. (2004). "The stoichiometry of Gag protein in HIV-1." Nat Struct Mol Biol **11**(7): 672-675.
Brook, I. (1987). "Approval of zidovudine (AZT) for acquired immunodeficiency syndrome. A challenge to the medical and pharmaceutical communities." JAMA **258**(11): 1517.
Buckman, J. S., W. J. Bosche, et al. (2003). "Human immunodeficiency virus type 1 nucleocapsid zn(2+) fingers are required for efficient reverse transcription, initial integration processes, and protection of newly synthesized viral DNA." J Virol **77**(2): 1469-1480.
Bukrinskaya, A., B. Brichacek, et al. (1998). "Establishment of a functional human immunodeficiency virus type 1 (HIV-1) reverse transcription complex involves the cytoskeleton." J Exp Med **188**(11): 2113-2125.
Bukrinskaya, A. G., G. K. Vorkunova, et al. (1992). "HIV-1 matrix protein p17 resides in cell nuclei in association with genomic RNA." AIDS Res Hum Retroviruses **8**(10): 1795-1801.
Bukrinsky, M. I., S. Haggerty, et al. (1993). "A nuclear localization signal within HIV-1 matrix protein that governs infection of non-dividing cells." Nature **365**(6447): 666-669.
Bukrinsky, M. I., N. Sharova, et al. (1992). "Active nuclear import of human immunodeficiency virus type 1 preintegration complexes." Proc Natl Acad Sci U S A **89**(14): 6580-6584.
Burton, G. F., B. F. Keele, et al. (2002). "Follicular dendritic cell contributions to HIV pathogenesis." Semin Immunol **14**(4): 275-284.
Caffrey, M., M. Cai, et al. (1998). "Three-dimensional solution structure of the 44 kDa ectodomain of SIV gp41." EMBO J **17**(16): 4572-4584.
Calnan, B. J., S. Biancalana, et al. (1991). "Analysis of arginine-rich peptides from the HIV Tat protein reveals unusual features of RNA-protein recognition." Genes Dev **5**(2): 201-210.
Campbell, E. M. and T. J. Hope (2015). "HIV-1 capsid: the multifaceted key player in HIV-1 infection." Nat Rev Microbiol **13**(8): 471-483.
Campbell, E. M., O. Perez, et al. (2007). "Labeling HIV-1 virions with two fluorescent proteins allows identification of virions that have productively entered the target cell." Virology **360**(2): 286-293.
Cao, H., B. Chen, et al. (2006). "CrAsH: a biarsenical multi-use affinity probe with low non-specific fluorescence." Chem Commun (Camb)(24): 2601-2603.
Carlson, L. A., J. A. Briggs, et al. (2008). "Three-dimensional analysis of budding sites and released virus suggests a revised model for HIV-1 morphogenesis." Cell Host Microbe **4**(6): 592-599.
Carlson, L. A., A. de Marco, et al. (2010). "Cryo electron tomography of native HIV-1 budding sites." PLoS Pathog **6**(11): e1001173.

Carlton, J. G. and J. Martin-Serrano (2009). "The ESCRT machinery: new functions in viral and cellular biology." Biochem Soc Trans **37**(Pt 1): 195-199.
Carneiro, F. A., M. L. Bianconi, et al. (2002). "Membrane recognition by vesicular stomatitis virus involves enthalpy-driven protein-lipid interactions." J Virol **76**(8): 3756-3764.
Carteau, S., S. C. Batson, et al. (1997). "Human immunodeficiency virus type 1 nucleocapsid protein specifically stimulates Mg2+-dependent DNA integration in vitro." J Virol **71**(8): 6225-6229.
Chamontin, C., P. Rassam, et al. (2015). "HIV-1 nucleocapsid and ESCRT-component Tsg101 interplay prevents HIV from turning into a DNA-containing virus." Nucleic Acids Res **43**(1): 336-347.
Charneau, P., M. Alizon, et al. (1992). "A second origin of DNA plus-strand synthesis is required for optimal human immunodeficiency virus replication." J Virol **66**(5): 2814-2820.
Chassagne, J., P. Verrelle, et al. (1986). "A monoclonal antibody against LAV gag precursor: use for viral protein analysis and antigenic expression in infected cells." J Immunol **136**(4): 1442-1445.
Chatel-Chaix, L., L. Abrahamyan, et al. (2007). "The host protein Staufen1 participates in human immunodeficiency virus type 1 assembly in live cells by influencing pr55Gag multimerization." J Virol **81**(12): 6216-6230.
Chatel-Chaix, L., K. Boulay, et al. (2008). "The host protein Staufen1 interacts with the Pr55Gag zinc fingers and regulates HIV-1 assembly via its N-terminus." Retrovirology **5**: 41.
Chatel-Chaix, L., J. F. Clement, et al. (2004). "Identification of Staufen in the human immunodeficiency virus type 1 Gag ribonucleoprotein complex and a role in generating infectious viral particles." Mol Cell Biol **24**(7): 2637-2648.
Checkley, M. A., B. G. Luttge, et al. (2011). "HIV-1 envelope glycoprotein biosynthesis, trafficking, and incorporation." J Mol Biol **410**(4): 582-608.
Chen, P. Y., D. Pearce, et al. (1988). "Membrane water and solute permeability determined quantitatively by self-quenching of an entrapped fluorophore." Biochemistry **27**(15): 5713-5718.
Chen, R. F. and J. R. Knutson (1988). "Mechanism of fluorescence concentration quenching of carboxyfluorescein in liposomes: energy transfer to nonfluorescent dimers." Anal Biochem **172**(1): 61-77.
Chertova, E., O. Chertov, et al. (2006). "Proteomic and biochemical analysis of purified human immunodeficiency virus type 1 produced from infected monocyte-derived macrophages." J Virol **80**(18): 9039-9052.
Chin, C. R., J. M. Perreira, et al. (2015). "Direct Visualization of HIV-1 Replication Intermediates Shows that Capsid and CPSF6 Modulate HIV-1 Intra-nuclear Invasion and Integration." Cell Rep **13**(8): 1717-1731.
Chojnacki, J., T. Staudt, et al. (2012). "Maturation-dependent HIV-1 surface protein redistribution revealed by fluorescence nanoscopy." Science **338**(6106): 524-528.
Chrystie, I. L. and J. D. Almeida (1988). "The morphology of human immunodeficiency virus (HIV) by negative staining." J Med Virol **25**(3): 281-288.
Chudakov, D. M., S. Lukyanov, et al. (2007). "Using photoactivatable fluorescent protein Dendra2 to track protein movement." Biotechniques **42**(5): 553, 555, 557 passim.
Chudakov, D. M., V. V. Verkhusha, et al. (2004). "Photoswitchable cyan fluorescent protein for protein tracking." Nat Biotechnol **22**(11): 1435-1439.
Chung, J., A. Mujeeb, et al. (2008). "A small molecule, Lys-Ala-7-amido-4-methylcoumarin, facilitates RNA dimer maturation of a stem-loop 1 transcript in vitro: structure-activity relationship of the activator." Biochemistry **47**(31): 8148-8156.
Chung, J., N. B. Ulyanov, et al. (2010). "Binding characteristics of small molecules that mimic nucleocapsid protein-induced maturation of stem-loop 1 of HIV-1 RNA." Biochemistry **49**(30): 6341-6351.
Cimarelli, A. and J. L. Darlix (2002). "Assembling the human immunodeficiency virus type 1." Cell Mol Life Sci **59**(7): 1166-1184.
Ciuffi, A. and F. D. Bushman (2006). "Retroviral DNA integration: HIV and the role of LEDGF/p75." Trends Genet **22**(7): 388-395.
Cochrane, A. W., M. T. McNally, et al. (2006). "The retrovirus RNA trafficking granule: from birth to maturity." Retrovirology **3**: 18.

Coffin, J. M., S. H. Hughes, et al. (1997). The Interactions of Retroviruses and their Hosts. Retroviruses. J. M. Coffin, S. H. Hughes and H. E. Varmus. Cold Spring Harbor (NY).
Courtial, J. and K. O'Holleran (2007). "Experiments with twisted light." The European Physical Journal Special Topics **145**(1): 35-47.
Cremer, C. and T. Cremer (1978). "Considerations on a laser-scanning-microscope with high resolution and depth of field." Microsc Acta **81**(1): 31-44.
Cronshaw, J. M., A. N. Krutchinsky, et al. (2002). "Proteomic analysis of the mammalian nuclear pore complex." J Cell Biol **158**(5): 915-927.
Dale, B., G. P. McNerney, et al. (2010). "Visualizing cell-to-cell transfer of HIV using fluorescent clones of HIV and live confocal microscopy." J Vis Exp(44).
Darlix, J. L., G. Cristofari, et al. (2000). "Nucleocapsid protein of human immunodeficiency virus as a model protein with chaperoning functions and as a target for antiviral drugs." Adv Pharmacol **48**: 345-372.
Darlix, J. L., J. Godet, et al. (2011). "Flexible nature and specific functions of the HIV-1 nucleocapsid protein." J Mol Biol **410**(4): 565-581.
Datta, S. A., L. G. Temeselew, et al. (2011). "On the role of the SP1 domain in HIV-1 particle assembly: a molecular switch?" J Virol **85**(9): 4111-4121.
De Guzman, R. N., Z. R. Wu, et al. (1998). "Structure of the HIV-1 nucleocapsid protein bound to the SL3 psi-RNA recognition element." Science **279**(5349): 384-388.
de Noronha, C. M., M. P. Sherman, et al. (2001). "Dynamic disruptions in nuclear envelope architecture and integrity induced by HIV-1 Vpr." Science **294**(5544): 1105-1108.
de Rocquigny, H., S. E. El Meshri, et al. (2014). "Role of the nucleocapsid region in HIV-1 Gag assembly as investigated by quantitative fluorescence-based microscopy." Virus Res **193**: 78-88.
de Rocquigny, H., V. Shvadchak, et al. (2008). "Targeting the viral nucleocapsid protein in anti-HIV-1 therapy." Mini Rev Med Chem **8**(1): 24-35.
Debaisieux, S., F. Rayne, et al. (2012). "The ins and outs of HIV-1 Tat." Traffic **13**(3): 355-363.
Deerinck, T. J., M. E. Martone, et al. (1994). "Fluorescence photooxidation with eosin: a method for high resolution immunolocalization and in situ hybridization detection for light and electron microscopy." J Cell Biol **126**(4): 901-910.
Dempsey, G. T., J. C. Vaughan, et al. (2011). "Evaluation of fluorophores for optimal performance in localization-based super-resolution imaging." Nat Methods **8**(12): 1027-1036.
Depienne, C., P. Roques, et al. (2000). "Cellular distribution and karyophilic properties of matrix, integrase, and Vpr proteins from the human and simian immunodeficiency viruses." Exp Cell Res **260**(2): 387-395.
Di Nunzio, F., A. Danckaert, et al. (2012). "Human nucleoporins promote HIV-1 docking at the nuclear pore, nuclear import and integration." PLoS One **7**(9): e46037.
Di Nunzio, F., T. Fricke, et al. (2013). "Nup153 and Nup98 bind the HIV-1 core and contribute to the early steps of HIV-1 replication." Virology **440**(1): 8-18.
Dismuke, D. J. and C. Aiken (2006). "Evidence for a functional link between uncoating of the human immunodeficiency virus type 1 core and nuclear import of the viral preintegration complex." J Virol **80**(8): 3712-3720.
Do, T., G. Murphy, et al. (2014). "Three-dimensional imaging of HIV-1 virological synapses reveals membrane architectures involved in virus transmission." J Virol **88**(18): 10327-10339.
Dobard, C. W., M. S. Briones, et al. (2007). "Molecular mechanisms by which human immunodeficiency virus type 1 integrase stimulates the early steps of reverse transcription." J Virol **81**(18): 10037-10046.
Dorfman, T., J. Luban, et al. (1993). "Mapping of functionally important residues of a cysteine-histidine box in the human immunodeficiency virus type 1 nucleocapsid protein." J Virol **67**(10): 6159-6169.
Dubochet, J., M. Adrian, et al. (1988). "Cryo-electron microscopy of vitrified specimens." Q Rev Biophys **21**(2): 129-228.
Dundr, M., G. H. Leno, et al. (1995). "The roles of nucleolar structure and function in the subcellular location of the HIV-1 Rev protein." J Cell Sci **108 (Pt 8)**: 2811-2823.

Dussupt, V., M. P. Javid, et al. (2009). "The nucleocapsid region of HIV-1 Gag cooperates with the PTAP and LYPXnL late domains to recruit the cellular machinery necessary for viral budding." PLoS Pathog **5**(3): e1000339.
Dussupt, V., P. Sette, et al. (2011). "Basic residues in the nucleocapsid domain of Gag are critical for late events of HIV-1 budding." J Virol **85**(5): 2304-2315.
Dutta, M., J. Liu, et al. (2014). "Visualization of retroviral envelope spikes in complex with the V3 loop antibody 447-52D on intact viruses by cryo-electron tomography." J Virol **88**(21): 12265-12275.
Eckhardt, M., M. Anders, et al. (2011). "A SNAP-tagged derivative of HIV-1--a versatile tool to study virus-cell interactions." PLoS One **6**(7): e22007.
Egner, A., C. Geisler, et al. (2007). "Fluorescence nanoscopy in whole cells by asynchronous localization of photoswitching emitters." Biophys J **93**(9): 3285-3290.
El Meshri, S. E., D. Dujardin, et al. (2015). "Role of the nucleocapsid domain in HIV-1 Gag oligomerization and trafficking to the plasma membrane: a fluorescence lifetime imaging microscopy investigation." J Mol Biol **427**(6 Pt B): 1480-1494.
Ellenberg, J., E. D. Siggia, et al. (1997). "Nuclear membrane dynamics and reassembly in living cells: targeting of an inner nuclear membrane protein in interphase and mitosis." J Cell Biol **138**(6): 1193-1206.
Endress, T., M. Lampe, et al. (2008). "HIV-1-cellular interactions analyzed by single virus tracing." Eur Biophys J **37**(8): 1291-1301.
Engelman, A., K. Mizuuchi, et al. (1991). "HIV-1 DNA integration: mechanism of viral DNA cleavage and DNA strand transfer." Cell **67**(6): 1211-1221.
Englander, S. W., D. B. Calhoun, et al. (1987). "Biochemistry without oxygen." Anal Biochem **161**(2): 300-306.
Erickson-Viitanen, S., J. Manfredi, et al. (1989). "Cleavage of HIV-1 gag polyprotein synthesized in vitro: sequential cleavage by the viral protease." AIDS Res Hum Retroviruses **5**(6): 577-591.
Fahrenkrog, B. and U. Aebi (2003). "The nuclear pore complex: nucleocytoplasmic transport and beyond." Nat Rev Mol Cell Biol **4**(10): 757-766.
Faivre-Moskalenko, C., J. Bernaud, et al. (2014). "RNA control of HIV-1 particle size polydispersity." PLoS One **9**(1): e83874.
Farahani, J. N., M. J. Schibler, et al. (2010). "Stimulated emission depletion (STED) microscopy: from theory to practice." Microscopy: science, technology, applications and education **2**: 1539.
Farjot, G., A. Sergeant, et al. (1999). "A new nucleoporin-like protein interacts with both HIV-1 Rev nuclear export signal and CRM-1." J Biol Chem **274**(24): 17309-17317.
Farmerie, W. G., D. D. Loeb, et al. (1987). "Expression and processing of the AIDS virus reverse transcriptase in Escherichia coli." Science **236**(4799): 305-308.
Fassati, A. and S. P. Goff (2001). "Characterization of intracellular reverse transcription complexes of human immunodeficiency virus type 1." J Virol **75**(8): 3626-3635.
Feng, Y. X., T. D. Copeland, et al. (1996). "HIV-1 nucleocapsid protein induces "maturation" of dimeric retroviral RNA in vitro." Proc Natl Acad Sci U S A **93**(15): 7577-7581.
Ferns, R. B., R. S. Tedder, et al. (1987). "Characterization of monoclonal antibodies against the human immunodeficiency virus (HIV) gag products and their use in monitoring HIV isolate variation." J Gen Virol **68 (Pt 6)**: 1543-1551.
Filice, G., G. Carnevale, et al. (1987). "Human immunodeficiency virus (HIV): an ultrastructural study." Microbiologica **10**(2): 209-216.
Finzi, A., A. Orthwein, et al. (2007). "Productive human immunodeficiency virus type 1 assembly takes place at the plasma membrane." J Virol **81**(14): 7476-7490.
Fischer, U., S. Meyer, et al. (1994). "Evidence that HIV-1 Rev directly promotes the nuclear export of unspliced RNA." EMBO J **13**(17): 4105-4112.
Fisher, R. J., M. J. Fivash, et al. (2006). "Complex interactions of HIV-1 nucleocapsid protein with oligonucleotides." Nucleic Acids Res **34**(2): 472-484.
Fisher, R. J., A. Rein, et al. (1998). "Sequence-specific binding of human immunodeficiency virus type 1 nucleocapsid protein to short oligonucleotides." J Virol **72**(3): 1902-1909.

Folling, J., M. Bossi, et al. (2008). "Fluorescence nanoscopy by ground-state depletion and single-molecule return." Nat Methods **5**(11): 943-945.
Fontana, J., K. A. Jurado, et al. (2015). "Distribution and Redistribution of HIV-1 Nucleocapsid Protein in Immature, Mature, and Integrase-Inhibited Virions: a Role for Integrase in Maturation." J Virol **89**(19): 9765-9780.
Forshey, B. M., U. von Schwedler, et al. (2002). "Formation of a human immunodeficiency virus type 1 core of optimal stability is crucial for viral replication." J Virol **76**(11): 5667-5677.
Fouchier, R. A., B. E. Meyer, et al. (1998). "Interaction of the human immunodeficiency virus type 1 Vpr protein with the nuclear pore complex." J Virol **72**(7): 6004-6013.
Francis, A. C., C. Di Primio, et al. (2014). "Second generation imaging of nuclear/cytoplasmic HIV-1 complexes." AIDS Res Hum Retroviruses **30**(7): 717-726.
Frankel, A. D. and J. A. Young (1998). "HIV-1: fifteen proteins and an RNA." Annu Rev Biochem **67**: 1-25.
Freed, E. O. (2001). "HIV-1 replication." Somat Cell Mol Genet **26**(1-6): 13-33.
Freed, E. O. (2015). "HIV-1 assembly, release and maturation." Nat Rev Microbiol **13**(8): 484-496.
Freed, E. O., G. Englund, et al. (1995). "Role of the basic domain of human immunodeficiency virus type 1 matrix in macrophage infection." J Virol **69**(6): 3949-3954.
Fu, W. and A. Rein (1993). "Maturation of dimeric viral RNA of Moloney murine leukemia virus." J Virol **67**(9): 5443-5449.
Fujii, T. (2009). "[HIV infection route]." Nihon Naika Gakkai Zasshi **98**(11): 2762-2766.
Furman, P. A., J. A. Fyfe, et al. (1986). "Phosphorylation of 3'-azido-3'-deoxythymidine and selective interaction of the 5'-triphosphate with human immunodeficiency virus reverse transcriptase." Proc Natl Acad Sci U S A **83**(21): 8333-8337.
Gaietta, G., T. J. Deerinck, et al. (2002). "Multicolor and electron microscopic imaging of connexin trafficking." Science **296**(5567): 503-507.
Gaietta, G. M., T. J. Deerinck, et al. (2011). "Fluorescence photoconversion of biarsenical-labeled cells for correlated electron microscopy (EM)." Cold Spring Harb Protoc **2011**(1): pdb prot5548.
Gaietta, G. M., B. N. Giepmans, et al. (2006). "Golgi twins in late mitosis revealed by genetically encoded tags for live cell imaging and correlated electron microscopy." Proc Natl Acad Sci U S A **103**(47): 17777-17782.
Galiani, S., B. Harke, et al. (2012). "Strategies to maximize the performance of a STED microscope." Opt Express **20**(7): 7362-7374.
Gallay, P., T. Hope, et al. (1997). "HIV-1 infection of nondividing cells through the recognition of integrase by the importin/karyopherin pathway." Proc Natl Acad Sci U S A **94**(18): 9825-9830.
Gallay, P., S. Swingler, et al. (1995). "HIV nuclear import is governed by the phosphotyrosine-mediated binding of matrix to the core domain of integrase." Cell **83**(4): 569-576.
Gallo, R. C., S. Z. Salahuddin, et al. (1984). "Frequent detection and isolation of cytopathic retroviruses (HTLV-III) from patients with AIDS and at risk for AIDS." Science **224**(4648): 500-503.
Gamble, T. R., S. Yoo, et al. (1997). "Structure of the carboxyl-terminal dimerization domain of the HIV-1 capsid protein." Science **278**(5339): 849-853.
Ganser, B. K., S. Li, et al. (1999). "Assembly and analysis of conical models for the HIV-1 core." Science **283**(5398): 80-83.
Gao, D., J. Wu, et al. (2013). "Cyclic GMP-AMP synthase is an innate immune sensor of HIV and other retroviruses." Science **341**(6148): 903-906.
Gao, K., R. J. Gorelick, et al. (2003). "Cofactors for human immunodeficiency virus type 1 cDNA integration in vitro." J Virol **77**(2): 1598-1603.
Garg, D. and B. E. Torbett (2014). "Advances in targeting nucleocapsid-nucleic acid interactions in HIV-1 therapy." Virus Res **193**: 135-143.
Gelderblom, H., M. Özel, et al. (1988). "Fine structure of human immunodeficiency virus (HIV), immunolocalization of structural proteins and virus-cell relation." Micron and Microscopica Acta **19**(1): 41-60.
Gelderblom, H. R., E. H. Hausmann, et al. (1987). "Fine structure of human immunodeficiency virus (HIV) and immunolocalization of structural proteins." Virology **156**(1): 171-176.

Giannone, G., E. Hosy, et al. (2010). "Dynamic superresolution imaging of endogenous proteins on living cells at ultra-high density." Biophys J **99**(4): 1303-1310.
Gitti, R. K., B. M. Lee, et al. (1996). "Structure of the amino-terminal core domain of the HIV-1 capsid protein." Science **273**(5272): 231-235.
Gladnikoff, M., E. Shimoni, et al. (2009). "Retroviral assembly and budding occur through an actin-driven mechanism." Biophys J **97**(9): 2419-2428.
Godet, J., C. Boudier, et al. (2012). "Comparative nucleic acid chaperone properties of the nucleocapsid protein NCp7 and Tat protein of HIV-1." Virus Res **169**(2): 349-360.
Goldschmidt, V., L. M. M. Jenkins, et al. (2010). "The nucleocapsid protein of HIV-1 as a promising therapeutic target for antiviral drugs."
Goldsmith, M. A., M. T. Warmerdam, et al. (1995). "Dissociation of the CD4 downregulation and viral infectivity enhancement functions of human immunodeficiency virus type 1 Nef." J Virol **69**(7): 4112-4121.
Gorelick, R. J., D. J. Chabot, et al. (1993). "The two zinc fingers in the human immunodeficiency virus type 1 nucleocapsid protein are not functionally equivalent." J Virol **67**(7): 4027-4036.
Gorelick, R. J., L. E. Henderson, et al. (1988). "Point mutants of Moloney murine leukemia virus that fail to package viral RNA: evidence for specific RNA recognition by a "zinc finger-like" protein sequence." Proc Natl Acad Sci U S A **85**(22): 8420-8424.
Gorlich, D. and U. Kutay (1999). "Transport between the cell nucleus and the cytoplasm." Annu Rev Cell Dev Biol **15**: 607-660.
Grewe, C., A. Beck, et al. (1990). "HIV: early virus-cell interactions." J Acquir Immune Defic Syndr **3**(10): 965-974.
Griffin, B. A., S. R. Adams, et al. (1998). "Specific covalent labeling of recombinant protein molecules inside live cells." Science **281**(5374): 269-272.
Griffin, B. A., S. R. Adams, et al. (1998). "Specific covalent labeling of recombinant protein molecules inside live cells." Science **281**(5374): 269-272.
Grigorov, B., A. Bocquin, et al. (2011). "Identification of a methylated oligoribonucleotide as a potent inhibitor of HIV-1 reverse transcription complex." Nucleic Acids Res **39**(13): 5586-5596.
Grotjohann, T., I. Testa, et al. (2011). "Diffraction-unlimited all-optical imaging and writing with a photochromic GFP." Nature **478**(7368): 204-208.
Gruenberg, J. and F. R. Maxfield (1995). "Membrane transport in the endocytic pathway." Curr Opin Cell Biol **7**(4): 552-563.
Guenzel, C. A., C. Herate, et al. (2014). "HIV-1 Vpr-a still "enigmatic multitasker"." Front Microbiol **5**: 127.
Gunewardene, M. S., F. V. Subach, et al. (2011). "Superresolution imaging of multiple fluorescent proteins with highly overlapping emission spectra in living cells." Biophys J **101**(6): 1522-1528.
Gunning, W. T. and E. P. Calomeni (2013). "A brief review of transmission electron microscopy and applications in pathology." Journal of Histotechnology.
Gunzenhauser, J., N. Olivier, et al. (2012). "Quantitative super-resolution imaging reveals protein stoichiometry and nanoscale morphology of assembling HIV-Gag virions." Nano Lett **12**(9): 4705-4710.
Gurskaya, N. G., V. V. Verkhusha, et al. (2006). "Engineering of a monomeric green-to-red photoactivatable fluorescent protein induced by blue light." Nat Biotechnol **24**(4): 461-465.
Gustafsson, M. G. (2000). "Surpassing the lateral resolution limit by a factor of two using structured illumination microscopy." J Microsc **198**(Pt 2): 82-87.
Gustafsson, M. G. (2005). "Nonlinear structured-illumination microscopy: wide-field fluorescence imaging with theoretically unlimited resolution." Proc Natl Acad Sci U S A **102**(37): 13081-13086.
Hänninen, P. E., M. Schrader, et al. (1995). "Two-photon excitation fluorescence microscopy using a semiconductor laser." Bioimaging **3**(2): 70-75.
Harrich, D., C. Ulich, et al. (1996). "A critical role for the TAR element in promoting efficient human immunodeficiency virus type 1 reverse transcription." J Virol **70**(6): 4017-4027.

Heath, M. J., S. S. Derebail, et al. (2003). "Differing roles of the N- and C-terminal zinc fingers in human immunodeficiency virus nucleocapsid protein-enhanced nucleic acid annealing." J Biol Chem **278**(33): 30755-30763.
Hein, B., K. I. Willig, et al. (2008). "Stimulated emission depletion (STED) nanoscopy of a fluorescent protein-labeled organelle inside a living cell." Proc Natl Acad Sci U S A **105**(38): 14271-14276.
Hell, S. and E. H. Stelzer (1992). "Properties of a 4Pi confocal fluorescence microscope." JOSA A **9**(12): 2159-2166.
Hell, S. W. (2007). "Far-field optical nanoscopy." Science **316**(5828): 1153-1158.
Hell, S. W. and J. Wichmann (1994). "Breaking the diffraction resolution limit by stimulated emission: stimulated-emission-depletion fluorescence microscopy." Opt Lett **19**(11): 780-782.
Henriet, S., D. Richer, et al. (2005). "Cooperative and specific binding of Vif to the 5' region of HIV-1 genomic RNA." J Mol Biol **354**(1): 55-72.
Hermida-Matsumoto, L. and M. D. Resh (2000). "Localization of human immunodeficiency virus type 1 Gag and Env at the plasma membrane by confocal imaging." J Virol **74**(18): 8670-8679.
Heymann, J. A., M. Hayles, et al. (2006). "Site-specific 3D imaging of cells and tissues with a dual beam microscope." J Struct Biol **155**(1): 63-73.
Heymann, J. A., D. Shi, et al. (2009). "3D imaging of mammalian cells with ion-abrasion scanning electron microscopy." J Struct Biol **166**(1): 1-7.
Hirsch, V. M., R. A. Olmsted, et al. (1989). "An African primate lentivirus (SIVsm) closely related to HIV-2." Nature **339**(6223): 389-392.
Hofmann, M., C. Eggeling, et al. (2005). "Breaking the diffraction barrier in fluorescence microscopy at low light intensities by using reversibly photoswitchable proteins." Proc Natl Acad Sci U S A **102**(49): 17565-17569.
Hoglund, S., L. G. Ofverstedt, et al. (1992). "Spatial visualization of the maturing HIV-1 core and its linkage to the envelope." AIDS Res Hum Retroviruses **8**(1): 1-7.
Hu, W. S. and S. H. Hughes (2012). "HIV-1 reverse transcription." Cold Spring Harb Perspect Med **2**(10).
Huang, B., M. Bates, et al. (2009). "Super-resolution fluorescence microscopy." Annu Rev Biochem **78**: 993-1016.
Huang, B., S. A. Jones, et al. (2008). "Whole-cell 3D STORM reveals interactions between cellular structures with nanometer-scale resolution." Nat Methods **5**(12): 1047-1052.
Huang, M., J. M. Orenstein, et al. (1995). "p6Gag is required for particle production from full-length human immunodeficiency virus type 1 molecular clones expressing protease." J Virol **69**(11): 6810-6818.
Hubner, W., G. P. McNerney, et al. (2009). "Quantitative 3D video microscopy of HIV transfer across T cell virological synapses." Science **323**(5922): 1743-1747.
Huet, T., R. Cheynier, et al. (1990). "Genetic organization of a chimpanzee lentivirus related to HIV-1." Nature **345**(6273): 356-359.
Hulme, A. E., Z. Kelley, et al. (2015). "Complementary Assays Reveal a Low Level of CA Associated with Viral Complexes in the Nuclei of HIV-1-Infected Cells." J Virol **89**(10): 5350-5361.
Hulme, A. E., O. Perez, et al. (2011). "Complementary assays reveal a relationship between HIV-1 uncoating and reverse transcription." Proc Natl Acad Sci U S A **108**(24): 9975-9980.
Huvent, I., S. S. Hong, et al. (1998). "Interaction and co-encapsidation of human immunodeficiency virus type 1 Gag and Vif recombinant proteins." J Gen Virol **79 (Pt 5)**: 1069-1081.
Igakura, T., J. C. Stinchcombe, et al. (2003). "Spread of HTLV-I between lymphocytes by virus-induced polarization of the cytoskeleton." Science **299**(5613): 1713-1716.
Iordanskiy, S., R. Berro, et al. (2006). "Intracytoplasmic maturation of the human immunodeficiency virus type 1 reverse transcription complexes determines their capacity to integrate into chromatin." Retrovirology **3**: 4.
Ivanchenko, S., W. J. Godinez, et al. (2009). "Dynamics of HIV-1 assembly and release." PLoS Pathog **5**(11): e1000652.
Jacks, T., M. D. Power, et al. (1988). "Characterization of ribosomal frameshifting in HIV-1 gag-pol expression." Nature **331**(6153): 280-283.

Jacob, D. T. and J. J. DeStefano (2008). "A new role for HIV nucleocapsid protein in modulating the specificity of plus strand priming." Virology **378**(2): 385-396.
Jalalirad, M. and M. Laughrea (2010). "Formation of immature and mature genomic RNA dimers in wild-type and protease-inactive HIV-1: differential roles of the Gag polyprotein, nucleocapsid proteins NCp15, NCp9, NCp7, and the dimerization initiation site." Virology **407**(2): 225-236.
Jayappa, K. D., Z. Ao, et al. (2012). "The HIV-1 passage from cytoplasm to nucleus: the process involving a complex exchange between the components of HIV-1 and cellular machinery to access nucleus and successful integration." Int J Biochem Mol Biol **3**(1): 70-85.
Jeang, K. T. and F. J. Rauscher, 3rd (1996). "The XVIII Symposium of the International Association for Comparative Research on Leukemia & Related Diseases (IACRLRD): leukemia and lymphoma/pathogenesis and treatment/molecular aspects." Cancer Res **56**(18): 4288-4292.
Jenkins, L. M., J. C. Byrd, et al. (2005). "Studies on the mechanism of inactivation of the HIV-1 nucleocapsid protein NCp7 with 2-mercaptobenzamide thioesters." J Med Chem **48**(8): 2847-2858.
Jenkins, T. M., A. Engelman, et al. (1996). "A soluble active mutant of HIV-1 integrase: involvement of both the core and carboxyl-terminal domains in multimerization." J Biol Chem **271**(13): 7712-7718.
Jenkins, Y., M. McEntee, et al. (1998). "Characterization of HIV-1 vpr nuclear import: analysis of signals and pathways." J Cell Biol **143**(4): 875-885.
Jimenez, N., E. G. Van Donselaar, et al. (2010). "Gridded Aclar: preparation methods and use for correlative light and electron microscopy of cell monolayers, by TEM and FIB-SEM." J Microsc **237**(2): 208-220.
Johannsdottir, H. K., R. Mancini, et al. (2009). "Host cell factors and functions involved in vesicular stomatitis virus entry." J Virol **83**(1): 440-453.
Jolly, C., K. Kashefi, et al. (2004). "HIV-1 cell to cell transfer across an Env-induced, actin-dependent synapse." J Exp Med **199**(2): 283-293.
Jouvenet, N., P. D. Bieniasz, et al. (2008). "Imaging the biogenesis of individual HIV-1 virions in live cells." Nature **454**(7201): 236-240.
Jouvenet, N., S. M. Simon, et al. (2009). "Imaging the interaction of HIV-1 genomes and Gag during assembly of individual viral particles." Proc Natl Acad Sci U S A **106**(45): 19114-19119.
Jouvenet, N., M. Zhadina, et al. (2011). "Dynamics of ESCRT protein recruitment during retroviral assembly." Nat Cell Biol **13**(4): 394-401.
Juette, M. F., T. J. Gould, et al. (2008). "Three-dimensional sub-100 nm resolution fluorescence microscopy of thick samples." Nat Methods **5**(6): 527-529.
Jungmann, R., M. S. Avendano, et al. (2014). "Multiplexed 3D cellular super-resolution imaging with DNA-PAINT and Exchange-PAINT." Nat Methods **11**(3): 313-318.
Kempf, N., V. Postupalenko, et al. (2015). "The HIV-1 nucleocapsid protein recruits negatively charged lipids to ensure its optimal binding to lipid membranes." J Virol **89**(3): 1756-1767.
Kienzle, N., M. Enders, et al. (1992). "Expression of the HIV-1 Nef protein in the baculovirus system: investigation of anti-Nef antibodies response in human sera and subcellular localization of Nef." Arch Virol **126**(1-4): 293-301.
Kim, G. H., F. P. Garcia de Arquer, et al. (2015). "High-Efficiency Colloidal Quantum Dot Photovoltaics via Robust Self-Assembled Monolayers." Nano Lett **15**(11): 7691-7696.
Kirkpatrick, N. D., E. Chung, et al. (2012). "Video-rate resonant scanning multiphoton microscopy: An emerging technique for intravital imaging of the tumor microenvironment." Intravital **1**(1).
Kiuchi, T., M. Higuchi, et al. (2015). "Multitarget super-resolution microscopy with high-density labeling by exchangeable probes." Nat Methods **12**(8): 743-746.
Klasens, B. I., M. Thiesen, et al. (1999). "The ability of the HIV-1 AAUAAA signal to bind polyadenylation factors is controlled by local RNA structure." Nucleic Acids Res **27**(2): 446-454.
Kleiman, L. (2002). "tRNA(Lys3): the primer tRNA for reverse transcription in HIV-1." IUBMB Life **53**(2): 107-114.
Kleiman, L. and S. Cen (2004). "The tRNALys packaging complex in HIV-1." Int J Biochem Cell Biol **36**(9): 1776-1786.

Kohl, J., J. Ng, et al. (2014). "Ultrafast tissue staining with chemical tags." Proc Natl Acad Sci U S A **111**(36): E3805-3814.
Kol, N., Y. Shi, et al. (2007). "A stiffness switch in human immunodeficiency virus." Biophys J **92**(5): 1777-1783.
Konig, R., Y. Zhou, et al. (2008). "Global analysis of host-pathogen interactions that regulate early-stage HIV-1 replication." Cell **135**(1): 49-60.
Kubitscheck, U. (2013). Fluorescence microscopy: from principles to biological applications, John Wiley & Sons.
Kukolj, G. and A. M. Skalka (1995). "Enhanced and coordinated processing of synapsed viral DNA ends by retroviral integrases in vitro." Genes Dev **9**(20): 2556-2567.
Kuznetsov, Y. G., J. G. Victoria, et al. (2003). "Atomic force microscopy investigation of human immunodeficiency virus (HIV) and HIV-infected lymphocytes." J Virol **77**(22): 11896-11909.
Lahaye, X., T. Satoh, et al. (2013). "The capsids of HIV-1 and HIV-2 determine immune detection of the viral cDNA by the innate sensor cGAS in dendritic cells." Immunity **39**(6): 1132-1142.
Lampe, M., J. A. Briggs, et al. (2007). "Double-labelled HIV-1 particles for study of virus-cell interaction." Virology **360**(1): 92-104.
Langhorst, M. F., S. Genisyuerek, et al. (2006). "Accumulation of FlAsH/Lumio Green in active mitochondria can be reversed by beta-mercaptoethanol for specific staining of tetracysteine-tagged proteins." Histochem Cell Biol **125**(6): 743-747.
Lapadat-Tapolsky, M., C. Gabus, et al. (1997). "Possible roles of HIV-1 nucleocapsid protein in the specificity of proviral DNA synthesis and in its variability." J Mol Biol **268**(2): 250-260.
Larson, D. R., M. C. Johnson, et al. (2005). "Visualization of retrovirus budding with correlated light and electron microscopy." Proc Natl Acad Sci U S A **102**(43): 15453-15458.
Le Blanc, I., P. P. Luyet, et al. (2005). "Endosome-to-cytosol transport of viral nucleocapsids." Nat Cell Biol **7**(7): 653-664.
Le Rouzic, E., A. Mousnier, et al. (2002). "Docking of HIV-1 Vpr to the nuclear envelope is mediated by the interaction with the nucleoporin hCG1." J Biol Chem **277**(47): 45091-45098.
Le Sage, V. and A. J. Mouland (2013). "Viral subversion of the nuclear pore complex." Viruses **5**(8): 2019-2042.
Lee, B. M., R. N. De Guzman, et al. (1998). "Dynamical behavior of the HIV-1 nucleocapsid protein." J Mol Biol **279**(3): 633-649.
Lee, C. A. (1988). Moire data interpretation by digital image processing, University of Wisconsin--Madison.
Lee, J. H., G. Ozorowski, et al. (2016). "Cryo-EM structure of a native, fully glycosylated, cleaved HIV-1 envelope trimer." Science **351**(6277): 1043-1048.
Lee, K., Z. Ambrose, et al. (2010). "Flexible use of nuclear import pathways by HIV-1." Cell Host Microbe **7**(3): 221-233.
Lehmann, M., S. Rocha, et al. (2011). "Quantitative multicolor super-resolution microscopy reveals tetherin HIV-1 interaction." PLoS Pathog **7**(12): e1002456.
Lelek, M., N. Casartelli, et al. (2015). "Chromatin organization at the nuclear pore favours HIV replication." Nat Commun **6**: 6483.
Lelek, M., F. Di Nunzio, et al. (2012). "Superresolution imaging of HIV in infected cells with FlAsH-PALM." Proc Natl Acad Sci U S A **109**(22): 8564-8569.
Leonard, C. K., M. W. Spellman, et al. (1990). "Assignment of intrachain disulfide bonds and characterization of potential glycosylation sites of the type 1 recombinant human immunodeficiency virus envelope glycoprotein (gp120) expressed in Chinese hamster ovary cells." J Biol Chem **265**(18): 10373-10382.
Leung, B. O. and K. C. Chou (2011). "Review of super-resolution fluorescence microscopy for biology." Appl Spectrosc **65**(9): 967-980.
Lever, A., H. Gottlinger, et al. (1989). "Identification of a sequence required for efficient packaging of human immunodeficiency virus type 1 RNA into virions." J Virol **63**(9): 4085-4087.

Levin, J. G., J. Guo, et al. (2005). "Nucleic acid chaperone activity of HIV-1 nucleocapsid protein: critical role in reverse transcription and molecular mechanism." Prog Nucleic Acid Res Mol Biol **80**: 217-286.
Li, S., C. P. Hill, et al. (2000). "Image reconstructions of helical assemblies of the HIV-1 CA protein." Nature **407**(6802): 409-413.
Lingappa, J. R., J. E. Dooher, et al. (2006). "Basic residues in the nucleocapsid domain of Gag are required for interaction of HIV-1 gag with ABCE1 (HP68), a cellular protein important for HIV-1 capsid assembly." J Biol Chem **281**(7): 3773-3784.
Liu, B., R. Dai, et al. (1999). "Interaction of the human immunodeficiency virus type 1 nucleocapsid with actin." J Virol **73**(4): 2901-2908.
Llano, M., S. Delgado, et al. (2004). "Lens epithelium-derived growth factor/p75 prevents proteasomal degradation of HIV-1 integrase." J Biol Chem **279**(53): 55570-55577.
Lochmann, T. L., D. V. Bann, et al. (2013). "NC-mediated nucleolar localization of retroviral gag proteins." Virus Res **171**(2): 304-318.
Lyonnais, S., R. J. Gorelick, et al. (2013). "A protein ballet around the viral genome orchestrated by HIV-1 reverse transcriptase leads to an architectural switch: from nucleocapsid-condensed RNA to Vpr-bridged DNA." Virus Res **171**(2): 287-303.
Ma, Y., Z. He, et al. (2016). "Real-Time Imaging of Single HIV-1 Disassembly with Multicolor Viral Particles." ACS Nano **10**(6): 6273-6282.
Madrid, A. S. and K. Weis (2006). "Nuclear transport is becoming crystal clear." Chromosoma **115**(2): 98-109.
Mak, J. and L. Kleiman (1997). "Primer tRNAs for reverse transcription." J Virol **71**(11): 8087-8095.
Maldarelli, F., M. Y. Chen, et al. (1993). "Human immunodeficiency virus type 1 Vpu protein is an oligomeric type I integral membrane protein." J Virol **67**(8): 5056-5061.
Malkusch, S., W. Muranyi, et al. (2013). "Single-molecule coordinate-based analysis of the morphology of HIV-1 assembly sites with near-molecular spatial resolution." Histochem Cell Biol **139**(1): 173-179.
Manley, S., J. M. Gillette, et al. (2008). "High-density mapping of single-molecule trajectories with photoactivated localization microscopy." Nat Methods **5**(2): 155-157.
Maranto, A. R. (1982). "Neuronal mapping: a photooxidation reaction makes Lucifer yellow useful for electron microscopy." Science **217**(4563): 953-955.
Margolick, J. B., A. Munoz, et al. (1995). "Failure of T-cell homeostasis preceding AIDS in HIV-1 infection. The Multicenter AIDS Cohort Study." Nat Med **1**(7): 674-680.
Mariani, R., D. Chen, et al. (2003). "Species-specific exclusion of APOBEC3G from HIV-1 virions by Vif." Cell **114**(1): 21-31.
Massiah, M. A., M. R. Starich, et al. (1994). "Three-dimensional structure of the human immunodeficiency virus type 1 matrix protein." J Mol Biol **244**(2): 198-223.
Matlin, K. S., H. Reggio, et al. (1982). "Pathway of vesicular stomatitis virus entry leading to infection." J Mol Biol **156**(3): 609-631.
Matreyek, K. A. and A. Engelman (2011). "The requirement for nucleoporin NUP153 during human immunodeficiency virus type 1 infection is determined by the viral capsid." J Virol **85**(15): 7818-7827.
Matreyek, K. A., S. S. Yucel, et al. (2013). "Nucleoporin NUP153 phenylalanine-glycine motifs engage a common binding pocket within the HIV-1 capsid protein to mediate lentiviral infectivity." PLoS Pathog **9**(10): e1003693.
Mattaj, I. W. and L. Englmeier (1998). "Nucleocytoplasmic transport: the soluble phase." Annu Rev Biochem **67**: 265-306.
Mattei, S., A. Flemming, et al. (2015). "RNA and Nucleocapsid Are Dispensable for Mature HIV-1 Capsid Assembly." J Virol **89**(19): 9739-9747.
Matthews, S., M. Mikhailov, et al. (1996). "The solution structure of the bovine leukaemia virus matrix protein and similarity with lentiviral matrix proteins." EMBO J **15**(13): 3267-3274.
Mayo, K., D. Huseby, et al. (2003). "Retrovirus capsid protein assembly arrangements." J Mol Biol **325**(1): 225-237.

McDonald, D., M. A. Vodicka, et al. (2002). "Visualization of the intracellular behavior of HIV in living cells." J Cell Biol **159**(3): 441-452.
McDonald, D., L. Wu, et al. (2003). "Recruitment of HIV and its receptors to dendritic cell-T cell junctions." Science **300**(5623): 1295-1297.
McKinney, S. A., C. S. Murphy, et al. (2009). "A bright and photostable photoconvertible fluorescent protein." Nat Methods **6**(2): 131-133.
Mekdad, H. E., E. Boutant, et al. (2016). "Characterization of the interaction between the HIV-1 Gag structural polyprotein and the cellular ribosomal protein L7 and its implication in viral nucleic acid remodeling." Retrovirology **13**(1): 54.
Melchior, F., T. Guan, et al. (1995). "GTP hydrolysis by Ran occurs at the nuclear pore complex in an early step of protein import." J Cell Biol **131**(3): 571-581.
Mely, Y., H. De Rocquigny, et al. (1996). "Zinc binding to the HIV-1 nucleocapsid protein: a thermodynamic investigation by fluorescence spectroscopy." Biochemistry **35**(16): 5175-5182.
Mely, Y., H. de Rocquigny, et al. (1995). "Binding of the HIV-1 nucleocapsid protein to the primer tRNA(3Lys), in vitro, is essentially not specific." J Biol Chem **270**(4): 1650-1656.
Mely, Y., N. Jullian, et al. (1994). "Spatial proximity of the HIV-1 nucleocapsid protein zinc fingers investigated by time-resolved fluorescence and fluorescence resonance energy transfer." Biochemistry **33**(40): 12085-12091.
Meng, X., G. Zhao, et al. (2011). "Structure of HIV-1 capsid assemblies by cryo-electron microscopy and iterative helical real-space reconstruction." J Vis Exp(54).
Meyer, B. E. and M. H. Malim (1994). "The HIV-1 Rev trans-activator shuttles between the nucleus and the cytoplasm." Genes Dev **8**(13): 1538-1547.
Meyerson, J. R., T. A. White, et al. (2011). "Determination of molecular structures of HIV envelope glycoproteins using cryo-electron tomography and automated sub-tomogram averaging." J Vis Exp(58).
Michalet, X., F. F. Pinaud, et al. (2005). "Quantum dots for live cells, in vivo imaging, and diagnostics." Science **307**(5709): 538-544.
Michel, N., I. Allespach, et al. (2005). "The Nef protein of human immunodeficiency virus establishes superinfection immunity by a dual strategy to downregulate cell-surface CCR5 and CD4." Curr Biol **15**(8): 714-723.
Miller, M., J. Schneider, et al. (1989). "Structure of complex of synthetic HIV-1 protease with a substrate-based inhibitor at 2.3 A resolution." Science **246**(4934): 1149-1152.
Miller, M. D., C. M. Farnet, et al. (1997). "Human immunodeficiency virus type 1 preintegration complexes: studies of organization and composition." J Virol **71**(7): 5382-5390.
Mirambeau, G., S. Lyonnais, et al. (2007). "HIV-1 protease and reverse transcriptase control the architecture of their nucleocapsid partner." PLoS One **2**(7): e669.
Mirambeau, G., S. Lyonnais, et al. (2006). "Transmission electron microscopy reveals an optimal HIV-1 nucleocapsid aggregation with single-stranded nucleic acids and the mature HIV-1 nucleocapsid protein." J Mol Biol **364**(3): 496-511.
Mire, C. E., J. M. White, et al. (2010). "A spatio-temporal analysis of matrix protein and nucleocapsid trafficking during vesicular stomatitis virus uncoating." PLoS Pathog **6**(7): e1000994.
Miyauchi, K., Y. Kim, et al. (2009). "HIV enters cells via endocytosis and dynamin-dependent fusion with endosomes." Cell **137**(3): 433-444.
Mojzisova, H., S. Bonneau, et al. (2009). "Photosensitizing properties of chlorins in solution and in membrane-mimicking systems." Photochem Photobiol Sci **8**(6): 778-787.
Monette, A., N. Pante, et al. (2011). "Examining the requirements for nucleoporins by HIV-1." Future Microbiol **6**(11): 1247-1250.
Monette, A., N. Pante, et al. (2011). "HIV-1 remodels the nuclear pore complex." J Cell Biol **193**(4): 619-631.
Morellet, N., H. de Rocquigny, et al. (1994). "Conformational behaviour of the active and inactive forms of the nucleocapsid NCp7 of HIV-1 studied by 1H NMR." J Mol Biol **235**(1): 287-301.
Mori, M., L. Kovalenko, et al. (2015). "Nucleocapsid Protein: A Desirable Target for Future Therapies Against HIV-1." Curr Top Microbiol Immunol **389**: 53-92.

Mori, M., A. Nucci, et al. (2014). "Functional and structural characterization of 2-amino-4-phenylthiazole inhibitors of the HIV-1 nucleocapsid protein with antiviral activity." ACS Chem Biol **9**(9): 1950-1955.
Morita, E., V. Sandrin, et al. (2007). "Identification of human MVB12 proteins as ESCRT-I subunits that function in HIV budding." Cell Host Microbe **2**(1): 41-53.
Morita, E., V. Sandrin, et al. (2011). "ESCRT-III protein requirements for HIV-1 budding." Cell Host Microbe **9**(3): 235-242.
Mouland, A. J., J. Mercier, et al. (2000). "The double-stranded RNA-binding protein Staufen is incorporated in human immunodeficiency virus type 1: evidence for a role in genomic RNA encapsidation." J Virol **74**(12): 5441-5451.
Muller, B., J. Daecke, et al. (2004). "Construction and characterization of a fluorescently labeled infectious human immunodeficiency virus type 1 derivative." J Virol **78**(19): 10803-10813.
Muranyi, W., S. Malkusch, et al. (2013). "Super-resolution microscopy reveals specific recruitment of HIV-1 envelope proteins to viral assembly sites dependent on the envelope C-terminal tail." PLoS Pathog **9**(2): e1003198.
Naldini, L., U. Blomer, et al. (1996). "In vivo gene delivery and stable transduction of nondividing cells by a lentiviral vector." Science **272**(5259): 263-267.
Navia, M. A., P. M. Fitzgerald, et al. (1989). "Three-dimensional structure of aspartyl protease from human immunodeficiency virus HIV-1." Nature **337**(6208): 615-620.
Neil, S. J., T. Zang, et al. (2008). "Tetherin inhibits retrovirus release and is antagonized by HIV-1 Vpu." Nature **451**(7177): 425-430.
Nermut, M. V. and A. Fassati (2003). "Structural analyses of purified human immunodeficiency virus type 1 intracellular reverse transcription complexes." J Virol **77**(15): 8196-8206.
Nermut, M. V., D. J. Hockley, et al. (1998). "Further evidence for hexagonal organization of HIV gag protein in prebudding assemblies and immature virus-like particles." J Struct Biol **123**(2): 143-149.
Niedrig, M., J. P. Rabanus, et al. (1988). "Monoclonal antibodies directed against human immunodeficiency virus (HIV) gag proteins with specificity for conserved epitopes in HIV-1, HIV-2 and simian immunodeficiency virus." J Gen Virol **69 (Pt 8)**: 2109-2114.
Nottet, H. S., I. Janse, et al. (1993). "Infection of epithelial cell line HEp-2 with human immunodeficiency virus type 1 is CD4 dependent." J Med Virol **40**(1): 39-43.
Ono, A., S. D. Ablan, et al. (2004). "Phosphatidylinositol (4,5) bisphosphate regulates HIV-1 Gag targeting to the plasma membrane." Proc Natl Acad Sci U S A **101**(41): 14889-14894.
Ono, A. and E. O. Freed (2001). "Plasma membrane rafts play a critical role in HIV-1 assembly and release." Proc Natl Acad Sci U S A **98**(24): 13925-13930.
Orloff, J. (1993). "High-resolution focused ion beams." Review of Scientific Instruments **64**(5): 1105-1130.
Ott, D. E. (2008). "Cellular proteins detected in HIV-1." Rev Med Virol **18**(3): 159-175.
Ott, D. E., L. V. Coren, et al. (2003). "Elimination of protease activity restores efficient virion production to a human immunodeficiency virus type 1 nucleocapsid deletion mutant." J Virol **77**(10): 5547-5556.
Ott, D. E., L. V. Coren, et al. (2005). "Redundant roles for nucleocapsid and matrix RNA-binding sequences in human immunodeficiency virus type 1 assembly." J Virol **79**(22): 13839-13847.
Ovesny, M., P. Krizek, et al. (2014). "ThunderSTORM: a comprehensive ImageJ plug-in for PALM and STORM data analysis and super-resolution imaging." Bioinformatics **30**(16): 2389-2390.
Paillart, J. C., M. Shehu-Xhilaga, et al. (2004). "Dimerization of retroviral RNA genomes: an inseparable pair." Nat Rev Microbiol **2**(6): 461-472.
Pancera, M., T. Zhou, et al. (2014). "Structure and immune recognition of trimeric pre-fusion HIV-1 Env." Nature **514**(7523): 455-461.
Pannecouque, C., B. Szafarowicz, et al. (2010). "Inhibition of HIV-1 replication by a bis-thiadiazolbenzene-1,2-diamine that chelates zinc ions from retroviral nucleocapsid zinc fingers." Antimicrob Agents Chemother **54**(4): 1461-1468.

Pantaleo, G., C. Graziosi, et al. (1993). "HIV infection is active and progressive in lymphoid tissue during the clinically latent stage of disease." Nature **362**(6418): 355-358.
Park, Y. I., K. T. Lee, et al. (2015). "Upconverting nanoparticles: a versatile platform for wide-field two-photon microscopy and multi-modal in vivo imaging." Chem Soc Rev **44**(6): 1302-1317.
Parr-Brownlie, L. C., C. Bosch-Bouju, et al. (2015). "Lentiviral vectors as tools to understand central nervous system biology in mammalian model organisms." Front Mol Neurosci **8**: 14.
Patterson, G. H. and J. Lippincott-Schwartz (2002). "A photoactivatable GFP for selective photolabeling of proteins and cells." Science **297**(5588): 1873-1877.
Pauli, G., E. Hausmann, et al. (1987). "LAV/HTLV-III: fine-structure analysis, localization of structural proteins, and detection of envelope antigens by patient sera." Haematol Blood Transfus **31**: 407-409.
Peeters, M., C. Honore, et al. (1989). "Isolation and partial characterization of an HIV-related virus occurring naturally in chimpanzees in Gabon." AIDS **3**(10): 625-630.
Peng, K., W. Muranyi, et al. (2014). "Quantitative microscopy of functional HIV post-entry complexes reveals association of replication with the viral capsid." Elife **3**: e04114.
Pereira, C. F., P. C. Ellenberg, et al. (2011). "Labeling of multiple HIV-1 proteins with the biarsenical-tetracysteine system." PLoS One **6**(2): e17016.
Pereira, C. F., J. Rossy, et al. (2012). "HIV taken by STORM: super-resolution fluorescence microscopy of a viral infection." Virol J **9**: 84.
Perrin-Tricaud, C., J. Davoust, et al. (1999). "Tagging the human immunodeficiency virus gag protein with green fluorescent protein. Minimal evidence for colocalisation with actin." Virology **255**(1): 20-25.
Peterlin, B. M., P. A. Luciw, et al. (1986). "Elevated levels of mRNA can account for the trans-activation of human immunodeficiency virus." Proc Natl Acad Sci U S A **83**(24): 9734-9738.
Petit, C., O. Schwartz, et al. (1999). "Oligomerization within virions and subcellular localization of human immunodeficiency virus type 1 integrase." J Virol **73**(6): 5079-5088.
Pettit, S. C., J. N. Lindquist, et al. (2005). "Processing sites in the human immunodeficiency virus type 1 (HIV-1) Gag-Pro-Pol precursor are cleaved by the viral protease at different rates." Retrovirology **2**: 66.
Pettit, S. C., M. D. Moody, et al. (1994). "The p2 domain of human immunodeficiency virus type 1 Gag regulates sequential proteolytic processing and is required to produce fully infectious virions." J Virol **68**(12): 8017-8027.
Pham, S., T. Tabarin, et al. (2015). "Cryo-electron microscopy and single molecule fluorescent microscopy detect CD4 receptor induced HIV size expansion prior to cell entry." Virology **486**: 121-133.
Piekna-Przybylska, D., L. DiChiacchio, et al. (2010). "A sequence similar to tRNA 3 Lys gene is embedded in HIV-1 U3-R and promotes minus-strand transfer." Nat Struct Mol Biol **17**(1): 83-89.
Pluymers, W., P. Cherepanov, et al. (1999). "Nuclear localization of human immunodeficiency virus type 1 integrase expressed as a fusion protein with green fluorescent protein." Virology **258**(2): 327-332.
Poljak, L., S. M. Batson, et al. (2003). "Analysis of NCp7-dependent activation of HIV-1 cDNA integration and its conservation among retroviral nucleocapsid proteins." J Mol Biol **329**(3): 411-421.
Popov, S., E. Popova, et al. (2008). "Human immunodeficiency virus type 1 Gag engages the Bro1 domain of ALIX/AIP1 through the nucleocapsid." J Virol **82**(3): 1389-1398.
Popov, S., E. Popova, et al. (2009). "Divergent Bro1 domains share the capacity to bind human immunodeficiency virus type 1 nucleocapsid and to enhance virus-like particle production." J Virol **83**(14): 7185-7193.
Popov, S., M. Rexach, et al. (1998). "Viral protein R regulates nuclear import of the HIV-1 pre-integration complex." EMBO J **17**(4): 909-917.
Popovic, M., E. Read-Connole, et al. (1984). "T4 positive human neoplastic cell lines susceptible to and permissive for HTLV-III." Lancet **2**(8417-8418): 1472-1473.
Popper, S. J., A. D. Sarr, et al. (2000). "Low plasma human immunodeficiency virus type 2 viral load is independent of proviral load: low virus production in vivo." J Virol **74**(3): 1554-1557.

Pornillos, O., B. K. Ganser-Pornillos, et al. (2011). "Atomic-level modelling of the HIV capsid." Nature **469**(7330): 424-427.
Post, K., B. Kankia, et al. (2009). "Fidelity of plus-strand priming requires the nucleic acid chaperone activity of HIV-1 nucleocapsid protein." Nucleic Acids Res **37**(6): 1755-1766.
Prabu-Jeyabalan, M., E. Nalivaika, et al. (2002). "Substrate shape determines specificity of recognition for HIV-1 protease: analysis of crystal structures of six substrate complexes." Structure **10**(3): 369-381.
Pradeepa, M. M., H. G. Sutherland, et al. (2012). "Psip1/Ledgf p52 binds methylated histone H3K36 and splicing factors and contributes to the regulation of alternative splicing." PLoS Genet **8**(5): e1002717.
Prescher, J., V. Baumgartel, et al. (2015). "Super-resolution imaging of ESCRT-proteins at HIV-1 assembly sites." PLoS Pathog **11**(2): e1004677.
Quercioli, F. (2011). Fundamentals of optical microscopy. Optical Fluorescence Microscopy, Springer**:** 1-36.
Quercioli, V., C. Di Primio, et al. (2016). "Comparative Analysis of HIV-1 and Murine Leukemia Virus Three-Dimensional Nuclear Distributions." J Virol **90**(10): 5205-5209.
Racine, P. J., C. Chamontin, et al. (2016). "Requirements for nucleocapsid-mediated regulation of reverse transcription during the late steps of HIV-1 assembly." Sci Rep **6**: 27536.
Raghavendra, N. K., N. Shkriabai, et al. (2010). "Identification of host proteins associated with HIV-1 preintegration complexes isolated from infected CD4+ cells." Retrovirology **7**: 66.
Ramboarina, S., N. Morellet, et al. (1999). "Structural investigation on the requirement of CCHH zinc finger type in nucleocapsid protein of human immunodeficiency virus 1." Biochemistry **38**(30): 9600-9607.
Raposo, G., M. Moore, et al. (2002). "Human macrophages accumulate HIV-1 particles in MHC II compartments." Traffic **3**(10): 718-729.
Rasaiyaah, J., C. P. Tan, et al. (2013). "HIV-1 evades innate immune recognition through specific cofactor recruitment." Nature **503**(7476): 402-405.
Reichert, W. M. and G. A. Truskey (1990). "Total internal reflection fluorescence (TIRF) microscopy. I. Modelling cell contact region fluorescence." J Cell Sci **96 (Pt 2)**: 219-230.
Rein, A., L. E. Henderson, et al. (1998). "Nucleic-acid-chaperone activity of retroviral nucleocapsid proteins: significance for viral replication." Trends Biochem Sci **23**(8): 297-301.
Reisch, A., P. Didier, et al. (2014). "Collective fluorescence switching of counterion-assembled dyes in polymer nanoparticles." Nat Commun **5**: 4089.
Reiser, J., G. Harmison, et al. (1996). "Transduction of nondividing cells using pseudotyped defective high-titer HIV type 1 particles." Proc Natl Acad Sci U S A **93**(26): 15266-15271.
Ribbeck, K., G. Lipowsky, et al. (1998). "NTF2 mediates nuclear import of Ran." EMBO J **17**(22): 6587-6598.
Rice, W. G., C. A. Schaeffer, et al. (1993). "The site of antiviral action of 3-nitrosobenzamide on the infectivity process of human immunodeficiency virus in human lymphocytes." Proc Natl Acad Sci U S A **90**(20): 9721-9724.
Rice, W. G., J. G. Supko, et al. (1995). "Inhibitors of HIV nucleocapsid protein zinc fingers as candidates for the treatment of AIDS." Science **270**(5239): 1194-1197.
Rice, W. G., J. A. Turpin, et al. (1997). "Azodicarbonamide inhibits HIV-1 replication by targeting the nucleocapsid protein." Nat Med **3**(3): 341-345.
Richardson, W. D., A. D. Mills, et al. (1988). "Nuclear protein migration involves two steps: rapid binding at the nuclear envelope followed by slower translocation through nuclear pores." Cell **52**(5): 655-664.
Riviere, L., J. L. Darlix, et al. (2010). "Analysis of the viral elements required in the nuclear import of HIV-1 DNA." J Virol **84**(2): 729-739.
Rodgers, W. (2002). "Making membranes green: construction and characterization of GFP-fusion proteins targeted to discrete plasma membrane domains." Biotechniques **32**(5): 1044-1046, 1048, 1050-1041.

Rout, M. P. and J. D. Aitchison (2000). "Pore relations: nuclear pore complexes and nucleocytoplasmic exchange." Essays Biochem **36**: 75-88.
Rowland-Jones, S. L. and H. C. Whittle (2007). "Out of Africa: what can we learn from HIV-2 about protective immunity to HIV-1?" Nat Immunol **8**(4): 329-331.
Rulli, S. J., Jr., C. S. Hibbert, et al. (2007). "Selective and nonselective packaging of cellular RNAs in retrovirus particles." J Virol **81**(12): 6623-6631.
Russell, R. S., C. Liang, et al. (2004). "Is HIV-1 RNA dimerization a prerequisite for packaging? Yes, no, probably?" Retrovirology **1**: 23.
Saad, J. S., E. Loeliger, et al. (2007). "Point mutations in the HIV-1 matrix protein turn off the myristyl switch." J Mol Biol **366**(2): 574-585.
Saad, J. S., J. Miller, et al. (2006). "Structural basis for targeting HIV-1 Gag proteins to the plasma membrane for virus assembly." Proc Natl Acad Sci U S A **103**(30): 11364-11369.
Saadatmand, J. and L. Kleiman (2012). "Aspects of HIV-1 assembly that promote primer tRNA(Lys3) annealing to viral RNA." Virus Res **169**(2): 340-348.
Sage, D., H. Kirshner, et al. (2015). "Quantitative evaluation of software packages for single-molecule localization microscopy." Nat Methods **12**(8): 717-724.
Salic, A. and T. J. Mitchison (2008). "A chemical method for fast and sensitive detection of DNA synthesis in vivo." Proc Natl Acad Sci U S A **105**(7): 2415-2420.
Sanchez-Pescador, R., M. D. Power, et al. (1985). "Nucleotide sequence and expression of an AIDS-associated retrovirus (ARV-2)." Science **227**(4686): 484-492.
Schaller, T., K. E. Ocwieja, et al. (2011). "HIV-1 capsid-cyclophilin interactions determine nuclear import pathway, integration targeting and replication efficiency." PLoS Pathog **7**(12): e1002439.
Schlichenmeyer, T. C., M. Wang, et al. (2014). "Video-rate structured illumination microscopy for high-throughput imaging of large tissue areas." Biomed Opt Express **5**(2): 366-377.
Schneider, C. A., W. S. Rasband, et al. (2012). "NIH Image to ImageJ: 25 years of image analysis." Nat Methods **9**(7): 671-675.
Schur, F. K., W. J. Hagen, et al. (2015). "Structure of the immature HIV-1 capsid in intact virus particles at 8.8 A resolution." Nature **517**(7535): 505-508.
Schur, F. K., M. Obr, et al. (2016). "An atomic model of HIV-1 capsid-SP1 reveals structures regulating assembly and maturation." Science **353**(6298): 506-508.
Sharonov, A. and R. M. Hochstrasser (2006). "Wide-field subdiffraction imaging by accumulated binding of diffusing probes." Proc Natl Acad Sci U S A **103**(50): 18911-18916.
Shehu-Xhilaga, M., H. G. Kraeusslich, et al. (2001). "Proteolytic processing of the p2/nucleocapsid cleavage site is critical for human immunodeficiency virus type 1 RNA dimer maturation." J Virol **75**(19): 9156-9164.
Sheng, N., S. C. Pettit, et al. (1997). "Determinants of the human immunodeficiency virus type 1 p15NC-RNA interaction that affect enhanced cleavage by the viral protease." J Virol **71**(8): 5723-5732.
Shim, S. H., C. Xia, et al. (2012). "Super-resolution fluorescence imaging of organelles in live cells with photoswitchable membrane probes." Proc Natl Acad Sci U S A **109**(35): 13978-13983.
Shvadchak, V., S. Sanglier, et al. (2009). "Identification by high throughput screening of small compounds inhibiting the nucleic acid destabilization activity of the HIV-1 nucleocapsid protein." Biochimie **91**(7): 916-923.
Siliciano, R. F. and W. C. Greene (2011). "HIV latency." Cold Spring Harb Perspect Med **1**(1): a007096.
Silvestri, G., A. Fedanov, et al. (2005). "Divergent host responses during primary simian immunodeficiency virus SIVsm infection of natural sooty mangabey and nonnatural rhesus macaque hosts." J Virol **79**(7): 4043-4054.
Skripkin, E., J. C. Paillart, et al. (1994). "Identification of the primary site of the human immunodeficiency virus type 1 RNA dimerization in vitro." Proc Natl Acad Sci U S A **91**(11): 4945-4949.
Sleiman, D., V. Goldschmidt, et al. (2012). "Initiation of HIV-1 reverse transcription and functional role of nucleocapsid-mediated tRNA/viral genome interactions." Virus Res **169**(2): 324-339.
Sosic, A., F. Frecentese, et al. (2013). "Design, synthesis and biological evaluation of TAR and cTAR binders as HIV-1 nucleocapsid inhibitors." MedChemComm **4**(10): 1388-1393.

Sosinsky, G. E., B. N. Giepmans, et al. (2007). "Markers for correlated light and electron microscopy." Methods Cell Biol **79**: 575-591.
Sougrat, R., A. Bartesaghi, et al. (2007). "Electron tomography of the contact between T cells and SIV/HIV-1: implications for viral entry." PLoS Pathog **3**(5): e63.
South, T. L. and M. F. Summers (1993). "Zinc- and sequence-dependent binding to nucleic acids by the N-terminal zinc finger of the HIV-1 nucleocapsid protein: NMR structure of the complex with the Psi-site analog, dACGCC." Protein Sci **2**(1): 3-19.
Spacek, J. and A. R. Lieberman (1974). "Three dimensional reconstruction in electron microscopy of the central nervous system." Sb Ved Pr Lek Fak Karlovy Univerzity Hradci Kralove **17**(3): 203-222.
Spiegelhalter, C., V. Tosch, et al. (2010). "From dynamic live cell imaging to 3D ultrastructure: novel integrated methods for high pressure freezing and correlative light-electron microscopy." PLoS One **5**(2): e9014.
Srivastava, P., M. Schito, et al. (2004). "Optimization of unique, uncharged thioesters as inhibitors of HIV replication." Bioorg Med Chem **12**(24): 6437-6450.
Stannard, L. M., F. D. van der Riet, et al. (1987). "The morphology of human immunodeficiency virus particles by negative staining electron microscopy." J Gen Virol **68 (Pt 3)**: 919-923.
Stauffer, S., S. A. Rahman, et al. (2014). "The nucleocapsid domain of Gag is dispensable for actin incorporation into HIV-1 and for association of viral budding sites with cortical F-actin." J Virol **88**(14): 7893-7903.
Stephen, A. G., K. M. Worthy, et al. (2002). "Identification of HIV-1 nucleocapsid protein: nucleic acid antagonists with cellular anti-HIV activity." Biochem Biophys Res Commun **296**(5): 1228-1237.
Stiel, A. C., M. Andresen, et al. (2008). "Generation of monomeric reversibly switchable red fluorescent proteins for far-field fluorescence nanoscopy." Biophys J **95**(6): 2989-2997.
Stiel, A. C., S. Trowitzsch, et al. (2007). "1.8 A bright-state structure of the reversibly switchable fluorescent protein Dronpa guides the generation of fast switching variants." Biochem J **402**(1): 35-42.
Strauss, J. D., J. E. Hammonds, et al. (2015). "Three-Dimensional Structural Characterization of HIV-1 Tethered to Human Cells." J Virol **90**(3): 1507-1521.
Sun, X., V. K. Yau, et al. (2005). "Role of clathrin-mediated endocytosis during vesicular stomatitis virus entry into host cells." Virology **338**(1): 53-60.
Sundquist, W. I. and H. G. Krausslich (2012). "HIV-1 assembly, budding, and maturation." Cold Spring Harb Perspect Med **2**(7): a006924.
Suntharalingam, M. and S. R. Wente (2003). "Peering through the pore: nuclear pore complex structure, assembly, and function." Dev Cell **4**(6): 775-789.
Suzuki, Y. and R. Craigie (2007). "The road to chromatin - nuclear entry of retroviruses." Nat Rev Microbiol **5**(3): 187-196.
Suzuki, Y. and Y. Suzuki (2011). Gene regulatable lentiviral vector system, INTECH Open Access Publisher.
Tahirov, T. H., N. D. Babayeva, et al. (2010). "Crystal structure of HIV-1 Tat complexed with human P-TEFb." Nature **465**(7299): 747-751.
Tam, J., G. A. Cordier, et al. (2014). "Cross-talk-free multi-color STORM imaging using a single fluorophore." PLoS One **9**(7): e101772.
Tanaka, M., B. A. Robinson, et al. (2015). "Mutations of Conserved Residues in the Major Homology Region Arrest Assembling HIV-1 Gag as a Membrane-Targeted Intermediate Containing Genomic RNA and Cellular Proteins." J Virol **90**(4): 1944-1963.
Tebit, D. M. and E. J. Arts (2011). "Tracking a century of global expansion and evolution of HIV to drive understanding and to combat disease." Lancet Infect Dis **11**(1): 45-56.
Tekeste, S. S., T. A. Wilkinson, et al. (2015). "Interaction between Reverse Transcriptase and Integrase Is Required for Reverse Transcription during HIV-1 Replication." J Virol **89**(23): 12058-12069.
Terry, L. J. and S. R. Wente (2009). "Flexible gates: dynamic topologies and functions for FG nucleoporins in nucleocytoplasmic transport." Eukaryot Cell **8**(12): 1814-1827.
Thomas, J. A., T. D. Gagliardi, et al. (2006). "Human immunodeficiency virus type 1 nucleocapsid zinc-finger mutations cause defects in reverse transcription and integration." Virology **353**(1): 41-51.

Thomas, J. A. and R. J. Gorelick (2008). "Nucleocapsid protein function in early infection processes." Virus Res **134**(1-2): 39-63.
Tompa, P. and P. Csermely (2004). "The role of structural disorder in the function of RNA and protein chaperones." FASEB J **18**(11): 1169-1175.
Turner, B. G. and M. F. Summers (1999). "Structural biology of HIV." J Mol Biol **285**(1): 1-32.
Turpin, J. A., M. L. Schito, et al. (2008). "Topical microbicides: a promising approach for controlling the AIDS pandemic via retroviral zinc finger inhibitors." Adv Pharmacol **56**: 229-256.
Turpin, J. A., Y. Song, et al. (1999). "Synthesis and biological properties of novel pyridinioalkanoyl thiolesters (PATE) as anti-HIV-1 agents that target the viral nucleocapsid protein zinc fingers." J Med Chem **42**(1): 67-86.
Turpin, J. A., S. J. Terpening, et al. (1996). "Inhibitors of human immunodeficiency virus type 1 zinc fingers prevent normal processing of gag precursors and result in the release of noninfectious virus particles." J Virol **70**(9): 6180-6189.
Ueno, T., K. Tokunaga, et al. (2004). "Nucleolin and the packaging signal, psi, promote the budding of human immunodeficiency virus type-1 (HIV-1)." Microbiol Immunol **48**(2): 111-118.
Urbaneja, M. A., B. P. Kane, et al. (1999). "Binding properties of the human immunodeficiency virus type 1 nucleocapsid protein p7 to a model RNA: elucidation of the structural determinants for function." J Mol Biol **287**(1): 59-75.
van de Linde, S., I. Krstic, et al. (2011). "Photoinduced formation of reversible dye radicals and their impact on super-resolution imaging." Photochem Photobiol Sci **10**(4): 499-506.
Van Engelenburg, S. B., G. Shtengel, et al. (2014). "Distribution of ESCRT machinery at HIV assembly sites reveals virus scaffolding of ESCRT subunits." Science **343**(6171): 653-656.
Van Heuverswyn, F., Y. Li, et al. (2006). "Human immunodeficiency viruses: SIV infection in wild gorillas." Nature **444**(7116): 164.
Vaughan, J. C., S. Jia, et al. (2012). "Ultrabright photoactivatable fluorophores created by reductive caging." Nat Methods **9**(12): 1181-1184.
Vercruysse, T., B. Basta, et al. (2012). "A phenyl-thiadiazolylidene-amine derivative ejects zinc from retroviral nucleocapsid zinc fingers and inactivates HIV virions." Retrovirology **9**: 95.
Verkhusha, V. V. and A. Sorkin (2005). "Conversion of the monomeric red fluorescent protein into a photoactivatable probe." Chem Biol **12**(3): 279-285.
Vicidomini, G., I. C. Hernandez, et al. (2014). "Gated CW-STED microscopy: a versatile tool for biological nanometer scale investigation." Methods **66**(2): 124-130.
Vink, C., D. C. van Gent, et al. (1991). "Human immunodeficiency virus integrase protein requires a subterminal position of its viral DNA recognition sequence for efficient cleavage." J Virol **65**(9): 4636-4644.
Vink, C., E. Yeheskiely, et al. (1991). "Site-specific hydrolysis and alcoholysis of human immunodeficiency virus DNA termini mediated by the viral integrase protein." Nucleic Acids Res **19**(24): 6691-6698.
Vodicka, M. A., D. M. Koepp, et al. (1998). "HIV-1 Vpr interacts with the nuclear transport pathway to promote macrophage infection." Genes Dev **12**(2): 175-185.
von Schwedler, U., R. S. Kornbluth, et al. (1994). "The nuclear localization signal of the matrix protein of human immunodeficiency virus type 1 allows the establishment of infection in macrophages and quiescent T lymphocytes." Proc Natl Acad Sci U S A **91**(15): 6992-6996.
Vuilleumier, C., E. Bombarda, et al. (1999). "Nucleic acid sequence discrimination by the HIV-1 nucleocapsid protein NCp7: a fluorescence study." Biochemistry **38**(51): 16816-16825.
Wain-Hobson, S. (1998). "More ado about HIV's origins." Nat Med **4**(9): 1001-1002.
Walter, B. (1988). Ann.Phys (Leipzig) **34**: 502-517.
Walter, B. (1988). Ann.Phys (Leipzig) **34**: 316-326.
Walter, B. (1988). Ann.Phys (Leipzig) **34**: 518-533.
Wang, Y. X., L. B. Shi, et al. (1991). "Functional water channels and proton pumps are in separate populations of endocytic vesicles in toad bladder granular cells." Biochemistry **30**(11): 2888-2894.
Warrilow, D., G. Tachedjian, et al. (2009). "Maturation of the HIV reverse transcription complex: putting the jigsaw together." Rev Med Virol **19**(6): 324-337.

Warui, D. M. and A. M. Baranger (2009). "Identification of specific small molecule ligands for stem loop 3 ribonucleic acid of the packaging signal Psi of human immunodeficiency virus-1." J Med Chem **52**(17): 5462-5473.
Watts, J. M., K. K. Dang, et al. (2009). "Architecture and secondary structure of an entire HIV-1 RNA genome." Nature **460**(7256): 711-716.
Weinstein, J. N., S. Yoshikami, et al. (1977). "Liposome-cell interaction: transfer and intracellular release of a trapped fluorescent marker." Science **195**(4277): 489-492.
Welker, R., H. Hohenberg, et al. (2000). "Biochemical and structural analysis of isolated mature cores of human immunodeficiency virus type 1." J Virol **74**(3): 1168-1177.
Westphal, V. and S. W. Hell (2005). "Nanoscale resolution in the focal plane of an optical microscope." Phys Rev Lett **94**(14): 143903.
White, J., K. Matlin, et al. (1981). "Cell fusion by Semliki Forest, influenza, and vesicular stomatitis viruses." J Cell Biol **89**(3): 674-679.
Wiedenmann, J., B. Vallone, et al. (2005). "Red fluorescent protein eqFP611 and its genetically engineered dimeric variants." J Biomed Opt **10**(1): 14003.
Wildanger, D., R. Medda, et al. (2009). "A compact STED microscope providing 3D nanoscale resolution." J Microsc **236**(1): 35-43.
Wilk, T., B. Gowen, et al. (1999). "Actin associates with the nucleocapsid domain of the human immunodeficiency virus Gag polyprotein." J Virol **73**(3): 1931-1940.
Willey, R. L., F. Maldarelli, et al. (1992). "Human immunodeficiency virus type 1 Vpu protein induces rapid degradation of CD4." J Virol **66**(12): 7193-7200.
Willig, K. I., B. Harke, et al. (2007). "STED microscopy with continuous wave beams." Nat Methods **4**(11): 915-918.
Wong, R. W., J. I. Mamede, et al. (2015). "Impact of Nucleoporin-Mediated Chromatin Localization and Nuclear Architecture on HIV Integration Site Selection." J Virol **89**(19): 9702-9705.
Woodward, C. L., S. N. Cheng, et al. (2015). "Electron cryotomography studies of maturing HIV-1 particles reveal the assembly pathway of the viral core." J Virol **89**(2): 1267-1277.
Woodward, C. L. and S. A. Chow (2010). "The nuclear pore complex: a new dynamic in HIV-1 replication." Nucleus **1**(1): 18-22.
Wright, E. R., J. B. Schooler, et al. (2007). "Electron cryotomography of immature HIV-1 virions reveals the structure of the CA and SP1 Gag shells." EMBO J **26**(8): 2218-2226.
Wu, H., M. Mitra, et al. (2014). "Differential contribution of basic residues to HIV-1 nucleocapsid protein's nucleic acid chaperone function and retroviral replication." Nucleic Acids Res **42**(4): 2525-2537.
Wu, J. Q., A. Ozarowski, et al. (1997). "Binding of the nucleocapsid protein of type 1 human immunodeficiency virus to nucleic acids studied using phosphorescence and optically detected magnetic resonance." Biochemistry **36**(41): 12506-12518.
Wu, X., H. Liu, et al. (1999). "Human immunodeficiency virus type 1 integrase protein promotes reverse transcription through specific interactions with the nucleoprotein reverse transcription complex." J Virol **73**(3): 2126-2135.
Xu, H., T. Franks, et al. (2013). "Evidence for biphasic uncoating during HIV-1 infection from a novel imaging assay." Retrovirology **10**: 70.
Yamashita, M. and M. Emerman (2004). "Capsid is a dominant determinant of retrovirus infectivity in nondividing cells." J Virol **78**(11): 5670-5678.
Yang, Y., T. Fricke, et al. (2013). "Inhibition of reverse transcriptase activity increases stability of the HIV-1 core." J Virol **87**(1): 683-687.
Yarchoan, R., R. W. Klecker, et al. (1986). "Administration of 3'-azido-3'-deoxythymidine, an inhibitor of HTLV-III/LAV replication, to patients with AIDS or AIDS-related complex." Lancet **1**(8481): 575-580.
Ye, R. G., L. B. Shi, et al. (1989). "Functional colocalization of water channels and proton pumps in endosomes from kidney proximal tubule." J Gen Physiol **93**(5): 885-902.
Yu, K. L., S. H. Lee, et al. (2016). "HIV-1 nucleocapsid protein localizes efficiently to the nucleus and nucleolus." Virology **492**: 204-212.

Zargarian, L., C. Tisne, et al. (2014). "Dynamics of linker residues modulate the nucleic acid binding properties of the HIV-1 nucleocapsid protein zinc fingers." PLoS One **9**(7): e102150.
Zhang, J. and C. S. Crumpacker (2002). "Human immunodeficiency virus type 1 nucleocapsid protein nuclear localization mediates early viral mRNA expression." J Virol **76**(20): 10444-10454.
Zhao, G., J. R. Perilla, et al. (2013). "Mature HIV-1 capsid structure by cryo-electron microscopy and all-atom molecular dynamics." Nature **497**(7451): 643-646.
Zhu, K., C. Dobard, et al. (2004). "Requirement for integrase during reverse transcription of human immunodeficiency virus type 1 and the effect of cysteine mutations of integrase on its interactions with reverse transcriptase." J Virol **78**(10): 5045-5055.
Zimmerman, C., K. C. Klein, et al. (2002). "Identification of a host protein essential for assembly of immature HIV-1 capsids." Nature **415**(6867): 88-92.

Résumé en français suivi des mots-clés en français

La protéine de nucléocapside du VIH-1 (NCp7) joue un rôle important dans plusieurs étapes du cycle viral. Ses interactions dans l'environnement intracellulaire dans les conditions proches d'une vraie infection sont peu décrites. L'objectif de ce projet de thèse a été de développer des approches d'imagerie permettant de suivre la NCp7 au cours des étapes précoces du cycle viral directement dans les cellules infectées. En analysant l'intensité des pseudovirus fluorescents nous avons montré un effet de « dequenching » de fluorescence témoignant d'une diminution de la concentration en NCp7 au sein des particules virales, résultant très probablement du relargage des molécules de nucléocapside à partir des complexes viraux. Ces résultats montrent pour la première fois la libération de la NCp7 dans le cytoplasme lors de la transcription inverse. Les pseudovirus NCp7-TC ont ensuite été imagés en haute résolution par microscopie PALM. Les images de distribution de la NCp7 marquée ont révélé la présence de la NCp7-TC à l'intérieur du noyau. Nous avons mis en evidence par microscopie électronique la presence de la NCp7-TC à proximité de pores nucléaires.

Mots clés: protéin de nucléocapside, transcription inverse, pseudovirus, étiquette tetracystéine, internalization dans le noya, PALM, microscopie electronique.

Résumé en anglais suivi des mots-clés en anglais

The nucleocapsid protein of HIV-1 (NCp7) plays an important role in several stages of the viral cycle. Its interactions in the intracellular environment under conditions close to true infection are not well described. The objective of this thesis project was to develop imaging approaches to monitor NCp7 during the early stages of the viral cycle directly in infected cells. By analyzing the intensity of the fluorescent pseudoviruses, we showed a fluorescence "dequenching" effect indicating a decrease in the NCp7 concentration within the virus particles, most likely resulting from the release of the nucleocapsid molecules from the viral complexes. These results show for the first time the release of NCp7 into the cytoplasm during reverse transcription. The pseudoviruses NCp7-TC were then imaged in high resolution by PALM microscopy. The distribution images of labeled NCp7 revealed the presence of NCp7-TC within the nucleus. We have demonstrated the presence of NCp7-TC in the vicinity of nuclear pores by electron microscopy.

Keywords : Nucleocapsid protein, reverse transcription, pseudovirus, tetracystin label, internalization in nucleus, PALM, electron microscopy.

Imagerie du trafic intracellulaire de la protéine de nucléocapside du VIH-1

Introduction

Dans le domaine de la virologie, les techniques microscopiques représentent des outils indispensables pour étudier la morphologie des particules virales, ainsi que de les suivre au cours des différentes étapes de l'infection. La microscopie électronique et la microscopie à force atomique permettent de résoudre la structure des virions avec une résolution de quelques nanomètres. La microscopie optique quant à elle, permet une imagerie dynamique dans des conditions *« in vivo ».* De plus, des récents progrès dans ce domaine ont repoussé les limites de la résolution spatiale permettant de distinguer des structures nanométriques. La taille de VIH-1 étant proche de 100 nm, cette avancée technique a ouvert un champ nouveau permettant de visualiser des fines modifications liées à la réorganisation de la particule virale, ainsi que sa co-localisation avec les partenaires cellulaires tout au long du cycle viral.

Pendant les étapes précoces de son cycle réplicatif, le VIH-1 s'associe aux récepteurs CD4 à la surface des cellules immunitaires. Après la fusion de son enveloppe avec la membrane plasmique, le complexe viral entre dans le cytoplasme et se dirige vers le noyau. L'ARN viral est retranscrit par la transcriptase inverse en ADN génomique. Cette étape est accompagnée d'importantes réorganisations du complexe de transcription inverse (RTC) qui se transforme progressivement en complexe de préintégration (PIC). Le PIC entre ensuite dans le noyau, par l'intermédiaire des pores nucléaires. Une fois dans le nucléoplasme, il intègre l'ADN viral dans le génome de la cellule hôte.

Dans cette étude, nous nous sommes intéressés plus particulièrement à la protéine de nucléocapside 7 (NCp7) du HIV-1. Il s'agit d'une petite protéine composée de 55 acides aminés qui forment deux doigts de zinc et une séquence portant plusieurs charges positives à son extrémité N-terminale. Du fait de son affinité pour les acides nucléiques, elle joue un rôle important en tant que protéine chaperonne au cours de l'infection. Dans les virions matures le dimère d'ARN génomique est recouvert et stabilisé par ~2000 molécules de NCp7. Pendant la transcription inverse la NCp7 assiste la transcriptase inverse (RT) en facilitant les deux sauts de brins obligatoires. Dans le noyau, elle participerait au processus d'intégration. Enfin pendant l'assemblage le domaine NC de la polyprotéine Gag fixe spécifiquement les ARN viraux. Bien que sa fonction ait été largement étudiée d'un point de vue mécanistique par les approches *« in vitro »,* son trafic intracellulaire ainsi que ses interactions avec les structures cellulaires au cours de l'infection restent peu connues. Dans cette optique, l'objectif de ce

travail de thèse est de suivre la NCp7 au cours des étapes précoces du cycle viral du VIH-1 pour visualiser l'effet du remodelage RTC - PIC et son entrée nucléaire par différentes techniques avancées de microscopie de fluorescence.

Résultats

Au cours de nos expériences nous avons utilisé comme modèle, les particules du VIH-1 pseudotypés avec la protéine d'enveloppe du virus de la stomatite vésiculaire (VSV-G) et portant le gène de la luciférase comme rapporteur d'infectivité. Dans ces pseudovirus, la protéine de nucléocapside ou l'intégrase sont fusionnées à un tag tetracysteine (TC). Nous avons montré que cette fusion diminuait l'infectivité des virus contenant la NCp7-TC de 60%, alors que l'infectivité des virus contenant IN-TC est resté au niveau des virus sauvages.

Ces pseudoparticules ont été ensuite utilisées pour suivre la NCp7 au cours des étapes précoces de l'infection. Dans ce but, nous avons employé différentes techniques de microscopie de fluorescence « classique » et de haute résolution, de l'AFM et de la microscopie électronique.

La libération cytoplasmique de la NCp7 pendant les étapes précoces de l'infection

Dans le virion mature, le dimère d'ARN est stabilisé par ~2000 molécules de NCp7. Compte tenu de la taille de la capside qui est approximativement d'une centaine de nanomètres, la concentration locale en NCp7 peut atteindre des dizaines de mM. Il est connu pour les fluorophores de type fluorescéine que ce confinement peut provoquer un autoquenching (extinction de la fluorescence). Afin de vérifier cette hypothèse nous avons produit et marqué par FlAsH (qui devient fluorescent en se liant au tag TC) les virus contenant différentes proportions de NCp7 taguée (100%, 50% et 15%). Les mesures de leur fluorescence ont montré une augmentation de signal inversement proportionnelle à la fraction de NCp7 marquée (Figure 1). Cet effet a été observé dans les virions isolés déposés sur une lamelle et également dans les cellules infectées. Nous avons donc montré qu'il est possible de suivre les modifications de la concentration de NCp7-TC/FlAsH dans les virions en suivant l'intensité de leur fluorescence.

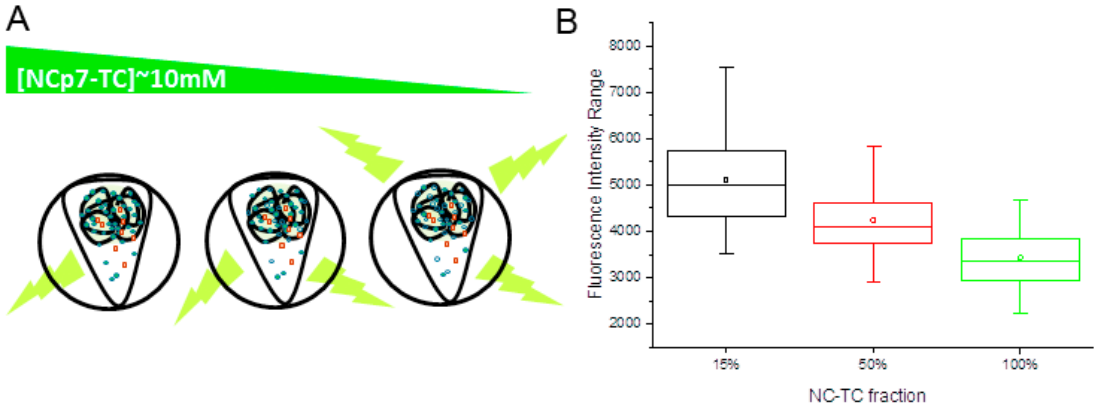

Figure 1 : Schéma du principe d'autoquenching du FlAsH dans les virions NCp7-TC (A) et distribution des intensités de fluorescence pour les complexes viraux contenant 100%, 50% et 15% de NCp7-TC (B).

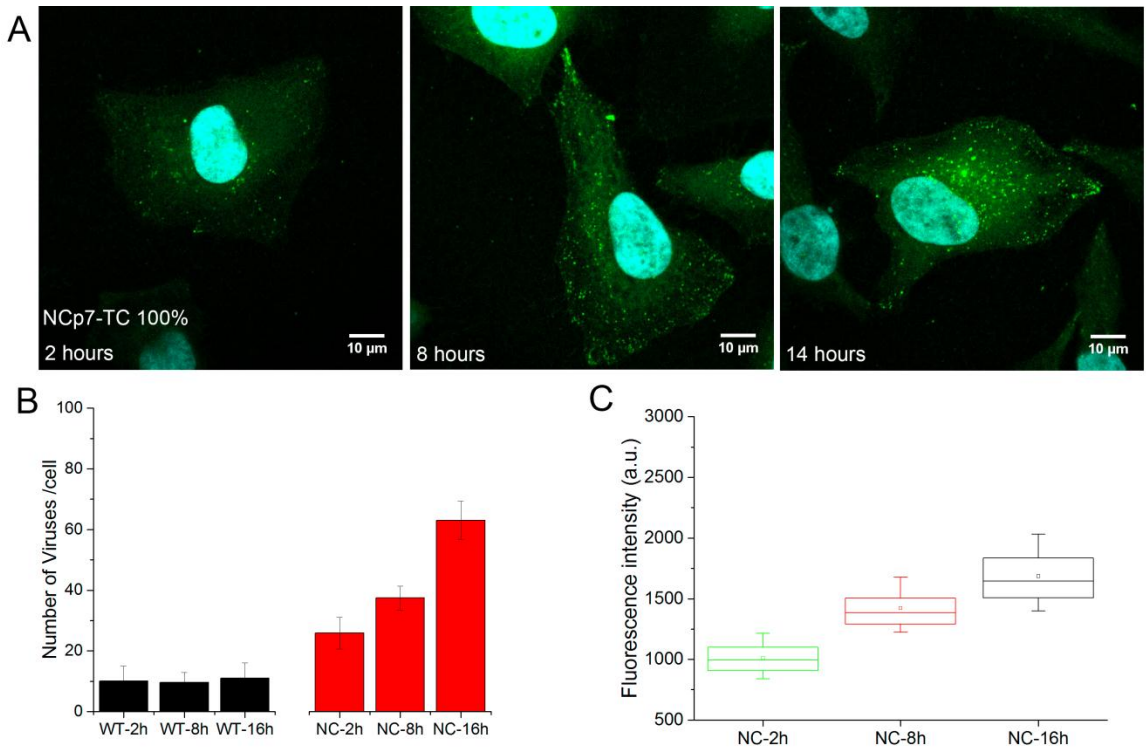

Figure 2: Images typiques des cellules HeLa infectées par les pseudovirus NCp7-TC / FlAsH à 2, 8 et 16 heures d'infection. (B) L'évolution du temps du nombre moyen de particules détectées par cellule pour différents types des peudoviruses avec protein NCp7 sauvage et 100% de NCp7-TC. (C) Évolution du temps de l'intensité de fluorescence moyenne de 1000-2000 points fluorescents détectés dans 30 à 40 cellules pour chaque point de temps pour 100% de NCp7-TC.

Ensuite, les modifications d'intensité de fluorescence des virus contenant 100% NCp7-TC ont été mesurées au cours de l'infection. Figure 2 montre les images typique des cellules HeLa infectées avec les pseudovirus VIH-1 pendant 2, 8 et 16 heures. De nombreux points de forte intensité présents dans le cytoplasme correspondent à des particules virales. Leur nombre augmente avec le temps probablement à cause d'internalisation progressive des virions initialement fixées à la surface de la membrane plasmique ou au cours de la dissolution des agrégats (Figure 2B). Les pseudovirus sauvages, qui ne portent pas de tag TC

montrent juste un faible signal de fluorescence du au marquage non spécifique. De plus le nombre des pseudovirus WT détectés dans les cellules reste constant au cours de l'infection (Figure 2B). En mesurant l'intesité de fluorescence au cours de temps nous avons mis en évidentce une augmentation de fluorescence des pseudovirus à 8 heures et à 14 heures post-infection. Compte tenu de nos expériences préliminaires, il est probable que cette augmentation de fluorescence reflète la diminution de concentration locale de la NCp7 dans le complexe viral. En plus cet effet n'a pas été observé pour les virus contenant IN-TC et il est significativement réduit en présence d'AZT, un inhibiteur spécifique de la RT. Ces observations suggèrent une libération de la NCp7 après la transcription inverse. L'analyse spatiale a révélé que ce relargage est plus efficace à proximité de noyau. Une augmentation de 60% a été mesurée dans le périmètre de 3.5µm de l'enveloppe par rapport à la périphérie des cellules, indiquant que la transcription inverse est réalisée quand les complexes viraux atteignent l'espace perinucléaire.

En conclusion nos données montrent, pour la première fois, la distribution de la protéine de nucléocapside pendant les réarrangements structuraux des complexes viraux liés à la RT. D'après de récents modèles, basés sur des expériences *« in-vitro »* ce réarrangement serait accompagné de la libération progressive de la NC. Nos résultats confirment cette hypothèse en mettant en évidence une diminution de la concentration de la NCp7-TC dépendante de la transcription inverse dans les virions à 8-14 heures post-infections.

Imagerie de haute résolution PALM-FlAsH de NCp7 au cours des stades précoces de l'infection

La taille des virus du VIH-1 est deux fois inférieure à la limite de résolution des microscopes optiques « classiques ». Par conséquent, pour imager les modifications structurales des virions au cours de l'infection nous avons choisi d'employer une de techniques de microscopie de haute résolution- PALM/STORM (Photo-Activation Localization Microscopy/Stochastic Optical Reconstruction Microscopy). Cette technique est basée sur des transitions successives des fluorophores entre états brillants et noirs, de sorte à avoir un seul fluorophore en état brillant dans la tache de diffraction. Les positions des fluorophores individuels sont ensuite extraites mathématiquement à partir de l'ajustement de la tache imagée à la forme de la PSF (fonction d'étalement du point) du microscope et l'image globale est reconstituée à partir de toutes les positions enregistrées. L'utilisation du marquage FlAsH pour PALM a été publiée une seule fois. Malgré cette publication, la mise au point de cette imagerie s'est avérée très complexe, nécessitant plusieurs mois d'optimisation des conditions expérimentales.

Dans un premier temps, nous avons imagé les pseudovirus contenant NCp7-TC et IN-TC déposés sur les lamelles. La distribution de tailles présente des maxima vers 90 nm pour les particules NCp7-TC et 70 nm pour IN-TC. Ces valeurs sont en accord avec les tailles observées pour les virions marqués sur MA, CA ou IN et avec nos observations par microscopie électronique (TEM) et AFM. Ensuite, les pseudovirus ont été imagés directement dans les cellules HeLa infectées. Comme nous l'avons vu par microscopie confocale, les cellules contiennent des particules de forte intensité dans le cytoplasme. La microscopie PALM nous a permis de visualiser les deux complexes viraux marqués sur IN et NC également à l'intérieur du noyau. La taille moyenne (110 à 115 nm) des pseudovirus marqués dans le cytoplasme est supérieure à celle des virus isolés. Par contre, les tailles des complexes nucléaires sont deux fois inférieures (~50 nm). Cette diminution témoigne clairement d'une forte réorganisation des complexes viraux à l'enveloppe nucléaire qui faciliterait l'internalisation dans le noyau.

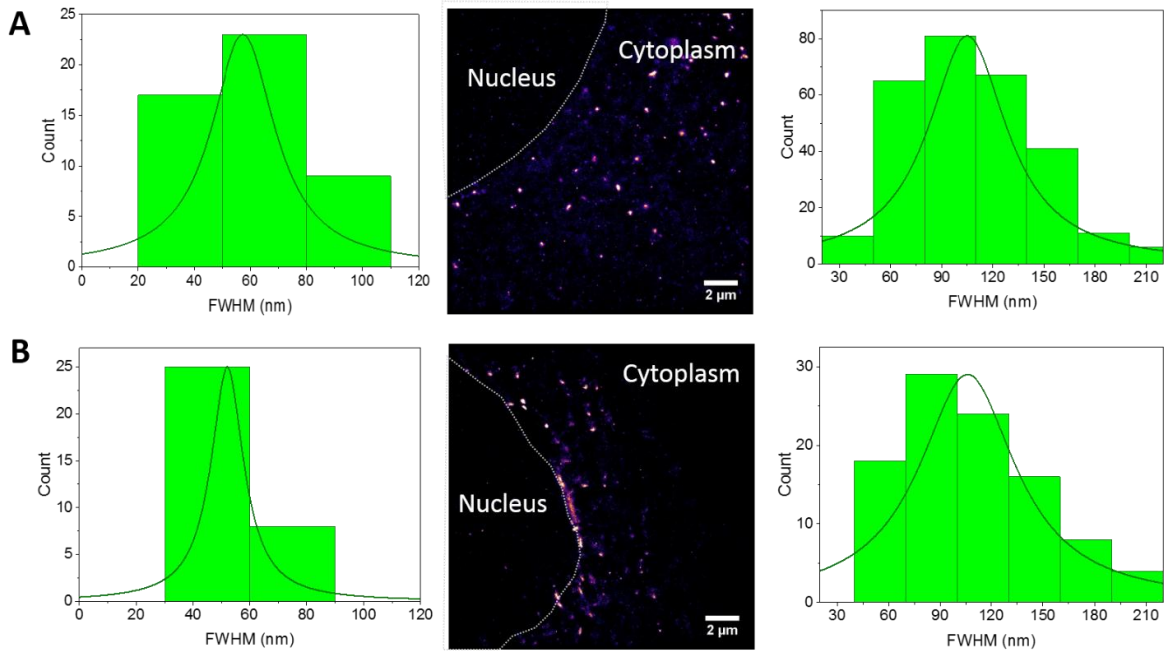

Figure 3 : Imagerie PALM des cellules HeLa infectées par les pseudovirus contenant (A) NCp7-TC et (B) IN-TC. Distribution des tailles des complexes nucléaires (gauche) et cytoplasmiques (droite).

Ensuite, nous avons étudié l'effet de l'inhibition de la RT sur la distribution cellulaire du NCp7-TC et de l'IN-TC dans les cellules HeLa. Les images typiques des cellules HeLa infectées par les pseudovirus contenant de la NCp7-TC pedant 2 et 14 heures sans ou en présence d'AZT sont montrées figure 4.

En présence de l'AZT, les taches nucléaires NCp7-TC n'ont été détectées que dans 40% des cellules imagées, ce qui indique que l'inhibition de la RT a pertubée l'import nucléaire. Le même effet a été observé pour l'In-TC. Ces résultats indiquent que l'inhibition

de la RT perturbe clairement le cycle viral et l'ARN non transcrit ne pénètre pas dans le noyau, même si certaines exceptions ont été observées (dans ces cellules, la densité nucléaire des complexes NCp7-TC/FlAsH et leur taille n'ont pas été modifiées (Figure 5)). Le signal nucléaire pourrait provenir des PIC qui échappaient à l'inhibition de la RT et la synthèse de l'ADN pendant les 2 premières heures d'infection avant l'addition de l'AZT, ou encore des RTC qui ont réussi à pénétrer dans le noyau en dépit de l'inhibition de la RT.

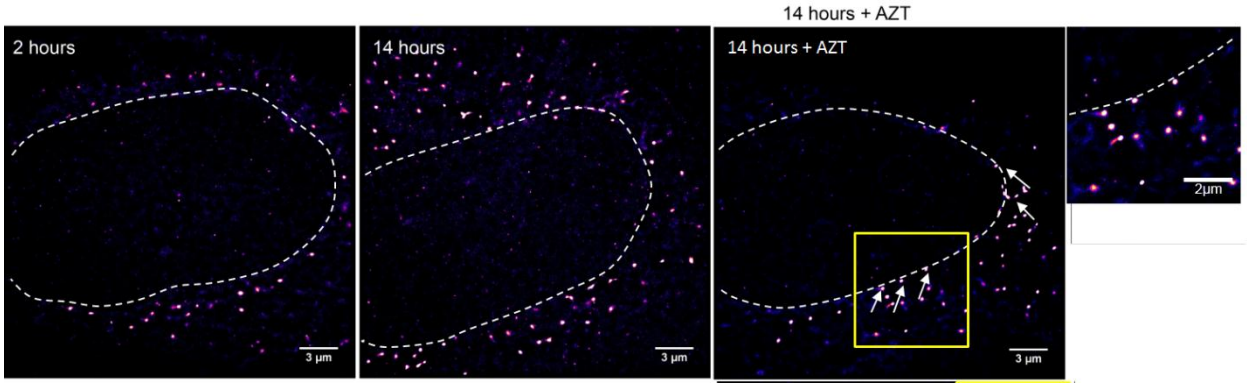

Figure 4: Influence de l'inhibiteur de RT sur la distribution intracellulaire de NCp7-TC. Images HR des cellules HeLa infectées par des particules pseudovirales contenant 100% de NCp7-TC / FlAsH pendant 2 et 14 heures en présence ou en l'absence d'AZT. Les complexess NCp7-TC / FlAsH (flèches blanches) ont révélé une localisation perinucléaire (région agrandie) après 14h d'infection en présence de l'AZT.

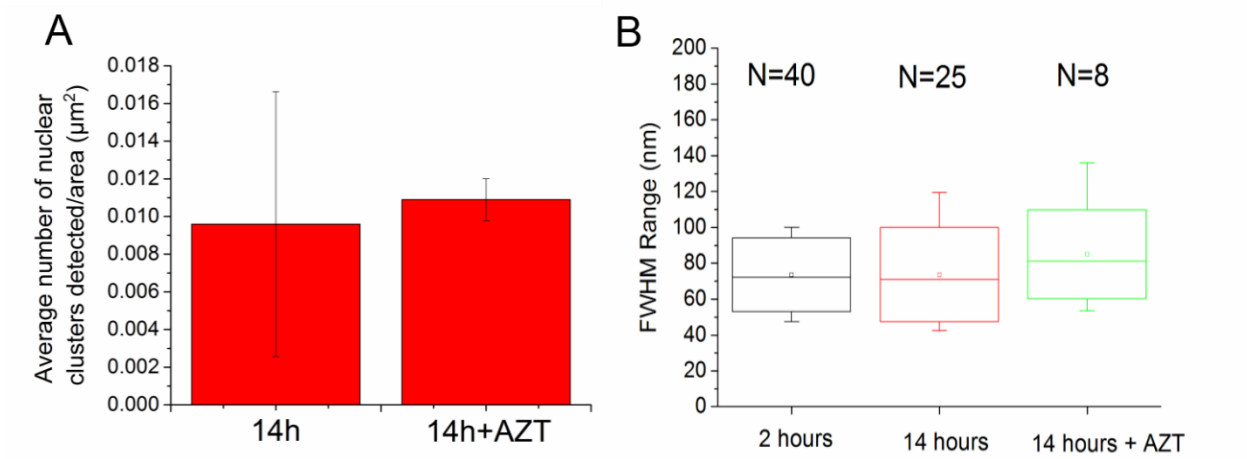

Figure 5: (A) Densité des complexes nucléaires détectées après 14 h d'infection. (B) La représentation graphique de la distribution de taille des particules nucléaires NCp7-TC détectées dans 7 cellules avec une valeur moyenne de 2 h est de 70 +/- 20 nm, 80 +/- 25 nm à 14 h p. je. Et 85 +/- 25 pour 14 h p.i. en présence de l'AZT.

La présence de l'intégrase à l'intérieur du noyau est attendue car cette enzyme est responsable de processus d'intégration. Néanmoins les données démontrant la localization nucléaire de la NCp7 lors de l'infection sont rares. Nos images permettent de renforcer l'hypothèse de son possible rôle biologique pendant les étapes nucléaires du cycle viral. De plus, les tailles des complexes contenant de la NCp7-TC correspondent bien à celles des

complexes comportant IN-TC, ce qui renforce l'hypothèse que les deux protéines font partie des mêmes complexes. Toutefois, la démonstration de ces d'hypothèses nécessiterait des expériences complémentaires (par exemple montrant la co-localization des deux protéines avec l'ADN viral), pour être vérifiée. De plus, pour comprendre le rôle de la NCp7 dans le noyau il est primordial de déterminer sa voie d'internalisation nucléaire.

Entrée nucléaire de la NCp7

En tenant compte de la petite taille de NCp7 et de son trafic pendant les étapes précoces de l'infection, son internalisation nucléaire pourrait être réalisée par deux voies différentes : (i) par diffusion passive en tant que molécule libre, relarguée lors de la transformation du RTC en PIC et/ou (ii) via un import actif en tant que composant du PIC. Dans le but d'identifier la voie d'entrée principale de la NCp7, nous avons étudié l'effet de l'inhibition de l'import nucléaire actif sur son entrée nucléaire ainsi que sa co-localisation avec les pores nucléaires (par microscopie photonique et électronique). Sachant que le PIC est internalisé par import actif, les pseudovirus marqués sur l'Intégrase ont été utilisés dans ces expériences comme contrôle positif.

Les cellules HeLa ont été infectées par les pseudovirus marqués dans les conditions « normales » et en déplétion d'énergie (qui inhibe l'import nucléaire actif). Les images PALM (Figure 6) ont révélé que la déplétion d'énergie a causé une baisse de 60% de la fraction nucléaire des complexes IN-TC, en accord avec le fait que l'entrée nucléaire de l'IN-TC au sein du PIC est réalisée par transport actif. De la même manière, la fraction nucléaire des complexes de NCp7-TC baisse de 40% indiquant que cette protéine entre également par la même voie d'internalisation nucléaire (Figure 7).

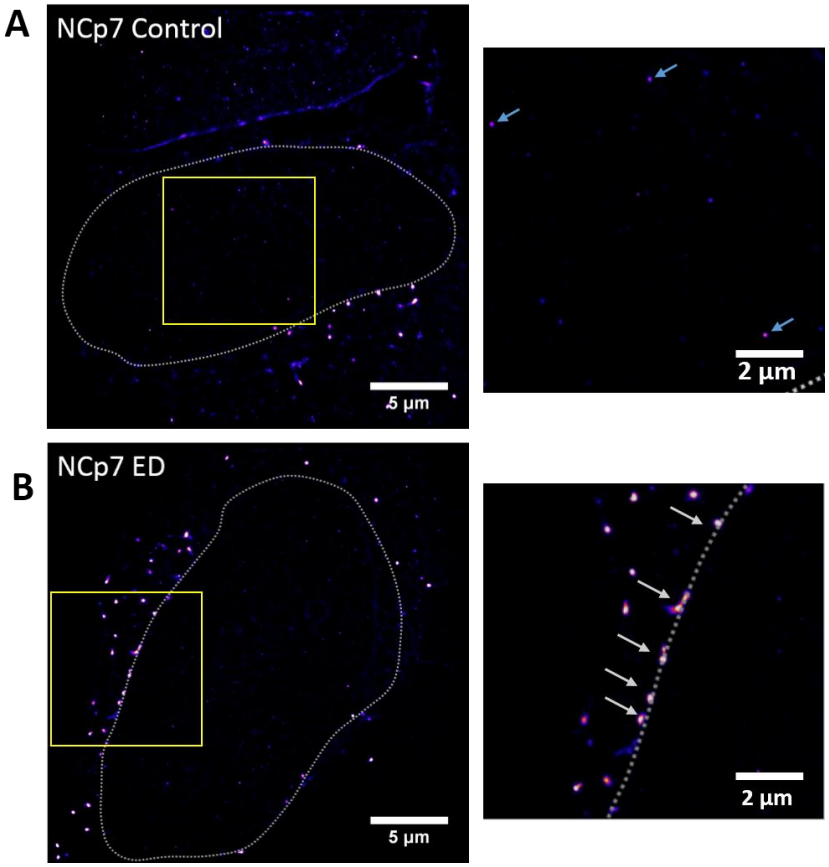

Figure 6: Influence de la déplétion d'énergie sur la localisation intracellulaire des pseudoparticules marquées par NCp7-TC / FlAsH. (A) des images PALM des ROI des cellules HeLa infectées par le NCp7-TC / FlAsH dans les conditions physiologiques (Contrôle) et (B) dans les condition de déplétion énergétique (ED). Les régions zoomées ont révélé une localisation nucléaire de NCp7 après 120 min d'infection dans l'échantillon témoin (A) et une forte localisation périnucléaire en condition ED

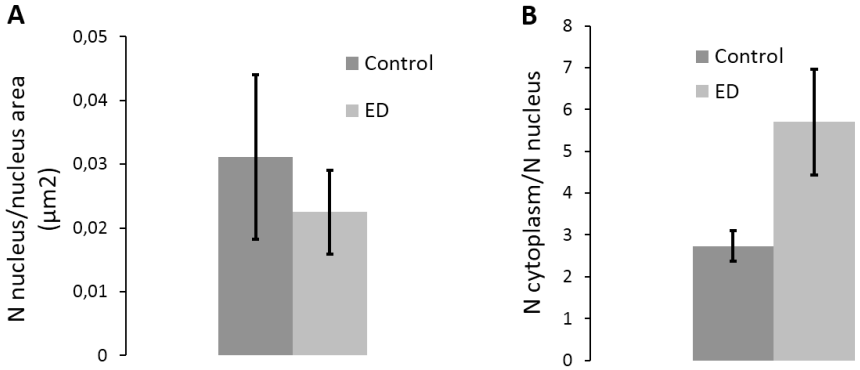

Figure 7: Quantification des complexes NC marqués à l'intérieur du compartiment nucléaire. (A) Nombre de complexes viraux détectés par zone de noyau et (B) entre le nombre de complexes trouvés dans le cytoplasme et le noyau.

Pour vérifier si la NCp7-TC entre dans le noyau au sein du PIC, nous avons comparé le niveau de co-localisation de la NCp7-TC avec les pores nucléaires à celui de l'lN-TC. Dans nos conditions expérimentales (microscopie confocale, milieu intracellulaire), il est impossible de détecter une molécule unique. Par conséquent, les points fluorescents observés représentent des complexes contenant plusieurs molécules de NCp7-TC. Il s'agirait donc de

RTC ou de PIC. Le niveau de co-localisation avec les NPC par rapport à celui de l'IN-TC nous renseigne sur la probabilité de présence de la NCp7 au sein du PIC avant ou pendant l'internalisation. Les images des pores nucléaires (Figure 8A, canal vert) dans les cellules HeLa infectées avec les virus TC marqués avec du ReAsH montrent des points co-localisés (jaune) et des virus qui ne se trouvent pas à proximité des pores nucléaires (rouge). Le taux de co-localisation moyen, mesuré sur 20 cellules pour 150 virus détectés à l'enveloppe nucléaire représente 22+/- 5 % pour IN-TC et 20+/-3% pour NCp7-TC (Figure 8B). Les niveaux de co-localisation sont donc pratiquement identiques, indiquant qu'une partie des molécules de NCp7 est probablement toujours fixée sur le PIC quand celui-ci est sur le point d'entrer dans le noyau.

Ces complexes de NCp7-TC, situés à proximité des pores nucléaires ont été également observés par microscopie électronique de transmission (Figure 9).

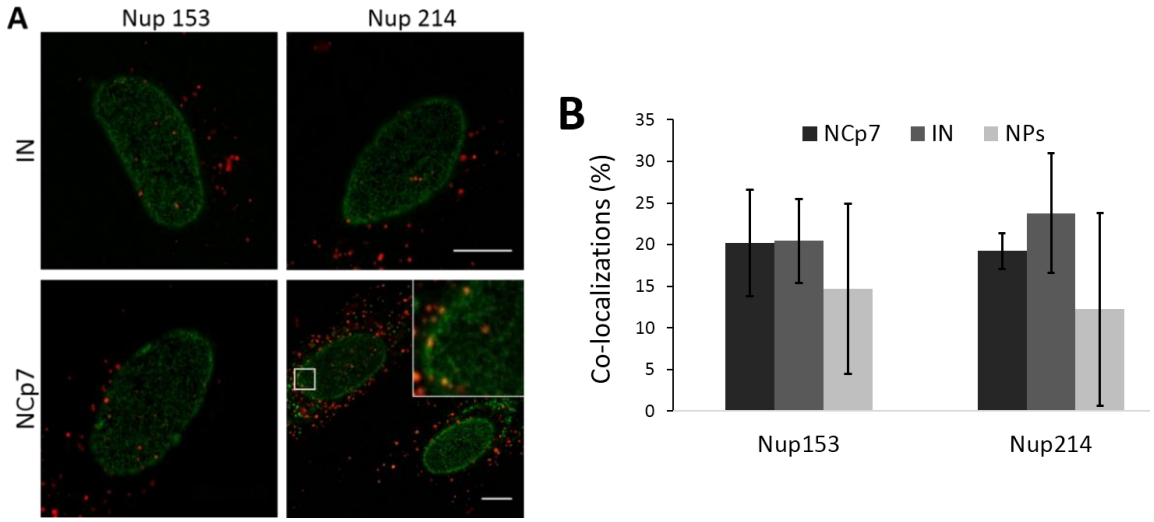

Figure 8 : (A) Cellules HeLa exprimant Nup153-eGFP (vert) 8h après infection par des pseudovirus NCp7-TC/ReAsH (rouge, barre 10 µm) et agrandissement de la zone du carré jaune et (B) pourcentage de co-localisations de NCp7 / IN-TC, NPs et Nup153 et Nup214 calculées à partir de 10 cellules pour chaque condition.

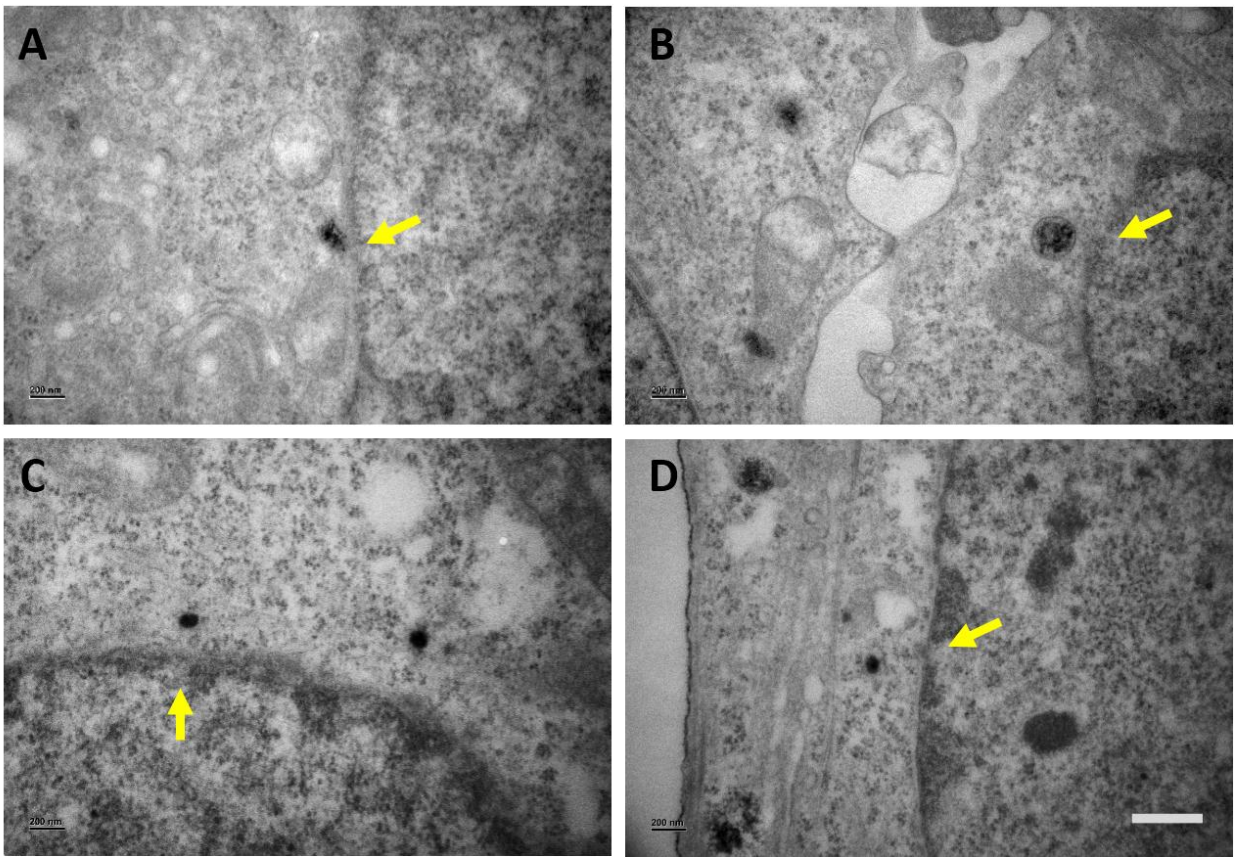

Figure 9 : Image TEM d'un complexe NCp7-TC/ReAsH à proximité d'un pore nucléaire. Les flèches jaunes indiquent les pores nucléaires. Barre d'échelle 400 nm.

Enfin, Iryna a lors de la partie Ukrainienne de sa thèse en co-tutelle, développé des nanoclusters d'argent qui auraient dû permettre de marquer les particules virales. L'enrobage des nanoclusters et leur stabilité dans le temps ont été complexes à maîtriser et n'ont pas permis de réaliser les marquages initialement prévus. Néanmoins, un papier a pu être publié (avec Iryna en 1er auteur) sur les différents enrobages testés et leurs effets sur la stabilité et les propriétés photophysiques des nanoclusters.

Conclusions et perspectives

Dans ce travail de thèse, nous avons utilisé différentes techniques microscopiques dans le but de suivre la protéine de nucléocapside du VIH-1 au cours des étapes précoces de l'infection. Le rôle de cette protéine en tant que chaperonne des acides nucléiques est bien connu, toutefois, son trafic intracellulaire et sa présence au sein du complexe viral pendant les différentes réorganisations structurales précédant son import nucléaire n'ont jamais été clairement établis dans le contexte de l'infection. En utilisant des pseudovirus VIH-1 contenant la NCp7 fusionnée à un tag tetracysteine marqué par FlAsH, nous avons pu imager cette protéine dans le cytoplasme et dans le noyau de la cellule hôte. Par des mesures d'intensité de fluorescence, nous avons mis en évidence un phénomène de dequenching relié à

la diminution de la concentration en NCp7 dans les complexes viraux qui témoigne, dans le contexte de l'infection, du relargage cytoplasmique d'une partie des molécules de NCp7 au cours de la transcription inverse. Par ailleurs, les complexes nucléaires correspondant vraisemblablement au PIC ont été mis en évidence par microscopie de haute résolution PALM. Nos résultats montrent que les PICs marqués par NCp7-TC ou IN-TC sont présents dans le nucléoplasme. Nous avons mis en évidence une forte diminution de taille entre les complexes cytoplasmiques et nucléaires, probablement suite à la réorganisation RTC-PIC, précédant l'internalisation nucléaire. En outre, nous avons montré une co-localisation des complexes contenant la NCp7 avec les pores nucléaires, comparable à celle des PICs. De plus, l'inhibition de l'import nucléaire actif a significativement réduit la fraction de complexes NCp7-TC nucléaires. Ces données montrent que la NCp7 est majoritairement internalisée par voie active (probablement au sein du PIC), même si elles n'excluent pas que des molécules de NCp7 entrent dans le nucléoplasme par diffusion libre.

Afin d'établir clairement la présence de la NCp7 au sein du PIC et son possible rôle pendant l'intégration, il est envisagé de continuer cette étude par le suivi de la co-localisation de la NCp7 avec les protéines du PIC ou le génome viral par imagerie PALM à deux-couleurs. Il serait également intéressant de suivre la dégradation de la NCp7 cytoplasmique après son relargage. D'après plusieurs études, la grande majorité serait dégradée par les protéases cellulaires. Toutefois, d'autres études ont montré des interactions spécifiques avec les protéines ou les ARN ribosomaux où elle pourrait influencer la traduction.

En conclusion, ce travail de thèse a permis de suivre la distribution cellulaire de la NCp7 dans un contexte proche d'une véritable infection par des techniques d'imagerie avancée. En plus des informations fondamentales sur le cycle réplicatif du VIH-1, les approches microscopiques développées pourront être mises à profit dans des études de détermination des mécanismes d'action d'inhibiteurs spécifiques de la NCp7 ou dans la phase d'optimisation du design de nouvelles molécules thérapeutiques. En parallèle, elles seront utiles pour identifier le rôle biologique des interactions de la NCp7 avec les partenaires cellulaires étudiés au laboratoire.